POLITECNICO DI MILANO
DEPARTMENT OF ENERGY
DOCTORAL PROGRAM IN ENERGY AND NUCLEAR SCIENCE AND TECHNOLOGY

REDUCED ORDER METHODS: APPLICATIONS TO NUCLEAR REACTOR CORE SPATIAL DYNAMICS

Supervisors:
Prof. Antonio Cammi
Prof. Lelio Luzzi
Prof. Gianluigi Rozza

Tutor:
Prof. Lelio Luzzi

The Chair of the Doctoral Program:
Prof. Carlo Enrico Bottani

Doctoral Dissertation of:
Alberto Sartori

27^{th} Cycle
February 2015 – Milano, Italy

A Maria

Abstract

THE context of the present PhD thesis is the research domain oriented towards the development and assessment of advanced simulation tools, employing the most recent reduced order methods, for nuclear reactor core spatial dynamics.

The potential of reduced order methods with respect to the current and/or classical approaches is firstly addressed. In particular, two modelling approaches based on a Modal Method and on the Proper Orthogonal Decomposition technique, for developing a control-oriented model of nuclear reactor spatial kinetics, are compared. The comparison of the outcomes provided by the two approaches focuses on the capability of evaluating the reactivity and the neutron flux shape in different reactor configurations, where different type of perturbations (i.e., homogeneous or localized) are applied.

Subsequently, taking advantage of the capabilities of reduced order models just highlighted, the modelling of control rods movement is dealt, solving *ad hoc* parametrized multi-group neutron diffusion equations both in the time-dependent and stationary formulations. Several accurate and reliable reduced order models have been developed, which are able to take into account the spatial effects induced by the rods movement still featuring a real-time computational time. A different sampling technique, within the Reduced Basis framework, has been employed, namely, the centroidal Voronoi tessellation, which allows for a hierarchical parameters space exploration, without relying on an *a posteriori* error estimation. In this way, the Offline computational time might be sensibly reduced.

Even though the aforementioned analysis is "limited" to neutronics only, the potential of a multi-physics approach (i.e., where all the involved physics are solved within the same computational environment) has been considered as well. In fact, a multi-physics time-dependent model for a Lead Fast Reactor single-channel analysis is developed and presented. Thereafter, relying on this work, a preliminary multi-physics reduced order model is proposed as proof of concept, where all the methodologies and skills acquired during the PhD work are applied.

Contents

Acronyms V

Introduction 1
Objectives and outline of the thesis 2

1 Potential of reduced order methods 5
1.1 Introduction 7
1.2 Modelling 9
1.3 Modal Method approach 13
1.4 POD-based approach 15
1.5 Reactivity evaluation by means of the Inverse Method 16
1.6 Results and discussion 18
1.7 Concluding remarks 33
Chapter 1 Nomenclature 34

2 Reduced basis approaches in time-dependent settings for control rod movement 35
2.1 Introduction 37
2.2 Modelling approach 38
2.3 Reduced basis method 39
2.4 One rod 3D modelling: piece-wise affine transformation 51
2.5 Three rods 3D modelling: a “staircase” approach 59
2.6 Concluding remarks 65

3 Reduced basis approach for generalized eigenvalue calculation 67
3.1 Introduction 69
3.2 Reduced basis strategies for generalized eigenvalue problems 69
3.3 Parametrized model 71
3.4 Representative results 77
3.5 Concluding remarks 82

4 Conclusions 85

A TRIGA Mark II reactor **89**

B A multi-physics time-dependent model for the Lead Fast Reactor single-channel analysis **93**
B.1 Multi-physics modelling approach 94
B.2 Validation of COMSOL neutronic model 104
B.3 Results and discussion 108
Appendix B Nomenclature 119

C A multi-physics reduced order model for the analysis of Lead Fast Reactor single channel **121**
C.1 Parametrized multi-physics model 122
C.2 Reduced basis strategies for the coupled problem 126
C.3 Numerical results 128
C.4 Concluding remarks and perspectives 136
Appendix C Nomenclature 138

D Algorithms and benchmarks **141**
D.1 Heat transfer: thermal block 141
D.2 Heat transfer: thermal block with a parametrized hole 145
D.3 Heat transfer: thermal fin 147
D.4 A linear elasticity block 152

Ringraziamenti **171**

Acronyms

BC	Boundary Conditions
BE	Backward Euler
BOL	Beginning Of Life
BWR	Boiling Water Reactor
CFD	Computational Fluid Dynamics
CVT	Centroidal Voronoi Tessellation
DAE	Differential Algebraic Equation
ECCO	European Cell COde
ELSY	European Lead-cooled SYstem
FE	Finite Element
ICTP	International Centre for Theoretical Physics
LFR	Lead Fast Reactor
MM	Modal Method
MOX	Modelling and Scientific Computing, Department of Mathematics
MP	Multi-Physics
MPM	Multi-Physics Modelling
MUMPS	MUltifrontal Massively Parallel sparse direct Solver
ODE	Ordinary Differential Equation
OSFA	Open Square Fuel Assembly
PK	Point Kinetics
POD	Proper Orthogonal Decomposition
PWR	Pressurized Water Reactor
RANS	Reynolds-Averaged Navier-Stokes
RB	Reduced Basis
RBEM	Reduced Basis Element Method
ROM	Reduced Order Model
SCM	Successive Constraint Method
SISSA	Scuola Internazionale Superiore di Studi Avanzati
SVD	Singular Value Decomposition
TRIGA	Training Research and Isotope production General Atomics

Introduction

In the analysis of the nuclear reactor dynamics, which is governed by the neutronics, the most spread approach is constituted by the *point-kinetics* equations (Schultz, 1961). This description of the neutronics is based on a set of coupled non-linear ordinary differential equations that describe both the time-dependence of the neutron population in the reactor and the decay of the delayed neutron precursors, allowing for the main feedback reactivity effects. Among the several assumptions entered in the derivation of these equations, the strongest approximation regards the shape of the neutron flux, which is assumed to be represented by a single, time-independent spatial mode.

Nuclear reactors are generally characterized by complex geometries and may feature asymmetric core configurations. Therefore, more accurate modelling approaches might be needed to provide more detailed insights concerning the reactor behaviour during operational transients. It is worth mentioning that the innovative reactor concepts, for instance Generation IV reactors (GIF, 2010), feature power density and temperature ranges, experienced by structural materials, such that the corresponding spatial dependence cannot be neglected. Moreover, in order to develop suitable control strategies for such reactors, the spatial effects induced by the movement of the control rods have to be taken into account as well.

From the modelling viewpoint, the highest fidelity approach is the so called Multi-Physics (MP) approach (see e.g., (Cammi et al., 2011; CASL, 2012; Mahadevan et al., 2012; Mylonakis et al., 2014)), where all the partial differential equations, which describe the involved physics, are solved within the same computational environment. The main drawback of the MP is that the computational burden is quite high, and simulating the entire core turns out to be very demanding in terms of computational costs and times. In addition, it is quite difficult to get the dynamics of the governing system and then set up a simulation tool that may assess and represent the dynamic response of the overall system at different operating conditions.

In this context, a computational reduced order technique, such as the Reduced Basis (RB) method (Rozza et al., 2008; Quarteroni et al., 2011), can lead to a simulation tool with real-time simulation, still solving a set of partial differential equations. The

goal of a computational reduction technique (Manzoni et al., 2012) is to capture the essential features of the input/output behavior of a system in a rapid and reliable way, i.e. (i) by improving computational performance and (ii) by keeping the approximation error between the reduced-order solution and the full-order one under control. In particular, the reduced order modelling is aimed at approximating a parametrized partial differential equation (or a set of partial differential equations) solution with a handful of degrees of freedom instead of thousands or millions that would be needed for a full-order approximation. In this way, the full-order problem has to be solved only for few instances of the input parameter (through a demanding Offline computational step), in order to be able to perform many low-cost reduced-order simulations (inexpensive Online computational step) for several new instances of the input.

It is worth mentioning that simplification – or approximation – of an equation, or a system of equations, describing a phenomenon is indeed a reduced order technique and it can be phrased as: "Reduce-then-discretize". The herein proposed reduced order methods are complementary and can be described as: "Discretize-then-reduce" and they can still benefit from the former approach.

This PhD work is aimed at tackling the need of nuclear engineering field to have accurate and reliable fast-running simulation tools, which can be tailored to common control systems, able to reproduce spatial effects, in particular those induced by the control rod movement. The present contribution can be considered as a first step towards building a bridge between the "world of design" and the "world of control". The goal is to demonstrate that reduced order modelling is suited to be applied in more complex (and coupled) industrial problems in order to introduce competitive computational performance and allowing, at the same time, a better investigation, thanks to the parametrization of involved phenomena. To this aim, a methodological approach for developing a reduced order model for systems with increasing complexity, up to a preliminary multi-physics LFR single channel, has been proposed as proof of concept.

Objective and outline of the work

The present thesis focuses on the development and assessment of innovative simulation tools, which are oriented to control and design purposes, for reactor core spatial dynamics, with particular attention to neutronics. The main novel contribution is the application of most recent advances in computational mathematics, namely the reduced order methods, such as the certified reduced basis method, to nuclear engineering field. According to the author's knowledge and to the current state of the art, this is the first time that such techniques have been employed in this context. Therefore, the work focused more on setting up and assessing an innovative methodology, rather than reproduce a real reference reactor.

Chapter 1 is devoted to address the potential of reduced order methods with respect to current and/or classical approaches, for developing control-oriented model of nuclear reactor spatial kinetics. This part was very important to understand *what* are the advantages of reduced order methods, *when* they might be useful, and *how* they can be applied. The potential and benefits of reduced order methods for reproduce spatial effects, highlighted in this analysis, have defined the track of the following research activity, which proceeded towards the modelling of control rods movement.

In particular, in Chapter 2 two approaches, based on the certified Reduced Basis

(RB) method, are developed for simulating the movement of nuclear reactors control rods in time-dependent (and non-coercive) settings. Throughout this Chapter, the RB method is detailed and applied to a set of parabolic equations (ten in this work) given by the multi-group neutron diffusion equations, which has been parametrized in order to allow for control rod movement. This work was the first step in the "RB world", and the skills as well as the methodological approach borrowed in this framework have been subsequently employed and improved.

An alternative quite popular in the reactor physics community to the direct discretization of the time-dependent neutron diffusion (or transport) equation is the so-called quasi-static approach (see e.g., Girardi et al., 2012). This approach is formally close to the adiabatic one (Duderstadt and Hamilton, 1976), except that the flux shape is recalculated at intervals during transients. Therefore, Chapter 3 is devoted to develop a reduced order model of a parametrized multi-group neutron diffusion equations in the stationary formulation, which is a generalized eigenvalue problem. The parametrization has been developed in order to allow for a continuous movement of the control rods. This contribution is thought to provide a methodological approach to improve the already employed control-oriented simulation tools, which are mostly based on the point-wise kinetics, allowing for the spatial effects. The main idea is that the temporal evolution can still be described according to PK equations, but at each time step the reactivity (and the neutron flux shape) is estimated by means of a fast-running and reliable reduced order model.

For these studies, the TRIGA (Training Research and Isotope production General Atomics) Mark II (General Atomic, 1964) of the University of Pavia (Italy) has been chosen as case study, because it is a pool-type reactor featuring a non-symmetric core configuration. The TRIGA reactor is briefly described in Appendix A.

Despite the fact that the aforementioned studies are "limited" to neutronics only, the potential of a multi-physics approach (i.e., where all the involved physics are solved within the same computational environment, allowing for higher-order coupling among the different physics, with respect to the classical approach based on the so-called coupled code techniques) has been considered as well and it is addressed in Appendix B. In fact, a multi-physics time-dependent model for a Lead Fast Reactor single-channel analysis is detailed. Thereafter, starting on this work, the methodologies developed in this thesis have been applied to a preliminary parametrized multi-physics LFR single channel, which is proposed as proof of concept in Appendix C. The potential of reduced order methods is addressed by taking into account both physical and geometric parameters. Moreover, a particular strategy for handling the non-linear coupling terms in order to achieve an efficient Offline/Online computational split is developed as well.

Throughout this PhD work, the reduced order models have been developed relying on different computational environments, i.e.: `FreeFem++` (Pironneau et al., 2012), `libMesh` (Kirk et al., 2006) within the `rbOOmit` framework (Knezevic and Peterson, 2011), and `FEniCS` (Logg et al., 2012). This has been done in order to emphasize that reduced order methods are not restricted to a particular software or library and that they can foster, in this way, a computational collaboration. Moreover, a developed on purpose procedure, which implements the certified reduced basis method, has been developed within the computational environment offered by the open-source finite element library `FEniCS`. Such procedure has been tested on different problems, which

are collected in Appendix D. It is worth mentioning that the developed procedure has begun to be used for teaching purposes within the SISSA (Scuola Internazionale Superiore di Studi Avanzati) doctoral programme Mathematical Analysis, Modelling and Applications (AMMA), as well as within the Master in High Performance Computing held by SISSA and ICTP (International Centre for Theoretical Physics).

CHAPTER 1

Potential of reduced order methods

To understand the potential of reduced order methods, with respect to current and/or classical approaches, two modelling approaches based on a Modal Method (MM) and on the Proper Orthogonal Decomposition (POD) technique, for developing a control-oriented model of nuclear reactor spatial kinetics, are presented and compared. Both these methods allow developing neutronics description by means of a set of ordinary differential equations. The comparison of the outcomes provided by the two approaches focuses on the capability of evaluating the reactivity and the neutron flux shape in different reactor configurations, with reference to a TRIGA Mark II reactor. The results given by the POD-based approach are higher-fidelity with respect to the reference solution than those computed according to the MM-based approach, in particular when the perturbation concerns a reduced region of the core. If the perturbation is homogeneous throughout the core, the two approaches allow obtaining comparable accuracy results on the quantities of interest. As far as the computational burden is concerned, the POD approach ensures a better efficiency rather than direct Modal Method, thanks to the ability of performing a longer computation in the preprocessing that leads to a faster evaluation during the Online phase. The advantage of reduced order methods, highlighted in this Chapter, have defined the track of the following research activity.

Main results are published in: Sartori, A., Baroli, D., Cammi, A., Chiesa, D., Luzzi, L., Ponciroli, R., Previtali, E., Ricotti, M.E., Rozza, G., Sisti, M., 2014, "Comparison of a Modal Method and a Proper Orthogonal Decomposition approach for multi-group time-dependent reactor spatial kinetics", Annals of Nuclear Energy 71, 217 – 229. The

methodology has been presented and discussed also into a seminar at MOX (Politecnico di Milano) entitled “Reduced Order Techniques in Nuclear Physics”, June 3, 2013.

1.1 Introduction

In the development of the control systems, the preliminary stage of modelling mainly concerns the correct evaluation of the representative system time constants, and getting the fundamental aspects related to the plant response to the outside perturbations. For this reason, in control oriented simulators, the model is usually based on non-linear systems of Differential-Algebraic Equations (DAEs), expressed by $\dot{\mathbf{x}} = \mathbf{f}(t, \mathbf{x}, \mathbf{z})$. Indeed, the system of Ordinary Differential Equations (ODEs) for $\mathbf{x}(t)$ depends on additional variables and the solution is forced to satisfy algebraic constraints $\mathbf{0} = \mathbf{g}(t, \mathbf{x}, \mathbf{z})$ (Ascher and Petzold, 1997). In many cases, it is sufficient to employ simplified lumped parameter models, which neglect the spatial dependence of the variables, studying only the average behaviour of the system and its temporal evolution. In addition, these systems of differential equations can be easily linearized in order to study the system behaviour close to a given operating condition. In this way, it is possible to use the tools of linear analysis, which allow achieving effective solutions that can be applied to the original non-linear models. For these reasons, in the analysis of the nuclear reactor dynamics, the most diffused approach is constituted by the *Point-Kinetics* (PK) equations (Schultz, 1961). This description of the neutronics is based on a set of coupled non-linear ODEs that describe both the time-dependence of the neutron population in the reactor and the decay of the delayed neutron precursors, allowing for the main feedback reactivity effects. Among the several assumptions entered in the derivation of these equations, the strongest approximation regards the shape of the neutron flux, which is assumed to be represented by a single, time-independent spatial mode. Indeed, it is common to adopt a shape function characterizing a critical core configuration if the reactor is close to the critical state or on a truly asymptotic period. When the changes in core composition are sufficiently slow, an instantaneous steady-state criticality calculation of the shape function can be performed, even though this shape will slowly change with time. Such a scheme is known as the *adiabatic approximation* (Duderstadt and Hamilton, 1976).

Otherwise, whether the reactors are characterized by complex geometries and asymmetric core configurations, more accurate modelling approaches may provide more detailed insights concerning the reactor behaviour during operational transients. It is worth mentioning that the development of innovative reactor concepts, for instance Generation IV reactors (GIF, 2010), feature power density and temperature ranges, experienced by structural materials, such that the corresponding spatial dependence cannot be neglected.

It is therefore necessary to develop a sufficiently accurate description of the reactor core spatial dynamics, based on a set of ODEs to be employed in a control-oriented simulator. To this aim, in the present Chapter, the capabilities of two approaches – the *Modal Method* (MM) (Stacey, 1969; Xia et al., 2012) and one based on the *Proper Orthogonal Decomposition* (POD) (Holmes et al., 1996; Chatterjee, 2000; Liang et al., 2002; Buchan et al., 2013) technique – are compared on a 2D domain. The comparison focuses on the capability of the two approaches of reproducing both the reactivity and the neutron flux shape for different reactor configuration, with reference to a TRIGA Mark II reactor (General Atomic, 1964). Such reactor has been selected as case study because it is a pool-type reactor, whose core features a non-symmetric configuration.

However, the focus of the present Chapter is the comparison of the above mentioned MM and POD approaches to find out the right track to be pursued in the future. Therefore, since this study is more concerned on the modelling approaches, rather than the reactor model itself, the geometry of the reactor has been taken 2D to speed up the computational time.

The MM approach was theorized in the sixties (Stacey, 1969) but it was not systematically employed because of the high computational burden for the determination of the higher order eigenfunctions of a reactor core. The MM, basically, approximates a function by means of a linear combination of its eigenfunctions. Nowadays, in literature it is possible to find many attempts in developing non-zero dimensional reactor models for different applications by means of modal synthesis method. For example, the harmonic synthesis method has been used to perform the reconstruction of a reactor core flux distribution starting from the Online data acquired inside the reactor itself (Fu et al., 1997). Subsequently, a 3D reactor power distribution control in a load-following mode was investigated based on this developed reactor kinetic model (Wenfeng et al., 2001). A similar modal method has been used to describe the neutron diffusion process (Miró et al., 2002). This method has been applied to investigate in-phase and out-of-phase oscillations in a BWR. An eigenvalue separation technique has been investigated (Obaidurrahman and Singh, 2010) for 3D neutronic coupling and decoupling aspects of a 1000 MW PWR nuclear reactor. The modal analysis has also been applied for studying temporary instabilities observed in a BWR (Ginestar et al., 2002). More recently, the MM approach has been applied to study the kinetics of a CANDU reactor (Xia et al., 2012, 2014).

Similarly to the MM, the POD was not recently theorized (Pearson, 1901) but it was not widely exploited until the advent of electronic computers. The POD is a reduction order technique aimed at obtaining the most characteristic structure of the problem using a low-dimensional approximate descriptions of a high-dimensional process (Quarteroni et al., 2011). Applications of POD include image processing, data compression, signal analysis, modelling and control of chemical reaction systems, turbulence models, coherent structures in fluids, control of fluids and electrical power grids. In the nuclear engineering field, POD has not been extensively employed, even though its potentialities have been underlined, e.g., (Merzari and Ninokata, 2011) and (Prill and Class, 2014) to name a few. In literature, examples of the application of POD to neutronics can be found in (Wols, 2010) and (Buchan et al., 2013). The former presents a POD-based reduced order model for the mono-energetic generalized eigenvalue equation, which is associated to the neutron diffusion equation in the steady state condition. In the latter, the multi-group time-dependent neutron flux is approximated as a linear combination of α-eigenfunctions, while the POD is briefly addressed and not applied to the time-dependent problem. The study reported in the present paper shares some aspects with the work of (Wols, 2010) and such approach has been further improved. Indeed, for the first time, the POD capabilities are exploited for solving the multi-group time-dependent neutron diffusion equation by training the POD basis to handle localized perturbations. In this work, two opportunities of this approach have been exploited: the primal Galerkin projection onto a low dimensional space, which is spanned by the so-called most energetic basis (Merzari and Ninokata, 2011), and Offline/Online decomposition strategies, which allow achieving small calculation cost for a high

performance in real-time simulation. As a major outcome, there is a great saving in Online computation for each input-output evaluation of the quantities of interest, while an increase of pre-processing (Offline) calculation has to be dealt with (Rozza et al., 2008).

The Chapter is organized as follows. Section 1.2 presents the reactor chosen as case study and its modelling. The MM and the POD approaches are described in Sections 1.3 and 1.4, respectively. In Section 1.5, the Inverse Method used to compute the reactivity according to the two approaches is presented. Subsequently, the comparison between the MM and POD results is detailed in Section 1.6. Finally, the main conclusions are drawn in Section 1.7. The adopted nomenclature is listed at the end of the Chapter.

1.2 Modelling

The TRIGA Mark II reactor of the University of Pavia (Italy) has been chosen as case study (see Appendix A on page 89).

In order to describe the neutron kinetics the multi-group diffusion theory (Duderstadt and Hamilton, 1976), with two energy groups and eight group of precursors (C_m) has been employed. In equations, it reads:

$$\begin{cases} \underline{\underline{V^{-1}}}\dfrac{\partial \underline{\Phi}}{\partial t} = \nabla \cdot \left(\underline{\underline{D}}\nabla\underline{\Phi}\right) - \underline{\underline{\Sigma_a}}\underline{\Phi} - \underline{\underline{\Sigma_s}}\underline{\Phi} + (1-\beta)\underline{\chi_p}\underline{F}^T\underline{\Phi} + \\ \qquad\qquad + \displaystyle\sum_m \lambda_m \underline{\chi_d} C_m \qquad (1.1) \\ \dfrac{\partial C_m}{\partial t} = -\lambda_m C_m + \beta_m \underline{F}^T \underline{\Phi} \quad \text{for} \quad m = 1, \cdots, 8 \qquad (1.2) \end{cases}$$

with a given initial condition

$$\underline{\Phi}(t=0) = \underline{\Phi_0} \quad \text{and} \quad C_m(t=0) = C_m^0 \qquad (1.3)$$

where

$$
\begin{cases}
\underline{\Phi} = \begin{bmatrix} \Phi_1(\mathbf{r},t) \\ \\ \Phi_2(\mathbf{r},t) \end{bmatrix} \\
\underline{\underline{V^{-1}}} = \begin{bmatrix} \dfrac{1}{v_1}(\mathbf{r}) & 0 \\ 0 & \dfrac{1}{v_2}(\mathbf{r}) \end{bmatrix} \\
\underline{\underline{D}} = \begin{bmatrix} D_1(\mathbf{r}) & 0 \\ 0 & D_2(\mathbf{r}) \end{bmatrix} \\
\underline{\underline{\Sigma_a}} = \begin{bmatrix} \Sigma_a^1(\mathbf{r}) & 0 \\ 0 & \Sigma_a^2(\mathbf{r}) \end{bmatrix} \\
\underline{\underline{\Sigma_s}} = \begin{bmatrix} \Sigma_s^{1\to2}(\mathbf{r}) & -\Sigma_s^{2\to1}(\mathbf{r}) \\ -\Sigma_s^{1\to2}(\mathbf{r}) & \Sigma_s^{2\to1}(\mathbf{r}) \end{bmatrix} \\
\underline{\chi_p} = \begin{bmatrix} \chi_p^1 \\ \\ \chi_p^2 \end{bmatrix} \\
\underline{F}^T = \begin{bmatrix} \nu\Sigma_f^1(\mathbf{r}) & \nu\Sigma_f^2(\mathbf{r}) \end{bmatrix} \\
\underline{\chi_d} = \begin{bmatrix} \chi_d^1 \\ \\ \chi_d^2 \end{bmatrix}
\end{cases}
\tag{1.4}
$$

1.2.1 Neutronic input generation with SERPENT

The neutronic parameters ($\underline{\underline{V^{-1}}}, \underline{\underline{D}}, \underline{\underline{\Sigma_a}}, \underline{\underline{\Sigma_s}}, \underline{\chi_p}, \underline{\underline{F}}^T, \underline{\chi_d}$) have been generated by means of the continuous energy Monte Carlo neutron transport code SERPENT (SERPENT, 2011, 2011), which features group constant generation capabilities, using the nuclear data library JEFF 3.1 (Koning et al., 2006). As far as the SERPENT model is concerned, the core and the pin geometries are represented, respectively, in Figs. 1.1 and 1.2. All the fuel pins have been taken into account with the surrounding cladding, the two irradiation channels have been considered empty (filled with air), whereas, for the sake of simplicity, the control rods, the dummy elements and the source have been "replaced" with water. The isotopic composition of the input materials is provided in Table 1.1.

The group constants have been obtained after runs of 10 millions active neutron histories. Simulations consist of 500 active cycles of $2 \cdot 10^4$ neutrons, leading to a standard deviation lower than 3% for all the computed parameters.[1] Fifty inactive cycles are adopted to allow the convergence of the fission source distribution employed for the active cycles. When the neutronic parameters for the void have been generated, the air has been homogenized with the surrounding water ensuring that the diffusion approximation holds. In addition, for the sake of simplicity, the fuel pins have been

[1] Thanks to the reduced values of the obtained standard deviations, performing an uncertainty propagation has not been considered necessary.

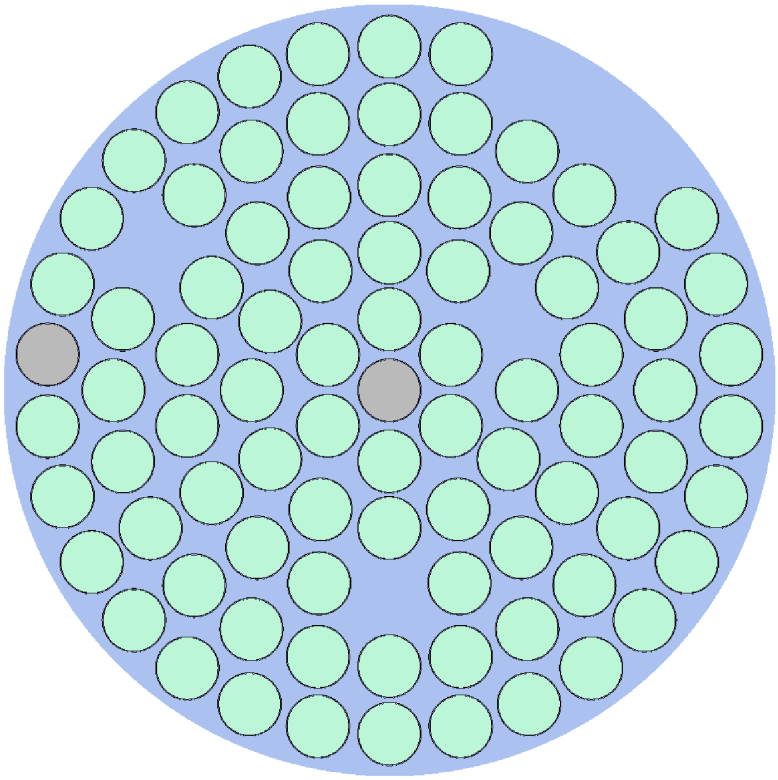

Figure 1.1: *Geometry employed in SERPENT code for representing the system configuration.*

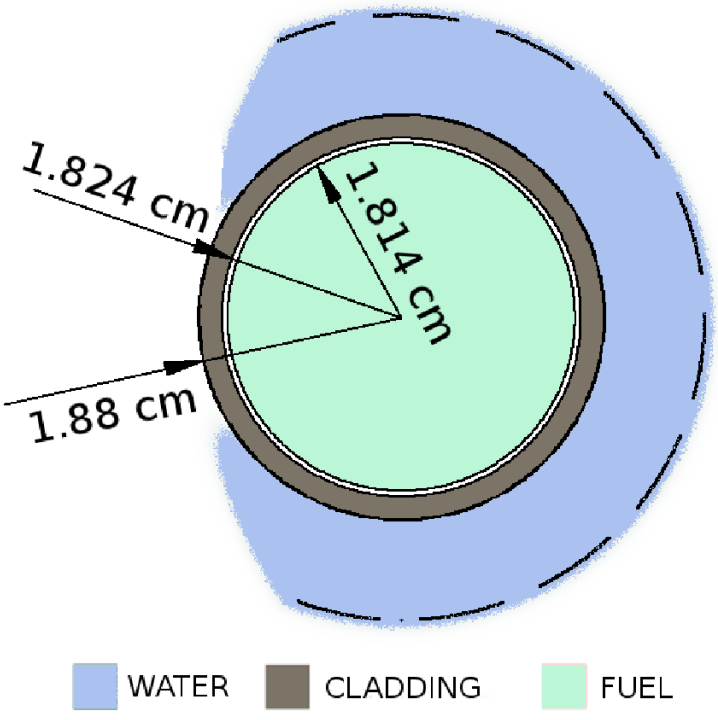

Figure 1.2: *Geometry of the pin employed in SERPENT code.*

Table 1.1: *Isotopic composition of the SERPENT input materials.*

Fuel		Cladding		Water	
Isotope	wt%	Isotope	wt%	Isotope	wa%
U-235	1.607	V-nat	0.10	O-16	1.0
U-238	6.531	Cr-nat	0.02	H-1	2.0
Zr-nat	90.836	Mn-nat	0.01		
H-1	1.026	Fe-nat	0.10	Air	
		Al-27	99.57	Isotope	wt%
		Cu-nat	0.10	O-16	10.0
		Ga-nat	0.10	N-14	90.0

Table 1.2: *Neutronic parameters generated by the SERPENT code.*

Parameter	Fuel	Water	Void
$D_1 \quad [cm]$	$8.77 \cdot 10^{-1}$	$8.51 \cdot 10^{-1}$	3.82
$D_2 \quad [cm]$	$1.92 \cdot 10^{-1}$	$1.39 \cdot 10^{-1}$	$7.13 \cdot 10^{-1}$
$\Sigma_a^1 \quad [cm^{-1}]$	$4.85 \cdot 10^{-3}$	$5.04 \cdot 10^{-4}$	$1.23 \cdot 10^{-4}$
$\Sigma_a^2 \quad [cm^{-1}]$	$7.53 \cdot 10^{-2}$	$1.70 \cdot 10^{-2}$	$4.18 \cdot 10^{-3}$
$\Sigma_f^1 \quad [cm^{-1}]$	$3.15 \cdot 10^{-3}$	–	–
$\Sigma_f^2 \quad [cm^{-1}]$	$1.08 \cdot 10^{-1}$	–	–
$\Sigma_s^{1\to2} \quad [cm^{-1}]$	$3.04 \cdot 10^{-2}$	$5.34 \cdot 10^{-2}$	$9.08 \cdot 10^{-3}$
$\Sigma_s^{2\to1} \quad [cm^{-1}]$	$3.21 \cdot 10^{-4}$	$2.49 \cdot 10^{-4}$	$1.18 \cdot 10^{-4}$
$1/v_1 \quad [s/cm]$	$5.87 \cdot 10^{-8}$	$7.58 \cdot 10^{-8}$	$6.58 \cdot 10^{-8}$
$1/v_2 \quad [s/cm]$	$3.00 \cdot 10^{-6}$	$3.47 \cdot 10^{-6}$	$3.30 \cdot 10^{-6}$
$\chi_p^1 \quad [-]$	1.0	–	–
$\chi_p^2 \quad [-]$	0.0	–	–
$\chi_d^1 \quad [-]$	1.0	–	–
$\chi_d^2 \quad [-]$	0.0	–	–

homogenized with the cladding and the coolant. The parameters generated, which have been used as input for both the MM and POD approaches, are reported in Table 1.2.

The homogeneous Dirichlet Boundary Conditions (BC) have been set, which lead to a good approximation of flux shape and reactivity value. Indeed, the core is surrounded by a ring of reflector of graphite, which improves the neutron thermalization. This leads to a small increase of the thermal flux near the border that cannot be taken into account with the employed BC. Therefore, the flux shape is correctly evaluated throughout the core, except near the external border. Since this work is more focused on the comparison of the two approaches, rather than on the development of an accurate model of the reactor, the adoption of such BC may be still considered acceptable.

1.2.2 Deriving the system of ODEs

In order to derive the system of ODEs, which describes the reactor kinetics, the flux has been approximated as follows:

$$\Phi(\mathbf{r}, t) \simeq \sum_{i=1}^{N} b_i(\mathbf{r}) a_i(t) \tag{1.5}$$

In Eq. (1.5), $b_i(\mathbf{r})$ is a spatial basis where the flux is projected, and $a_i(t)$ are the time-dependent coefficients, which are the unknowns of the obtained ODEs system. In this work, two spatial bases have been considered, one generated by the eigenfunctions associated to Eq. (1.1) (MM approach), and one generated by means of the POD technique.

Once the Eqs. (1.1) and (1.2) are projected onto the corresponding spatial basis, the following N equations are obtained for both the approaches:

$$\begin{cases} \sum_{i=1}^{N} \underline{\underline{\tau_{ji}}}\,\underline{\dot{a}_i}(t) = \sum_{i=1}^{N} \left[\underline{\underline{A_{ji}}}\,\underline{a_i}(t) + (1-\beta)\underline{\underline{F_{p,ji}}}\,\underline{a_i}(t)\right] + \\ \qquad + \sum_{m=1}^{8} \lambda_m \underline{C_{mj}}(t) \end{cases} \tag{1.6}$$

$$\underline{\dot{C}_{mj}}(t) = -\lambda_m \underline{C_{mj}}(t) + \beta_m \sum_{i=1}^{N} \underline{\underline{F_{d,ji}}}\,\underline{a_i}(t) \text{ for } m = 1, \cdots, 8 \tag{1.7}$$

where the expressions for the parameters $\underline{\underline{\tau_{ji}}}, \underline{\underline{A_{ji}}}, \underline{\underline{F_{p,ji}}}, \underline{C_{mj}}, \underline{\underline{F_{d,ji}}}$ will be given in Section 1.3 and 1.4 for the MM and POD approach, respectively.

The needed calculations for the definition of the two spatial bases have been performed using the finite element method (Quarteroni and Valli, 2008). The mesh employed (Fig. 1.3) features a 2D geometry using tri-noded triangular elements, where, for the sake of simplicity, all the fuel pins have been homogenized and only the two irradiation channel regions have been taken separated.

1.3 Modal Method approach

The essential feature of modal methods is spanning the expansion of spatial modes generated from the reference configuration, which is described by the non symmetric generalized eigenvalue problem associated to the Eq. (1.1), namely:

$$\left(-\nabla \cdot \underline{\underline{D}}\nabla + \underline{\underline{\Sigma_a}} + \underline{\underline{\Sigma_s}}\right) \underline{\psi_i} = \lambda_i \underline{\chi_p}\,\underline{F}^T \underline{\psi_i} \tag{1.8}$$

where the first eigenfunctions of each group $\underline{\psi_0}$ give the fundamental flux distribution. The core criticality condition is determined by the inverse of λ_0.

The former equation can be rewritten in the operator theory context as follows:

$$\mathcal{L}\underline{\psi_i} = \lambda_i \mathcal{M} \underline{\psi_i} \tag{1.9}$$

where the operators denoted in (1.9) are the neutronic removal operator

$$\mathcal{L} = \left(-\nabla \cdot \underline{\underline{D}}\nabla + \underline{\underline{\Sigma_a}} + \underline{\underline{\Sigma_s}}\right)$$

and the production operator $\mathcal{M}$ is given by

$$\mathcal{M} = \underline{\chi_p}\,\underline{F}^T$$

Because of the non-Hermitian operator $\mathcal{L}$, the adjoint generalized problem associated to Eq. (1.8) has to be solved, in order to obtain the bi-orthogonal adjoint eigenvectors

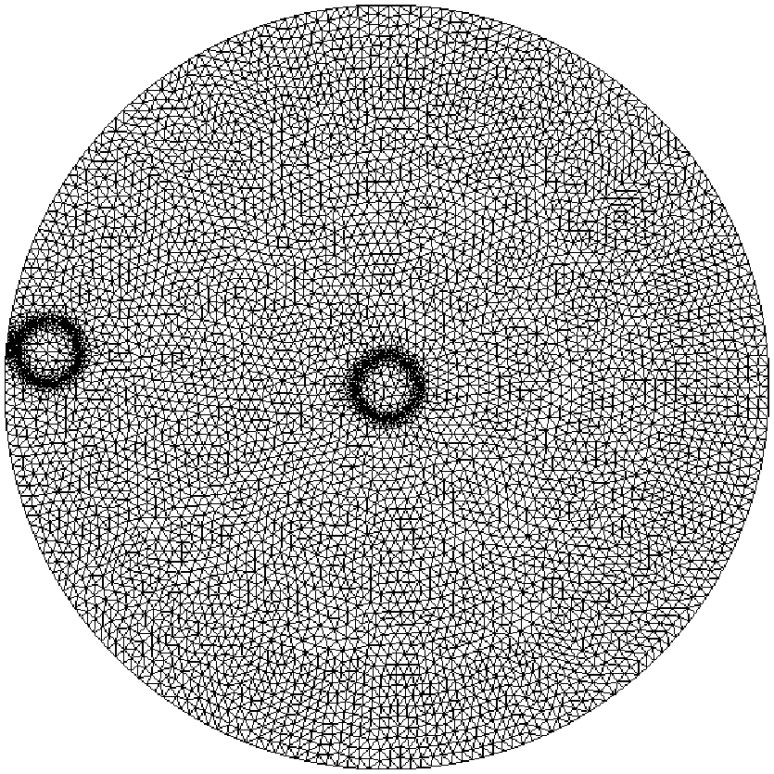

Figure 1.3: *Mesh employed for the finite element calculations.*

$\underline{\psi}_i^\dagger$ for the former harmonic function. From finite element fashion, the modal approach appears as a Petrov-Galerkin projection on high dimensional space where the trial functions are the harmonic modes and the test functions are the adjoint modes.

The steps necessary to derive the system of ODEs, which describes the reactor spatial dynamics according to the MM approach, are the following:

1. compute N eigenfunctions $\underline{\psi}_i$ from Eq. (1.8);
2. compute N adjoint eigenfunctions $\underline{\psi}_i^\dagger$ from the adjoint problem;
3. flux $\underline{\Phi}$ is approximated as

$$\underline{\Phi} \simeq \sum_{i=1}^{N} \underline{\underline{\psi}}_i \underline{a}_i(t) \tag{1.10}$$

where

$$\begin{cases} \underline{\underline{\psi}}_i = \begin{bmatrix} \psi_i^1(\mathbf{r}) & 0 \\ 0 & \psi_i^2(\mathbf{r}) \end{bmatrix} \\ \underline{a}_i(t) = \begin{bmatrix} a_i^1(t) \\ \\ a_i^2(t) \end{bmatrix} \end{cases} \tag{1.11}$$

4. substitute the expression of Eq. (1.10) into Eqs. (1.1) and (1.2);
5. pre-multiply Eq. (1.1) by $\underline{\underline{\psi}}_j^\dagger$ and Eq. (1.2) by $\underline{\underline{\psi}}_j^\dagger \underline{\chi}_d$;

6. integrate over the spatial domain Ω.

Finally, for the Eqs. (1.6) and (1.7), the following parameters have been obtained:

$$\begin{cases} \underline{\underline{\tau_{ji}}} = \int\limits_{\Omega} \underline{\underline{\psi_j^\dagger}} \underline{\underline{V^{-1}}} \underline{\underline{\psi_i}} d\Omega \\ \underline{\underline{A_{ji}}} = \int\limits_{\Omega} \underline{\underline{\psi_j^\dagger}} \left[\nabla \cdot \underline{\underline{D}} \nabla - \underline{\underline{\Sigma_a}} - \underline{\underline{\Sigma_s}} \right] \underline{\underline{\psi_i}} d\Omega \\ \underline{\underline{F_{p,ji}}} = \int\limits_{\Omega} \underline{\underline{\psi_j^\dagger}} \underline{\chi_p} \underline{F^T} \underline{\underline{\psi_i}} d\Omega \\ \underline{\underline{C_{mj}}} = \int\limits_{\Omega} \underline{\underline{\psi_j^\dagger}} \underline{\chi_d} C_m d\Omega \\ \underline{\underline{F_{d,ji}}} = \int\limits_{\Omega} \underline{\underline{\psi_j^\dagger}} \underline{\chi_d} \underline{F^T} \underline{\underline{\psi_i}} d\Omega \end{cases} \tag{1.12}$$

It is worth mentioning that for such approach, the number of eigenfunctions needed to represent the quantities of interest with a certain level of accuracy for a given perturbed reactor configuration cannot be evaluated *a priori* (i.e., before the eigenfunctions are computed) nor *a posteriori* (i.e., once the eigenfunctions have been computed).

1.4 POD-based approach

The Proper Orthogonal Decomposition method by means of the snapshot technique (Sirovich, 1987) gives the possibility to reduce the dimensionality of a system by transforming the original solutions, called *snapshots*, onto a set of uncorrelated modes such that the first few modes retain most of the energy (i.e., most of the information) present in all of the original variables (Quarteroni et al., 2011). In this way, it is possible to obtain a reduced representation through a spectral decomposition by means of the Singular Value Decomposition (SVD). Each snapshot is the solution of the generalized eigenvalue problem associated to a given vector $\underline{\underline{D}}, \underline{\underline{\Sigma_a}}, \underline{\underline{\Sigma_s}}$.

Thanks to the possibility of decomposing the computation in Offline and Online, the greatly expensive computation for generating the snapshots and the computation of the SVD is performed in the Offline phase. Given a discrete set of train of data Θ_{train}, which for this work reads $\Theta_{\text{train}}(\underline{\underline{D}}, \underline{\underline{\Sigma_a}}, \underline{\underline{\Sigma_s}})$, the Offline computation consists in the following steps:

1. compute N_s snapshots $\omega_1(\underline{\mu_1}), \ldots, \omega_{N_s}(\underline{\mu_{N_s}})$, where $\underline{\mu_i} \in \Theta_{\text{train}}$;
2. build the vector of the snapshots $\underline{X} = [\omega_1, \ldots, \omega_{N_s}]$;
3. perform the SVD on $\underline{X}$, so as to obtain:

$$\underline{X} = \underline{\underline{U}}\,\underline{\underline{S}}\,\underline{\underline{V}}$$

In this work, the number of retained snapshots is equal to one hundred. Once the SVD is computed, the columns of the matrix $\underline{\underline{U}}$, $\underline{u_i}$, are the POD orthonormal modes, while the singular values, s_i, associated to each mode are sorted in descending order in

the diagonal matrix $\underline{\underline{S}}$. The singular value is proportional to the energy of each mode (i.e., to the information carried by the mode itself). As a major outcome of the POD approach, the subspace V^{POD} spanned by the $\underline{u_i}$ constitutes the optimal approximation of the full discrete original problem in the least square sense.

Once the Eqs. (1.1) and (1.2) are projected onto the POD basis, the same functional forms of Eqs. (1.6) and (1.7) are obtained in which the following parameters have been employed:

$$\begin{cases} \underline{\underline{\tau_{ji}}} = \int\limits_{\Omega} \underline{\underline{u_j}}\,\underline{\underline{V^{-1}}}\,\underline{\underline{u_i}} d\Omega \\ \underline{\underline{A_{ji}}} = \int\limits_{\Omega} \underline{\underline{u_j}} \left[\nabla \cdot \underline{\underline{D}}\nabla - \underline{\underline{\Sigma_a}} - \underline{\underline{\Sigma_s}}\right] \underline{\underline{u_i}} d\Omega \\ \underline{\underline{F_{p,ji}}} = \int\limits_{\Omega} \underline{\underline{u_j}}\,\underline{\chi_p}\,\underline{F^T}\,\underline{\underline{u_i}} d\Omega \\ \underline{\underline{C_{mj}}} = \int\limits_{\Omega} \underline{\underline{u_j}}\,\underline{\chi_d}\,C_m d\Omega \\ \underline{\underline{F_{d,ji}}} = \int\limits_{\Omega} \underline{\underline{u_j}}\,\underline{\chi_d}\,\underline{F^T}\,\underline{\underline{u_i}} d\Omega \quad \forall \underline{\underline{u_i}}, \underline{\underline{u_j}} \in V^{POD} \end{cases} \tag{1.13}$$

Differently from the Modal Method, the POD approach ensures an *a posteriori* estimate about the amount of information stored in the V^{POD} space, defined by the following criterion (Atwell and King, 2004):

$$\frac{\sum\limits_{i=1}^{e} s_i}{\sum\limits_{i=1}^{N_s} s_i} > E \tag{1.14}$$

where e provides an estimate of the number of basis functions necessary for an approximation with a desired mean square error less than $(1-E)\sum_{i=1}^{N_s} s_i$. In this way, the e modes retain $E \cdot 100$ percent of the information stored in the vector of the snapshots $\underline{X}$. The set of train Θ_{train} has been defined as a random sampling of the values of the parameters $\underline{\underline{D}}$, $\underline{\underline{\Sigma_a}}$, and $\underline{\underline{\Sigma_s}}$, which can vary only within the spatial regions of the two irradiation channels (central and RABBIT, see Fig. A.1 on page 90).

1.5 Reactivity evaluation by means of the Inverse Method

In the Introduction, it has been stated that the developed approaches allow getting the system spatial dynamics, in addition to the time-dependent one, in order to monitor the evolution during operational transients of quantities of interest. Conversely, the most relevant output variable that allows the operator to effectively programme the control rod motion is the system reactivity, whose value determines the time-dependence of the externally imposed reactivity to yield a certain power variation. Therefore, from a control and safety oriented perspective, it is fundamental to evaluate the contribution of the several reactivity feedbacks.

Indeed, the perturbation performed on the system will be localized to certain zone of the core. According to the position, the reactivity variation will be different, and the

model should get these aspects and predict how the perturbation will extend to other core regions, reproducing these spatial dynamics effects. In the present work, the evaluation of the reactivity has been derived by means of the Inverse Method (Duderstadt and Hamilton, 1976). After a brief description of the classical formulation, it will be indicated how the algorithm has been modified and related to the time-dependent variables of the Modal-based and the POD-based approaches.

The Inverse Method refers to the following system of non-linear equations constituting the PK model:

$$\begin{cases} \dfrac{\mathrm{d}\Psi}{\mathrm{d}t} = \dfrac{\rho(t)-\beta}{\Lambda}\Psi + \displaystyle\sum_{m=1}^{8}\frac{\beta_m}{\Lambda}\eta_m & (1.15) \\ \dfrac{\mathrm{d}\eta_m}{\mathrm{d}t} = \lambda_m\Psi - \lambda_m\eta_m & (1.16) \end{cases}$$

The state of the system is represented by the following normalized variables:

$$\begin{cases} \Psi(t) = \dfrac{P(t)}{P(0)} & (1.17) \\ \eta_m(t) = \dfrac{C_m(t)}{C_m(0)} & (1.18) \end{cases}$$

whose initial conditions are defined as $\eta_m(0) = 1$ and $\Psi(0) = 1$. By substituting the analytical solution of precursor concentration into Eq. (1.15), it is possible to write:

$$\frac{\mathrm{d}\Psi}{\mathrm{d}t} = \frac{\rho(t)-\beta}{\Lambda}\Psi + \sum_{m=1}^{8}\frac{\beta_m}{\Lambda}\left[e^{-\lambda_m t} + \int_0^t \left[\lambda_m\Psi(t')e^{\lambda_m(t'-t)}\right]\mathrm{d}t'\right] \tag{1.19}$$

Once defined the delay quantity $\tau = t - t'$ and identified the "delayed neutron kernel" as:

$$D(\tau) = \sum_{m=1}^{8}\left(\frac{\lambda_m\beta_m}{\beta}\right)e^{-\lambda_m\tau}$$

it is possible to rearrange the Eq. (1.19), obtaining an integro-differential form of the reactor point kinetics:

$$\begin{aligned}\rho(t) = \beta + \frac{\Lambda}{\Psi(t)}\frac{\mathrm{d}\Psi}{\mathrm{d}t} - \frac{1}{\Psi(t)}\sum_{m=1}^{8}\beta_m e^{-\lambda_m t} + \\ - \frac{\beta}{\Psi(t)}\int_0^t D(\tau)\Psi(t-\tau)\mathrm{d}\tau\end{aligned} \tag{1.20}$$

This expression indicates that by properly combining the PK equations it is possible to get an expression of the overall system reactivity, $\rho(t)$, as a function of the normalized power $\Psi(t)$. Given this result, the classical formulation of the Inverse Method has been extended, starting from the outcomes provided by the Modal and POD approaches. First of all, the expression of the thermal power density can be expressed

as:

$$q'''(\mathbf{r},t) = \sum_{l} w_f^{(l)} N_l(\mathbf{r}) \int_0^{\infty} \sigma_f^{(l)}(E)\Phi(\mathbf{r},E,t)\mathrm{d}E \tag{1.21}$$

where l refers to the $l-th$ fissile isotope, $w_f^{(l)}$ is the recoverable energy for each isotope fission event, $N_l(\mathbf{r})$ is the isotope density, $\sigma_f^{(l)}(E)$ is the microscopic fission cross section for the $l-th$ isotope, $\Phi(\mathbf{r},E,t)$ is the neutron flux as function of position, energy and time. In the developed model, two neutron energy groups have been taken into account. Therefore, in the Eq. (1.21) the integral is substituted by the following expression:

$$q'''(\mathbf{r},t) = \sum_{l} w_f^{(l)} N_l(\mathbf{r}) \cdot \left[\sigma_{f_1}^{(l)}(E)\Phi_1(\mathbf{r},t) + \sigma_{f_2}^{(l)}(E)\Phi_2(\mathbf{r},t)\right] \tag{1.22}$$

After having obtained the fission macroscopic cross section for the considered domain, by integrating the above expression (1.22) on the fuel pins volume, it possible to derive the value of the overall thermal power produced as follows:

$$P(t) = w_f \cdot \int_V \left[\Sigma_f^1(E)\Phi_1(\mathbf{r},t) + \Sigma_f^2(E)\Phi_2(\mathbf{r},t)\right] \mathrm{d}V \tag{1.23}$$

According to the presented approaches, the thermal and fast neutron fluxes have been expressed as a series of suitably defined functions in the form:

$$\Phi_1(\mathbf{r},t) = \sum_{i=1}^{N} b_i^1(\mathbf{r}) a_i^1(t) \qquad \Phi_2(\mathbf{r},t) = \sum_{i=1}^{N} b_i^2(\mathbf{r}) a_i^2(t) \tag{1.24}$$

By substituting these expressions in the Eq. (1.23), the instantaneous value of the thermal power produced in the reactor core is achieved:

$$P(t) = w_f \cdot \sum_{i=1}^{N} \left[a_i^1(t) \cdot \langle \Sigma_f^1 | b_i^1 \rangle_V + a_i^2(t) \cdot \langle \Sigma_f^2 | b_i^2 \rangle_V\right] \tag{1.25}$$

The terms $\langle \Sigma_f^1 | b_i^1 \rangle_V$ and $\langle \Sigma_f^2 | b_i^2 \rangle_V$ of the summation are evaluated Offline, while the $a_i^1(t)$ and $a_i^2(t)$ coefficients are computed by solving the developed ODE system defined by Eqs. (1.6) and (1.7). In order to derive the normalized power $\Psi(t)$, represented by Eq. (1.17), it is necessary to refer $P(t)$ to the power at nominal conditions $P(0)$. In this work, it has been assumed $P(0) = 1 \cdot w_f$. Therefore, $\Psi(t)$ is simply given by:

$$\Psi(t) = \frac{P(t)}{P(0)} = \sum_{i=1}^{N} \left[a_i^1(t) \cdot \langle \Sigma_f^1 | b_i^1 \rangle_V + a_i^2(t) \cdot \langle \Sigma_f^2 | b_i^2 \rangle_V\right] \tag{1.26}$$

By substituting $\Psi(t)$ into Eq. (1.20), the system reactivity ρ can be derived.

1.6 Results and discussion

The comparison of the outcomes provided by the MM and the POD approaches focuses on the capability of evaluating the reactivity and the neutron flux shape. The different considered reactor configurations are the following:

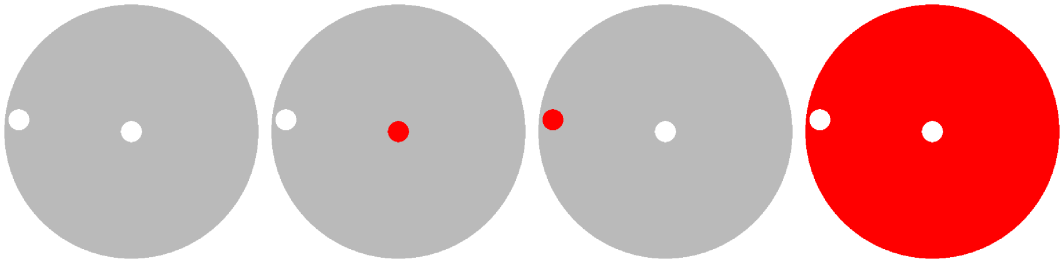

(a) *Case i* **(b)** *Case ii* **(c)** *Case iii* **(d)** *Case iv*

Figure 1.4: *The four reactor configurations simulated. The perturbed areas, with respect to nominal configuration (Case i), are highlighted in red.*

(i) both the irradiation channels are empty (nominal configuration,[2] unperturbed);

(ii) water in the central channel, the RABBIT is empty;

(iii) water in the RABBIT, the central one is empty;

(iv) absorption cross sections have been reduced by $3‰$.

The above mentioned configurations, which are shown in Fig. 1.4, have been chosen in order to test the reliability and accuracy of the two approaches on the basis of both localized perturbations (Cases ii and iii) and homogeneous perturbation (Case iv). The POD basis has been trained with localized perturbations on the two irradiation channels, hence it is expected that the POD approach leads to high-fidelity results for Cases (ii) and (iii). On the other hand, the MM approach is likely to give good results for a homogeneous perturbation. The Cases (ii) and (iii) have been selected in order to asses if the two approaches manage to take into account spatial effects. Indeed, the same perturbation (i.e., void is replaced by water) is applied to different positions of the core where the neutron flux importance is different. Hence, the reactivity values are expected to be different in these two cases.

1.6.1 Methodology

For each configuration, an eigenvalue calculation – see Eq. (1.8) – has been performed by means of the open source finite element code `FreeFem++` (Pironneau et al., 2012) relying on the ARPACK packages (Lehoucq et al., 1998), which implement an efficient implicit Arnoldi procedure, and on the MUltifrontal Massively Parallel sparse direct Solver (MUMPS) (Amestoy et al., 2000). The obtained reactivity value and flux shape will be referred to as *reference* solution.

Subsequently, using the MATLAB/Simulink environment (MATLAB® and SIMULINK® software, 2005), the evolution of the system described by Eqs. (1.6) and (1.7), within the first 60 seconds, has been simulated according to the MM and POD approaches. The reactivity has been estimated by means of the described procedure of the Inverse Method (Section 1.5). In order to compare the computed flux shapes with the reference one, which is time-independent, the former, at the end of the simulation, are normalized

[2] The eigenfunctions of the MM have been computed for this configuration.

Table 1.3: *Reactivity calculations for the configuration corresponding to Case i.*

# of functions	Reactivity [pcm]		
	Reference	POD	MM
1	0	-765.3	4.5
2	0	-14.7	4.5
3	0	-0.7	4.5
4	0	0.8	4.5
5	0	0.8	4.5
6	0	0.8	4.5
7	0	0.8	4.5
8	0	0.8	4.5
9	0	0.8	4.5
10	0	0.8	4.5
50	0	0.8	4.5
100	0	0.8	4.5

as follows:

$$\int_{\Omega} (\Phi_1 + \Phi_2) d\Omega = 1 \tag{1.27}$$

A sensitivity analysis for the outcomes provided by the MM and POD approaches has been carried out varying the number of basis functions up to 100. For the sake of completeness, the trivial case with only one basis function has been considered as well, showing the necessity of allowing for an increased number of modes.

In the following, the outcomes of the two approaches, for each reactor configuration, will be presented and discussed.

1.6.2 Case i: unperturbed configuration

This case is the nominal configuration (unperturbed) of the reactor. According to the two approaches, the estimated values of reactivity, varying the number of basis functions, are reported in Table 1.3, and they are graphically compared in Fig. 1.5. The POD prediction, if the basis is made of only the first function, is very far from the reference value but it gets closer when two and three functions are used. If four or more functions are employed, the value of the reactivity does not change anymore. Even increasing the number of functions employed, the reactivity values estimated by means of the MM approach does not change, since the reference flux shape is precisely the first eigenfunction of each group. The flux shape of the energy group 2 (from now on referred to as thermal group) given by the two approaches is compared to the reference one in Fig. 1.6. In particular, the reference flux shape (a), POD (b) using 4 functions, and MM (c) employing 10 eigenfunctions are depicted. The MM flux shape is coincident with the reference one, while the POD flux shape is very close.

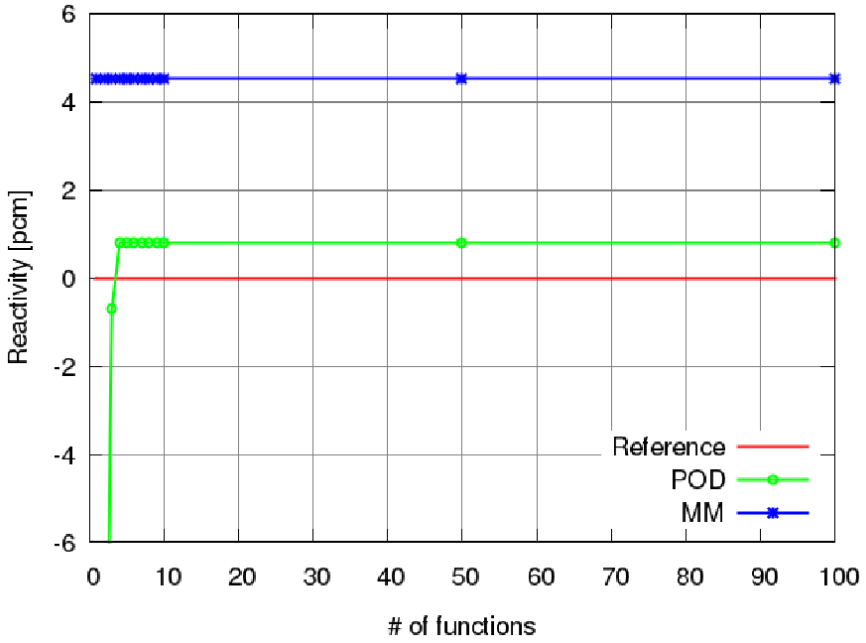

Figure 1.5: *Reactivity calculations for the configuration corresponding to Case i.*

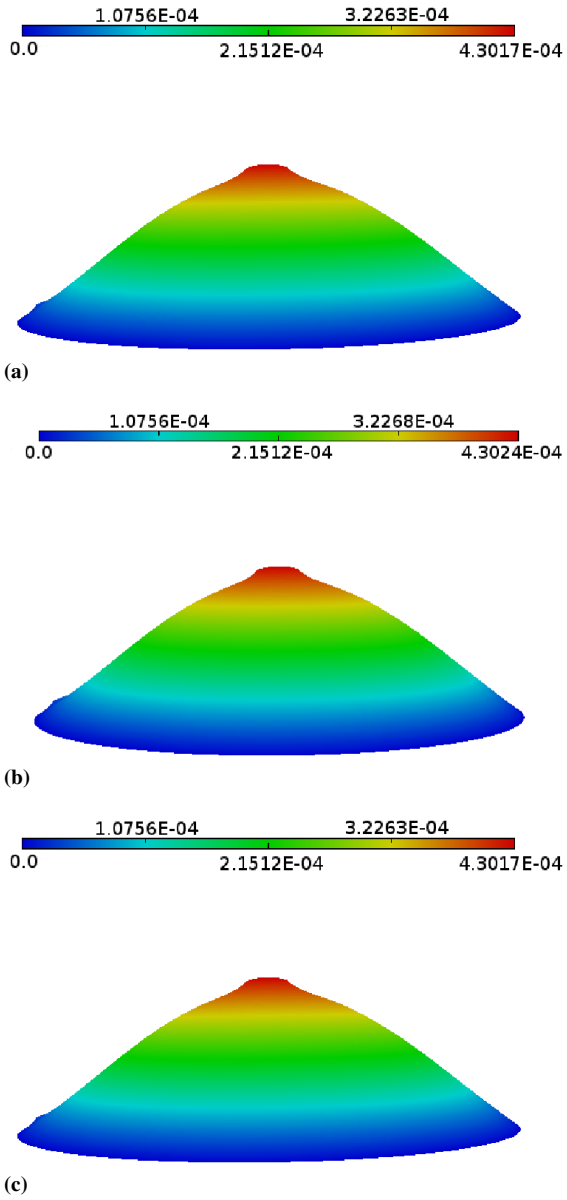

Figure 1.6: *Thermal flux shape for Case i: reference (a), POD (b), and MM (c). Data are reported in arbitrary units.*

Table 1.4: *Reactivity calculations for the configuration corresponding to Case ii.*

# of functions	Reactivity [pcm]		
	Reference	POD	MM
1	166.4	650.4	365.2
2	166.4	155.6	365.2
3	166.4	167.5	365.2
4	166.4	167.2	365.2
5	166.4	167.2	365.1
6	166.4	167.2	345.5
7	166.4	167.2	345.5
8	166.4	167.2	345.5
9	166.4	167.2	345.4
10	166.4	167.2	345.4
50	166.4	167.2	300.4
100	166.4	167.2	266.9

1.6.3 Case ii: water in the central channel

This kind of perturbation may be considered as the worst case, since the perturbation is quite localized in a position where the neutron flux is higher. The reactivity values provided by the two approaches, employing different number of basis functions, are reported in Table 1.4, and the chart shown in Fig. 1.7 compares the results. The POD prediction, if the basis is made of only the first function is very far from the reference value but it gets closer when two and three functions are used. If four or more functions are employed, the value of the reactivity does not change anymore. The reactivity values estimated by means of the MM approach slightly converges to the reference value as the number of functions employed increases. This slight change is due the fact that for such perturbation, only the odd eigenfunctions manage to reflect a change in the middle of the core, but the series of all eigenfunction does not inherit this property. As a result, even employing 100 eigenfunctions, the reactivity is overestimated by a factor of 1.6. Conversely, by employing only four POD functions, the reactivity differs from the reference value by 0.8 pcm, which is the offset when compared to the unperturbed configuration (Case i, see Table 1.3). In Fig. 1.8, the reference (a) flux shape, the one computed according to the POD approach (b) employing 4 functions, and according to the MM approach (c) using 10 functions, are represented. The MM approach cannot represent any flux shape variation if compared to the nominal configuration (see Fig. 1.6) – even though the estimated reactivity is more than twice the reference one. On the other hand, the flux shape computed by the POD approach fits very well the reference one.

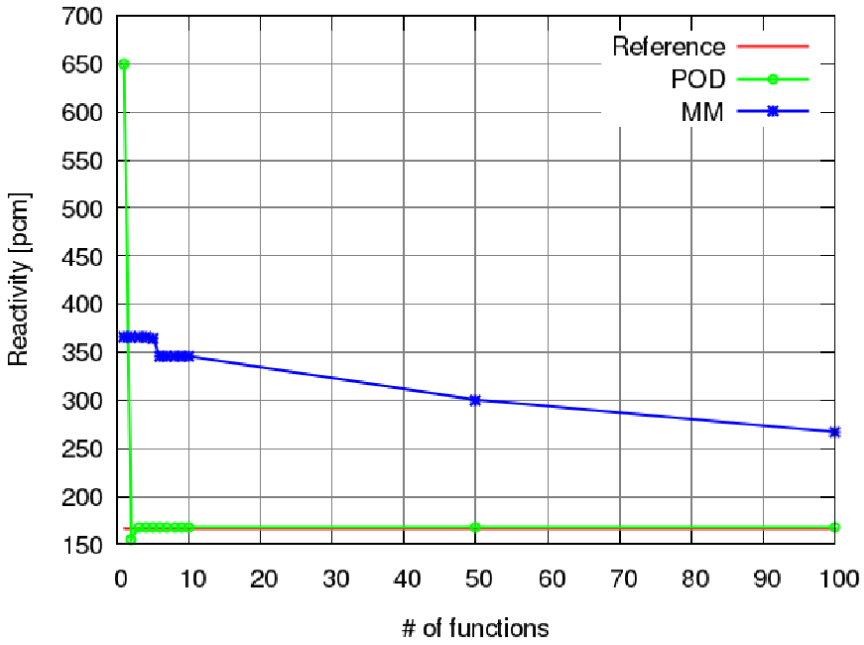

Figure 1.7: *Reactivity calculations for the configuration corresponding to Case ii.*

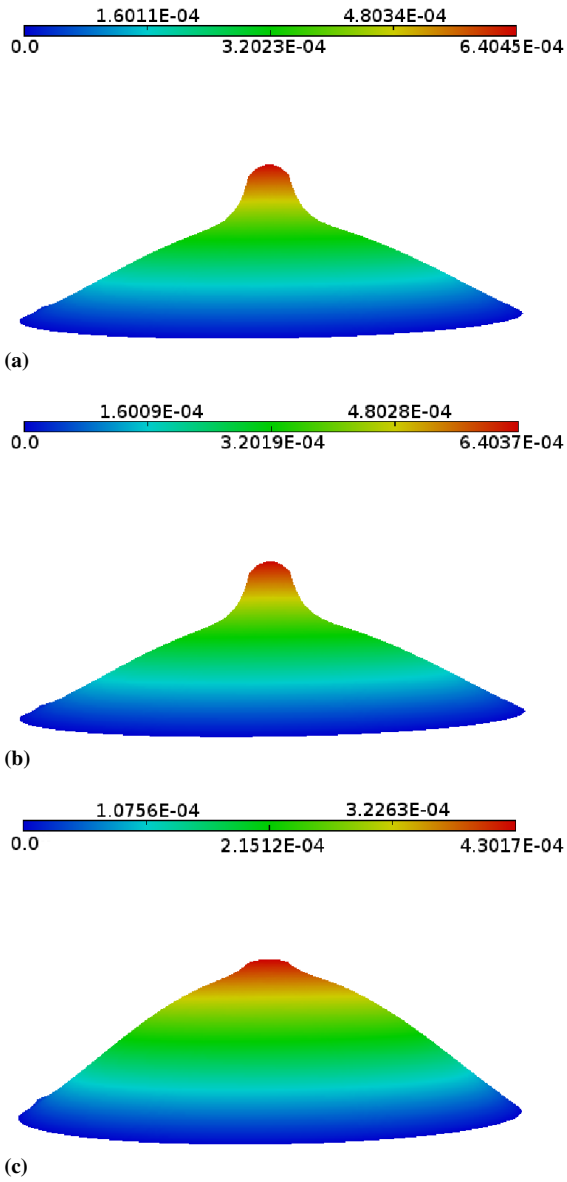

Figure 1.8: *Thermal flux shape for Case ii: reference (a), POD (b), and MM (c). Data are reported in arbitrary units.*

Table 1.5: *Reactivity calculations for the configuration corresponding to Case iii.*

# of functions	Reactivity [pcm]		
	Reference	POD	MM
1	3.4	-745.0	1.510
2	3.4	7.5	1.505
3	3.4	3.6	1.505
4	3.4	4.2	1.504
5	3.4	4.2	1.490
6	3.4	4.2	1.502
7	3.4	4.2	1.490
8	3.4	4.2	1.485
9	3.4	4.2	1.485
10	3.4	4.2	1.468
50	3.4	4.2	0.985
100	3.4	4.2	0.577

1.6.4 Case iii: water in the RABBIT channel

In this test case, the same perturbation as in the previous Case (ii) is applied, but localized in a different position. In fact, the water is placed in the peripheral RABBIT channel, where the flux importance is much lower compared to the middle of the reactor core. This leads to a lower reactivity change, in comparison with the previous case. The estimated reactivity, according to the two approaches, varying the number of functions employed, is reported in Table 1.5, and the corresponding chart is shown in Fig. 1.9. The POD prediction behaves as discussed in the previous cases. Indeed, if the basis is made of only the first function, the outcome is quite different from the reference value, while with four or more basis functions employed the value of the reactivity does not change anymore. The difference between the prediction of the POD approach differs by 0.8 pcm with respect to the reference value, which is the offset when compared to the unperturbed configuration (Case i, see Table 1.3). The reactivity values estimated by means of the MM approach barely change by increasing the number of functions employed, but the trend seems to be divergent in comparison with the reference value. If the entity of this perturbation, in terms of reactivity, is compared to the previous one, it can be deduced that both the two approaches effectively reproduce the system spatial effects. Indeed, both the methods have provided a bigger reactivity change, with respect to the unperturbed configuration, when the perturbation is applied in the center of the core. Otherwise, a smaller effect has been seen when the same perturbation is applied where the importance of the neutron flux is much lower.

In this case, the flux shape variation is small, hence it is not worthy to show the neutron fluxes provided by the two approaches.

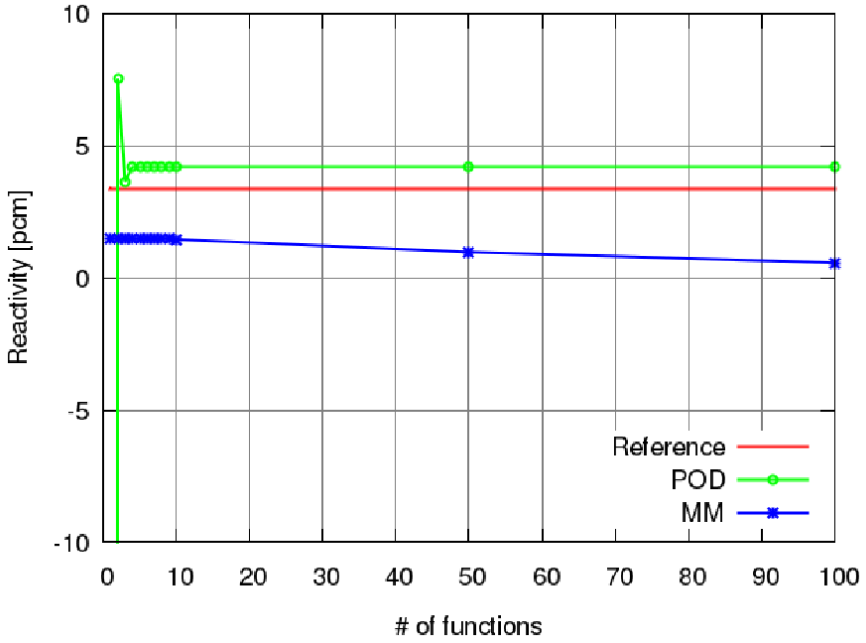

Figure 1.9: *Reactivity calculations for the configuration corresponding to Case iii.*

Table 1.6: *Reactivity calculations for the configuration corresponding to Case iv.*

# of functions	Reactivity [pcm]		
	Reference	POD	MM
1	309.0	-462.6	297.936
2	309.0	287.8	297.936
3	309.0	301.8	297.936
4	309.0	303.3	297.936
5	309.0	303.3	297.936
6	309.0	303.3	297.936
7	309.0	303.3	297.935
8	309.0	303.3	297.935
9	309.0	303.3	297.935
10	309.0	303.3	297.935
50	309.0	303.3	297.935
100	309.0	303.3	297.935

1.6.5 Case iv: homogeneous perturbation

In this case, a homogeneous perturbation throughout the core is simulated by reducing the absorption cross sections by $3‰$. According to the two approaches, the computed reactivity values, varying the number of basis functions, are given in Table 1.6, and they are graphically compared in Fig. 1.10. Also for this kind of perturbation, the outcomes provided by the POD approach are not accurate when only one basis function is employed. If four or more modes are adopted, the reactivity value is closer to the reference one and it does not change anymore by increasing the number of functions. The estimation of the reactivity provided by the MM does not change sensitively by increasing the number of functions employed. However, the outcomes of both approaches are in fair agreement with the reference value.

As in the previous test case (Case iii), the homogeneous perturbation does not change significantly the flux shape, hence the neutron fluxes provided by the two approaches are not worthy of remarks.

1.6.6 Discussion

The comparison between the presented control-oriented approaches for the nuclear reactor kinetics has been performed on different reactor configurations.[3] Whether a homogeneous perturbation is evaluated (Case iv), both the approaches exhibit good capabilities to approximate the flux shape. On the other hand, if the perturbation is localized, the MM requires a considerable number of eigenfunctions to correctly predict the reactivity. Moreover, the flux shape predicted according to the MM does not reflect the localized perturbation. Conversely, the outcomes provided by the POD approach, employing only four basis functions, are high-fidelity with respect to the reference ones, in terms of reactivity and flux shape, independently on the kind of applied perturbation.

The motivation of the better results obtained by POD are due to the difference between the shape of the corresponding POD (Fig. 1.11) and MM (Fig. 1.12) basis functions, where for brevity only the modes for the thermal group are shown. The first POD

[3] The considered reactor core configurations have been achieved starting from an unperturbed configuration, to which either localized or homogeneous perturbations have been applied.

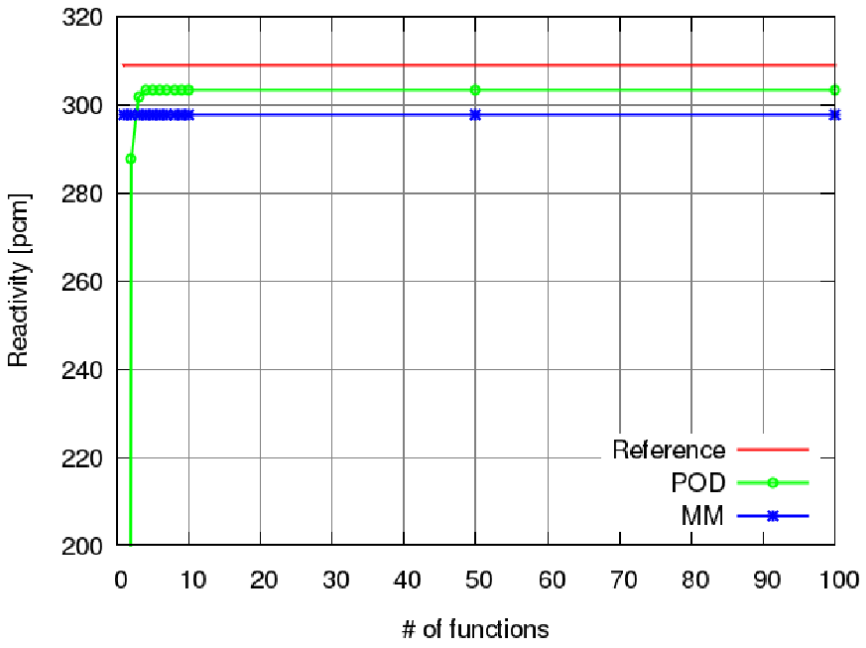

Figure 1.10: *Reactivity calculations for the configuration corresponding to Case iv.*

function (starting from the left) provides the overall flux shape, while the higher order functions give contributions only where the perturbations can be applied. On the other hand, the shape of the MM functions depends on the operators $\mathcal{L}$ and $\mathcal{M}$ of the generalized eigenvalue equation (1.9) and on the geometry of the unperturbed core. Therefore, the MM basis has no information where the perturbations may occur.

For each case considered, the outcomes provided by the POD approach behave in the same way. In particular, if a single basis function is employed, the reactivity value is quite far from the reference one, whereas it gets closer when two and three functions are used. If four or more functions are employed, the value is in good agreement with the reference one and does not change anymore. Indeed, the importance of contribution given by each POD function is decreasing, meaning that the next function carries less information (or energy) than the previous one. The energy associated to each POD function is shown in Fig. 1.13. The difference between the first and the fourth value is equal to several orders of magnitude. This means that the information stored in the vector of the snapshots can be reproduced by only few functions. Relying on the *a posteriori* criterion, Eq. (1.14), the retained information, expressed in percent, with respect to the number of functions employed, is reported in Fig. 1.14. It can be seen that with two basis functions more than the 99% of the information stored in the vector of the snapshots is allowed for, and with four functions all the information is reproduced. Hence, the contribution of the functions beyond the fourth one is negligible. For this reason, the outcomes, obtained employing more than four functions, do not change considerably.

Conversely, the outcomes provided by the MM approach behave differently in the considered cases. In particular, for the unperturbed configuration, the quantities of interest do not change by increasing the number of functions. For Case (ii), as the number of modes is increased, the reactivity value slightly converges to the reference

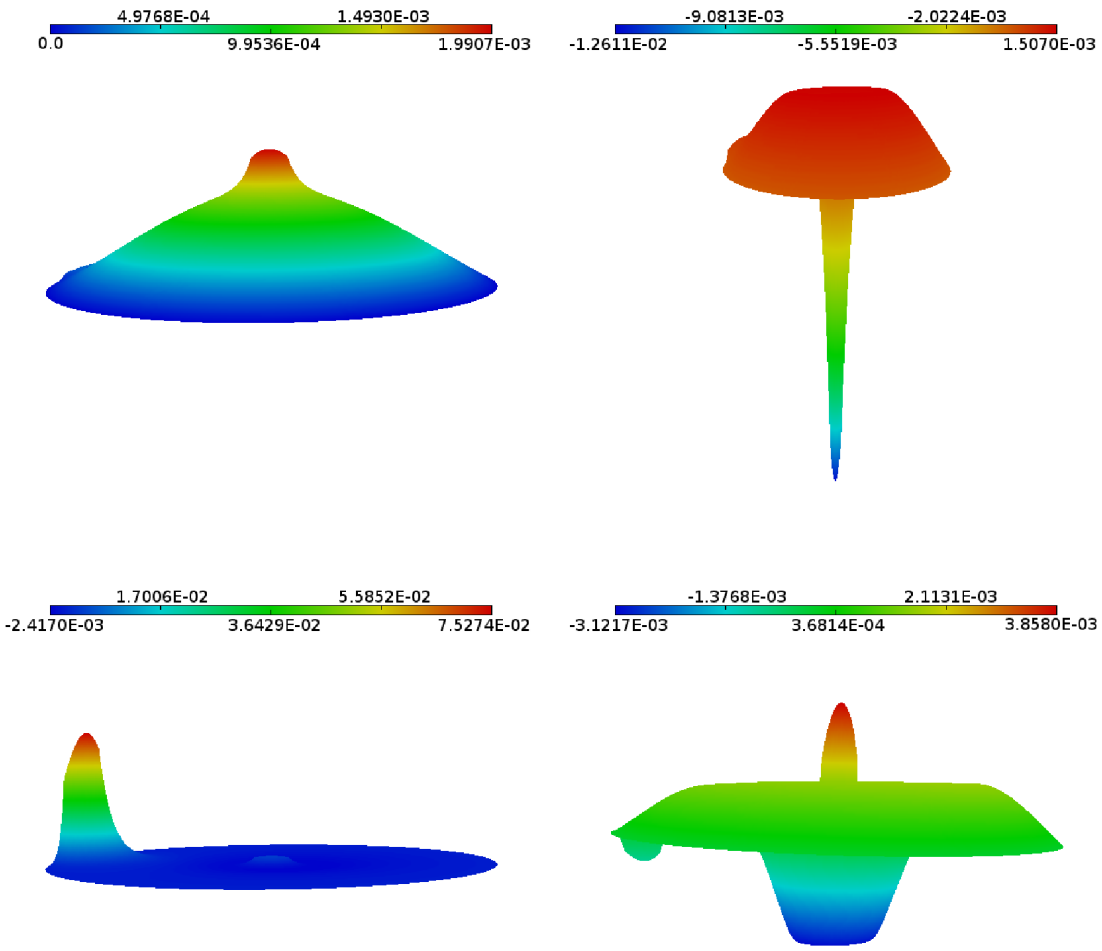

Figure 1.11: *The first four POD basis functions for the thermal group.*

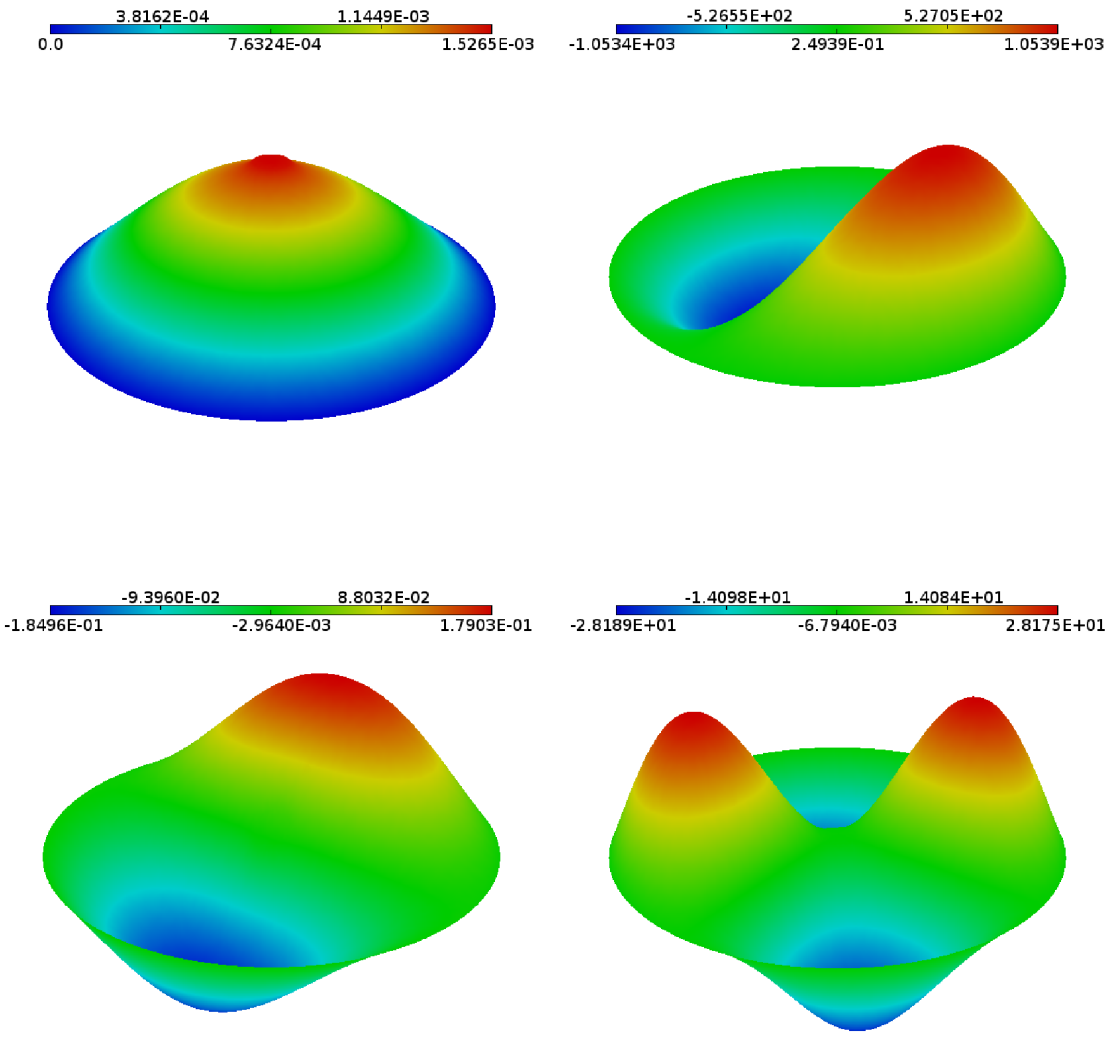

Figure 1.12: *The first four MM basis functions for the thermal group.*

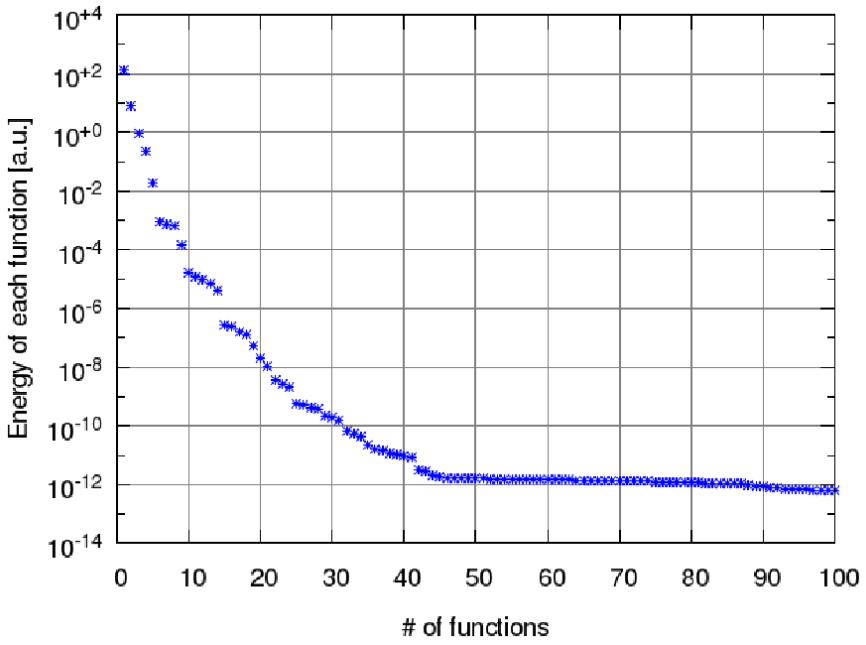

Figure 1.13: *Energy of POD functions for the thermal group.*

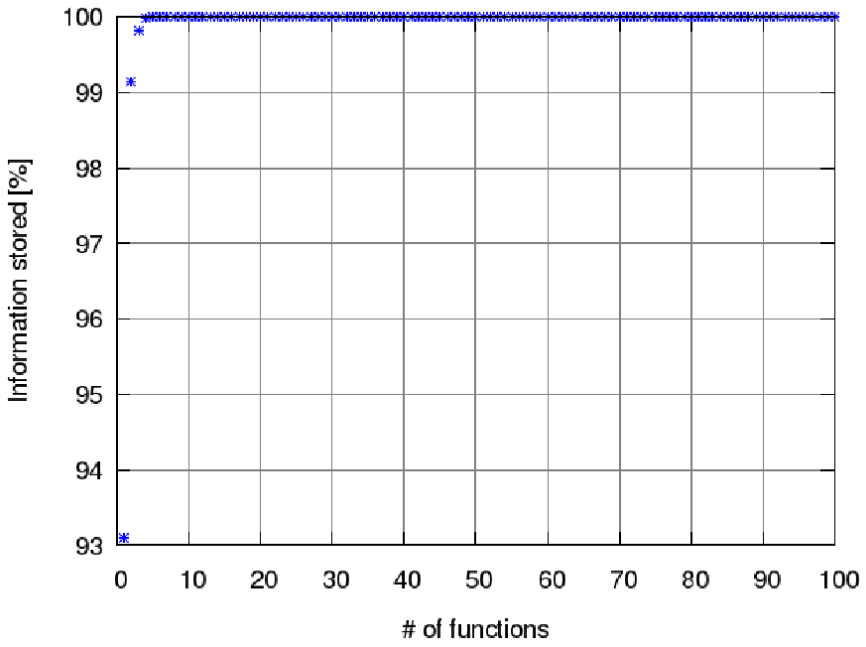

Figure 1.14: *Relative information taken into account with respect to the number of functions employed for the POD spatial basis.*

value. In Case (iii), although the reactivity value is close to the reference one, there is a divergent trend. Finally, when a homogeneous perturbation is applied (Case iv), the reactivity value does not change by increasing the number of functions. The importance of each eigenfunction depends on the kind of perturbation, and it cannot be provided neither *a priori* nor *a posteriori* estimation. For example, in the Case (ii), only the odd eigenfunctions can contribute to reveal a change in the middle of the core.

1.7 Concluding remarks

In this Chapter, two control-oriented approaches, based on a Modal Method (MM) and on the Proper Orthogonal Decomposition (POD) technique, for the nuclear reactor kinetics have been presented and compared. Both are able to simulate the spatial dynamics of the reactor, while the usually adopted point-wise kinetics is not sensible to spatial effects. In order to asses the reliability of these two approaches, different reactor core perturbations have been simulated, with reference to a TRIGA Mark II reactor. In particular, either localized or homogeneous perturbations have been investigated. The system reactivity and the neutron flux shape predicted by the MM and POD approaches have been the subject of the comparison. The outcomes provided by the POD approach, employing as few as four basis functions, are high-fidelity, with respect to the reference ones, for all the cases considered. Conversely, the MM approach leads to good results when the perturbation is homogeneous. On the other hand, if the perturbation is localized, a considerable number of eigenfunctions may be required to correctly predict the reactivity.

In the present investigation, several advantages of reduced order methods have been addressed. In particular, they are suited for handling *parametrized* partial differential equations; they promote a competitive Offline/Online computational decouple; the basis is *trained* to reproduce many configurations given by the parameters; the space spanned by the basis functions obtained is *hierarchical*, meaning that increasing the number of basis functions, the accuracy of the outcomes will improve – this is not necessarily verified for the MM approach.

The capabilities of reduced order methods, which have been highlighted throughout this Chapter, have defined the track of the following research activity towards the modelling of the control rods movement, which is dealt in the following Chapters.

Chapter 1 Nomenclature

Latin symbols

b_i^g	i^{th} generic spatial basis function of the g^{th} energy group [$cm\ s^{-1}$]
C_m	concentration of the m^{th} precursor group [cm^{-3}]
D_g	neutron diffusion coefficient in the g^{th} energy group [cm]
g	refers to the considered energy group ($g = 1$ for the fast group, $g = 2$ for the thermal group)
N	number of the employed basis functions [-]
N_s	number of the computed snapshots [-]
m	subscript referring to the precursor groups ($m = 1, \cdots, 8$)
P	thermal power [W]
$\mathbf{r}$	spatial coordinate [cm]
t	time [s]
u_i^g	i^{th} POD basis functions of the g^{th} energy group [$cm\ s^{-1}$]
v_g	neutron speed of the g^{th} energy group [$cm\ s^{-1}$]
$w_f^{(l)}$	recoverable thermal energy per fission event for the l-isotope [MeV]

Greek symbols

β	total delayed neutron fraction [-]
β_m	delayed neutron fraction of the m^{th} precursor group [-]
η_i	normalized concentration of the i^{th} precursor group [-]
λ_i	i^{th} eigenvalue [-]
λ_m	decay constant of the m^{th} precursor group [s^{-1}]
Λ	prompt neutron generation time [s]
ν	average number of neutrons emitted per fission [-]
ρ	system reactivity [pcm]
Σ	macroscopic cross-section [cm^{-1}]
Σ_a^g	macroscopic absorption cross-section in the g^{th} energy group [cm^{-1}]
Σ_f^g	macroscopic fission cross-section in the g^{th} energy group [cm^{-1}]
$\Sigma_s^{g\to g'}$	macroscopic group transfer cross-section from energy group g to g' [cm^{-1}]
Φ_g	neutron flux in the g^{th} energy group [$m^{-2}\ s^{-1}$]
χ_d^g	fraction of delayed neutrons generated in the g^{th} energy group [-]
χ_p^g	fraction of prompt neutrons generated in the g^{th} energy group [-]
ψ_i^g	i^{th} spatial eigenfunction of the neutron flux in the g^{th} energy group [$m^{-2}\ s^{-1}$]
Ψ	normalized thermal power [-]
Ω	spatial domain [cm^2]

CHAPTER 2

Reduced basis approaches in time-dependent settings for control rod movement

After that the capabilities of reduced order models in order to correctly estimate spatial effects have been addressed in the previous Chapter 1, in this new Chapter, two approaches, based on the certified Reduced Basis method, have been developed for simulating the movement of nuclear reactor control rods, in time-dependent non-coercive settings featuring a 3D geometrical framework. In particular, in a first approach, a piece-wise affine transformation based on subdomains division has been implemented for modelling the movement of one control rod. In the second approach, a "staircase" strategy has been adopted for simulating the movement of all the three rods featured by the nuclear reactor chosen as case study. Both the reduced order models, developed according to the two approaches, provided a very good accuracy compared with high-fidelity results, assumed as "truth" solutions. At the same time, the computational speed-up in the Online phase, with respect to the fine "truth" finite element discretization, achievable by both the proposed approaches is at least of three orders of magnitude, allowing a real-time simulation of the rod movement and control.

The main results presented in this Chapter are contained in: Sartori, A. Cammi, A., Luzzi, L. and Rozza, G., "Reduced basis approaches in time-dependent non-coercive settings for modelling the movement of nuclear reactor control rods". Submitted in a revised form to Communication in Computational Physics, 2015. The methodology has been presented at the 22nd International Conference on Nuclear Engineering

(ICONE22) in Prague, Czech Republic in July 2014 [1] and at INDAM YS3 Young Scientists Seminars Series on Reduced Order Modelling, Trieste, Italy, October 8-9, 2014.

[1] Sartori, A., Baroli, D., Cammi, A., Luzzi, L., and Rozza, G. "A Reduced Order Model for Multi-Group Time-Dependent Parametrized Reactor Spatial Kinetics". In: Proceedings of the 2014 22nd International Conference on Nuclear Engineering (ICONE22), Prague Czech Republic, July 7-11, 2014. Paper 30707, ©ASME 2014.

2.1 Introduction

A computational reduced order technique, such as the Reduced Basis (RB) method (Rozza et al., 2008; Quarteroni et al., 2011), can lead to a computational tool with real-time simulation, still solving a set of partial differential equations. The goal of a computational reduction technique (Manzoni et al., 2012) is to capture the essential features of the input/output behavior of a system in a rapid and reliable way, i.e.: (i) by improving computational performances and (ii) by keeping the approximation error between the reduced-order solution and the full-order solution under control. In particular, it aims at approximating a parametrized partial differential equation (or a set of partial differential equations) solution with a handful of degrees of freedom instead of thousands or millions that would be needed for a full-order approximation. In this way, the full-order problem has to be solved for a suitable number of instances of the input parameter (through a very demanding Offline computational step), in order to be able to perform many low-cost real-time simulations (inexpensive Online computational step) for several new instances of the input.

The first use of reduced basis methods can be found in computational nonlinear mechanics for the instability analysis of structures (Noor and Peters, 1980). The next decades saw further expansion into different applications and classes of equations, such as fluid dynamics and in particular the incompressible Navier-Stokes equations (Peterson, 1989; Ito and Ravindran, 1998, 2001). During the last ten years, the efforts within the RB framework has been devoted to the development of *a posteriori* error estimation procedures, as well as effective sampling strategies (Veroy et al., 2003; Grepl and Patera, 2005; Cuong et al., 2005). Most recent applications of RB can be found within the Haemodynamics context (Ballarin et al., 2013), as well as uncertainty quantification (Chen et al., 2013) and spectral element methods (Pitton and Rozza, 2015). According to the author's knowledge, the present PhD work employs for the first time the RB methods within the nuclear engineering field.

In this Chapter, the Reduced Basis method (built upon a high-fidelity "truth" Finite Element (FE) approximation, relying on the `libMesh` library (Kirk et al., 2006)) has been applied to model real-time control rod movement within a nuclear reactor, simulating a 3D framework, with reference to the TRIGA Mark II nuclear reactor (General Atomic, 1964) of the University of Pavia (Italy). In particular, two different parametrized models have been considered: a first one, with just one rod, then a second one with three control rods. The physics has been modeled by time-dependent non-coercive parametrized equations. Indeed, the neutron kinetics has been described by means of parametrized multi-group time-dependent diffusion equations (Duderstadt and Hamilton, 1976), which are a set (ten in the present work) of coupled parabolic equations where the heights of the control rods (i.e., how much the rods are inserted) play the role of the varying parameters. For the one-rod model, a piecewise affine transformation based on subdomain division has been implemented (Rozza et al., 2008). On the other hand, for the three-rods model, the movement of the control rods has been discretized by splitting the rods in many subdomains, which are like "steps".

This contribution stems from the need of nuclear engineering field to have a fast-running simulation tool, which can be tailored to common control systems, able to reproduce spatial effects (Sartori et al., 2014a), in particular those induced by the con-

trol rod movement, in order to build a bridge between the "world of design" and the "world of control". The goal is to demonstrate that reduced order modelling is suited to be applied in more complex (and coupled) industrial problems in order to introduce competitive computational performances and allowing, at the same time, a better investigation, thanks to parametrization of involved phenomena. The original elements introduced in this Chapter are related to reduced order modelling approaches in a complex parametrized industrial systems modelled into a 3D geometrical setting, which is held by several time-dependent non-coercive equations whose solutions have been verified by accurate error bounds. At the best of our knowledge and at the current state of the art this is the first time that the certified reduced basis method has been employed to these problems.

The Chapter is organized as follows. The modelling approach for describing the reactor kinetics is briefly introduced in Section 2.2. Thereafter, the Reduced Basis method, which is detailed in Section 2.3, is applied to the parametrized reactor spatial kinetics for the one-rod model (Section 2.4) and for the three-rods model (Section 2.5), highlighting some representative results. The main conclusions are presented in Section 2.6.

2.2 Modelling approach

As anticipated, the TRIGA Mark II reactor (General Atomic, 1964) of the University of Pavia (Italy) has been chosen as case study (see Appendix A on page 89). It is worth recalling that this work is more focused on testing and assessing an innovative methodology for a 3D reactor spatial dynamics, rather than reproducing the real reference reactor. Therefore, simplified 3D models have been adopted, and they will be presented in the following Sections.

As stated in the Introduction, the so called multi-group diffusion theory (Duderstadt and Hamilton, 1976) has been employed. According to this approximation, the spectrum of the neutron energy is split into groups and, for each group, equivalent cross sections are computed that are constant in the energy range of the group. In particular, two energy groups and eight groups of precursors (c_i), where c_i is the concentration of the i-th precursor group, have been employed leading to a set of ten coupled parabolic equations, reported below in their strong formulation.[2]

$$\frac{1}{\mathrm{v}_1}\frac{\partial \Phi_1}{\partial t} = \nabla\cdot(D_1\nabla\Phi_1) + \left[(1-\beta)\nu\Sigma_{f_1} - \Sigma_{a_1} - \Sigma_{s_{1\to 2}}\right]\Phi_1 + \left[(1-\beta)\nu\Sigma_{f_2} + \Sigma_{s_{2\to 1}}\right]\Phi_2 + \sum_{i=1}^{8}\lambda_i c_i, \tag{2.1}$$

$$\frac{1}{\mathrm{v}_2}\frac{\partial \Phi_2}{\partial t} = \nabla\cdot(D_2\nabla\Phi_2) + \Sigma_{s_{1\to 2}}\Phi_1 - \left[\Sigma_{a_2} + \Sigma_{s_{2\to 1}}\right]\Phi_2, \tag{2.2}$$

$$\frac{\partial c_i}{\partial t} = -\lambda_i c_i + \beta_i\left[\nu\Sigma_{f_1}\Phi_1 + \nu\Sigma_{f_2}\Phi_2\right], \ i = 1,\dots,8, \tag{2.3}$$

with a given initial condition

$$\Phi_1(t=0) = \Phi_1^0, \quad \Phi_2(t=0) = \Phi_2^0, \quad c_i(t=0) = c_i^0, \tag{2.4}$$

[2] All the parameters and fluxes are spatially dependent, however this dependence has not been reported in order not to further burden the notation.

Table 2.1: *Neutronic parameters generated by means of the SERPENT code.*

Parameter	Fuel	Water	Rod
D_1 [cm]	$8.77 \cdot 10^{-1}$	$8.51 \cdot 10^{-1}$	$7.52 \cdot 10^{-1}$
D_2 [cm]	$1.92 \cdot 10^{-1}$	$1.39 \cdot 10^{-1}$	$1.32 \cdot 10^{-1}$
Σ_{a_1} [cm^{-1}]	$4.85 \cdot 10^{-3}$	$5.04 \cdot 10^{-4}$	$7.07 \cdot 10^{-2}$
Σ_{a_2} [cm^{-1}]	$7.53 \cdot 10^{-2}$	$1.70 \cdot 10^{-2}$	$4.57 \cdot 10^{-1}$
$\nu\Sigma_{f_1}$ [cm^{-1}]	$3.65 \cdot 10^{-3}$	0.0	0.0
$\nu\Sigma_{f_2}$ [cm^{-1}]	$1.25 \cdot 10^{-1}$	0.0	0.0
$\Sigma_{s_{1\to2}}$ [cm^{-1}]	$3.02 \cdot 10^{-2}$	$5.34 \cdot 10^{-2}$	$1.36 \cdot 10^{-2}$
$\Sigma_{s_{2\to1}}$ [cm^{-1}]	$3.27 \cdot 10^{-4}$	$2.49 \cdot 10^{-4}$	$5.83 \cdot 10^{-4}$
$1/\mathrm{v}_1$ [s/cm]	$5.87 \cdot 10^{-8}$	$7.58 \cdot 10^{-8}$	$2.61 \cdot 10^{-8}$
$1/\mathrm{v}_2$ [s/cm]	$3.00 \cdot 10^{-6}$	$3.47 \cdot 10^{-6}$	$3.14 \cdot 10^{-6}$

Precursor group	λ [s^{-1}]	β [-]
1	$1.25 \cdot 10^{-02}$	$3.83 \cdot 10^{-04}$
2	$2.83 \cdot 10^{-02}$	$1.34 \cdot 10^{-03}$
3	$4.25 \cdot 10^{-02}$	$9.63 \cdot 10^{-04}$
4	$1.33 \cdot 10^{-01}$	$1.92 \cdot 10^{-03}$
5	$2.92 \cdot 10^{-01}$	$3.08 \cdot 10^{-03}$
6	$6.66 \cdot 10^{-01}$	$8.61 \cdot 10^{-04}$
7	1.63	$7.88 \cdot 10^{-04}$
8	3.55	$2.31 \cdot 10^{-04}$

where the subscript 1 refers to the fast group (i.e., the most energetic group) and 2 to the thermal one; v is the velocity of the neutrons, Φ is the neutron flux, D is the diffusion coefficient, β is the fraction of delayed neutrons and $\beta = \sum_{i=1}^{8} \beta_i$, $\nu\Sigma_f$ are the number of neutrons emitted per fission reaction, Σ_a is the absorption cross section, $\Sigma_{s_{i\to j}}$ is the scattering cross section from group i to group j, λ_i is the decay constant of the precursor group i. It is worth mentioning that the bilinear form associated to the elliptic part of the equations is non-coercive and non-symmetric. Different spatial domains have been defined for the two approaches developed in the present work and they will be introduced in the following Sections. For the sake of simplicity, the homogeneous Dirichlet boundary conditions have been employed.

The FE discretization of the Eqs. (2.1)–(2.3), adopting the uniform Backward Euler (BE) in time with twenty time intervals of length 5×10^{-4} s, has been assumed as the "truth" solution. All the simulations needed by the RB method, for both the Offline and Online step, have been performed relying on the C++ library `libMesh` (Kirk et al., 2006) within the `rbOOmit` framework (Knezevic and Peterson, 2011).

The neutronic parameters (v, D, Σ_a, Σ_s, $\nu\Sigma_f$, β_i) have been generated by means of the continuous energy Monte Carlo neutron transport code SERPENT (SERPENT, 2011), which features group constant generation capabilities – i.e. it is able to compute the equivalent cross sections – using the nuclear data library JEFF 3.1 (Koning et al., 2006). The computed parameters are reported in Tab. 2.1, and such neutronic quantities have been taken constant for all the simulations.

2.3 Reduced basis method

In this Section, the strategies upon which the Reduced Basis (RB) method relies are firstly recalled. Subsequently, the essential ingredients of the RB for parabolic partial

differential equations (herein PDEs), with reference to the multi-group time-dependent neutron diffusion equations, are presented. For a general comprehensive presentation of the RB method the reader may refer to (Patera and Rozza, 2007; Rozza et al., 2008; Rozza, 2014), and, for the parabolic case, to (Grepl and Patera, 2005).

2.3.1 Reduced basis strategies

The philosophy of reduced order methods, such as RB, even if based on Galerkin projection method, is very different with respect to finite element method. In fact, finite element method approximates the exact solution u, which belongs to an *infinite* dimensional space X, of a partial differential equation with $u_{\mathcal{N}}$, that is a piece-wise polynomial approximation, which belongs to a *finite* dimensional space $X_{\mathcal{N}}$. On the other hand, RB approximates $u_{\mathcal{N}}$ using a *low* dimensional space X_N. The basis functions (also called shape functions) employed for constructing the space $X_{\mathcal{N}}$ feature "small" support (i.e. the support is given by a few elements of the mesh on which a finite element approximation has been built for this work), and they are *independent* of the problem considered. Conversely, RB employs *ad hoc* built basis functions, whose support is the entire spatial domain, and strictly related to the considered case.

Before going more deeply inside the methodology, the essential ingredients of RB methodology (Quarteroni et al., 2011), employed in this Chapter, can be summarized as follows: a Galerkin projection onto a low-dimensional space of basis functions properly selected, an affine parametric dependence enabling to perform a competitive Offline-Online splitting in the computational procedure, and a rigorous a posteriori error estimation used for both the basis selection and the certification of the solution. The combination of these three factors yields substantial computational savings which are at the basis of an efficient model order reduction, ideally suited for real-time simulation and many-query contexts (for example, optimization, control or parameter identification). It is worth recalling that the rational of this approach stands in the fact that the set of all solutions, as function of the parameters, behaves well (Patera and Rozza, 2007), or, more precisely, that the Kolmogorov n-width is small (Maday, 2006).

The Offline step can be depicted as in the flow chart reported in Fig. 2.1. The starting point is the "truth" model, which is a high fidelity finite element approximation of a set of parametrized partial differential equations (PDEs). Relying on a POD-greedy algorithm, which is recalled in Section 2.3.2, the "truth" model is solved for a suitable number of parameter instances, and matrices for the Reduced Order Model (ROM) as well as for error bounds estimation are computed and stored (more details are given in Sections 2.3.2 and 2.3.2, respectively). At the end of this step, the RB method leads to a ROM of the "truth" one, along with an *a posteriori* error estimation for the greedy parameter space exploration and basis functions selection. The Offline step is performed only once and it may be very expensive in terms of computational burden. Most of the physical information (or energy) of the system is stored in the RB space.

When the ROM is obtained, the Online step consists of the input/output evaluation for a given parameter μ, as shown in Fig. 2.2. The computational time required to solve the ROM, is usually very short. The gain of the so obtained reduced model can be expressed as the ratio between the time required to solve the "truth" model with respect to the Online step duration. Such gain is referred to as computational speed-up. Finally, the number of basis functions employed can be set Online, so the ROM matrices can

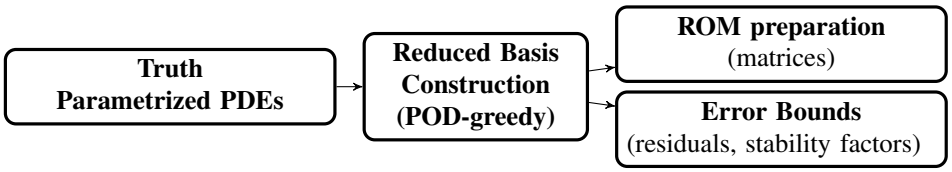

Figure 2.1: *Conceptual flow chart for the Offline step.*

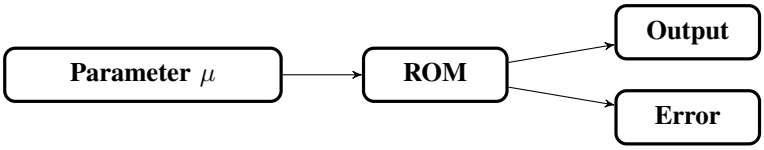

Figure 2.2: *Conceptual flow chart for the Online step.*

have (in the scalar case) dimension $N \times N$, for $N = 1, \dots, N_{\max}$, and $N \ll \mathcal{N}$, where $\mathcal{N}$ is the finite element space dimension of the "truth" model.

2.3.2 Application to neutron diffusion equations

As shown in Section 2.2, the neutron kinetics has been described according to the so-called multi-group time-dependent neutron diffusion equation (Duderstadt and Hamilton, 1976), which is a set of coupled parabolic PDEs. Moreover the bilinear form, associated to the elliptical part of the equations, is not symmetric neither coercive.

Abstract formulation

A parabolic model problem, parametrized with respect to the input parameter p-vector μ, can be defined as follows (Quarteroni et al., 2011): given $\mu \in \mathcal{D} \subset \mathbb{R}^p$, $\forall t \in I = [0, t_f]$, find $u(t;\mu) \in L^2(I; X(\Omega_o))$ – the subscript o will be clear in the following – is such that

$$m\left(\frac{\partial u(t;\mu)}{\partial t}, v; \mu\right) + a\left(u(t;\mu), v; \mu\right) = f(v), \ \forall v \in X(\Omega_o), \forall t \in I, \tag{2.5}$$

subject to initial condition $u(0;\mu) = u_0$. Ω_o is a spatial domain in $\mathbb{R}^d$ (for $d = 2$ or 3), $X = X(\Omega_o)$ is a suitable Hilbert space, with a given inner product $(\cdot,\cdot)_X$ and an induced norm $\|\cdot\|_X = \sqrt{(\cdot,\cdot)_X}$. In the considered case $u(t;\mu)$ can be defined as follows:

$$u(t;\mu) = \begin{bmatrix} \Phi_1(t;\mu) \\ \Phi_2(t;\mu) \\ c_1(t;\mu) \\ \vdots \\ c_8(t;\mu) \end{bmatrix}, \tag{2.6}$$

and the test function v as

$$v = \begin{bmatrix} \psi_{\Phi_1} \\ \psi_{\Phi_2} \\ \psi_{c_1} \\ \vdots \\ \psi_{c_8} \end{bmatrix}. \tag{2.7}$$

In the following, the dependence of the neutron flux and precursors on the time and parameter μ has to be intended, nut is not reported in order to not overburden the notation. The operators m and a can be formulated as follows:

$$m(u(t;\mu),v) = \int_{\Omega_o(\mu)} \left[\frac{1}{\mathrm{v}_1} \frac{\partial \Phi_1}{\partial t} \psi_{\Phi_1} + \frac{1}{\mathrm{v}_2} \frac{\partial \Phi_2}{\partial t} \psi_{\Phi_2} + \sum_{i=1}^{8} c_i \psi_{c_i} \right], \tag{2.8}$$

$$\begin{aligned} a(u(t),v) = & \underbrace{\int_{\Omega_o(\mu)} D_1 \nabla \Phi_1 \cdot \nabla \psi_{\Phi_1}}_{a^1} + \underbrace{\int_{\Omega_o(\mu)} D_2 \nabla \Phi_2 \cdot \nabla \psi_{\Phi_2}}_{a^2} + \underbrace{\int_{\Omega_o(\mu)} \Sigma_{a_1} \Phi_1 \psi_{\Phi_1}}_{a^3} \\ & + \underbrace{\int_{\Omega_o(\mu)} \Sigma_{s_{1\to 2}} \Phi_1 \psi_{\Phi_1}}_{a^4} - \underbrace{\int_{\Omega_o(\mu)} (1-\beta) \nu \Sigma_{f_1} \Phi_1 \psi_{\Phi_1}}_{a^5} \\ & - \underbrace{\int_{\Omega_o(\mu)} \Sigma_{s_{2\to 1}} \Phi_2 \psi_{\Phi_1}}_{a^6} - \underbrace{\int_{\Omega_o(\mu)} (1-\beta) \nu \Sigma_{f_2} \Phi_2 \psi_{\Phi_1}}_{a^7} - \underbrace{\int_{\Omega_o(\mu)} \sum_{i=1}^{8} \lambda_i c_i \psi_{\Phi_1}}_{a^8} \\ & - \underbrace{\int_{\Omega_o(\mu)} \Sigma_{s_{1\to 2}} \Phi_1 \psi_{\Phi_2}}_{a^9} + \underbrace{\int_{\Omega_o(\mu)} \Sigma_{a_2} \Phi_2 \psi_{\Phi_2}}_{a^{10}} + \underbrace{\int_{\Omega_o(\mu)} \Sigma_{s_{2\to 1}} \Phi_2 \psi_{\Phi_2}}_{a^{11}} \\ & - \underbrace{\int_{\Omega_o(\mu)} \sum_{i=1}^{8} \beta_i \nu \Sigma_{f_1} \Phi_1 \psi_{c_i}}_{a^{12}} - \underbrace{\int_{\Omega_o(\mu)} \sum_{i=1}^{8} \beta_i \nu \Sigma_{f_2} \Phi_2 \psi_{c_i}}_{a^{13}} \\ & + \underbrace{\int_{\Omega_o(\mu)} \sum_{i=1}^{8} \lambda_i c_i \psi_{c_i}}_{a^{14}}, \end{aligned} \tag{2.9}$$

(2.10)

where ψ is the test function for the corresponding variable. For the neutron fluxes and corresponding test functions, the $H^1(\Omega_0(\mu))$ Hilbert space has been chosen, whereas the $L^2(\Omega_0(\mu))$ space has been used for the precursors. It is worth pointing out that the bilinear form a is non-symmetric. Moreover, it has been observed that the production terms a^7 and a^8 make the bilinear form non-coercive, for the values of the neutronic quantities reported in Tab 2.1 on page 39. In order to have a stationary neutron flux distribution when the reactor is subcritical (i.e., when the number of neutrons produced is lower than the number of neutrons absorbed), a uniform source, equal to $1\,\text{neutron cm}^{-2}\,\text{s}^{-1}$, within the fuel has been considered. In weak formulation, it reads

$$f(v) = \int_{\Omega_o^{\text{fuel}}} 1 \times \psi_{\Phi_1}. \tag{2.11}$$

It is assumed that the bilinear forms $a(u(t;\mu),v;\mu)$ and $m(u(t;\mu),v;\mu)$ are contin-

uous with continuity constants γ and ρ,

$$a(u,v;\mu) \leq \gamma(\mu)\|u\|_X\|v\|_X \leq \gamma_0\|u\|_X\|v\|_X, \ \forall u,v \in X, \forall \mu \in \mathcal{D}, \tag{2.12}$$

$$m(u,v;\mu) \leq \rho(\mu)\|u\|_X\|v\|_X \leq \rho_0\|u\|_X\|v\|_X, \ \forall u,v \in X, \forall \mu \in \mathcal{D}. \tag{2.13}$$

Finally, it is assumed that a and m depend *affinely* on the parameter μ, hence they can be expressed as

$$a(u,v;\mu) = \sum_{q=1}^{Q_a} \Theta_a^q(\mu) a^q(u,v), \quad \forall u,v \in X, \forall \mu \in \mathcal{D}, \tag{2.14}$$

$$m(u,v;\mu) = \sum_{q=1}^{Q_m} \Theta_m^q(\mu) m^q(u,v), \quad \forall u,v \in X, \forall \mu \in \mathcal{D}, \tag{2.15}$$

for some integers Q_a and Q_m. The coefficients of the affine expansions (2.14) and (2.15) can be easily derived when they are related to physical properties (e.g., diffusion coefficients, thermal conductivity). Whether the μ-vector includes geometric properties, the derivation of the $\Theta(\mu)$ coefficients may require a dedicated treatment. When affine parameter dependence is not valid, as well as in case of non-linearities, an equivalent recovered affine formulation (to allow offline-online computational decomposition) can rely on a well established Empirical Interpolation Method (Barrault et al., 2004).

Geometric parametrization

Let $\Omega_o(\mu)$ be a parametrized spatial domain, which is called *original* domain. The RB framework requires also a *reference* (μ-independent) domain $\Omega = \Omega_o(\mu_{\text{ref}})$ in order to compare, and combine, FE solutions that would be otherwise computed on different domains and grids. For this reason, $\Omega_o(\mu)$ has to be mapped to Ω in order to get the *transformed* problem, which is the point of departure of the RB approach[3]. In order to build a parametric mapping related to geometrical properties, a conforming domain decomposition of $\Omega_o(\mu)$ has to be introduced

$$\Omega_o(\mu) = \bigcup_{l=1}^{L_{\text{dom}}} \Omega_o^l(\mu), \tag{2.16}$$

consisting of mutually non-overlapping open subdomains $\Omega_o^l(\mu)$, such that $\Omega_o^l(\mu) \cap \Omega_o^{l'}(\mu) = \emptyset, \ 1 \leq l < l' \leq L_{\text{dom}}$. Original and reference subdomains must be linked *via* a mapping $\mathcal{T}(\cdot;\mu) : \Omega^l \to \Omega_o^l(\mu), \ 1 \leq l \leq L_{\text{dom}}$ such that

$$\Omega_o^l(\mu) = \mathcal{T}^l(\Omega^l;\mu), \ 1 \leq l \leq L_{\text{dom}}. \tag{2.17}$$

These maps must be individually bijective, collectively continuous, and such that

$$\mathcal{T}^l(\mathbf{x};\mu) = \mathcal{T}^{l'}(\mathbf{x};\mu), \ \forall \mathbf{x} \in \Omega^l \cap \Omega^{l'}, \ 1 \leq l < l' \leq L_{\text{dom}}. \tag{2.18}$$

In this work, the following affine transformation, for $\mu \in \mathcal{D}$ and $\mathbf{x} \in \Omega^l$, has been employed

$$\mathcal{T}_i^l(\mathbf{x};\mu) = C_i^l(\mu) + \sum_{j=1}^{d} G_{ij}^l(\mu) x_j, \qquad 1 \leq i \leq d, \tag{2.19}$$

[3] From finite element consolidated fashion, such mapping may be seen as the isoparametric transformation from the original mesh element to the reference element to perform the Gaussian integration.

for given translation vector $C^l : \mathcal{D} \to \mathbb{R}^d$ and linear transformation matrices $G^l : \mathcal{D} \to \mathbb{R}^{d\times d}$. The following terms, which will be useful later on, can be defined

$$J^l(\mu) = |\det(G^l(\mu))|, \qquad 1 \le l \le L_{\text{dom}}, \tag{2.20}$$

$$D^l(\mu) = (G^l(\mu))^{-1}, \qquad 1 \le l \le L_{\text{dom}}. \tag{2.21}$$

The class of admissible operators, which allow an affine expansion for a geometric parametrization, can be expressed by the following associated bilinear forms (Rozza et al., 2008)

$$a_o(w,\psi;\mu) = \sum_{l=1}^{L_{\text{dom}}} \int_{\Omega_o^l(\mu)} \begin{bmatrix} \dfrac{\partial w}{\partial x} & \dfrac{\partial w}{\partial y} & \dfrac{\partial w}{\partial z} & w \end{bmatrix} \mathcal{K}_o^l(\mu) \begin{bmatrix} \dfrac{\partial \psi}{\partial x} \\ \dfrac{\partial \psi}{\partial y} \\ \dfrac{\partial \psi}{\partial z} \\ \psi \end{bmatrix}, \tag{2.22}$$

where, w is a generic variable (e.g., Φ_1, c_1, etc.), ψ the corresponding test function, $\mathcal{K}_o^l : \mathcal{D} \to \mathbb{R}^{(d+1)\times(d+1)}, 1 \le l \le L_{\text{dom}}$, are prescribed coefficients. In particular, the upper $d \times d$ principal submatrix of $\mathcal{K}_o^l$ is the matrix of diffusivity; the $(d+1, d+1)$ element of $\mathcal{K}_o^l$ represents the reaction terms; the other terms are set to zero. For example, substituting w and ψ with Φ_1 and ψ_{Φ_1}, respectively, the $\mathcal{K}_o^l$ can be expressed as follows:

$$\mathcal{K}_o^l = \begin{bmatrix} D_1 & 0 & 0 & 0 \\ 0 & D_1 & 0 & 0 \\ 0 & 0 & D_1 & 0 \\ 0 & 0 & 0 & \Sigma_{a_1} + \Sigma_{s_{1\to 2}} - (1-\beta)\nu\Sigma_{f_1} \end{bmatrix}. \tag{2.23}$$

In addition, the following relation has to be considered as well

$$m_o(w,\psi;\mu) = \sum_{l=1}^{L_{\text{dom}}} \int_{\Omega_o^l(\mu)} w\mathcal{M}_o^l(\mu)\psi, \tag{2.24}$$

where $\mathcal{M}_o^l : \mathcal{D} \to \mathbb{R}$ represents the identity operator. By identifying $u(t;\mu) = u_o(t;\mu) \circ \mathcal{T}(\cdot;\mu) \forall t > 0$, and tracing (2.22) back to the reference domain Ω by the mapping $\mathcal{T}(\cdot;\mu)$, it follows that the bilinear form $a(w,\psi;\mu)$ can be expressed as

$$a(w,\psi;\mu) = \sum_{l=1}^{L_{\text{dom}}} \int_{\Omega^l} \begin{bmatrix} \dfrac{\partial w}{\partial x} & \dfrac{\partial w}{\partial y} & \dfrac{\partial w}{\partial z} & w \end{bmatrix} \mathcal{K}^l(\mu) \begin{bmatrix} \dfrac{\partial \psi}{\partial x} \\ \dfrac{\partial \psi}{\partial y} \\ \dfrac{\partial \psi}{\partial z} \\ \psi \end{bmatrix}, \tag{2.25}$$

where $\mathcal{K}^l : \mathcal{D} \to \mathbb{R}^{4\times 4}$ is given by

$$\mathcal{K}^l(\mu) = J^l(\mu)\, \mathcal{G}^l(\mu)\, \mathcal{K}_o^l(\mu)\, \left(\mathcal{G}^l(\mu)\right)^T, \tag{2.26}$$

and

$$\mathcal{G}^l(\mu) = \begin{bmatrix} D^l(\mu) & \mathbf{0} \\ \mathbf{0} & 1 \end{bmatrix}. \tag{2.27}$$

Similarly, the transformed bilinear form $m(\cdot,\cdot;\mu)$ can be expressed as

$$m(w,\psi;\mu) = \sum_{l=1}^{L_{\text{dom}}} \int_{\Omega_l} w\mathcal{M}^l\psi, \tag{2.28}$$

where $\mathcal{M}^l : \mathcal{D} \to \mathbb{R}$ is given by

$$\mathcal{M}^l(\mu) = J^l(\mu)\mathcal{M}^l_o(\mu). \tag{2.29}$$

At this point, the original problem has been reformulated on the reference domain, resulting in a parametrized problem where the effect of geometry variations is traced back onto its parametrized transformation tensors. For example, the affine formulation (2.14) can be derived by expanding the expression (2.25) in terms of the subdomains Ω_l and the different entries of $\mathcal{K}^l_{ij}$ leading to

$$a(w,\psi;\mu) = \mathcal{K}^1_{11}(\mu)\int_{\Omega_1} \frac{\partial w}{\partial x}\frac{\partial \psi}{\partial x} + \mathcal{K}^1_{22}(\mu)\int_{\Omega_1} \frac{\partial w}{\partial y}\frac{\partial \psi}{\partial y} + \dots \tag{2.30}$$

It is worth pointing out that $\mathcal{K}^l$ can be non-diagonal even if $\mathcal{K}^l_o$ is diagonal.

Construction of the reduced basis approximation

The RB method is built upon a fine approximation (i.e., finite element or finite volume), assumed as "truth" solution. This implies that the error of the RB solution is estimated with respect to the fine approximation. The error of the "truth" solution, with respect to the real world, is inherited by the ROM. Let the following expression be the discretization of the parabolic problem (2.5) adopting the finite difference in time, using the Backward Euler (BE) method, and Finite Element (FE) (Quarteroni and Valli, 2008) in space

$$\begin{aligned} &\frac{1}{\Delta t} m(u^k(\mu) - u^{k-1}(\mu), v;\mu) + a(u^k(\mu), v;\mu) \\ &\quad = f(v), \quad \forall v \in X^{\mathcal{N}}, 1 \le k \le K, \end{aligned} \tag{2.31}$$

subject to initial condition $(u^0, v) = (u_0, v), \forall v \in X^{\mathcal{N}}$, where the time interval I has been divided into K subintervals of equal length $\Delta t = t_f/K$, $t^k = k\Delta t$, and $X^{\mathcal{N}}$ is the FE approximation space of dimension $\mathcal{N}$ (usually very large).

Then, given a positive integer $N_{\max}$, let X_N, for $N = 1, \dots, N_{\max}$, be an associated sequence of approximation spaces (RB spaces), where X_N is a N-dimensional subspace of $X^{\mathcal{N}}$. The RB spaces are such that they are *hierarchical*

$$X_1 \subset X_2 \subset \cdots \subset X_{N_{\max}} \subset X^{\mathcal{N}}. \tag{2.32}$$

The RB approximation of the discretized parabolic problem (2.31) can be stated as follows

$$\begin{aligned} &\frac{1}{\Delta t} m(u^k_N(\mu) - u^{k-1}_N(\mu), v;\mu) + a(u^k_N(\mu), v;\mu) \\ &\quad = f(v), \quad \forall v \in X_N, 1 \le k \le K, \end{aligned} \tag{2.33}$$

subject to initial condition $(u_N^0, v) = (u_0, v), \forall v \in X_N$. Let $\xi_n^{\mathcal{N}} \in X^{\mathcal{N}}, 1 \leq n \leq N_{\max}$ be a set of orthonormal functions and let such functions be the basis of the RB spaces

$$X_N = \text{span}\left\{\xi_n^{\mathcal{N}}, 1 \leq n \leq N\right\}, \quad 1 \leq N \leq N_{\max}. \tag{2.34}$$

The RB approximation $u_N^k(\mu) \in X_N$ can be expressed as

$$u_N^k(\mu) = \sum_{i=1}^{N} u_{N,i}^k(\mu)\xi_i^{\mathcal{N}}. \tag{2.35}$$

Then, by denoting

$$\mathcal{Z} = \left[\xi_1^{\mathcal{N}} | \ldots | \xi_N^{\mathcal{N}}\right] \in \mathbb{R}^{\mathcal{N} \times N}, \quad 1 \leq N \leq N_{\max}, \tag{2.36}$$

the bilinear forms a^q and m^q can be projected onto the RB space X_N as follows

$$\mathbf{A}_N^q = \mathcal{Z}^T A_{\mathcal{N}}^q \mathcal{Z}, \tag{2.37}$$
$$\mathbf{M}_N^q = \mathcal{Z}^T M_{\mathcal{N}}^q \mathcal{Z}, \tag{2.38}$$
$$\mathbf{f}_N = \mathcal{Z}^T F_{\mathcal{N}}, \tag{2.39}$$

where

$$(A_{\mathcal{N}}^q)_{ij} = a^q(\psi_j, \psi_i), \tag{2.40}$$
$$(M_{\mathcal{N}}^q)_{ij} = m^q(\psi_j, \psi_i), \tag{2.41}$$
$$(F_{\mathcal{N}})_i = f(\psi_i), \tag{2.42}$$

being $\{\psi_i\}_{i=1}^{\mathcal{N}}$ the basis of the FE space $X^{\mathcal{N}}$. Hence, the following algebraic equations associated to the parabolic problem (2.33) are obtained

$$\left[\sum_{q=1}^{Q_a} \Theta_a^q(\mu)\mathbf{A}_n^q + \frac{1}{\Delta t}\sum_{q=1}^{Q_m} \Theta_m^q(\mu)\mathbf{M}_n^q\right] \mathbf{u}_N(t^k;\mu) = \mathbf{f}_N + \frac{1}{\Delta t}\sum_{q=1}^{Q_m} \Theta_m^q(\mu)\mathbf{M}_n^q\, \mathbf{u}_N(t^{k-1};\mu), \tag{2.43}$$

where $\left(\mathbf{u}_N(t^k;\mu)\right)_i = u_{N,i}^k(\mu)$. It is worth mentioning that the linear system (2.43), which is $N \times N$, is independent of the FE space dimension $\mathcal{N}$, and $N \ll \mathcal{N}$. This means that the size of the reduced model does not depend on the mesh of the "truth" problem, but on the number of bilinear forms a^q and m^q and the number of basis functions.

A posteriori error estimation

Effective *a posteriori* error bounds for field variables and outputs of interest are crucial for both the efficiency and the reliability of RB approximations (Quarteroni et al., 2011). The first ingredient is the dual norm of the residual

$$\varepsilon_N(t^k;\mu) = \sup_{v \in X^{\mathcal{N}}} \frac{r_N(v;t^k;\mu)}{\|v\|_X}, \quad 1 \leq k \leq K, \tag{2.44}$$

where $r_N(v;t^k;\mu)$ is the residual associated with the RB approximation (2.33) and it is given by

$$r_N(v;t^k;\mu) = f(v) - \frac{1}{\Delta t} m\left(u_N^k(\mu) - u_N^{k-1}(\mu), v;\mu\right) - a(u_N^k(\mu), v;\mu), \quad \forall v \in X^{\mathcal{N}}, 1 \le k \le K. \tag{2.45}$$

The second ingredient is a lower bound for the inf-sup constant $\beta_{\text{inf}-\text{sup}}^{\mathcal{N}}(\mu)$ such that

$$0 < \beta_{\text{LB}}^{\mathcal{N}}(\mu) \le \beta_{\text{inf}-\text{sup}}^{\mathcal{N}}(\mu), \quad \forall \mu \in \mathcal{D}. \tag{2.46}$$

The error bounds can thus be defined (Quarteroni et al., 2011) for all $\mu \in \mathcal{D}$ and all N

$$\|u^k(\mu) - u_N^k(\mu)\|_\mu \le \Delta_N^k(\mu) \quad 1 \le k \le K, \tag{2.47}$$

where $\Delta_N^k(\mu) \equiv \Delta_N(t^k;\mu)$ is given by

$$\Delta_N^k(\mu) = \left(\frac{\Delta t}{\beta_{\text{LB}}^{\mathcal{N}}(\mu)} \sum_{m=1}^{k} \varepsilon_N^2(t^m;\mu)\right)^{1/2}. \tag{2.48}$$

The above presented error bounds are without any utility if not accompanied by an Offline-Online computational approach, which is an equivalent formulation of (2.43). To begin with (Nguyen et al., 2010), the residual equation (2.45) can be rewritten according to the affine expansion, Eqs. (2.14) and (2.15), and the reduced basis representation (2.35)

$$r_N(v,t^k;\mu) = f(v) - \frac{1}{\Delta t}\sum_{q=1}^{Q_m}\sum_{i=1}^{N} \Theta_m^q(\mu)\left[u_{N,i}^k(\mu) - u_{N,i}^{k-1}(\mu)\right] m^q(\xi_i^{\mathcal{N}}, v) - \sum_{q=1}^{Q_a}\sum_{i=1}^{N} \Theta_a^q(\mu)\left[u_{N,i}^k(\mu) - u_{N,i}^{k-1}(\mu)\right] a^q(\xi_i^{\mathcal{N}}, v), \tag{2.49}$$

for $1 \le k \le K$. It shall prove convenient to introduce the Riesz representation of $r_N(v,t^k;\mu) : \hat{e}_N(t^k;\mu) \in X^{\mathcal{N}}$ satisfies

$$\left(\hat{e}_N(t^k;\mu), v\right)_X = r_N(v;t^k;\mu), \quad \forall v \in X^{\mathcal{N}}. \tag{2.50}$$

It now follows directly from (2.50) and (2.49) that

$$\hat{e}_N(t^k;\mu) = \Gamma + \frac{1}{\Delta t}\sum_{q=1}^{Q_m}\sum_{i=1}^{N} \Theta_m^q(\mu)\left[u_{N,i}^k(\mu) - u_{N,i}^{k-1}(\mu)\right]\Lambda_N^{q,i} + \sum_{q=1}^{Q_a}\sum_{i=1}^{N} \Theta_a^q(\mu)\left[u_{N,i}^k(\mu) - u_{N,i}^{k-1}(\mu)\right]\Upsilon_N^{q,i}, \tag{2.51}$$

where

$$(\Gamma, v)_X = f(v), \quad \forall v \in X^{\mathcal{N}}, \tag{2.52}$$

$$(\Lambda_N^{q,i}, v)_X = -m^q(\xi_i^{\mathcal{N}}, v), \quad \forall v \in X^{\mathcal{N}}, \quad 1 \le q \le Q_m, \quad 1 \le i \le N, \tag{2.53}$$

$$(\Upsilon_N^{q,i}, v)_X = -a^q(\xi_i^{\mathcal{N}}, v), \quad \forall v \in X^{\mathcal{N}}, \quad 1 \le q \le Q_a, \quad 1 \le i \le N. \tag{2.54}$$

For duality arguments, the $\varepsilon_N(t^k;\mu)$ can be expressed as

$$\varepsilon_N^2(t^k;\mu) = \|\hat{e}_N(t^k;\mu)\|_X^2, \quad 1 \le k \le K. \tag{2.55}$$

Substituting Eq. (2.51) into the above expression follows that

$$\begin{aligned}\varepsilon_N^2(t^k;\mu) = C^{ff} &+ \sum_{i=1}^{N}\sum_{j=1}^{N} u_{N,i}^k(\mu)\, u_{N,j}^k(\mu)\, C_{Ni,j}^{aa}(\mu) \\ &+ \frac{1}{\Delta t^2}\sum_{i=1}^{N}\sum_{j=1}^{N}\left[u_{N,i}^k(\mu) - u_{N,i}^{k-1}(\mu)\right]\left[u_{N,j}^k(\mu) - u_{N,j}^{k-1}(\mu)\right] C_{Ni,j}^{mm}(\mu) \\ &+ 2\sum_{i=1}^{N} u_{N,i}^k(\mu) C_{Ni}^{fa}(\mu) + \frac{2}{\Delta t}\sum_{i=1}^{N}\left[u_{N,i}^k(\mu) - u_{N,i}^{k-1}(\mu)\right] C_{Ni}^{fm}(\mu) \\ &+ \frac{2}{\Delta t}\sum_{i=1}^{N}\sum_{j=1}^{N}\left[u_{N,i}^k(\mu) - u_{N,i}^{k-1}(\mu)\right] u_{N,j}^k(\mu)\, C_{Ni,j}^{am}(\mu), \quad 1 \le k \le K,\end{aligned} \tag{2.56}$$

where

$$C^{ff} = (\Gamma,\Gamma)_X\,, \tag{2.57}$$

$$C_{Ni,j}^{aa}(\mu) = \sum_{q=1}^{Q_a}\sum_{q'=1}^{Q_a}\Theta_a^q(\mu)\Theta_a^{q'}(\mu)\left(\Upsilon_N^{q,i},\Upsilon_N^{q',j}\right)_X, \quad 1 \le i,j \le N, \tag{2.58}$$

$$C_{Ni,j}^{mm}(\mu) = \sum_{q=1}^{Q_m}\sum_{q'=1}^{Q_m}\Theta_m^q(\mu)\Theta_m^{q'}(\mu)\left(\Lambda_N^{q,i},\Lambda_N^{q',j}\right)_X, \quad 1 \le i,j \le N, \tag{2.59}$$

$$C_{Ni}^{fa}(\mu) = \sum_{q=1}^{Q_a}\Theta_a^q(\mu)\left(\Upsilon_N^{q,i},\Gamma\right)_X, \quad 1 \le i \le N, \tag{2.60}$$

$$C_{Ni}^{fm}(\mu) = \sum_{q=1}^{Q_m}\Theta_m^q(\mu)\left(\Lambda_N^{q,i},\Gamma\right)_X, \quad 1 \le i \le N, \tag{2.61}$$

$$C_{Ni,j}^{am}(\mu) = \sum_{q=1}^{Q_m}\sum_{q'=1}^{Q_a}\Theta_m^q(\mu)\Theta_a^{q'}(\mu)\left(\Lambda_N^{q,i},\Upsilon_N^{q',j}\right)_X, \quad 1 \le i,j \le N. \tag{2.62}$$

Therefore, in the Offline phase, $\Gamma, \Lambda_N^{q,i}$ and $\Upsilon_N^{q,i}$ are found and the inner products $(\Gamma,\Gamma)_X$, $\left(\Upsilon_{N_{\max}}^{q,i},\Upsilon_{N_{\max}}^{q',j}\right)_X$, $\left(\Lambda_{N_{\max}}^{q,i},\Lambda_{N_{\max}}^{q',j}\right)_X$, $\left(\Upsilon_{N_{\max}}^{q,i},\Gamma\right)_X$, $\left(\Lambda_{N_{\max}}^{q,i},\Gamma\right)_X$, $\left(\Lambda_{N_{\max}}^{q,i},\Upsilon_{N_{\max}}^{q',j}\right)_X$ are computed.

$\beta_{\inf-\sup}$ stability constant computation

The *inf-sup* condition (Quarteroni et al., 2011), for a parametrized non-coercive bilinear form $a(\cdot,\cdot;\mu): X^1 \times X^2 \to \mathbb{R}$, can be formulated as follows:

$$\exists \beta_0 > 0 : \beta_{\inf-\sup}(\mu) := \inf_{w\in X^1}\sup_{v\in X^2}\frac{a(w,v;\mu)}{\|w\|_{X^1}\|v\|_{X^2}} \ge \beta_0, \quad \forall \mu \in \mathcal{D}. \tag{2.63}$$

This condition can be reformulated (Quarteroni et al., 2011) in terms of the so-called *inner supremizer* operator $T^\mu : X^1 \to X^2$,

$$(T^\mu w, v)_{X^2} = a(w, v; \mu), \quad \forall w \in X^1, \forall v \in X^2; \tag{2.64}$$

by Cauchy-Schwarz inequality and taking $v = T^\mu w$, it follows that for any $w \in X^1$,

$$a\left(w, T^\mu w; \mu\right) \geq \beta_{\text{inf}-\text{sup}}(\mu) \|w\|_{X^1} \|T^\mu w\|_{X^2}. \tag{2.65}$$

Equivalently, the $\beta_{\text{inf}-\text{sup}}$ constant can be computed as follows:

$$\beta^2_{\text{inf}-\text{sup}} = \inf_{w \in X^1} \frac{(T^\mu w, T^\mu w)_{X^2}}{\|w\|^2_{X^1}}, \tag{2.66}$$

which is a Rayleigh quotient.

It must pointed out that the computation of the $\beta_{\text{inf}-\text{sup}}(\mu)$ has to be performed only over the symmetric part of the bilinear form $a(\cdot, \cdot)$. The reader may refer to (Huynh et al., 2007; Quarteroni et al., 2011) for some examples.

Usually, the Successive Constraint Method (SCM) (Huynh et al., 2007, 2010) is used in order to provide accurate and inexpensive approximations of a lower bound for the $\beta_{\text{inf}-\text{sup}}(\mu)$. However, different approaches may be considered as well (e.g., (Lassila et al., 2012)). Indeed, in the present work, surrogate models for the $\beta_{\text{inf}-\text{sup}}(\mu)$ have been developed by interpolating over a suitable set of values of $\beta_{\text{inf}-\text{sup}}(\mu)$ obtained solving the generalized eigenvalue problem (2.66). In Fig. 2.3, the exponential fit of the computed $\beta_{\text{inf}-\text{sup}}(\mu)$ is reported as function of the parameter μ, which is the height of the control rod[1].

Sampling strategy: POD-greedy approach

During the Offline phase the RB approximation space X_N is built using a POD-greedy procedure (Haasdonk and Ohlberger, 2008; Quarteroni et al., 2011; Nguyen et al., 2009): the greedy algorithm selects for whom μ_i^* the FE system (2.5) is solved, while the POD (Proper Orthogonal Decomposition (Holmes et al., 1996; Chatterjee, 2000)) is used to capture the causality associated with the evolution equation. As a result, one or more functions $\zeta_i^{\mathcal{N}}(\mu_i^*) \in X^{\mathcal{N}}$ are retained for each μ_i^*. Then, the RB space can be generated as

$$X_N = \text{span}\left\{\zeta_i^{\mathcal{N}}, 1 \leq i \leq N\right\}. \tag{2.67}$$

Such procedure is performed iteratively until either $N = N_{\max}$ or when the error bound $\Delta_N^k(\mu)$ is beyond a threshold ε^*, where both $N_{\max}$ and ε^* are given by the user. As a result, a uniform rapid convergence over the parameter domain is provided (Quarteroni et al., 2011).

For the sake of clearness, a greedy algorithm is first presented for a stationary problem (i.e., time-independent), subsequently the POD-greedy procedure will be given as well. The greedy sampling procedure can be implemented as described in Algorithm 2.1. Initially, the full-order problem is solved for a given $\boldsymbol{\mu}_1$ and the reduced

[1] For the three-rods model, the superposition of the effects has been hypothesized to hold, i.e. the three rods have been assumed as independent. Actually, there is a sort of "control rod shadowing" (Lamarsh, 1977), meaning that the effect induced by one rod may rely on the positions of the other rods. However, the hypotheses entered in the derivation of the model itself introduce errors, with respect to the real phenomena, that are more important than this one. Therefore, the "control rod shadowing" has been considered negligible for the purposes of the present Chapter.

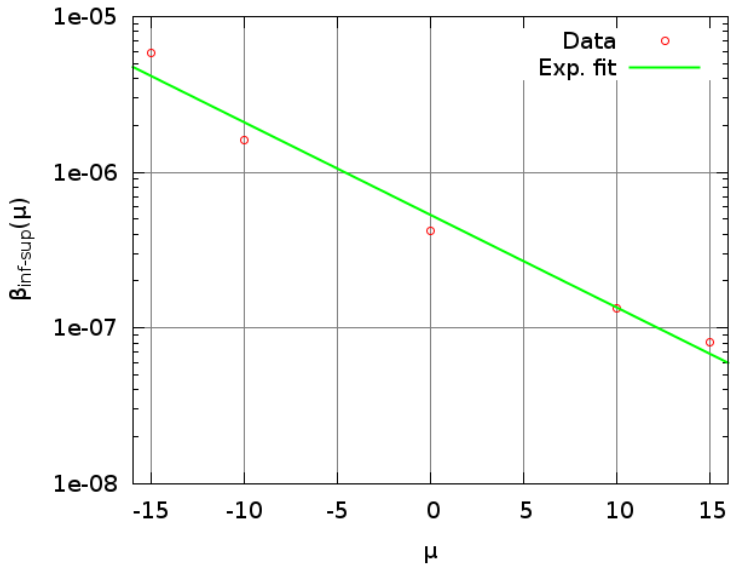

Figure 2.3: *Exponential fit of the* $\beta_{\text{inf}-\text{sup}}$ *stability constant.*

Algorithm 2.1: Greedy algorithm (no time dependency)

```
1   compute u_N(μ_1);
2   X_1^RB = span{u_N(μ_1)};
3     for N = 2 : N_max
4       μ* = arg max_{μ∈Ξ_train} ||u_{N-1}(μ) − u_N(μ)||;
5       ε_{N-1} = ||u_{N-1}(μ*) − u_N(μ*)||;
6       if ε_{N-1} ≤ ε_tol
7         break;
8       end
9       compute u_N(μ*);
10      X_N^RB = X_{N-1}^RB ∪ span u_N(μ*);
11    end
```

space X^{RB} is simply given by the just computed snapshot. Then, within a loop (line 3 of the Algorithm 2.1), it is found for which $\boldsymbol{\mu}$ – over all candidates $\boldsymbol{\mu} \in \Xi_{\text{train}}$ – the error between the reduced order solution and the full order one is maximum (line 4 of the Algorithm 2.1). If such maximum error ε_{N-1} is below a given tolerance the reduced order model has reached the desired accuracy and the loop can be escaped (line 7 of the Algorithm 2.1), otherwise the reduced space has to be enriched with the snapshot computed for μ^* (lines 9-10 of the Algorithm 2.1). Such implementation is not efficient because it requires to solve the full order problem for all $\boldsymbol{\mu} \in \Xi_{\text{train}}$ in order to compute ε_{N-1}. Therefore, in order to implement an efficient greedy procedure (Algorithm 2.2), the true error has to be replaced by the *a posteriori* error estimation, which is sharp and computationally inexpensive.

Algorithm 2.3 implements an efficient POD-greedy algorithm. The starting point is the solution of the full order problem, for a given $\boldsymbol{\mu}^*$, for all the time steps K (line 2 of Algorithm 2.3). Subsequently, the POD is performed onto the vector of the just

Algorithm 2.2: Efficient greedy algorithm (no time dependency)

```
1   compute u_N(μ_1);
2   X_1^RB = span{u_N(μ_1)};
3     for N = 2 : N_max
4     μ* = arg max_{μ∈Ξ_train} Δ_{N-1}(μ);
5     ε_{N-1} = Δ_{N-1}(μ*);
6       if ε_{N-1} ≤ ε_tol
7         break;
8       end
9       compute u_N(μ*);
10      X_N^RB = X_{N-1}^RB ∪ span u_N(μ*);
11    end
```

Algorithm 2.3: Efficient POD-greedy algorithm (time-dependent) (Quarteroni et al., 2011)

```
1   set Z = ∅;
2   compute {u_N^k(μ*), 1 ≤ k ≤ K};
3   while N ≤ N_max
4     {χ_m, 1 ≤ m ≤ M_1} = POD({u_N^k(μ*), 1 ≤ k ≤ K}, M_1);
5     Z ← {Z, {χ_m, 1 ≤ m ≤ M_1}};
6     N ← N + M_2;
7     {ξ_n, 1 ≤ n ≤ N} = POD(Z, N);
8     X_N^RB = span{ξ_n, 1 ≤ n ≤ N};
9     μ* = arg max_{μ∈Ξ_train} Δ_N^k|_{k=K}(μ*);
10    ε_N = Δ_N^k|_{k=K}(μ*);
11    if ε_N ≤ ε_tol
12      break;
13    end
14  end
```

computed solutions, where the first M_1 basis are retained (line 4 of Algorithm 2.3). Thereafter, in order to avoid/minimize duplication on the RB space, a second POD is performed onto the vector of the basis $\mathcal{Z}$ computed so far (line 7 of Algorithm 2.3). Typically, M_1 is set in order to satisfy and internal POD error criterion, and $M_2 \leq M_1$ (Quarteroni et al., 2011). When the new RB space is constructed (line 8 of Algorithm 2.3), the next candidate $\boldsymbol{\mu}^*$ is the one for which the error bound, at the last time step K, is maximum (line 9 of Algorithm 2.3). The procedure is repeated until either a tolerance ε_{tol} or a maximum number of basis functions $N_{\max}$ is reached. It is worth mentioning that a pure greedy approach both in time and $\boldsymbol{\mu}$ might "stall" (Grepl and Patera, 2005).

2.4 One rod 3D modelling: piece-wise affine transformation

The RB method has been applied to model the parametrized movement of a control rod (the SHIM rod, see Fig. A.1 on page 90) in a 3D simplified domain of the TRIGA Mark II reactor.The considered model is reported in Figs. 2.4a and 2.4b, where the position

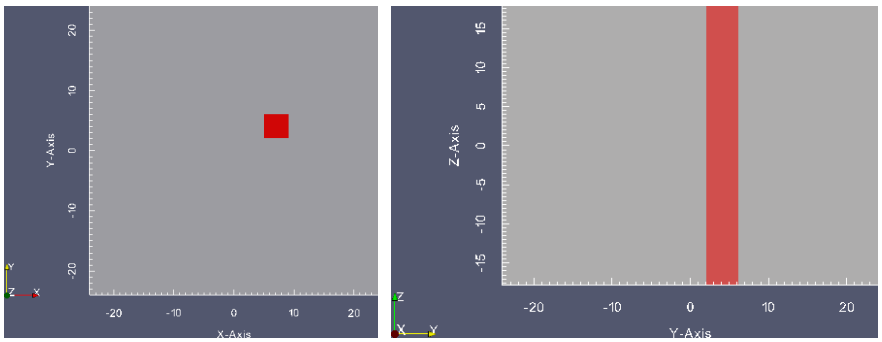

(a) $x - y$ *cross section view.* **(b)** $y - z$ *cross section view.*

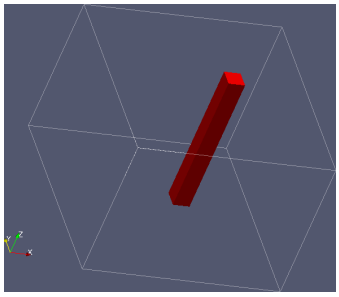

(c) *3D view of the control rod volume.*

Figure 2.4: *Simplified 3D model employed*

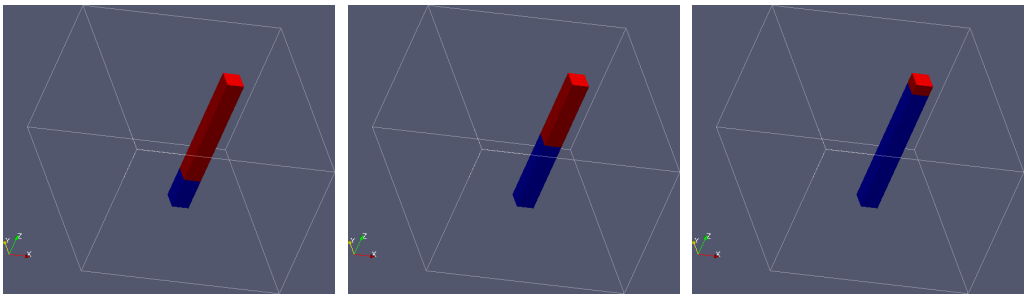

(a) **(b)** **(c)**

Figure 2.5: *Three different positions of the control rod, in red, followed by water, in blue.*

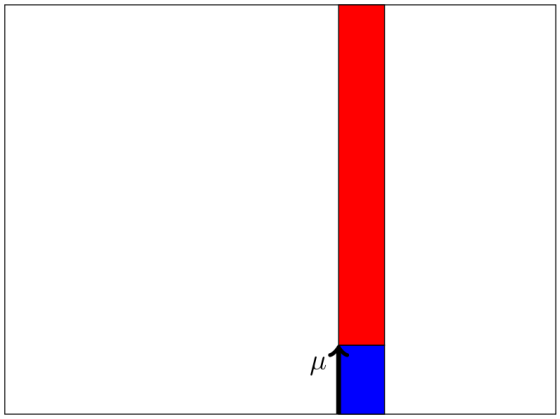

Figure 2.6: $y - z$ *view of the parametrized domain.*

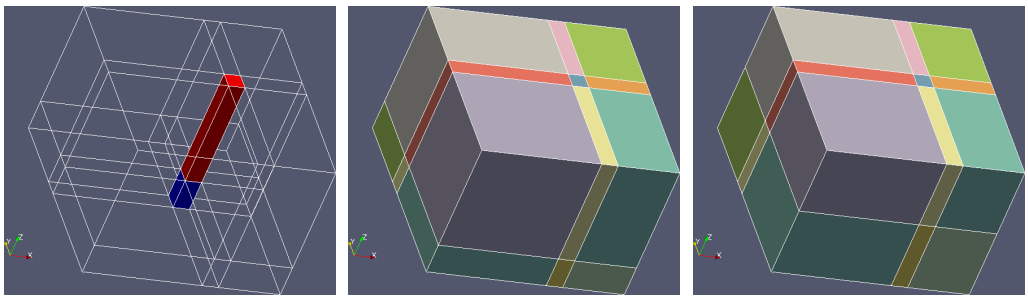

(a) (b) (c)

Figure 2.7: *Domain decomposition of: the original domain with $\mu = -10\,\text{cm}$ (a) and (b); reference domain (c).*

of the control rod is highlighted in red. The rod is surrounded by a fissile material. In particular, a rectangular parallelepiped of dimension $48\,\text{cm} \times 48\,\text{cm} \times 35.6\,\text{cm}$ has been considered, where a control rod, having square basis of side equal to $2\,\text{cm}$, is placed in a non-symmetric position. Figure 2.4c highlights the portion of the domain where the control rod can move. When the rod is withdrawn, its volume is filled by water. Figure 2.5 shows an example of three different configurations that the developed model has to handle in a rapid and reliable way, when the height of the rod (i.e., the parameter μ) is set in the Online phase. To this aim, the $y - z$ view of the parametrized geometry is reported in Fig. 2.6. The movement of the rod has been modeled according to a piecewise affine transformation based on subdomain division (Rozza et al., 2008). In order to guarantee the continuity between elements of the mesh, the original domain has to be divided in suitable subdomains. In Fig. 2.7, the original domain, when $\mu = 10\,\text{cm}$, is reported with the corresponding subdomain decomposition. As stated in the Section 2.3.2, the RB framework requires also a reference (μ-independent) domain in order to compare, and combine, finite element solutions that would be otherwise computed on different domains and grids. The reference domain has been chosen with $\mu = 0$, and it is depicted in Fig. 2.7c. The reference domain has been discretized using $P1$-elements by means of the Gmsh mesh generator (Geuzaine and Remacle, 2009). The mesh, which is shown in Fig. 2.9, is made by $365\,362$ elements, with a mesh size of $\sim 6\,\text{mm}$. When the "truth" model has been solved, a tolerance of 1×10^{-9} has been set.

According to the adopted subdomain splitting, the variation of the original subdomains with respect to the reference ones are simply stretching deformations. In order to understand how to compute the affine transformation (2.19), it is now defined for a tetrahedron, which is the most elementary building block for a 3D geometry. More details can be found in (Gelsomino and Rozza, 2011).

Let the two tetrahedra shown in Fig. 2.8 be considered. The reference domain is $\mu-$independent, while the desired, or original, domain is $\mu-$dependent. In order to derive the translation vector $C : \mathcal{D} \to \mathbb{R}^3$ and linear transformation matrix $G : \mathcal{D} \to$

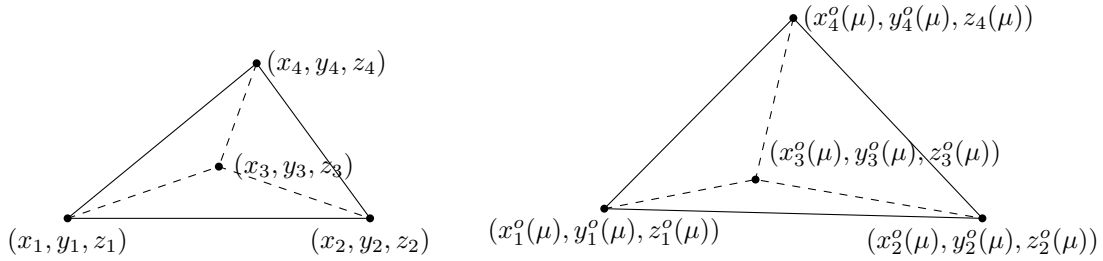

Figure 2.8: *(a) Reference domain Ω, and (b) Original domain $\Omega(\mu)$.*

$\mathbb{R}^{3\times3}$ let the following matrix $\mathbb{B} \in \mathbb{R}^{12\times12}$ and vector $\mathbb{V}(\mu)$ be defined,

$$\mathbb{B} = \begin{bmatrix} 1 & 0 & 0 & x_1 & y_1 & z_1 & 0 & 0 & 0 & 0 & 0 & 0 \\ 0 & 1 & 0 & 0 & 0 & 0 & x_1 & y_1 & z_1 & 0 & 0 & 0 \\ 0 & 0 & 1 & 0 & 0 & 0 & 0 & 0 & 0 & x_1 & y_1 & z_1 \\ 1 & 0 & 0 & x_2 & y_2 & z_2 & 0 & 0 & 0 & 0 & 0 & 0 \\ 0 & 1 & 0 & 0 & 0 & 0 & x_2 & y_2 & z_2 & 0 & 0 & 0 \\ 0 & 0 & 1 & 0 & 0 & 0 & 0 & 0 & 0 & x_2 & y_2 & z_2 \\ 1 & 0 & 0 & x_3 & y_3 & z_3 & 0 & 0 & 0 & 0 & 0 & 0 \\ 0 & 1 & 0 & 0 & 0 & 0 & x_3 & y_3 & z_3 & 0 & 0 & 0 \\ 0 & 0 & 1 & 0 & 0 & 0 & 0 & 0 & 0 & x_3 & y_3 & z_3 \\ 1 & 0 & 0 & x_4 & y_4 & z_4 & 0 & 0 & 0 & 0 & 0 & 0 \\ 0 & 1 & 0 & 0 & 0 & 0 & x_4 & y_4 & z_4 & 0 & 0 & 0 \\ 0 & 0 & 1 & 0 & 0 & 0 & 0 & 0 & 0 & x_4 & y_4 & z_4 \end{bmatrix}, \quad \mathbb{V}(\mu) = \begin{bmatrix} x_1^o(\mu) \\ y_1^o(\mu) \\ z_1^o(\mu) \\ x_2^o(\mu) \\ y_2^o(\mu) \\ z_2^o(\mu) \\ x_3^o(\mu) \\ y_3^o(\mu) \\ z_3^o(\mu) \\ x_4^o(\mu) \\ y_4^o(\mu) \\ z_4^o(\mu) \end{bmatrix}, \quad (2.68)$$

where $\mathbb{V}(\mu)$ is the vector of coordinates of nodes of the original domain. Then, the translation vector $C : \mathcal{D} \to \mathbb{R}^3$ and linear transformation matrix $G : \mathcal{D} \to \mathbb{R}^{3\times3}$ can be obtained as follows:

$$[C_1(\mu),\ C_2(\mu), C_3(\mu),\ G_{11}(\mu),\ G_{12}(\mu),\ G_{13}(\mu),\ G_{21}(\mu),\ G_{22}(\mu),\ G_{23}(\mu), \\ G_{31}(\mu),\ G_{32}(\mu),\ G_{33}(\mu)]^T = \mathbb{B}^{-1}\,\mathbb{V}(\mu). \quad (2.69)$$

It is worth mentioning that $\mathbb{B}$ is non-singular as long as the four points on the reference domain do not belong to the same plane. Therefore, the affine transformation (2.19), for the problem addressed in this Chapter, can be computed choosing four points, among the vertices of the subdomain, which do not belong to the same plane.

2.4.1 Parametrized formulation

As already pointed out, the varying parameter is the height of the control rod position $\mu \in [-16\,\text{cm},\ 16\,\text{cm}]$. Such parameter, according to the piece-wise affine transformation based on subdomain division, does not explicitly enter in the equations, but in

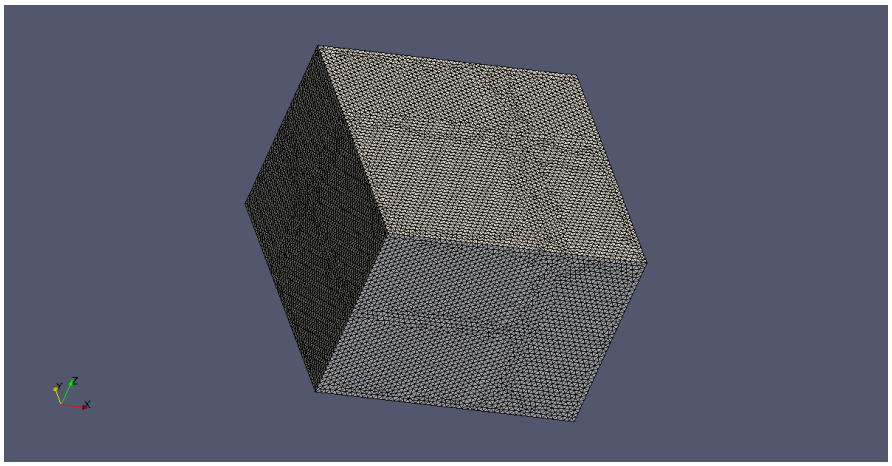

Figure 2.9: *Spatial mesh adopted for the one rod model.*

the shape of the subdomains $\Omega_o^l(\mu)$, as reported in Section 2.3.2. For each subdomain $\Omega_o^l(\mu)$, the following bilinear forms have been defined

$$m_l = \int_{\Omega_o^l(\mu)} \left[\frac{1}{\mathrm{v}_1}\Phi_1\psi_{\Phi_1} + \frac{1}{\mathrm{v}_2}\Phi_2\psi_{\Phi_2} + \sum_{i=1}^{8} c_i\psi_{c_i} \right], \tag{2.70}$$

$$\begin{aligned} a_l^1 = & \int_{\Omega_o^l(\mu)} \left[D_1 \frac{\partial\Phi_1}{\partial x}\frac{\partial\psi_{\Phi_1}}{\partial x} + D_2 \frac{\partial\Phi_2}{\partial x}\frac{\partial\psi_{\Phi_2}}{\partial x} \right] \\ & + \int_{\Omega_o^l(\mu)} \left[D_1 \frac{\partial\Phi_1}{\partial y}\frac{\partial\psi_{\Phi_1}}{\partial y} + D_2 \frac{\partial\Phi_2}{\partial y}\frac{\partial\psi_{\Phi_2}}{\partial y} \right] \\ & + \int_{\Omega_o^l(\mu)} \left[\Sigma_{a_1} + \Sigma_{s_{1\to 2}} - (1-\beta)\nu\Sigma_{f_1} \right] \Phi_1\psi_{\Phi_1} \\ & - \int_{\Omega_o^l(\mu)} \left[\Sigma_{s_{2\to 1}} + (1-\beta)\nu\Sigma_{f_2} \right] \Phi_2\psi_{\Phi_1} \\ & - \int_{\Omega_o^l(\mu)} \sum_{i=1}^{8} \lambda_i c_i \psi_{\Phi_1} - \int_{\Omega_o^l(\mu)} \Sigma_{s_{1\to 2}} \Phi_1\psi_{\Phi_2} \\ & + \int_{\Omega_o^l(\mu)} \left[\Sigma_{a_2} + \Sigma_{s_{2\to 1}} \right] \Phi_2\psi_{\Phi_2} - \int_{\Omega_o^l(\mu)} \sum_{i=1}^{8} \beta_i\nu\Sigma_{f_1}\Phi_1\psi_{c_i} \\ & - \int_{\Omega_o^l(\mu)} \sum_{i=1}^{8} \beta_i\nu\Sigma_{f_2}\Phi_2\psi_{c_i} + \int_{\Omega_o^l(\mu)} \sum_{i=1}^{8} \lambda_i c_i \psi_{c_i}, \end{aligned} \tag{2.71}$$

$$a_l^2 = \int_{\Omega_o^l(\mu)} \left[D_1 \frac{\partial\Phi_1}{\partial z}\frac{\partial\psi_{\Phi_1}}{\partial z} + D_2 \frac{\partial\Phi_2}{\partial z}\frac{\partial\psi_{\Phi_2}}{\partial z} \right], \tag{2.72}$$

where ψ is the test function for the corresponding variable. Due to symmetry, the total number of bilinear forms can be reduced. Indeed, all the subdomains belonging to the upper part of the domain are subjected to the same affine transformation. Similarly, for the subdomains of the lower part of the domain. Therefore, according to the affine expansions (2.14) and (2.15), $Q_a = 4$ and $Q_m = 2$.

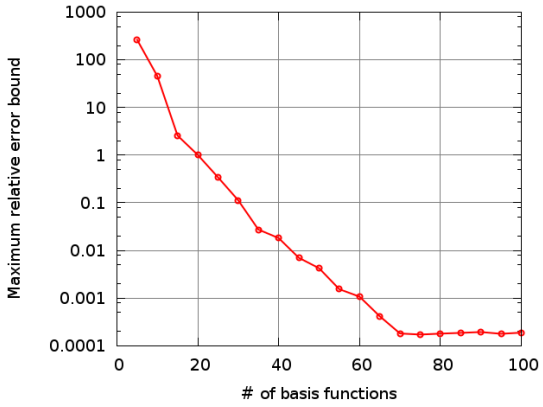

Figure 2.10: *Non-dimensional maximum relative error bound, with respect to the number of basis functions employed.*

2.4.2 Some representative results

We now consider the main results obtained both during the Offline and Online phases are presented.

Offline phase

During the Offline phase, the RB space is constructed and the "truth" model is projected on it to obtain the ROM, and a *a posteriori* error estimation is provided as well for the greedy parameter space exploration and basis functions selection. Figure 2.10 shows the maximum relative error bound with respect to the number of basis functions employed. After 70 basis functions, the accuracy of the solution provided by the ROM reaches an imposed tolerance.

The value of the parameter for each point in the graph is chosen according to a POD-greedy algorithm (Haasdonk and Ohlberger, 2008; Nguyen et al., 2009, 2010). The whole Offline phase lasted almost 20 hours of cpu time on the IBM PLX supercomputer of the Cineca (Italy)[2].

Online phase

The developed reduced order model has been tested for different values of the parameter μ. In Fig. 2.11, the flux shape distribution provided by the ROM, employing seventy basis functions, is reported for four different heights of the rod. The corresponding "truth" solutions are depicted in Fig. 2.12. As it can be seen, the outcomes provided by the ROM are high-fidelity with respect to the "truth" solutions.

As far as the computational time is concerned, in Tab. 2.2 the times required to solve the "truth" FE problem and the developed ROM for the four values of μ are reported. The proposed reduced model allows an Online computational speed-up of more than $60\,000$ times per single time step per single cpu. Therefore, the Offline step is offset by the achievement of a modelling tool with real-time simulation, which was the goal of the present work. In addition, it must be pointed out that when the reduced model is

[2] All the calculations have been performed on such supercomputing facility. Therefore, all the computational times are referred to the above mentioned supercomputer and the reference to it will be omitted in the following.

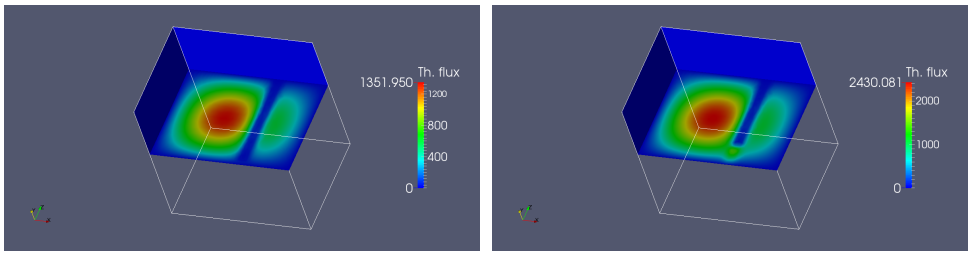

(a) $\mu = -16\,\text{cm}$ **(b)** $\mu = -10\,\text{cm}$

(c) $\mu = 3\,\text{cm}$ **(d)** $\mu = 13\,\text{cm}$

Figure 2.11: *Thermal neutron flux shape* $[1/\text{cm}^2\ \text{s}]$ *provided by the ROM, employing* $N = 70$ *basis functions, at the last time step.*

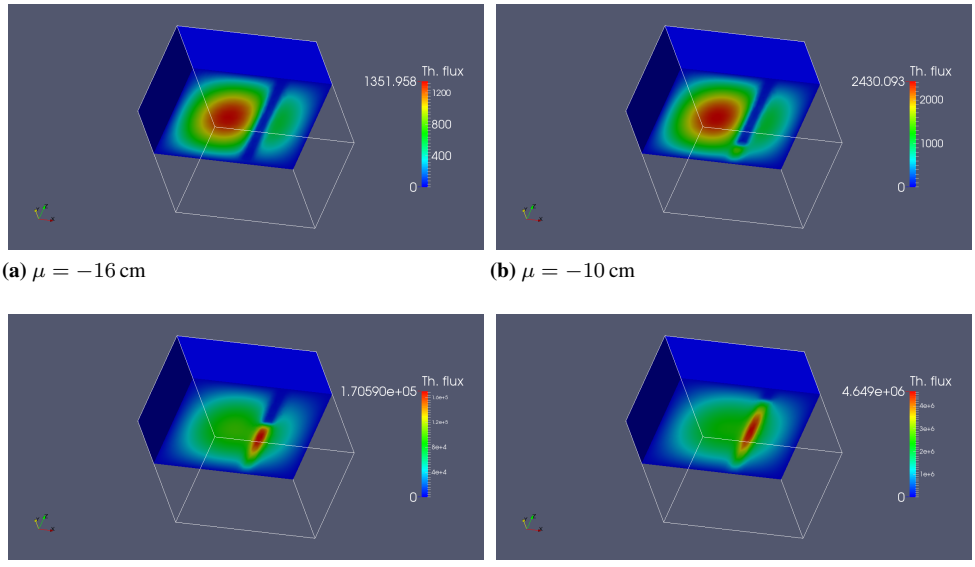

(a) $\mu = -16\,\text{cm}$ **(b)** $\mu = -10\,\text{cm}$

(c) $\mu = 3\,\text{cm}$ **(d)** $\mu = 13\,\text{cm}$

Figure 2.12: *Thermal neutron flux shape* $[1/\text{cm}^2\ \text{s}]$ *assumed as "truth" solution, at the last time step.*

Table 2.2: *Computational time per single cpu per single time step.*

	Truth	ROM	Speed-up
$\mu = -16\,\text{cm}$	148.35 s	2.2 ms	67 432
$\mu = -10\,\text{cm}$	148.02 s	2.1 ms	70 486
$\mu = 3\,\text{cm}$	148.68 s	2.5 ms	59 472
$\mu = 13\,\text{cm}$	148.72 s	2.4 ms	61 967

Table 2.3: *Relative error bounds in L^2 norm, at the last time step.*

	Error bounds
$\mu = -16\,\text{cm}$	9.36×10^{-6}
$\mu = -10\,\text{cm}$	2.48×10^{-4}
$\mu = 3\,\text{cm}$	4.65×10^{-4}
$\mu = 13\,\text{cm}$	1.85×10^{-4}

solved, the *a posteriori* error estimation is performed as well to certify the outcomes. In Tab. 2.3, the relative error bounds are reported, which have been computed as the ratio between the L^2 norms of the error and the solution (more details about the error bounds can be found in Section 2.3.2). Error bounds are an *estimate* of the error between the RB solution and the high order one. In order to be efficient, the error bounds should overestimate a bit the error and never underestimate it. The ratio between the estimated error with respect to the true error is called *effectivity*. Therefore, the effectivity should be always greater than one but not too big. The average, maximum and minimum effectivity, for several instances of the parameter, are reported in Tab. 2.4, where, for the sake of completeness, the influence of the mesh size on the effectivity has been addressed as well. Effectivities increase when the mesh size is increased, on the other hand, when the mesh size is reduced.

For the sake of completeness, it must be introduced the computational break-even, i.e., the number of full order simulations after that the RB method is more efficient and recommended. The break-even can be defined as follows:

$$\text{break-even} = \frac{\text{Whole Offline computational time}}{\text{Time of one FE simulation}} = \frac{\sim 20\,\text{h}}{\sim 8\,\text{min}} = 150\,. \tag{2.73}$$

Therefore, if more than 150 full-order simulations have to be computed, the reduced order model should be preferred.

It is worth recalling that the aim of the present work is to develop a fast-running simulation tool able to accurately reproduce spatial effects induced by the control rods, with respect to the "truth" solutions. To achieve this goal we had to face and incorporate into the computational tool the capability to manage parabolic non-coercive problems, as well as theirs error bounds (and stability factors).

Table 2.4: *Effectivity.*

Mesh size	Average	Maximum	Minimum
h=6 mm	16.749	52.826	3.574
h/2	18.879	289.395	3.535
2h	62.340	199.983	17.453
4h	499.970	6850.664	268.990

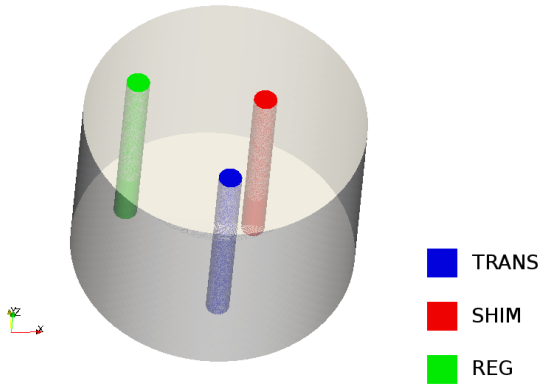

Figure 2.13: *3D model of the TRIGA reactor with three control rods.*

2.4.3 Additional remarks

The presented methodology, namely the piece-wise affine transformation based on subdomain division, can be used also with multiple rods. In this case, the elementary building block will be tetrahedron and the subdomain shapes will not be simple parallelepipeds as in the presented work and the computation of the affine transformation will be much more involved. Moreover, cylindrical control rods may be employed as well. For example, the cylinder might be inscribed within the parallelepiped, or even curvy-triangles may be considered (see e.g. Rozza et al., 2008).

2.5 Three rods 3D modelling: a “staircase” approach

In this Section, the modelling of three control rod movement is addressed employing a different technique from the previous Section. The geometry of the model considered for this approach is reported in Fig. 2.13. The TRIGA Mark II reactor is equipped with a pneumatic bar (TRANS), which can be completely inserted or completely withdrawn, without other positions in between. Conversely, the other two rods, REG and SHIM, can assume different positions. The idea behind such approach is to simulate a *discrete* movement (like a staircase). To do so, the portion of the spatial domain (i.e., the three cylinders) occupied by the rods has been divided as shown in Fig. 2.14. In particular: SHIM and REG, the cylinders have been split into 15 “steps”; TRANS, only 1 big “step”. The spatial mesh has been generated by discretizing the domain using the Gmsh software and the $P1$-elements. Such mesh is reported in Fig. 2.15 and it features $287\,577$ elements, with an average mesh size of ~ 6 mm. A tolerance of 1×10^{-9} has been chosen for the solution of the “truth” model.

The movement is simulated by “turning on” or “turning off” the water (or the rod) within each “step”. According to this kind of approach, the parameters are the height of the control rods (REG and SHIM), which are discrete – from 0, inserted, to 15, withdrawn – and if the TRANS is inserted or withdrawn, namely 0 or 1. Therefore, the following bilinear forms have been defined:[3]

[3] Since the domain does not change, like in the previous Section, the subscript o will be omitted.

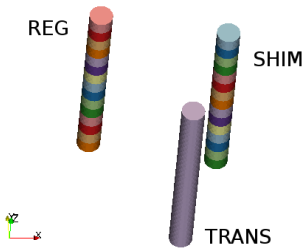

Figure 2.14: *Control rods spatial domain subdivision.*

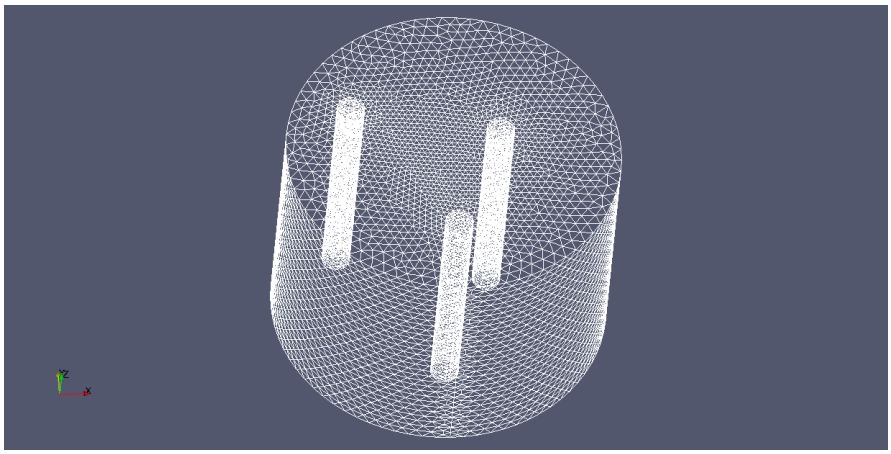

Figure 2.15: *Spatial mesh adopted for the three rods model.*

- within fuel domain

$$m_{\text{fuel}} = \int_{\Omega_{\text{fuel}}} \left[\frac{1}{\text{v}_1^f} \Phi_1 \psi_{\Phi_1} + \frac{1}{\text{v}_2^f} \Phi_2 \psi_{\Phi_2} + \sum_{i=1}^{8} c_i \psi_{c_i} \right], \tag{2.74}$$

$$\begin{aligned} a_{\text{fuel}} = & \int_{\Omega_{\text{fuel}}} D_1^f \nabla \Phi_1 \cdot \nabla \psi_{\Phi_1} + \int_{\Omega_{\text{fuel}}} D_2^f \nabla \Phi_2 \cdot \nabla \psi_{\Phi_2} \\ & + \int_{\Omega_{\text{fuel}}} \left[\Sigma_{a_1}^f + \Sigma_{s_{1\to 2}}^f - (1-\beta)\nu\Sigma_{f_1} \right] \Phi_1 \psi_{\Phi_1} \\ & - \int_{\Omega_{\text{fuel}}} \left[\Sigma_{s_{2\to 1}}^f + (1-\beta)\nu\Sigma_{f_2} \right] \Phi_2 \psi_{\Phi_1} \\ & - \int_{\Omega_{\text{fuel}}} \sum_{i=1}^{8} \lambda_i c_i \psi_{\Phi_1} - \int_{\Omega_{\text{fuel}}} \Sigma_{s_{1\to 2}}^f \Phi_1 \psi_{\Phi_2} \\ & + \int_{\Omega_{\text{fuel}}} \left[\Sigma_{a_2}^f + \Sigma_{s_{2\to 1}}^f \right] \Phi_2 \psi_{\Phi_2} - \int_{\Omega_{\text{fuel}}} \sum_{i=1}^{8} \beta_i \nu\Sigma_{f_1} \Phi_1 \psi_{c_i} \\ & - \int_{\Omega_{\text{fuel}}} \sum_{i=1}^{8} \beta_i \nu\Sigma_{f_2} \Phi_2 \psi_{c_i} + \int_{\Omega_{\text{fuel}}} \sum_{i=1}^{8} \lambda_i c_i \psi_{c_i}, \end{aligned} \tag{2.75}$$

- within each subdomain of the control rods

$$m_l = \mu_l \, m_r + (1-\mu_l) \, m_w, \quad \mu_l = 0 \text{ or } 1 \tag{2.76}$$

$$a_l = \mu_l \, a_r + (1-\mu_l) \, a_w, \quad \mu_l = 0 \text{ or } 1 \tag{2.77}$$

where

$$m_r = \int_{\Omega} \left[\frac{1}{\text{v}_1^r} \Phi_1 \psi_{\Phi_1} + \frac{1}{\text{v}_2^r} \Phi_2 \psi_{\Phi_2} + \sum_{i=1}^{8} c_i \psi_{c_i} \right], \tag{2.78}$$

$$m_w = \int_{\Omega} \left[\frac{1}{\text{v}_1^w} \Phi_1 \psi_{\Phi_1} + \frac{1}{\text{v}_2^w} \Phi_2 \psi_{\Phi_2} + \sum_{i=1}^{8} c_i \psi_{c_i} \right], \tag{2.79}$$

$$\begin{aligned} a_r = & \int_{\Omega} D_1^r \nabla \Phi_1 \cdot \nabla \psi_{\Phi_1} + \int_{\Omega} D_2^r \nabla \Phi_2 \cdot \nabla \psi_{\Phi_2} \\ & + \int_{\Omega} \left[\Sigma_{a_1}^r + \Sigma_{s_{1\to 2}}^r - (1-\beta)\nu\Sigma_{f_1} \right] \Phi_1 \psi_{\Phi_1} \\ & - \int_{\Omega} \left[\Sigma_{s_{2\to 1}}^r + (1-\beta)\nu\Sigma_{f_2} \right] \Phi_2 \psi_{\Phi_1} \\ & - \int_{\Omega} \sum_{i=1}^{8} \lambda_i c_i \psi_{\Phi_1} - \int_{\Omega} \Sigma_{s_{1\to 2}}^r \Phi_1 \psi_{\Phi_2} \\ & + \int_{\Omega} \left[\Sigma_{a_2}^r + \Sigma_{s_{2\to 1}}^r \right] \Phi_2 \psi_{\Phi_2} - \int_{\Omega} \sum_{i=1}^{8} \beta_i \nu\Sigma_{f_1} \Phi_1 \psi_{c_i} \\ & - \int_{\Omega} \sum_{i=1}^{8} \beta_i \nu\Sigma_{f_2} \Phi_2 \psi_{c_i} + \int_{\Omega} \sum_{i=1}^{8} \lambda_i c_i \psi_{c_i}, \end{aligned} \tag{2.80}$$

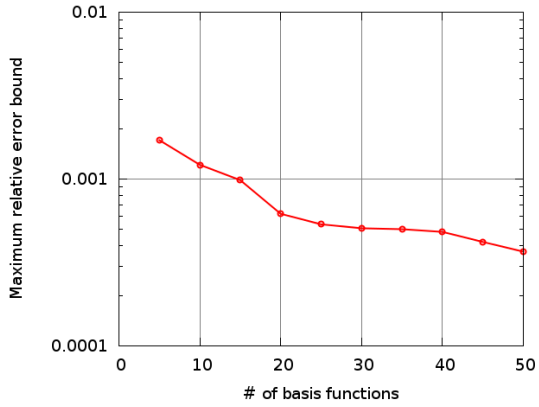

Figure 2.16: *Non-dimensional maximum relative error bound, with respect to the number of basis functions employed.*

$$
\begin{aligned}
a_w \quad = \quad & \int_\Omega D_1^w \nabla\Phi_1 \cdot \nabla\psi_{\Phi_1} + \int_\Omega D_2^w \nabla\Phi_2 \cdot \nabla\psi_{\Phi_2} \\
& + \int_\Omega \left[\Sigma_{a_1}^w + \Sigma_{s_{1\to 2}}^w - (1-\beta)\nu\Sigma_{f_1}\right] \Phi_1\psi_{\Phi_1} \\
& - \int_\Omega \left[\Sigma_{s_{2\to 1}}^w + (1-\beta)\nu\Sigma_{f_2}\right] \Phi_2\psi_{\Phi_1} \\
& - \int_\Omega \sum_{i=1}^{8} \lambda_i c_i \psi_{\Phi_1} - \int_\Omega \Sigma_{s_{1\to 2}}^w \Phi_1\psi_{\Phi_2} \\
& + \int_\Omega \left[\Sigma_{a_2}^w + \Sigma_{s_{2\to 1}}^w\right] \Phi_2\psi_{\Phi_2} - \int_\Omega \sum_{i=1}^{8} \beta_i \nu\Sigma_{f_1} \Phi_1\psi_{c_i} \\
& - \int_\Omega \sum_{i=1}^{8} \beta_i \nu\Sigma_{f_2} \Phi_2\psi_{c_i} + \int_\Omega \sum_{i=1}^{8} \lambda_i c_i \psi_{c_i}
\end{aligned} \tag{2.81}
$$

Therefore, according to the affine expansion (2.14) and (2.15), $Q_a = Q_m = 32$.

2.5.1 Some representative results

In this Section, the main results obtained both during the Offline and Online phases are presented.

Offline phase

During this phase, the RB space is built, the ROM is obtained by projecting the "truth" model on it, and the *a posteriori* error estimation is provided as well. Figure 2.16 shows the maximum relative error bound with respect to the number of basis functions employed. The values of the parameters for each point in the graph is chosen according to a POD-greedy algorithm (Haasdonk and Ohlberger, 2008; Nguyen et al., 2010). The whole Offline step lasted almost 200 hours of cpu time. The great increase of the Offline duration, with respect to the approach proposed in the previous Section, is due to the

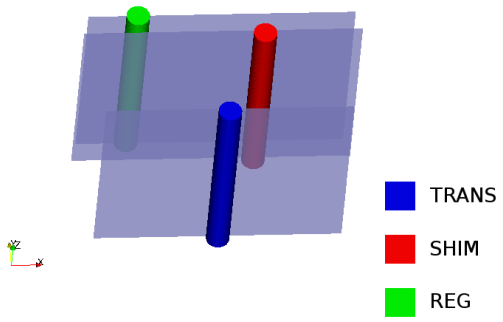

Figure 2.17: *Employed sections to visualize the thermal flux.*

Table 2.5: *Computational time per single cpu per single time step.*

$\mu = \{\text{TRANS, REG, SHIM}\}$	Truth	ROM	Speed-up
$\mu = \{0, 4, 8\}$	191.0 s	110 ms	1736
$\mu = \{1, 2, 10\}$	190.4 s	110 ms	1730
$\mu = \{1, 16, 16\}$	191.1 s	112 ms	1705

higher number of Q_a and Q_m. Almost the 60% of the time is spent to compute the terms needed by the *a posteriori* error estimation (see Section 2.3.2).

Online phase

During the Online step, the thermal flux has been reconstructed for different combinations of parameters employing 50 basis functions. In the following, the thermal flux is presented within the region of the control rods, on the planes reported in Fig. 2.17, without displaying the flux within the fuel region for the sake of clarity. In particular, the outcomes provided by the developed ROM are reported in Fig. 2.18. On the other hand, the solutions assumed as "truth" are depicted in Fig. 2.19. As it can be seen, the spatial effects induced by the movement of the control rods are accurately reproduced by the reduced model.

Comparing the cpu times required to solve the "truth" finite element problem and the developed ROM, reported in Tab. 2.5, the computational speed-up is of $\sim$ 2000 times per single time step per single cpu. The lower speed-up, with respect to the model developed in the previous Section, is due to the higher number of bilinear forms required by the affine decomposition.

The ratio between the L^2 norms of the error and the solution, for the cases considered, provided by the developed ROM and computed as described in Section 2.3.2, are reported in Tab. 2.6. Finally, in order to verify the efficiency and rigor of the error bounds, the average, maximum and minimum effectivity (i.e., the ratio between the error bound and the true error between the reduced solution and the high order one) are reported in Tab. 2.7. Such values have been computed for several instances of the parameters and for different mesh size in order to investigate the influence of the mesh size on the effectivity and they are in agreement with general considerations in (Patera

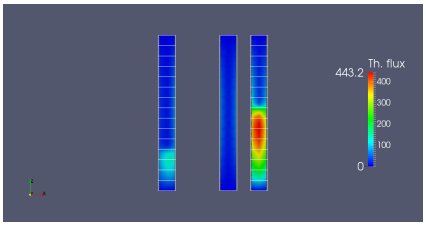

(a) *TRANS is inserted, and the height of the REG and SHIM is 4 and 8 "steps", respectively*

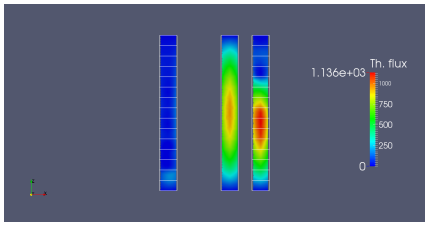

(b) *TRANS is withdrawn, and the height of the REG and SHIM is 2 and 10 "steps", respectively*

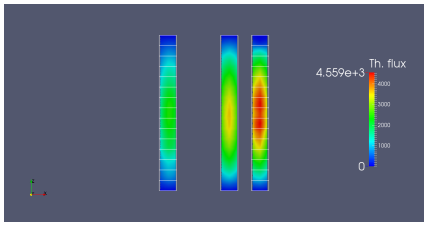

(c) *TRANS is withdrawn, and the height of the REG and SHIM is 16 and 16 "steps", respectively*

Figure 2.18: *Thermal flux* $[1/\mathrm{cm}^2\ \mathrm{s}]$*, provided by the ROM, inside the control rod spatial domains for different combination of the parameters.*

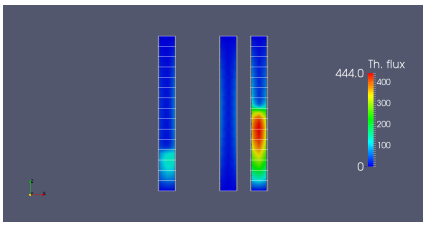

(a) *TRANS is inserted, and the height of the REG and SHIM is 4 and 8 "steps", respectively*

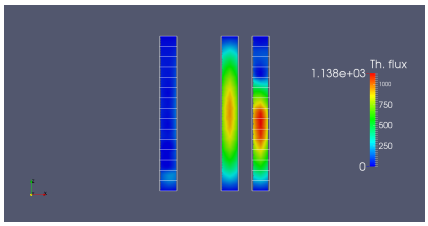

(b) *TRANS is withdrawn, and the height of the REG and SHIM is 2 and 10 "steps", respectively*

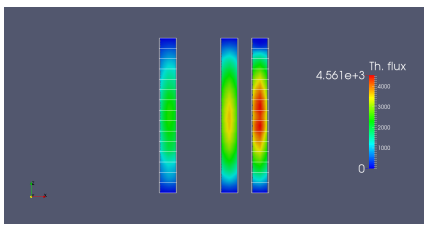

(c) *TRANS is withdrawn, and the height of the REG and SHIM is 16 and 16 "steps", respectively*

Figure 2.19: *Thermal flux* $[1/\mathrm{cm}^2\ \mathrm{s}]$*, assumed as "truth" solution, inside the control rod spatial domains for different combination of the parameters.*

Table 2.6: *Relative error bounds in L^2 norm, at the last time step.*

$\mu = \{\text{TRANS, REG, SHIM}\}$	Error bounds
$\mu = \{0, 4, 8\}$	6.02×10^{-5}
$\mu = \{1, 2, 10\}$	1.92×10^{-4}
$\mu = \{1, 16, 16\}$	1.14×10^{-4}

and Rozza, 2007; Rozza et al., 2008).

Table 2.7: *Effectivity.*

Mesh size	Average	Maximum	Minimum
h=6 mm	4.768	10.480	1.670
h/2	5.027	10.795	1.656
2h	24.552	48.230	10.937

The break-even (see Eq (2.73)) for this case is given by

$$\text{break-even} = \frac{\sim 200\,\text{h}}{\sim 10\,\text{min}} = 1200\,. \tag{2.82}$$

Therefore, if more than 1200 full-order simulations have to be computed, the reduced order model should be preferred.

2.6 Concluding remarks

In this Chapter, two different approaches for simulating the movement of nuclear reactor control rods, in a 3D framework, have been proposed. In order to provide the outcomes in a rapid and reliable way, the certified Reduced Basis method has been employed. The neutronic behaviour has been modeled according to the so-called multi-group diffusion equation, which is, in fact, a set of coupled (parametrized) parabolic equations (ten in our problem). The heights of the rods (i.e., how much the rods are withdrawn) are the varying parameters, which are geometric-type parameters. The parametrized bilinear form associated to the elliptic part of the system is non-symmetric and non-coercive, yet it can be affinely decomposed. The efforts have been focused on the methodological approach.

As far as the first approach is considered, the movement of a single control rod has been modeled. In particular, a piece-wise affine transformation based on subdomain division has been developed, where the subdomain shapes change in order to simulate the movement of the rod. On the other hand, in the second approach, all the three control rods of the TRIGA Mark II nuclear reactor of the University of Pavia (Italy) have been taken into account. In order to present a different methodology, the movement of the rods has been discretized like a staircase. Both the reduced models are capable to accurately reproduce the neutron flux distribution allowing to take into account the spatial effects induced by the control rods, whose height can be set in the Online phase. Moreover, the computational time required to solve the reduced system is four (three) order of magnitude lower with respect to the fine finite element discretization, for the first (second) approach, respectively. The lower speed-up provided by the second approach is due to the higher number of the terms of the affine expansion.

It is worth mentioning that the presented methodology is general and it could also be employed for other industrial applications with different 3D parametrized time-dependent problems representing other complex phenomena.

An alternative to the direct discretization of the time-dependent neutron diffusion equation, as presented in this Chapter, is the so-called quasi-static approach (Girardi et al., 2012). Such approach is formally close to the adiabatic one (Duderstadt and Hamilton, 1976), except that the flux shape is recalculated at intervals during transients. Therefore, in the following Chapter a reduced order model for parametrized multi-group neutron diffusion equations in the stationary formulation, which is a generalized eigenvalue problem, will be discussed.

CHAPTER 3

Reduced basis approach for generalized eigenvalue calculation

This Chapter presents an alternative Reduced Order Model (ROM), with respect to those presented in the previous Chapter, aimed at simulating nuclear reactor control rods movement and featuring fast-running prediction of reactivity and neutron flux distribution as well. In particular, the neutronics has been modelled according to a parametrized stationary version of the multi-group neutron diffusion equation, which can be formulated as a generalized eigenvalue problem. Within the reduced basis framework, the centroidal Voronoi tessellation is employed as sampling technique thanks to the possibility of a hierarchical parameter space exploration, without relying on a "classical" a posteriori error estimation, and saving an important amount of computational time in the Offline phase. The here proposed ROM is capable to correctly predict, with respect to the high-fidelity finite element approximation, both the reactivity and neutron flux shape. In this way, a computational speed-up of at least three orders of magnitude is achieved.

The main results presented in this Chapter are collected in: Sartori, A., Cammi, A., Luzzi, L., and Rozza, G. "A Reduced basis approach for modelling the movement of nuclear reactors control rods". Submitted to Journal of Nuclear Engineering and Radiation Science, 2014.

3.1 Introduction

THE present contribution would offer, with respect to the previous Chapter 2, an alternative methodological approach to improve the already developed simulation tools, which are based on point-wise kinetics, allowing for the spatial effects. The main idea, based on the so-called quasi-static approach (Girardi et al., 2012), is that the temporal evolution can still be described according to PK equations, but at each time step the reactivity is estimated by means of a fast-running Reduced Order Model (ROM). Indeed, a ROM for simulating nuclear reactors control rods movement, which features fast-running computational time for both reactivity and flux shape prediction, has been developed relying on the reduced basis method (Rozza et al., 2008; Quarteroni et al., 2011). The reactivity and neutron flux shape are computed solving the stationary version of the multi-group neutron diffusion equation (Duderstadt and Hamilton, 1976), which can be formulated as a generalized eigenvalue problem. A 2D $x - z$ model featuring two control rods surrounded by fissile material, with reference to a TRIGA Mark II nuclear reactor (General Atomic, 1964), has been employed. The governing partial differential equations have been parametrized allowing for geometric deformations of the subdomains in order to model a continuous movement of the control rods, where the heights of the rods are the varying parameters. Within the reduced basis method framework, the centroidal Voronoi tessellation has been employed as sampling technique for the parameter space exploration. All the simulations have been performed relying on a procedure developed on purpose within the computational environment offered by the open-source `FEniCS` library (Logg et al., 2012).

The Chapter is organized as follows. The reduced basis strategies are firstly presented in Section 3.2 for a generalized eigenvalue model problem. The parametrized reactor spatial kinetics and the implementation of the reduced basis method are addressed in Section 3.3. The main representative results are given in Section 3.4. Finally, in Section 3.5, the main conclusions and future perspectives are presented.

3.2 Reduced basis strategies for generalized eigenvalue problems

In this Section, the fundamental mathematical aspects of the Reduced Basis (RB) method for a generalized eigenvalue problem are addressed. For the sake of brevity, a scalar problem is considered, since the extension to the vectorial case is straightforward. A detailed presentation of RB methodology for elliptic and parabolic problems can be found in (Grepl and Patera, 2005; Patera and Rozza, 2007; Rozza et al., 2008; Quarteroni et al., 2011), while for eigenvalue problems Refs. (Machiels et al., 2000; Zanon and Veroy-Grepl, 2013) might be of interest.

Let the following be the abstract formulation of a generalized eigenvalue model problem, parametrized with respect to the input parameter p-vector μ. Given $\mu \in \mathcal{D} \subset \mathbb{R}^p$, evaluate $(u(\mu), \lambda(\mu))$ – eigenvector and eigenvalue, respectively – such that

$$a\left(u(\mu), v; \mu\right) = \lambda(\mu) m\left(u(\mu), v\right), \ \forall v \in X(\Omega), \tag{3.1}$$

where $a(\cdot, \cdot)$ and $m(\cdot, \cdot)$ are the bilinear forms associated to the left and right hand side, respectively, v is the test function, Ω is a spatial domain in $\mathbb{R}^d$ (for $d = 2$ or 3), $X = X(\Omega)$ is a suitable Hilbert space, with a given inner product $(\cdot, \cdot)_X$ and an induced norm

$\|\cdot\|_X = \sqrt{(\cdot,\cdot)_X}$. It is worth recalling that the reactivity of a nuclear system is related to the smallest real eigenvalue, and the neutron flux distribution reflects the associated eigenvector. Therefore, in the present work, only the couple $\left(u^{\min}(\mu), \lambda^{\min}(\mu)\right)$ will be computed. In the following, the superscript "min" will be omitted so as not overburden the notation.

In order to have a complete Offline/Online decoupling, the bilinear forms a and m are *affinely* decomposed on the parameter μ:

$$a(w, v; \mu) = \sum_{q=1}^{Q_a} \Theta_a^q(\mu) a^q(w, v), \quad \forall w, v \in X, \forall \mu \in \mathcal{D} \tag{3.2}$$

$$m(w, v; \mu) = \sum_{q=1}^{Q_m} \Theta_m^q(\mu) m^q(w, v), \quad \forall w, v \in X, \forall \mu \in \mathcal{D} \tag{3.3}$$

for some integers Q_a and Q_m.

The coefficients of the affine expansions (3.2) and (3.3) can be easily derived when they are related to physical properties (e.g., diffusion coefficients, thermal conductivity). Whether the μ-vector includes geometric properties, the derivation of the $\Theta(\mu)$ coefficients may require a dedicated treatment, see e.g. (Rozza et al., 2008; Sartori et al., 2014b).

The RB method is built upon a fine approximation (i.e., finite element or finite volume), assumed as "truth" solution. Let the following expression be the discretization of the eigenvalue problem (3.1) adopting the Finite Element (FE) (Quarteroni and Valli, 2008) in space

$$a\left(u_{\mathcal{N}}(\mu), v; \mu\right) = \lambda_{\mathcal{N}}(\mu) m\left(u_{\mathcal{N}}(\mu), v\right), \ \forall v \in X^{\mathcal{N}}, \tag{3.4}$$

where $X^{\mathcal{N}}$ is the FE approximation space of dimension $\mathcal{N}$ (usually very large); $u_{\mathcal{N}}$ and $\lambda_{\mathcal{N}}$ are the "high-fidelity" eigenvector and eigenvalue, respectively.

Then, given a positive integer $N_{\max}$, let X^N, for $N = 1, \ldots, N_{\max}$, be an associated sequence of approximation spaces (RB spaces), where X^N is a N-dimensional subspace of $X^{\mathcal{N}}$. Let $\xi_n^{\mathcal{N}} \in X^{\mathcal{N}}, 1 \leq n \leq N_{\max}$ be a set of orthonormal functions and let such functions be the basis of the RB spaces

$$X^N = \operatorname{span}\left\{\xi_n^{\mathcal{N}}, 1 \leq n \leq N\right\}, \quad 1 \leq N \leq N_{\max}. \tag{3.5}$$

Typically, the orthonormal functions $\xi_n^{\mathcal{N}}$ are solutions of the problem (3.4), computed for different instances of the parameter μ, that are orthogonalized by means a Gram-Schimdt procedure.

The RB approximation of the discretized eigenvalue problem (3.4) can be stated as follows

$$a\left(u_N(\mu), v; \mu\right) = \lambda_N(\mu) m\left(u_N(\mu), v\right), \ \forall v \in X^N, \tag{3.6}$$

where the RB approximation of the eigenvector $u_N(\mu) \in X^N$ can be expressed as a projection of the basis functions $\xi_i^{\mathcal{N}}$

$$u_N(\mu) = \sum_{i=1}^{N} u_{N,i}(\mu) \xi_i^{\mathcal{N}}, \tag{3.7}$$

while $\lambda_N(\mu)$ is the eigenvalue associated to the eigenvector $u_N(\mu)$. Finally, the algebraic system to be solved in order to compute the weights $u_{N,i}(\mu)$ has to be derived. To this aim, by denoting

$$\mathcal{Z} = \left[\xi_1^{\mathcal{N}} | \dots | \xi_N^{\mathcal{N}}\right] \in \mathbb{R}^{\mathcal{N} \times N}, \quad 1 \leq N \leq N_{\max}, \tag{3.8}$$

the bilinear forms a^q and m^q can be projected onto the RB space X^N as follows

$$\mathbf{A}_N^q = \mathcal{Z}^T A_{\mathcal{N}}^q \mathcal{Z}, \tag{3.9}$$
$$\mathbf{M}_N^q = \mathcal{Z}^T M_{\mathcal{N}}^q \mathcal{Z}, \tag{3.10}$$

where

$$(A_{\mathcal{N}}^q)_{ij} = a^q(\psi_j, \psi_i), \tag{3.11}$$
$$(M_{\mathcal{N}}^q)_{ij} = m^q(\psi_j, \psi_i), \tag{3.12}$$

being $\{\psi_i\}_{i=1}^{\mathcal{N}}$ the basis of the FE space $X^{\mathcal{N}}$. Hence, the following algebraic equations associated to the reduced eigenvalue problem (3.6) are obtained

$$\mathbb{A}_N(\mu)\ \mathbf{u}_N(\mu) = \lambda_N(\mu)\mathbb{M}_N(\mu)\ \mathbf{u}_N(\mu), \tag{3.13}$$

where

$$\mathbb{A}_N(\mu) = \sum_{q=1}^{Q_a} \Theta_a^q(\mu)\mathbf{A}_N^q, \tag{3.14}$$

$$\mathbb{M}_N(\mu) = \sum_{q=1}^{Q_m} \Theta_m^q(\mu)\mathbf{M}_N^q, \tag{3.15}$$

and

$$\left(\mathbf{u}_N(\mu)\right)_i = u_{N,i}(\mu). \tag{3.16}$$

It is worth mentioning that the eigenvalue problem (3.13), which is $N \times N$, is independent of the FE space dimension $\mathcal{N}$, and $N \ll \mathcal{N}$.

During the Offline phase, the functions $\xi_n^{\mathcal{N}}$ and the matrices $\mathbf{A}_N^q$ and $\mathbf{M}_N^q$, which are μ-independent, are computed and stored. In the Online phase, for each instance of the parameter, the system (3.13) is assembled and solved. In this way, the Offline phase is $\mathcal{N}-$dependent while the Online phase in $\mathcal{N}-$independent.

3.3 Parametrized model

The neutron kinetics has been modeled according to the stationary multi-group diffusion equation (Duderstadt and Hamilton, 1976) with two energy groups. In equations it reads:

$$\left(-\nabla \cdot \underline{\underline{D}}\nabla + \underline{\underline{\Sigma_a}} + \underline{\underline{\Sigma_s}}\right) \underline{\Phi} = \lambda \underline{\chi} \underline{F}^T \underline{\Phi}, \tag{3.17}$$

where

$$
\begin{cases}
\underline{\Phi} = \begin{bmatrix} \Phi_1(\mathbf{r}) \\ \\ \Phi_2(\mathbf{r}) \end{bmatrix}, \\
\underline{\underline{D}} = \begin{bmatrix} D_1(\mathbf{r}) & 0 \\ 0 & D_2(\mathbf{r}) \end{bmatrix}, \\
\underline{\underline{\Sigma_a}} = \begin{bmatrix} \Sigma_a^1(\mathbf{r}) & 0 \\ 0 & \Sigma_a^2(\mathbf{r}) \end{bmatrix}, \\
\underline{\underline{\Sigma_s}} = \begin{bmatrix} \Sigma_s^{1\to 2}(\mathbf{r}) & -\Sigma_s^{2\to 1}(\mathbf{r}) \\ -\Sigma_s^{1\to 2}(\mathbf{r}) & \Sigma_s^{2\to 1}(\mathbf{r}) \end{bmatrix}, \\
\underline{\chi} = \begin{bmatrix} \chi^1 \\ \\ \chi^2 \end{bmatrix}, \\
\underline{F}^T = \begin{bmatrix} \nu\Sigma_f^1(\mathbf{r}) & \nu\Sigma_f^2(\mathbf{r}) \end{bmatrix}.
\end{cases}
\tag{3.18}
$$

The subscript 1 refers to the fast group and 2 to the thermal one; Φ is the neutron flux, D is the diffusion coefficient, $\nu\Sigma_f$ are the number of neutrons emitted per fission reaction, Σ_a is the absorption cross section, $\Sigma_{s_{i\to j}}$ is the scattering cross section from group i to group j, χ is the fission yield. For the sake of simplicity, the homogeneous Dirichlet boundary conditions (i.e., neutron flux equal to zero) have been employed.

Being the introduction of an innovative approach for reactor spatial dynamics the focus of the present contribution, a simplified 2D $x-z$ model has been adopted, with reference to the TRIGA Mark II reactor (General Atomic, 1964) of the University of Pavia (Italy). Such system features a non-symmetric core configuration. Figure 3.1a shows the map of the core, which is equipped with three control rods (SHIM, TRANSIENT, REGULATING), two irradiation channels (C.T., RABBIT), and one channel where the source for the start-up of the reactor is placed surrounded by two elements of graphite (DUMMY). All other elements are fuel pins. The employed model has been developed considering the section drawn in Fig. 3.1a, where the fuel pins and the C.T. have been homogenized except for the REG and the SHIM, which have been explicitly taken into account. In Fig. 3.1b, the parametric $x-z$ model of the TRIGA core is depicted. In particular, the control rods are depicted in green, the water is in blue, and in the other region a homogeneous mixture between the fuel and coolant has been considered, which will be referred to as fuel.

The neutronic parameters (v, D, Σ_a, Σ_s, $\nu\Sigma_f$, χ) have been computed by means of a full 3D core calculation based on the SERPENT code (SERPENT, 2011) and they are reported in Tab. 3.1. Such neutronic quantities have been taken constant for all the simulations.

The FE discretization of the Eq. (3.17), employing $P1$ elements, has been assumed as the "truth" solution. An *ad hoc* procedure has been implemented within the computational environment offered by the open-source library `FEniCS` (Logg et al., 2012) in order to perform all calculations needed by the RB method, for both the Offline and Online step. For the solution of the generalized eigenvalue FE problem, the `PETSc` suite

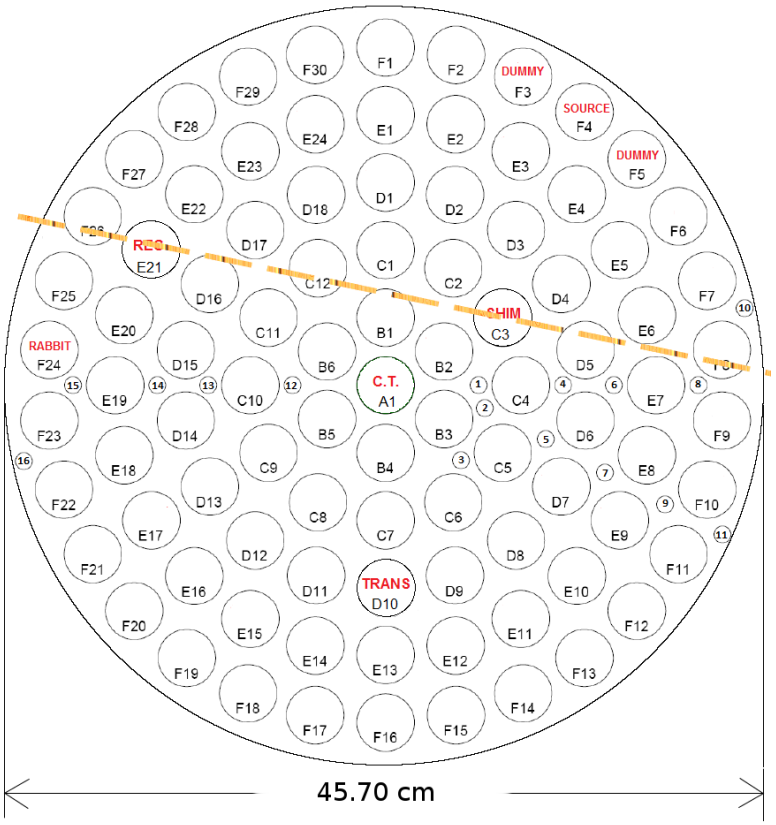

(a) *Map of the TRIGA Mark II reactor core.*

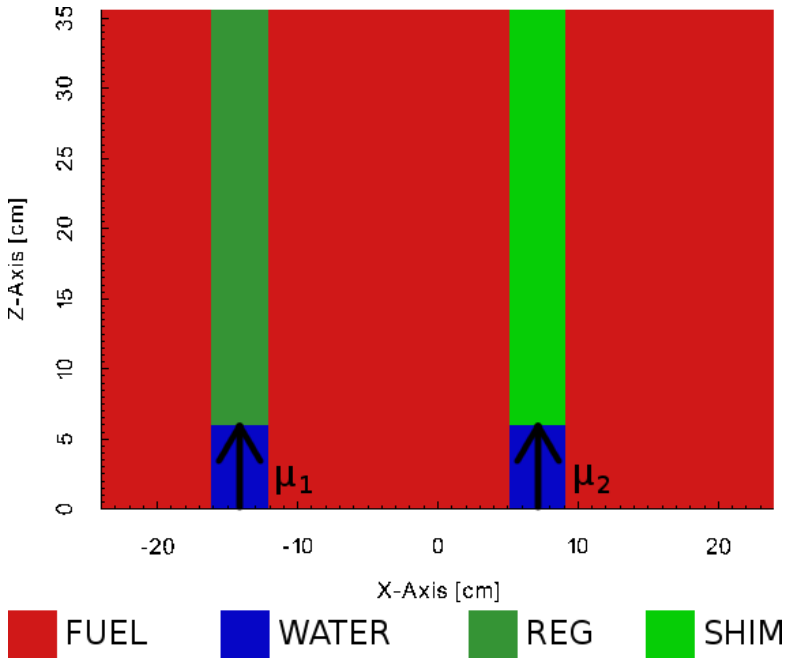

(b) $x - z$ *model for the RB method.*

Figure 3.1: *Map of the TRIGA Mark II reactor core (a), and* $x - z$ *model employed for the RB method.*

Table 3.1: *Neutronic quantities employed for the simulations (Sartori et al., 2014b).*

Parameter	Fuel	Water	Rod
D_1 [cm]	$8.77 \cdot 10^{-1}$	$8.51 \cdot 10^{-1}$	$7.52 \cdot 10^{-1}$
D_2 [cm]	$1.92 \cdot 10^{-1}$	$1.39 \cdot 10^{-1}$	$1.32 \cdot 10^{-1}$
Σ_{a_1} [cm^{-1}]	$4.85 \cdot 10^{-3}$	$5.04 \cdot 10^{-4}$	$7.07 \cdot 10^{-2}$
Σ_{a_2} [cm^{-1}]	$7.53 \cdot 10^{-2}$	$1.70 \cdot 10^{-2}$	$4.57 \cdot 10^{-1}$
$\nu\Sigma_{f_1}$ [cm^{-1}]	$3.65 \cdot 10^{-3}$	–	–
$\nu\Sigma_{f_2}$ [cm^{-1}]	$1.25 \cdot 10^{-1}$	–	–
$\Sigma_{s_{1\to2}}$ [cm^{-1}]	$3.02 \cdot 10^{-2}$	$5.34 \cdot 10^{-2}$	$1.36 \cdot 10^{-2}$
$\Sigma_{s_{2\to1}}$ [cm^{-1}]	$3.27 \cdot 10^{-4}$	$2.49 \cdot 10^{-4}$	$5.83 \cdot 10^{-4}$
$1/\mathrm{v}_1$ [s/cm]	$5.87 \cdot 10^{-8}$	$7.58 \cdot 10^{-8}$	$2.61 \cdot 10^{-8}$
$1/\mathrm{v}_2$ [s/cm]	$3.00 \cdot 10^{-6}$	$3.47 \cdot 10^{-6}$	$3.14 \cdot 10^{-6}$
χ^1 [–]	1.0	–	–
χ^2 [–]	0.0	–	–

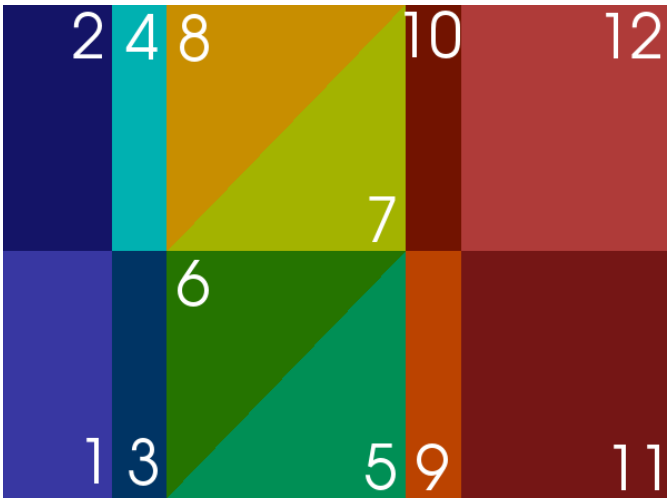

Figure 3.2: *RB triangulation of the reference domain.*

(Balay et al., 2014) and the `SLEPc` library (Hernandez et al., 2005) have been employed. While, in the Online phase, the reduced eigenvalue problem has been solved by means of the Python SciPy package (Jones et al., 2001–).

3.3.1 Geometrical parametrization

The piece-wise affine transformations based on subdomains division (Rozza et al., 2008; Sartori et al., 2014b) has been implemented for modelling a continuous movement of the rods. According to such technique, the parametrized spatial domain (also called original domain) $\Omega_o(\mu)$ is divided into a suitable number of subdomains $\Omega_o^l(\mu)$ (the so-called RB triangulation) such that

$$\Omega_o(\mu) = \bigcup_{l=1}^{L_{\mathrm{dom}}} \Omega_o^l(\mu). \tag{3.19}$$

The movements of the rods are modelled by a geometric deformations of the subdomains $\Omega_o^l(\mu)$. The RB methodology requires a μ-independent domain, called reference

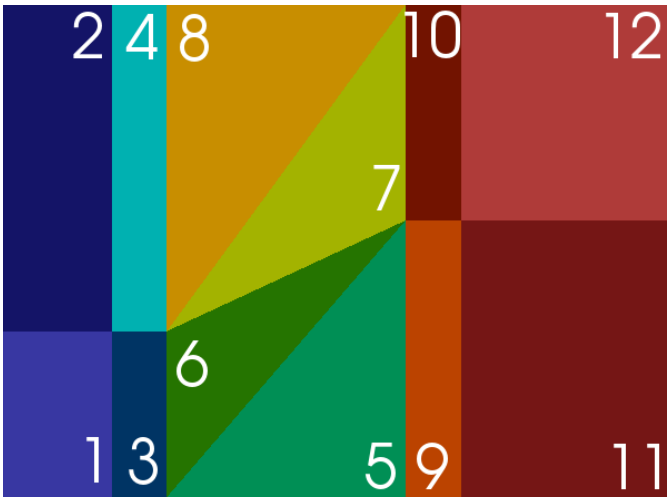

Figure 3.3: *RB triangulation of the original domain* $\Omega_o(\mu)$.

domain Ω in order to compare, and combine, FE solutions that would be otherwise computed on different grids. The chosen reference domain, with its RB triangulation is depicted in Fig. 3.2. The original domains are mapped onto the reference domain and a *transformed* problem is obtained, which is the point of departure of the RB approach. In Fig. 3.3, it is shown the RB triangulation of the parametric original domain when $\mu = (12, 20)$.

The height of the control rods REG and SHIM (i.e., how much they are inserted within the core) are the parameters $\mu = (\mu_1, \mu_2)$, and they can vary within the range $[1, 35]$ cm. For each subdomain $\Omega_o^l(\mu)$, belonging to the original domain $\Omega_o(\mu)$, the following bilinear forms have been defined

$$\begin{aligned} a_l^1 \;=\; & \int_{\Omega_o^l(\mu)} \left[D_1 \frac{\partial \Phi_1}{\partial x}\frac{\partial \psi_1}{\partial x} + D_2 \frac{\partial \Phi_2}{\partial x}\frac{\partial \psi_2}{\partial x} \right] \\ & + \int_{\Omega_o^l(\mu)} \left[\Sigma_{a_1} + \Sigma_{s_{1\to 2}}\right] \Phi_1 \psi_1 \\ & - \int_{\Omega_o^l(\mu)} \Sigma_{s_{2\to 1}} \Phi_2 \psi_1 - \int_{\Omega_o^l(\mu)} \Sigma_{s_{1\to 2}} \Phi_1 \psi_2 \\ & + \int_{\Omega_o^l(\mu)} \left[\Sigma_{a_2} + \Sigma_{s_{2\to 1}}\right] \Phi_2 \psi_2 \end{aligned} \tag{3.20}$$

$$a_l^2 \;=\; \int_{\Omega_o^l(\mu)} \left[D_1 \frac{\partial \Phi_1}{\partial z}\frac{\partial \psi_1}{\partial z} + D_2 \frac{\partial \Phi_2}{\partial z}\frac{\partial \psi_2}{\partial z} \right] \tag{3.21}$$

$$m_l \;=\; \int_{\Omega_o^l(\mu)} \nu\Sigma_{f_1} \Phi_1 \psi_1 + \nu\Sigma_{f_2} \Phi_2 \psi_1 \tag{3.22}$$

where ψ is the test function for the corresponding variable. Due to symmetry, the total number of bilinear forms can be reduced to one half leading to the number of $m_l = 4$ and $a_l = 8$. Therefore, according to the affine expansions (3.2) and (3.3), $Q_a = 8$ and $Q_m = 4$.

Mapping the bilinear forms (3.22)-(3.22) onto the reference domain, as detailed in

(Sartori et al., 2014b), the $\Theta_a^q(\mu)$ coefficients are obtained. Roughly speaking, from finite element consolidated fashion, such mapping may be seen as the isoparametric transformation from the original mesh element to the reference element to perform the Gaussian integration (Sartori et al., 2014b).

3.3.2 Sampling strategy

The effectivity of the RB approximation relies on the RB space, which is generated by the span of the snapshots (i.e., solutions of the high fidelity FE problem) computed for the sampled values of the parameters. Clearly, an efficient sampling technique, employed in the Offline phase, is essential for exploring the parameter space without wasting computational time, as can occur, for example, by means of a simplistic random sampling. Naturally, different sampling strategies may be adopted. For example, with an *a posteriori* error estimation[1], a *greedy* algorithm (Rozza et al., 2008; Haasdonk and Ohlberger, 2008; Quarteroni et al., 2011; Nguyen et al., 2009) may be employed. For this kind of problem (i.e., parametrized eigenvalue problems), two methods for the error bound estimation have been proposed (Prud'homme et al., 2002), but one method is asymptotic, meaning that the error estimation is good only for $N \to \infty$, the other relies on quantities that are not self-evident or that are not readily computed, and is very computational expensive. To overcome this issue, in this work, the Centroidal Voronoi Tessellation (Du et al., 1999; Burkardt et al., 2006), within the RB framework, has been employed. The proposed CVT does not require an error *estimation*, but relies on the *true* error between the computed snapshots and the reduced order model that is constructed (or updated) at each iteration. Starting from an initial discrete set Θ_{train} of values of μ (for example, the corners of the parameter domain $\mathcal{D}$), the sampling procedure can be described by the following steps:

1. Compute a Delaunay triangulation[2] (Watson, 1981) in the parameter space where the vertexes are the points belonging to Θ_{train}. For example, in Fig. 3.4a, the Delaunay triangulation (blue line) and the Voronoi tessellation (dotted line) of the initial discrete set Θ_{train} are depicted. The computed snapshots, which are the eigenvectors associated to the minimum eigenvalue for the different values of the parameter μ, are depicted with red dots.

2. Compute the residuals between the reduced order solution and the FE one in each vertex of the Delaunay triangulation. In this work, the residuals have been computed as the difference between the minimum eigenvalue, which is related to the reactivity of the system, provided by the reduced order model and the FE one.

3. For each triangle, compute the sum of the residuals in its vertexes times the area of the triangle itself (Bergmann et al., 2014).

4. The next snapshot will be computed for μ^*, which is given by the barycenter of the element for whom the sum of the residuals times the area of the element is maximum. For example, the upper left triangle of Fig. 3.4a featured the maximum residual, and Fig. 3.4b shows the Delaunay triangulation and the Voronoi

[1] The error estimation refers to the residual between the reduced order solution and the high-fidelity FE.
[2] It is worth recalling that in $\mathbb{R}^2$ the Dealaunay triangulation is the dual tessellation of the CVT (Du et al., 1999).

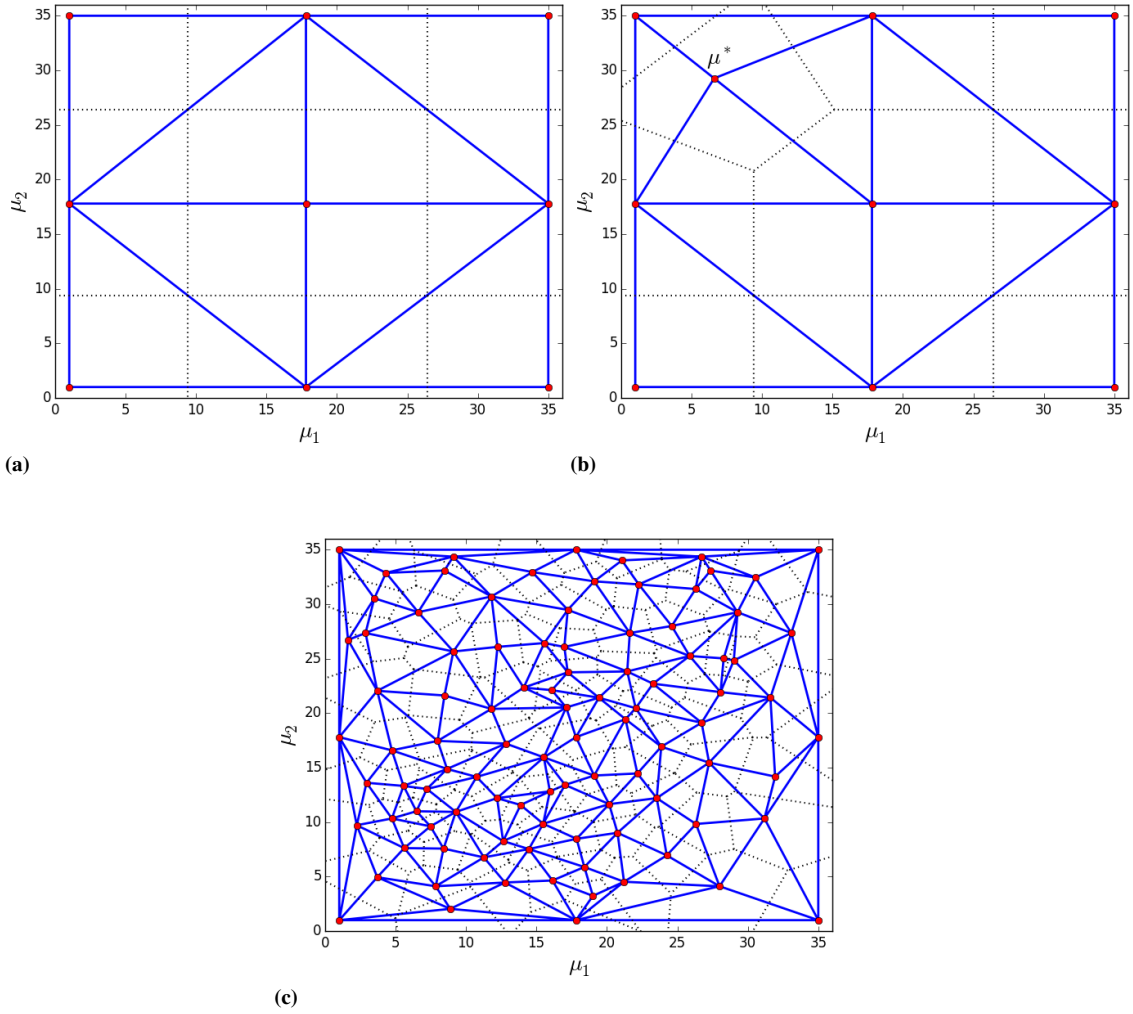

Figure 3.4: *Delaunay triangulation (blue line) and Voronoi tessellation (dotted line) of the initial set (a), of the next iteration (b), and at last iteration.*

tessellation of the next iteration, where $\mu^* = (6.600, 29.267)$ has been added to Θ_{train}.

Such procedure is iterated until a given tolerance is reached (e.g., a maximum number of the snapshots). For example, Fig. 3.4c reports the Delaunay triangulation and the Voronoi tessellation at the last iteration, where 97 snapshots have been computed. At the end of the simulation, in order to further reduce the dimension of the basis – and of the reduced order model itself – a Proper Orthogonal Decomposition (POD) (Sirovich, 1987; Holmes et al., 1996; Chatterjee, 2000) has been performed on the vector of the computed snapshots. In Fig. 3.5, energy (i.e., the information retained) by each POD mode is reported.

3.4 Representative results

In this Section, the performance of the developed reduced order model are presented. It is worth recalling that this work is more focused on testing and assessing an innovative

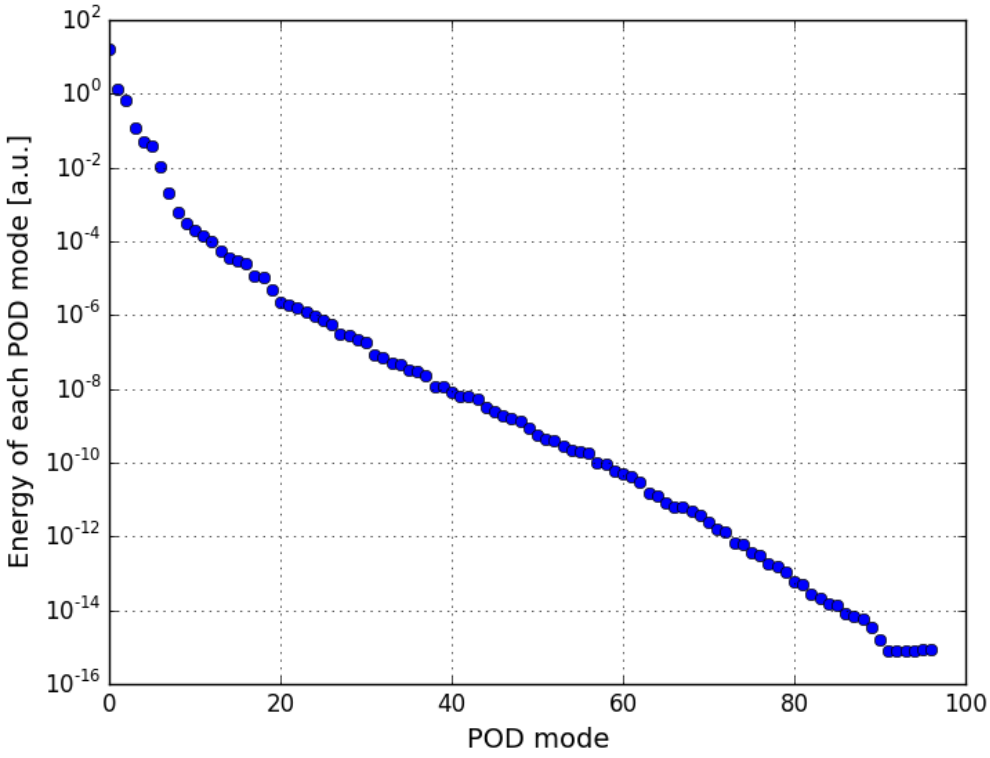

Figure 3.5: *Energy of the POD modes.*

Table 3.2: *Absolute error $e_\lambda(\mu)$ [pcm] with respect to number of basis functions employed. Values have been computed for 100 samples, randomly chosen.*

# basis functions	$< e_\lambda(\mu) >$	$\max e_\lambda(\mu)$
10	196.998	601.788
20	19.134	166.892
40	1.551	25.248
60	0.436	5.388
80	0.157	3.248

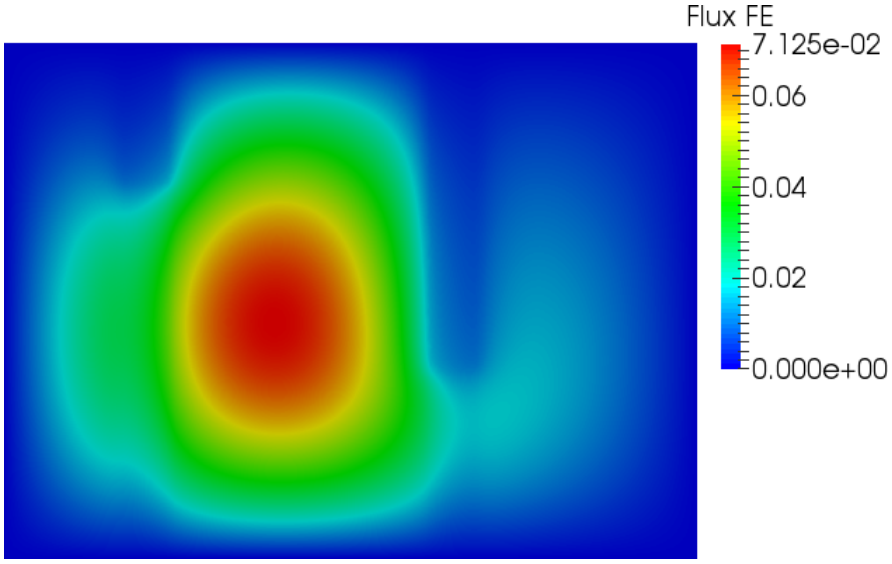

Figure 3.6: *High fidelity FE spatial flux distribution [$\mathrm{cm}^{-2}\ \mathrm{s}^{-1}$].*

methodology, rather than reproducing the real reference reactor.

The capabilities of the developed reduced model has been tested for different values of the parameters in the Online step for different number of basis functions. Both the eigenvalue prediction and the flux shape have been taken into account.

3.4.1 Reactivity estimation

The minimum eigenvalue is the inverse of system reactivity. The error between the value of the reactivity provided by the ROM and FE solution $e_\lambda(\mu)$ has been computed as follows:

$$e_\lambda(\mu) = |\lambda_N(\mu) - \lambda_\mathcal{N}(\mu)| \tag{3.23}$$

In Table 3.2, the average and the maximum absolute error $e_\lambda(\mu)$ are reported as function of the number of basis functions. Values have been computed for 100 samples, randomly chosen, of $\mu = (\mu_1, \mu_2)$. The reliability of the outcomes provided by the ROM increases as the number of basis functions employed is increased. Forty basis functions are sufficient for correctly estimate the reactivity at the order of the pcm, on average. To further reduce the error, much more basis functions are required.

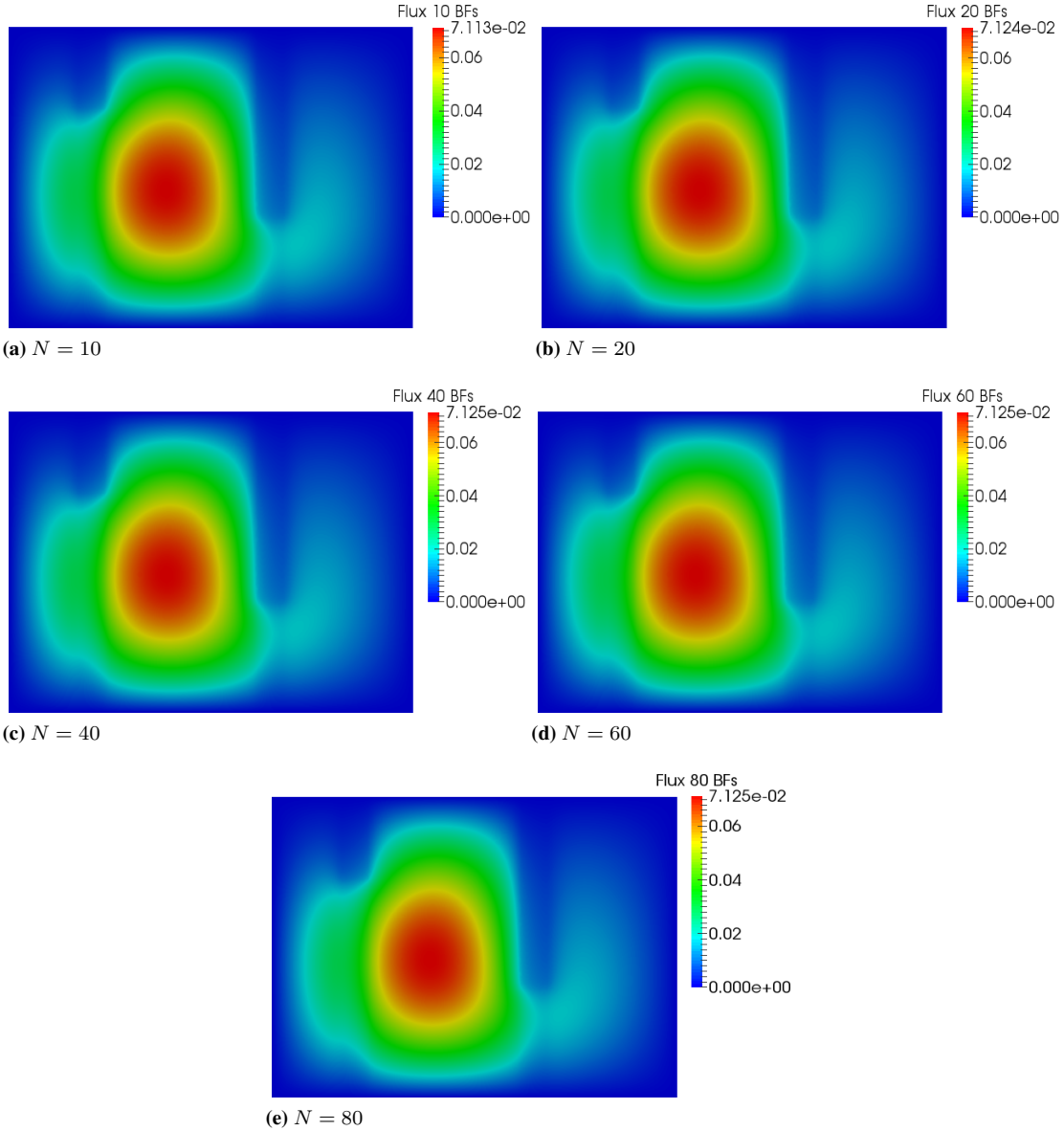

(a) $N = 10$ **(b)** $N = 20$

(c) $N = 40$ **(d)** $N = 60$

(e) $N = 80$

Figure 3.7: *Neutron flux distribution* $[\mathrm{cm}^{-2}\ \mathrm{s}^{-1}]$ *provided by the ROM, as function of* N.

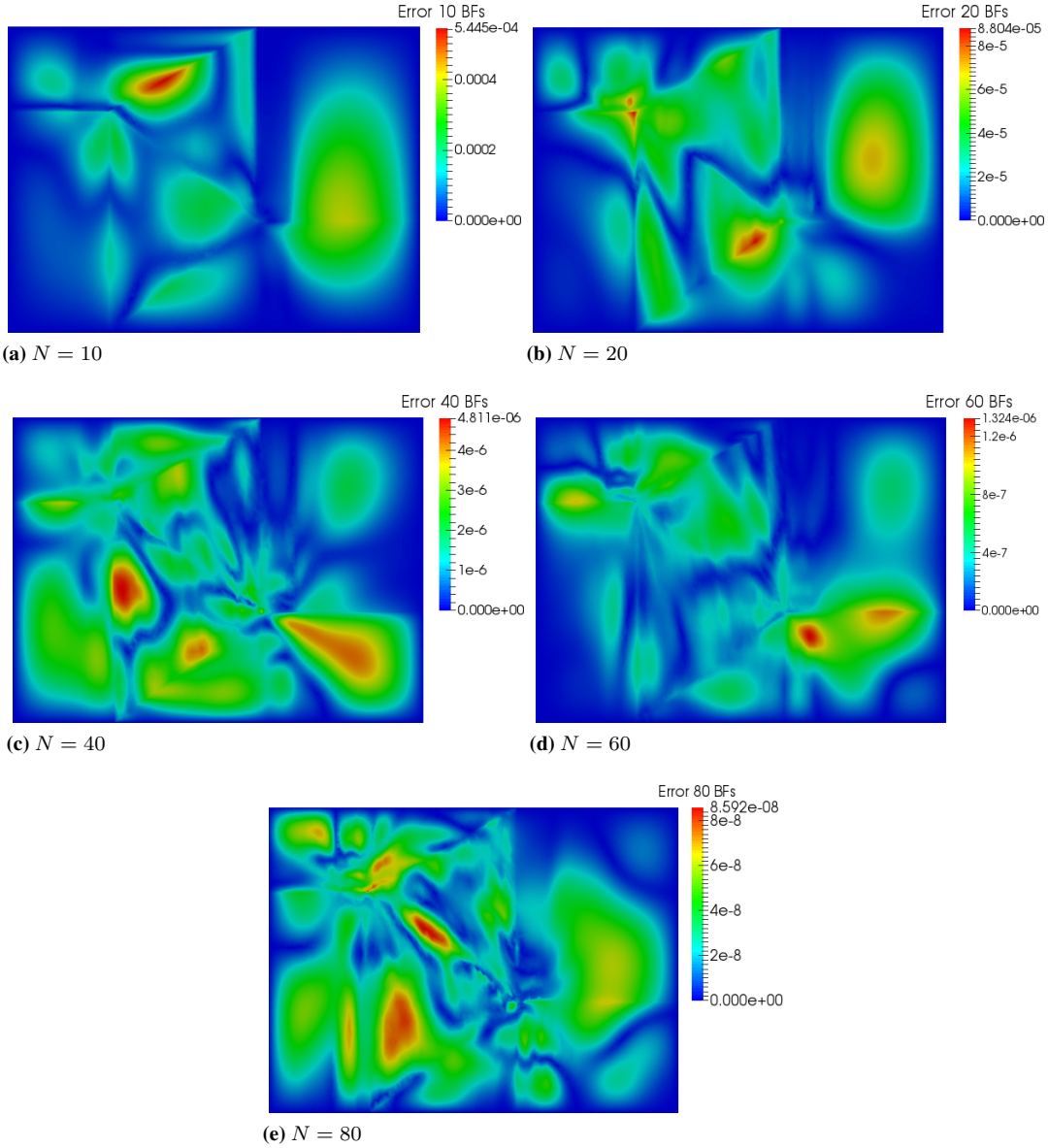

(a) $N = 10$ **(b)** $N = 20$

(c) $N = 40$ **(d)** $N = 60$

(e) $N = 80$

Figure 3.8: *Spatial error between the ROM and the FE solution [a.u.], as function of* N.

Table 3.3: *Error $e_\Phi(\mu)$ between the neutron flux provided by the ROM and by the high fidelity FE model.*

# basis functions	Error
10	5.09×10^{-3}
20	4.88×10^{-3}
40	2.83×10^{-5}
60	1.75×10^{-5}
80	1.52×10^{-6}

Table 3.4: *Average computational time $[s]$ and speed-up.*

# basis functions	ROM	FE	Speed-up
10	0.0057	33.423	5862
20	0.0064	33.423	5221
40	0.0094	33.423	3554
60	0.0162	33.423	2062
80	0.0289	33.423	1156

3.4.2 Neutron flux shape reconstruction

For the sake of brevity, in this subsection the outcomes provided by the ROM, employing different number of basis functions, for only one case with $\mu = (25.67, 12.93)$, are discussed. Figure 3.6 shows the high fidelity FE spatial flux distribution. Figure 3.7 reports the neutron flux distribution provided by the ROM employing 10, 20, 40, 60 and 80 Basis Functions (BFs), respectively, while the corresponding spatial error is depicted in Fig. 3.8. The error $e_\Phi(\mu)$ between the total neutron flux provided by the ROM and the FE one has been computed as follows:

$$e_\Phi(\mu) = \int_\Omega |\Phi_\mathcal{N}(\mu) - \Phi_N(\mu)|. \tag{3.24}$$

In Table 3.3, the error $e_\Phi(\mu)$ is reported as function of the basis functions employed. As it can be seen, $e_\Phi(\mu)$ and $e_\lambda(\mu)$ has the same order of magnitude as function of basis functions employed

As final remark, in Tab. 3.4, the average computational times required to solve the FE problem given by Eq. (3.17) and the developed ROM are reported. The developed reduced order model allows a speed-up of at least three orders of magnitude. It is worth recalling that the time required to solve the ROM is degrees-of-freedom-independent, while the FE problem is strongly dependent on the degrees of freedom. Therefore, employing a finer mesh, or more energy groups, would end up with an even higher computational speed-up.

3.5 Concluding remarks

The reduced basis method has been employed in this Chapter to develop a Reduced Order Model (ROM) for simulating control rods movement. In particular, the reactivity and neutron flux distribution have been estimated solving a parametrized generalized eigenvalue problem associated to the stationary formulation of the multi-group neutron diffusion equation. In fact, the movement of two control rods, surrounded by fissile material, has been simulated. An alternative sampling technique, with respect to the

more "classical" option provided by greedy algorithms, has been adopted by proposing the Centroidal Voronoi Tessellation (Burkardt et al., 2006). To further reduce the basis dimension, a proper orthogonal decomposition has been performed on the vector of the snapshots computed according to the CVT.

The presented ROM is capable to provide high-fidelity outcomes, with respect to a fine finite element discretization, in terms of both reactivity and neutron flux shape, employing only forty basis functions. In particular, with such number of basis, the reactivity is correctly predicted up to the pcm. Obviously, increasing the number of basis functions, the accuracy is improved. Moreover, the ROM features a computational speed-up of at least three orders of magnitude.

This contribution is intended to be useful for control-oriented studies. Indeed, already developed simulation tools, based on the classical point-wise approach, could be improved by computing, at each time step, the system reactivity by a ROM similar to the here proposed one, in order to take into account spatial effects.

CHAPTER 4

Conclusions

This PhD work is aimed at tackling the need of nuclear engineering field to have a fast-running simulation tool, which can be tailored to common control systems, able to reproduce spatial effects, in particular those induced by the control rod movement. The present contribution can be considered as a first step towards building a bridge between the "world of design" and the "world of control". The goal has been to demonstrate that reduced order modelling is suited to be applied in more complex (and coupled) industrial problems in order to introduce competitive computational performance and allowing, at the same time, a better investigation, thanks to the parametrization of involved phenomena. To this aim, a methodological approach for developing a reduced order model for systems with increasing complexity, up to a multi-physics LFR single channel, has been set up.

In the present PhD thesis, innovative simulation tools have been developed for reactor core spatial dynamics, with particular attention to neutronics, relying on the most advanced computational techniques, namely, the reduced basis method. The efforts have been focused on the methodological approach, whose main achievements can be summarized as follows:

- The potential of reduced basis methods, both for control and design oriented studies, has been highlighted in comparison with the approaches conventionally adopted in the nuclear reactor analysis.

- Several accurate, reliable reduced order methods for control rod movement have been developed, solving the parametrized multi-group neutron diffusion equation. The reduced order models are able to accurately taken into account the spatial effects induced by the rods' movement, still featuring a real-time computational time.

- The reduced basis method, for modelling the nuclear reactor control rods, has been employed both in time-dependent and stationary settings.
- For the time-dependent neutron diffusion equation, a surrogate model for the $\beta_{\mathrm{inf-sup}}$ stability factor has been developed, relying on the observed monotonicity of the $\beta_{\mathrm{inf-sup}}$ with respect to the reactivity of the reactor, which is related to the movement of the control rods.
- A different sampling technique, within the Reduced Basis framework, has been employed, namely, the centroidal Voronoi tessellation, which allows for a hierarchical parameters space exploration, without relying on an *a posteriori* error estimation with a greedy algorithm (considerable part of the Offline phase is spent in computing the components needed for the error estimation between the reduced order model and the full order one). Skipping this part, the Offline computational time may be sensibly reduced.

During the doctoral research, attention has also been paid to the multi-physics modelling approach, where all the involved physics are solved within the same computational environment. In fact, a multi-physics and time-dependent model for single-channel transient analysis of a Lead Fast Reactor (LFR) has been developed (see Appendix B on page 93). The work focused on the coupling among the neutronic, the thermal-elastic and the fluid-dynamic phenomena. A purpose-made six-group neutron diffusion model has been developed, which allows taking into account the local dependency of the neutron macroscopic cross-sections on the temperature and density fields. It is worth mentioning that the majority of LFR analyses available in literature, which employ computational fluid dynamics codes, do not allow for explicit neutronic feedbacks. Relying on this work, a reduced order model of a *parametrized* multi-physics model of a LFR single channel has been developed (see Appendix C on page 121). The potential of such approach has been addressed by choosing both geometrical and physical parameters. Indeed, the outcomes provided by the developed reduced order model have the same accuracy of the full-order multi-physics problem and a fast-running computational time, allowing estimation of a wide set of output of interest in real-time. A particular strategy for handling the nonlinear coupling terms has been proposed in order to allow for an efficient Offline/Online decoupling.

Numerous possible extensions of the present work are desirable. Since the thesis work was focused on the methodological approach, more detailed description of the TRIGA Mark II reactor, as well as the adoption of the neutron transport equation are foreseen in order to benchmark the outcomes with *ad hoc* collected experimental data. The performance of the reduced basis method achieved in the conducted studies gives encouragement for pursuing this track. In particular, the investigation of the so-called Reduced Basis Element Method (RBEM) would be interesting. According to RBEM, the reduced order model is computed for several "simple" domains where the boundary/interface conditions are parametrized. In the Online phase, the modelled physics are solved on more complex domains, obtained by combining the "simple" domains. For example, it would be interesting to develop a parametrized multi-physics ROM for a single fuel assembly, and then try to model the whole core as a repetition of the same fuel assembly, with proper interface conditions. Different strategies for handling non-linearities, such as the Empirical Interpolation Method, might be considered as well.

In the multi-physics modelling approach, mechanical and irradiation-induced effects were beyond the scope of the work. Nevertheless, such phenomena, along with the handling of pellet-cladding mechanical interaction, might be the object of future investigations. The reduced order model of the parametrized multi-physics LFR single channel model could be improved by taking into account the coupling with the thermo-elasticity. Moreover, the extension to the time-dependent settings should be considered as well.

APPENDIX $\mathcal{A}$

TRIGA Mark II reactor

THE TRIGA (Training Research and Isotope production General Atomics) Mark II is a pool type reactor moderated and cooled by light water. It has a nominal power of 250 kW in stationary-state operation. The core is shaped as a right cylinder and contains 90 slots, distributed over 5 concentric rings. Figure A.1 shows the map of the core, which features three control rods (SHIM, TRANSIENT, REGULATING), two irradiation channels (C.T., RABBIT), and one channel where the source for the start-up of the reactor is placed surrounded by two elements of graphite (DUMMY). All other elements are fuel pins.

TRIGA fuel consists of a uniform mixture of zirconium hydride (ZrH) and uranium, enriched 19.75% wt in ^{235}U. Fuel rod structure is described in Fig. A.2: the fuel itself [A] is placed at the center, while the top and bottom parts of the rod, made of nuclear graphite, play the role of axial neutron reflectors [B]. Two burnable poison disks [C], containing samarium oxide (Sm_2O_3) are placed between the fuel and the reflectors. Everything is contained by a 0.76 mm-thick aluminum cladding [E] and by two aluminum endcaps [D].

The TRIGA Mark II reactivity control is handled by three absorbing rods, named SHIM, Regulating (REG) and Transient (TRANS). The SHIM and REG control rods are made of hot-pressed boron carbide powder (B_4C); the TRANS rod is a solid graphite rod containing 25% wt free boron. The documentation at our disposal describes just the SHIM and REG rods geometrical structure in great detail (Fig. A.3); the Transient rod was modeled in the same way, assuming that there are no great differences between the three rods.

The interested reader can find more details in (General Atomic, 1964; Cammi et al., 2013; Alloni et al., 2014).

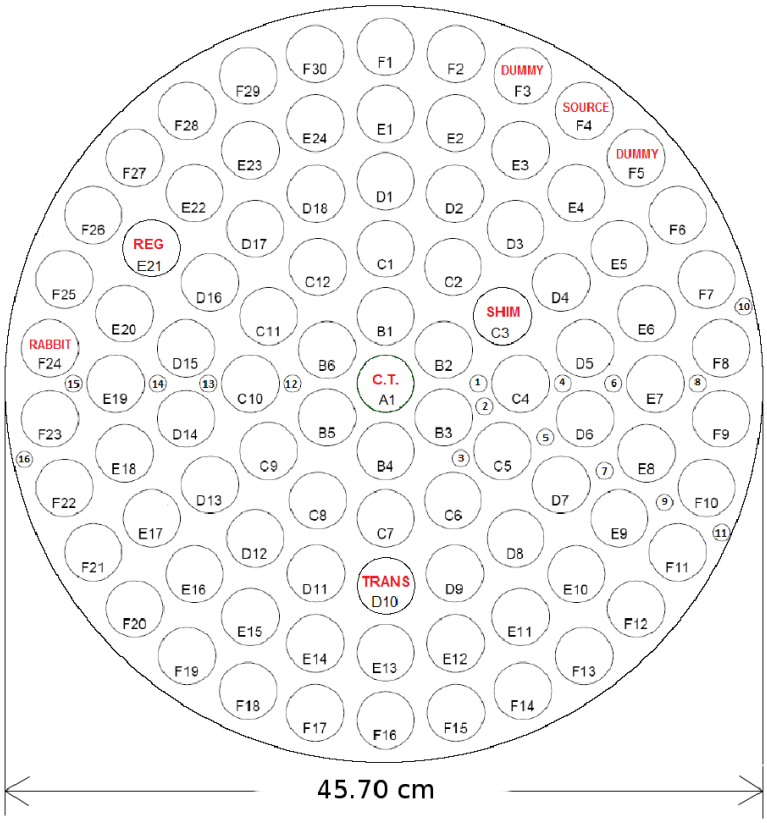

Figure A.1: *Map of the TRIGA Mark II reactor core.*

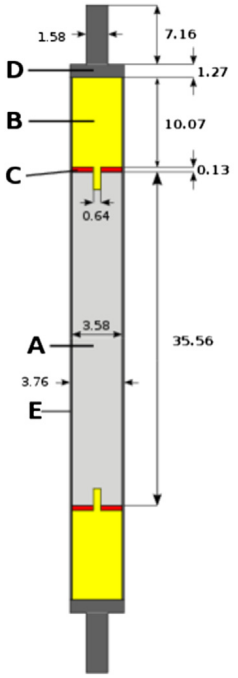

Legend and composition

A	**HZr-U Fuel** [Table 1]
B	**Graphite reflectors** [99.0% C, 0.8% Fe, 0.1% Cu, 0.1% Ti, 5*ppm* B] $\rho \sim 1.7 \mathrm{g/cm^3}$
C	**Burnable poison disks** [Table 1]
D	**Aluminum endcaps**
E	**Aluminum cladding** [99.6% Al, 0.2% Cu, 0.1% Fe, 0.1% V] $\rho = 2.71 \mathrm{g/cm^3}$

Figure A.2: *Fuel rod structures. Values are measured in centimeters [cm].*

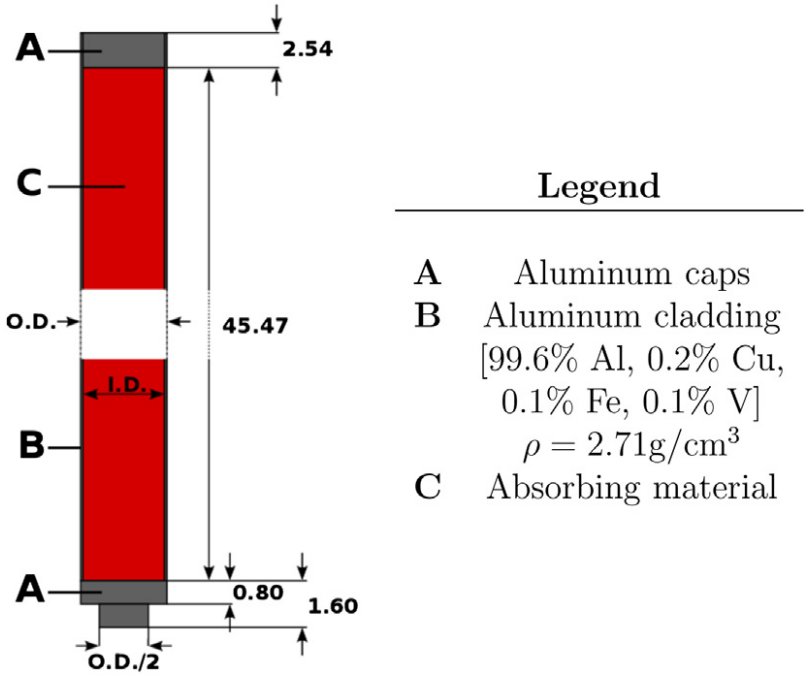

Figure A.3: *Control rod structure. Values are measured in centimeters [cm].*

APPENDIX B

A multi-physics time-dependent model for the Lead Fast Reactor single-channel analysis[1]

TRADITIONALLY, nuclear reactor analysis is performed by coupling neutron kinetics and thermal-hydraulic codes (Avramova and Ivanov, 1997; Salah et al., 2008). These coupled code techniques are often based on the operator-splitting technique, in which the time-dependent solution is reached using the output from one code (e.g., the neutron kinetics code) as input to another code (e.g., the thermal-hydraulic code) at each time step. Often, the nonlinearities due to the coupling are not resolved in a time step, possibly reducing the overall accuracy (Mahadevan et al., 2012). The developed Multi-Physics Modelling (MPM) approach allows for higher-order coupling between the different physics, and it is possible to perform solver iteration up to a desired degree of accuracy.

Concerning the Lead Fast Reactor study (LFR), the MPM approach allows to simultaneously evaluate a wide set of core parameters (e.g., temperature field, velocity field, and neutron fluxes). This advantage may be valuable for core designing, when verifying the satisfaction of the above mentioned operational constraints. It is worth mentioning that the majority of LFR analyses available in literature, which adopt Computational Fluid Dynamic (CFD) codes (e.g., Tuček et al., 2006), do not allow for explicit neutronic feedbacks.

In this Appendix, the MPM approach is adopted to study the behaviour of an LFR single-channel representative of the active-core average conditions (from now on referred to as core-average channel). Reference is made to the European Lead-cooled System (ELSY) (Alemberti et al., 2011), developed in the frame of the EU-FP6-ELSY

[1]The main results presented in this Appendix have been published in: Aufiero, M., Cammi, A., Fiorina, C., Luzzi, L., Sartori, A., 2013, "A multi-physics time-dependent model for the Lead Fast Reactor single-channel analysis", Nuclear Engineering and Design 256, 14–27.

project. The choice of ELSY as case study is mainly due to the availability of detailed core design specifications.

The present work is focused on the coupling among neutronics, fluid dynamics, heat transfer, and thermal expansions.

The multi-group neutron diffusion model, the CFD model, and the linear elasticity model are implemented in the same computational environment offered by the general purpose finite-element software COMSOL Multiphysics (COMSOL, 2011). For the CFD and the solid mechanics treatment the models available in COMSOL are employed. On the other hand, for the neutronic treatment, a purpose-made six-group diffusion model is developed. This model is proved against the Monte Carlo code SERPENT (SERPENT, 2011).

The proposed Multi-Physics (MP) model is adopted to investigate both the steady-state conditions of the ELSY core-average channel, and two transients: an insertion of reactivity and a perturbed inlet lead temperature transient. Such transients are simulated both taking into account and neglecting the thermal expansion effects. Through these studies, the importance of thermal expansion effects is caught. It is also shown that the presented MP model represents a suitable simulation tool for a preliminary investigation of the LFR transient behaviour.

The Appendix is organised as follows. Section B.1 describes how the different models are implemented in the MPM approach. The validation of the neutronic model is detailed in Section B.2. In Section B.3, the results obtained by the present MP model are shown in terms of steady-state spatial distribution of some quantities of interest, and two case studies are presented to exemplify the MPM capabilities for simulating the transient behaviour. At the end of the Appendix, the Nomenclature is reported.

B.1 Multi-physics modelling approach

In this section, the MP scheme of analysis is presented by describing the different equations adopted for neutronics, fluid dynamics, and heat transfer, and solved in the same simulation environment. Thermal expansion effects are included in such scheme via the equations of solid mechanics and combining them with the other physics, by means of the "moving mesh" technique.

B.1.1 System description

The single-channel layout chosen for the present study is based on the ELSY reactor with the Open Square Fuel Assembly (OSFA) design (Alemberti et al., 2011; Sarotto et al., 2009). The core is arranged in 162 fuel assemblies, having fuel pins disposed in a square array, and surrounded by reflector assemblies. Such reactor features a core thermal power of about 1500 MW_{th}. The inlet temperature of the lead, at nominal condition, is set equal to 400°C, in order to avoid solidification. The outlet temperature of the lead, at nominal condition, is set to 480°C in order to limit the corrosion of the structural and cladding materials that becomes significant at temperatures higher than 550°C. The active-core diameter is equal to 4.65 m, and the active height is equal to 0.90 m. The proposed MP model is a two-dimensional axial-symmetric representation (r, z) of a single-channel, limited to the active height. Reference is made to the core average conditions at Beginning Of Life (BOL). Table B.1 gives the main parameters of

Table B.1: *Main parameters of the analysed core single-channel (Sarotto et al., 2009)*

Average linear power	23.5	$kW\ m^{-1}$
Inlet lead temperature	400	$°C$
Outlet lead temperature	480	$°C$
Inlet lead velocity	1.6	$m\ s^{-1}$
Pu enrichment	17	$vol.\%$
Fuel density	95	$\%TD$ [1]
Fuel pin active height	900	mm
Fuel pellet hole diameter	2.0	mm
Fuel pellet outer diameter	9.0	mm
Cladding inner diameter	9.3	mm
Cladding outer diameter	10.5	mm
Pin-pitch	13.9	mm
Additional model parameters		
UO_2 thermal insulator height	20	mm
Spring height	50	mm
Upper plug height	50	mm
Inactive channel length	300	mm

Table B.2: *Energy structure adopted in multi-group neutron diffusion*

Group number	Upper boundary		Lower boundary	
1	20	MeV	2.23	MeV
2	2.23	MeV	0.82	MeV
3	0.82	MeV	67.38	keV
4	67.38	keV	15.03	keV
5	15.03	keV	0.75	keV
6	0.75	keV	0	keV

the presented model. Figure B.1 shows a transversal cross section of the analysed fuel pin. Figure B.2 represents the longitudinal (r, z) view of the modelled geometry (for clarity, the aspect ratio of the image is not preserved). An inactive channel length, below the active height, is adopted to allow for a complete lead flow development in order to avoid inaccurate estimation of the heat transfer between the lead and the cladding in the first centimetres of the active height. The evaluation of the effects related to the core radial expansion cannot be intrinsically caught by single channel analysis. The adoption of artificial corrective factors to take into account this effect is out of the scope of the present work.

B.1.2 Neutronics

The multi-group diffusion theory is employed in the neutronic model of the ELSY single-channel (Duderstadt and Hamilton, 1976). Integrating over a set of six energy intervals (see Table B.2) the continuous neutron diffusion equation, along with the balance equations for eight groups of precursors, the following set of partial differential equations is obtained:

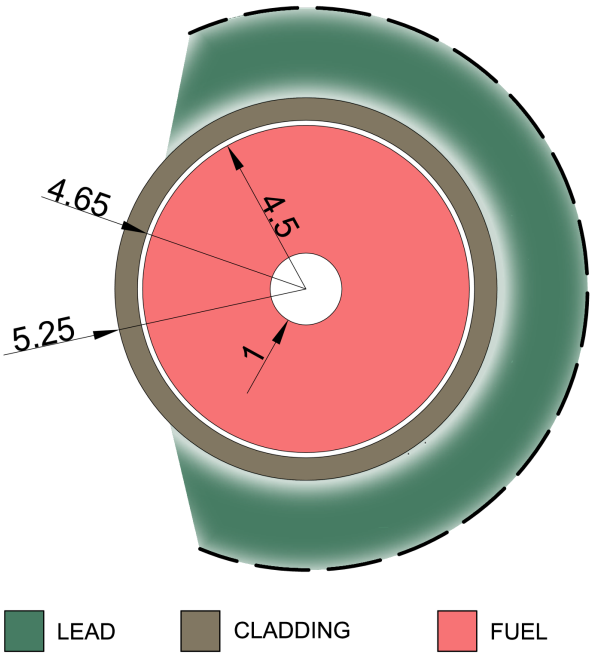

Figure B.1: *Analysed fuel pin and surrounding lead. Radial sizes at nominal conditions (room temperature), expressed in* mm.

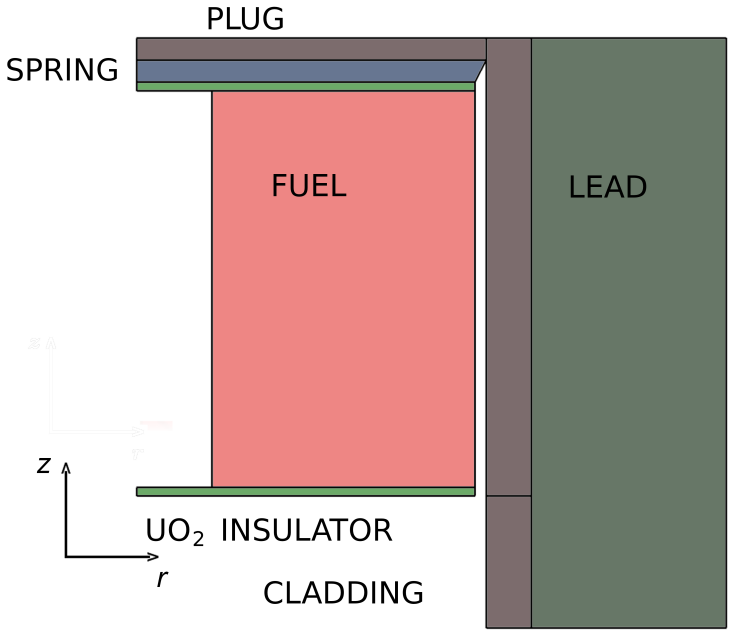

Figure B.2: *Longitudinal* (r, z) *view of the modelled geometry.*

$$\frac{1}{v_g}\frac{\partial \phi_g}{\partial t} = \nabla \cdot D_g \nabla \phi_g - \Sigma_{a,g}\phi_g - \sum_{g' \neq g} \Sigma_{s,gg'}\phi_g + \tag{B.1}$$

$$+ \sum_{g' \neq g} \Sigma_{s,g'g}\phi_{g'} + (1-\beta)\,\chi_{p,g} \sum_{g'=1}^{6} \left(\nu\Sigma_f\right)_{g'} \phi_{g'} +$$

$$+ \sum_{i=1}^{8} \chi_{d,g}\lambda_i c_i \qquad g = 1 \div 6$$

$$\frac{\partial c_i}{\partial t} = -\lambda_i c_i + \beta_i \sum_{g=1}^{6} \left(\nu\Sigma_f\right)_g \phi_g \qquad i = 1 \div 8 \tag{B.2}$$

All the group constants are given in the COMSOL model as input. In the fuel, the dependency of the macroscopic neutron cross-sections on the local temperature and density is taken into account by means of the following equation:

$$\Sigma(T,\rho) = \left(\frac{\rho}{\rho_0}\right)\left[\Sigma_0 + \alpha\, log\left(\frac{T}{T_0}\right)\right] \tag{B.3}$$

For the lead cross-sections, the above functional form is reduced to:

$$\Sigma(T,\rho) = \left(\frac{\rho}{\rho_0}\right)\Sigma_0 \tag{B.4}$$

neglecting the Doppler broadening effects. For the sake of simplicity, the cross-sections are kept constant in the cladding, spring, plug, and thermal insulator domains. The functional forms of Eqs. (B.3) and (B.4) allow for the heterogeneity of temperature and density fields inside the core channel, in this way the thermal-hydraulic feedbacks on reactivity are caught. The accuracy of such simple approach will be assessed in Section B.2.

B.1.3 Fluid dynamics and heat transfer

The model of the fluid flow (liquid lead) is based on the incompressible form of the Reynolds-Averaged Navier-Stokes (RANS) equations, considering in particular the standard $k-\varepsilon$ turbulence model described by the following equations:

$$\rho\frac{\partial \mathbf{v}}{\partial t} + \rho\left(\mathbf{v}\cdot\nabla\right)\mathbf{v} = \nabla\cdot\left[-p\mathbf{I} + \left(\eta+\eta_T\right)\left(\nabla\mathbf{v} + \left(\nabla\mathbf{v}\right)^T - \frac{2}{3}\rho k\mathbf{I}\right)\right] \tag{B.5}$$

$$\nabla\cdot\mathbf{v} = 0 \tag{B.6}$$

$$\rho\frac{\partial k}{\partial t} + \rho\mathbf{v}\cdot\nabla k = \nabla\cdot\left[\left(\eta + \frac{\eta_T}{\sigma_k}\right)\nabla k\right] - \rho\varepsilon + \eta_T\left[\nabla\mathbf{v} : \left(\nabla\mathbf{v} + \left(\nabla\mathbf{v}\right)^T\right)\right] \tag{B.7}$$

$$\rho\frac{\partial \varepsilon}{\partial t} + \rho\mathbf{v}\cdot\nabla\varepsilon = \nabla\cdot\left[\left(\eta + \frac{\eta_T}{\sigma_\varepsilon}\right)\nabla\varepsilon\right] - \frac{C_{\varepsilon 2}\rho\varepsilon^2}{k} +$$

$$+ C_{\varepsilon 1}\frac{\varepsilon}{k}\eta_T\left[\nabla\mathbf{v} : \left(\nabla\mathbf{v} + \left(\nabla\mathbf{v}\right)^T\right)\right] \tag{B.8}$$

The empirical constants are given as $C_{\varepsilon 1} = 1.44$, $C_{\varepsilon 2} = 1.92$, $C_{\mu} = 0.09$, $\sigma_k = 1.0$, $\sigma_{\varepsilon} = 1.3$.

The heat transfer model within the lead domain is described as follows:

$$\rho C_p \frac{\partial T}{\partial t} + \nabla \cdot \left[- \left(K + K_T \right) \nabla T \right] = \rho C_p \mathbf{v} \cdot \nabla T \tag{B.9}$$

The turbulent thermal conductivity K_T is given by

$$K_T = \frac{C_p \, \eta_T}{Pr_T} \tag{B.10}$$

The turbulent Prandtl number Pr_T is calculated using the extended Kays-Crawford model (Weigand et al., 1997):

$$Pr_T = \left[\frac{1}{2 Pr_{T_\infty}} + \frac{0.3}{\sqrt{Pr_{T_\infty}}} \frac{C_p \eta_T}{K} - \left(0.3 \frac{C_p \eta_T}{K} \right)^2 \left(1 - e^{- \frac{K}{0.3 C_p \eta_T Pr_{T_\infty}}} \right) \right]^{-1} \tag{B.11}$$

where

$$Pr_{T_\infty} = 0.85 + \frac{100 \, K}{C_p \eta \left(Re_\infty \right)^{0.888}} \tag{B.12}$$

and Re_∞ is set to 1.1×10^5.

As to the heat transfer modelling in the cladding, thermal insulator and plug materials, the following energy balance equation is adopted:

$$\rho C_p \frac{\partial T}{\partial t} = \nabla \cdot \left(K \nabla T \right) \tag{B.13}$$

with the corresponding values for the thermal conductivity, the density and the specific heat. Eq. (B.14) is adopted in the fuel domain:

$$\rho C_p \frac{\partial T}{\partial t} + \nabla \cdot \left(- K \nabla T \right) = Q \tag{B.14}$$

The volumetric heat source Q is explicitly computed, by means of the calculated neutron fluxes:

$$Q = \sum_{g=1}^{6} \left(\Sigma_{f,g} \cdot E_f \cdot \phi_g \right) \tag{B.15}$$

where $\Sigma_{f,g}$ are the macroscopic fission cross-sections, and E_f is the value of the average energy released per fission. The heat is considered to be released instantaneously and locally (i.e., disregarding gamma transport and delayed nuclear decay).

The heat transfer model takes into account the heat conduction and the radiative contribution across the helium gap between the fuel and the cladding. The radiative heat transfer is modelled by means of a heat flux from the fuel outer surface to the cladding inner surface as follows:

$$q(z)'' = \sigma_B \frac{1}{\frac{1}{\varepsilon_{fuel}} + \frac{1}{\varepsilon_{cladding}} - 1} \left[T^4_{fuel}(z) - T^4_{cladding}(z) \right] \tag{B.16}$$

where ε_{fuel} and $\varepsilon_{cladding}$ are the emissivities of the outer fuel surface and of the inner cladding surface, respectively. These values are kept constant during the simulations (ε_{fuel} = 0.95 and $\varepsilon_{cladding}$ = 0.5).

It is worth noting that the radiative contribution is computed locally at each node of the mesh at the outer boundary of the fuel and at the inner boundary of the cladding.

In order to speed up and simplify the calculations, effective and constant values of the thermo-physical properties C_p and K are adopted for the considered materials (Helium, MOX, UO_2, T91 steel and lead). It is noteworthy that the local value of temperature and density are adopted to compute the macroscopic cross-sections in order to intrinsically catch the thermal-hydraulic feedbacks on reactivity .

B.1.4 Solid mechanics and moving mesh

In order to take into account the fuel and cladding thermal expansion effects, the following equations of linear elasticity are introduced into the MP model:

$$\rho \frac{\partial^2 \mathbf{u}}{\partial t^2} = \nabla \cdot \boldsymbol{\sigma} \tag{B.17}$$

$$\boldsymbol{\epsilon} = \frac{1}{2}\left[(\nabla \mathbf{u}) + (\nabla \mathbf{u})^T\right] \tag{B.18}$$

$$\boldsymbol{\sigma} = \mathbf{C} : (\boldsymbol{\epsilon} - \alpha_{th}(T - T_{ref})\mathbf{I}) \tag{B.19}$$

The coefficient of thermal expansion, as well as the Young modulus and the Poisson coefficient are kept constant with the temperature in order to simplify the problem solution. The Poisson coefficient and the Young modulus are used to derive the stiffness tensor **C** under the isotropic material hypothesis. The column of fuel pellets is modelled as a unique continuous structure. Cracking, irradiation induced and other mechanical (e.g., creep) effects are neglected. In general, the dynamics of these effects can be considered slow when compared to the time-scales of the transients treated in this work. The evaluation of such phenomena is beyond the scope of this work, which is focused on the intrinsic computation of the coupled effects involving the thermal expansion. The spring between the plug and the upper thermal insulator is simply modelled as a solid cylinder with a suitable Young modulus modified to reproduce the spring mechanical properties . For the sake of simplicity, the gravitational force is neglected.

The "moving mesh" technique offered by COMSOL allows to dynamically deform the mesh of the simulated domain. In the present work, the thermal-mechanical deformations are used to redefine the geometry, at each solver iteration. In this way, the different physics are influenced by the displacement field of the fuel and the cladding. Hence, the coupled effects due to thermal expansion (e.g., gap thermal resistance reduction, fuel expansion feedbacks on neutronics) are explicitly considered. Due to axial expansion of the fuel and the cladding, the two domains undergo high relative displacement during transients. This leads to a continuous change of the mesh boundary nodes facing each other across the gap. Such phenomenon gives rise to a computational concern for the radiative heat transfer model. To handle this issue, a boundary mapping is performed between the nodes of the fuel outer surface and the nodes of the cladding inner surface. In this way, at each time step, each node of the fuel outer boundary always interacts with the closest node belonging to the cladding inner boundary.

B.1.5 Boundary conditions

Below, the used boundary conditions are dealt with. Figure B.3 summarizes the main boundary conditions applied for the neutronic model. The present model is limited to

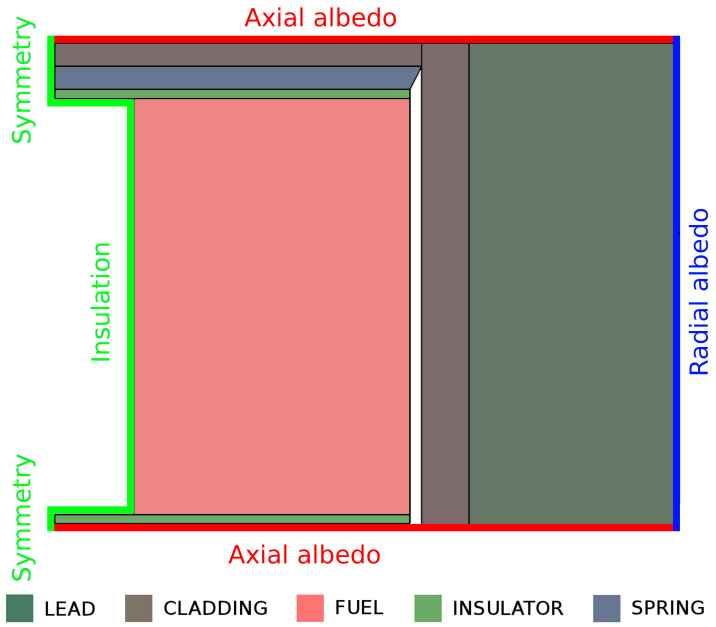

Figure B.3: *Main boundary conditions applied for the neutronic model.*

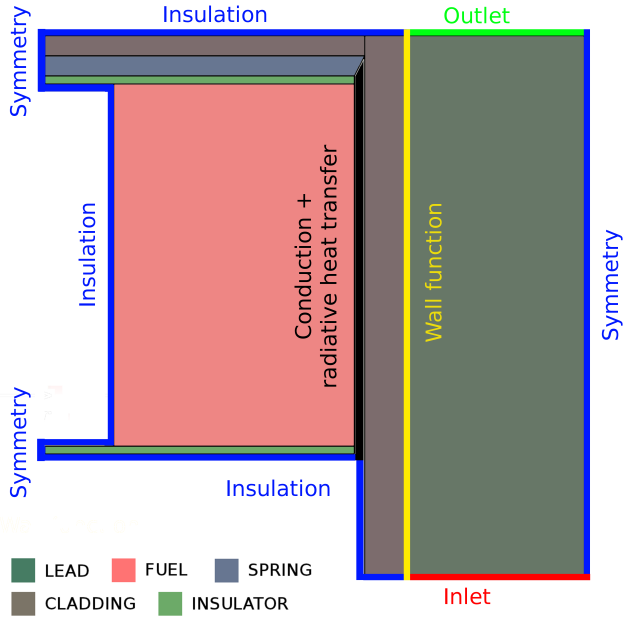

Figure B.4: *Main boundary conditions applied for the thermal-fluid dynamic model.*

a core single-channel. As a consequence, the choice of the neutronic boundary conditions is a relevant issue. The albedo boundary conditions are judged to be a suitable compromise between accuracy of the spatial characterization of the neutron fluxes and computational requirements. Albedo boundary conditions are imposed at the upper, lower and radial boundaries of the COMSOL model domain, namely:

$$\mathbf{n} \cdot (D \nabla \phi_g) = -\gamma_z \phi_g \tag{B.20}$$

$$\mathbf{n} \cdot (D \nabla \phi_g) = -\gamma_r \phi_g \tag{B.21}$$

The computation of γ_z and γ_r is discussed in sub-section B.1.7.

Figure B.4 summarizes the main boundary conditions applied for the thermal-fluid dynamic model. A condition of thermal insulation is applied to the lower boundary of the lower thermal insulator and to the upper boundary of the steel plug. Symmetry conditions are considered at the outer radius of the fluid domain, accounting for the surrounding channel. At the lower boundary, the lead inlet velocity and temperature are imposed (T_{in}, v_{in}). In order to allow for a proper flow development below the active height, an inactive entrance channel 30 cm long is considered in the model. At the upper boundary of the fluid domain, the outlet boundary condition is applied, imposing the outlet pressure (p_{out}) and no viscous stress. The boundary condition at the interface between cladding and molten lead is treated by means of the standard wall function approach available in COMSOL (COMSOL, 2011).

As far as the solid mechanics model is concerned, a condition of no axial displacement is applied to the lower boundaries of the lower thermal insulator and of the cladding domain. No radial displacement of the mesh is allowed at the outer radius of the channel. Within the lead domain, at the upper boundary, the moving mesh is forced to follow the cladding axial thermal expansion.

B.1.6 Numerical solution

The set of partial differential equations described above has been simultaneously solved by means of the "general-purpose" finite element software COMSOL Multiphysics.

The geometry described in sub-section B.1.1 is meshed so as to achieve a good compromise between numerical accuracy and computational requirements. In particular, as shown in Fig. B.5, a mapped mesh is judged suitable for the cladding and lead domains. A progressive mesh refinement near the wall is adopted in the lead domain (in green), while the fuel (in red) is meshed with triangular elements. The adopted elements are Lagrangian and quadratic-order. In order to reduce the computational cost of the simulation, the segregated solver is adopted. Table B.3 shows the variables belonging to the different segregated groups. Segregated groups 1 to 4 are solved using the MUltifrontal Massively Parallel Sparse direct Solver (MUMPS). The equations of the RANS $k - \varepsilon$ turbulence treatment are solved by means of the PARallel sparse Direct and multi-recursive Iterative linear SOlver (PARDISO). Transient analyses are treated with the implicit second order Backward Differentiation Formula (BDF) time integration method.

B.1.7 Neutronic input generation with SERPENT

The group constants (D_g, v_g, β_i, $\nu\Sigma_{f,g}$, $\Sigma_{a,g}$, $\Sigma_{s,gg'}$, $\chi_{d,g}$, $\chi_{p,g}$) are calculated by means of the Monte Carlo neutron transport code SERPENT, using the nuclear data library

Table B.3: *Segregated groups*

Group		Variables
1	$\phi_1 ... \phi_6$	neutron fluxes
2	$c_1 ... c_6$	precursors density
3	T, $\mathbf{u}$	temp. and displacement
4	p, $\mathbf{v}$	pressure and velocity
5	k, ε	turbulence variables

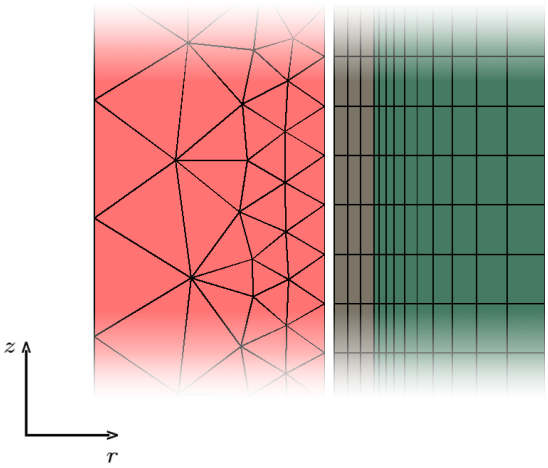

Figure B.5: *Meshed geometry*

JEFF 3.1 (Koning et al., 2006). SERPENT is a three-dimensional continuous energy Monte Carlo neutron transport code, with group constant generation capabilities. The results presented in the following are obtained after runs of 250 million active neutron histories with the version 1.1.17 of the code. Simulations consist in 500 active cycles of $5{\cdot}10^5$ neutrons subdivided in 32 parallel tasks. Fifty inactive cycles are adopted to allow for the convergence of the fission source distribution. Results related to reactivities are obtained by means of the k (multiplication factor) implicit estimate. Detectors with collision estimate of neutron flux are adopted to obtain the axial flux profiles.

As far as the SERPENT model is concerned, an infinite lattice of pins is simulated on the transversal (x, y) plane. Infinite lead reflectors are adopted above the steel plug and below the lower thermal insulator. Figures B.6 and B.7 show the transversal (x, y) and longitudinal (x, z) cross section views of the SERPENT geometry, respectively.

The γ_z coefficient of Eq. (B.20) is calculated so as to have the same k_{eff} in both COMSOL and SERPENT models at nominal conditions. Then, t he γ_r coefficient of Eq. (B.21) is set to allow for the radial leakage term and calculated so as to bring the system critical.

Table B.4 gives the isotopic composition of the input materials.

An ad-hoc Octave (Eaton et al., 2008) procedure is developed for the conversion of the neutronic input for the different materials (i.e., fuel, lead, cladding, insulators and spring) from the SERPENT output to a COMSOL readable format. The procedure automatically produces a set of temperature and density dependent cross-sections and diffusion coefficients, according to Eqs. (B.3) and (B.4). The other neutronic parameters (i.e., v_g, β_i, λ_i, $\chi_{d,g}$, $\chi_{p,g}$), which are calculated at nominal conditions, are kept

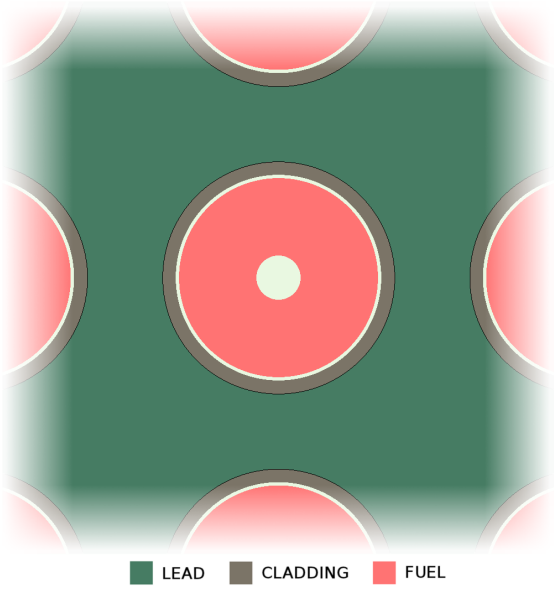

Figure B.6: *Transversal (x, y) cross section view of the SERPENT geometry.*

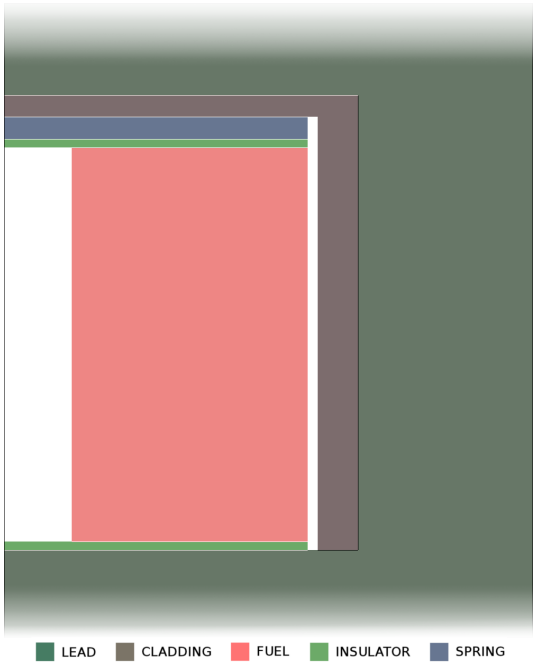

Figure B.7: *Longitudinal (x, z) cross section view of the SERPENT geometry.*

Table B.4: *Isotopic composition of the SERPENT input materials.*

Fuel		T91 Steel		Lead	
Isotope	wt%	Isotope	wt%	Isotope	wt%
U-234	0.002	Si-nat	0.50	Pb-204	1.4
U-235	0.295	V-nat	0.25	Pb-206	24.1
U-238	72.479	Cr-nat	9.00	Pb-207	22.1
Pu-238	0.364	Mo-nat	1.00	Pb-208	52.4
Pu-239	8.839	Fe-nat	88.30		
Pu-240	4.197	Ni-nat	0.13	Thermal Insulator	
Pu-241	0.949	Mn-55	0.60	Isotope	wt%
Pu-242	1.197	Nb-93	0.10	U-238	88.32
O-16	11.678	C-nat	0.12	O-16	11.68

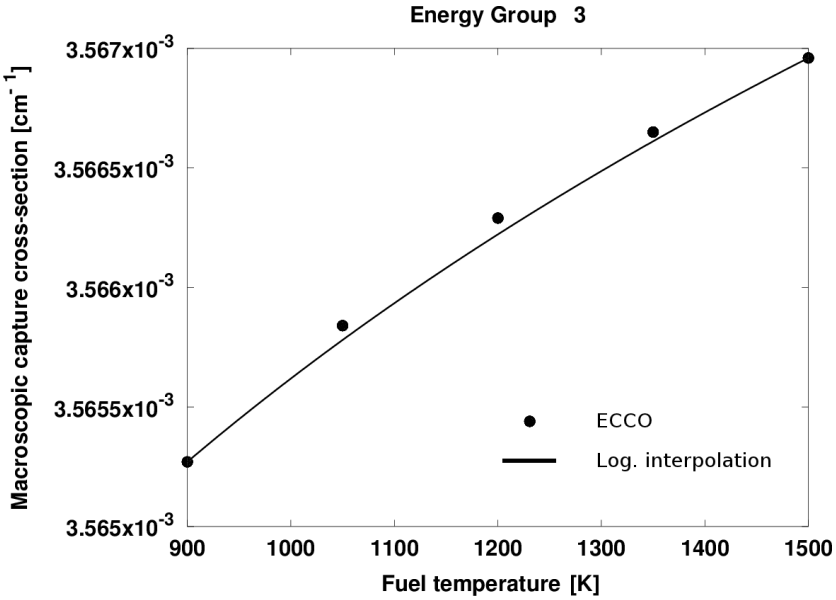

Figure B.8: *Fuel macroscopic capture cross-section versus temperature of energy group 3.*

constant during the simulations.

B.2 Validation of COMSOL neutronic model

B.2.1 Validation of the macroscopic cross-sections functional form

In the following, a brief discussion about the suitability of functional forms of Eqs. (B.3) and (B.4) is presented. For this purpose, the deterministic ECCO cell code (Rimpault, 2005) is employed to evaluate the macroscopic cross-sections over a wide range of fuel and lead temperatures and densities. Subsequently, the data are compared with the macroscopic cross-sections calculated according to the Eq. (B.3). The choice of a deterministic code for this particular analysis is mainly due to its low computational requirements and the absence of statistical scattering of the points in the following comparisons.

Figure B.8 shows the fuel macroscopic capture cross-sections versus temperature, for the energy group 3. This group is chosen as the most representative because almost

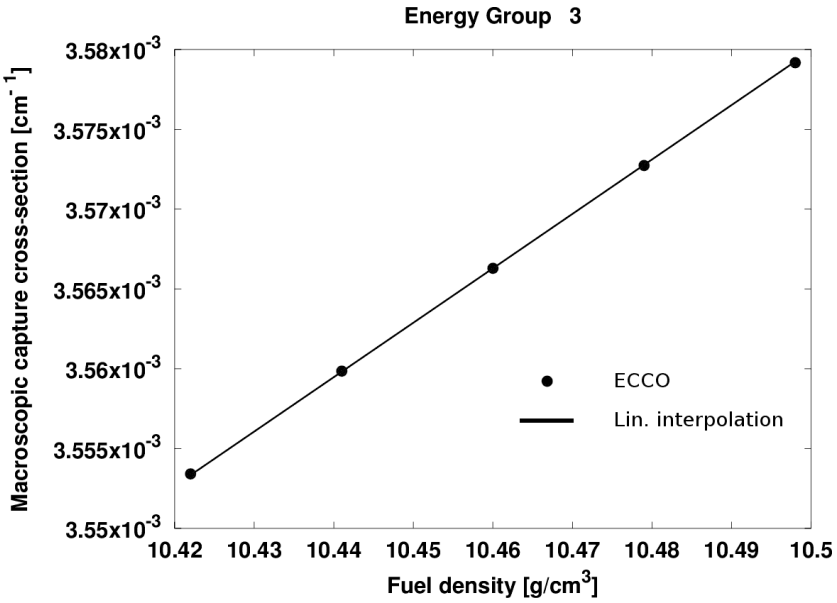

Figure B.9: *Fuel macroscopic capture cross-section versus density of energy group 3.*

40% of the neutrons belong to the energy range between 0.82 MeV and 67.38 keV, in nominal conditions. The macroscopic cross-sections of the other energy groups exhibit a similar behaviour and are not shown for brevity. For such analysis the fuel density is kept constant at nominal value (10.46 g/cm^3). The α coefficient of Eq. (B.3) is calculated as follows:

$$\alpha = \frac{\Sigma_2 - \Sigma_1}{ln\frac{T_2}{T_1}} \tag{B.22}$$

where T_1 is 900 K, T_2 is 1500 K, Σ_1 and Σ_2 are the macroscopic cross-sections evaluated at these temperatures. As it can be seen in Fig. B.8, the logarithmic approximation well estimates the evaluated cross-sections over a wide range of temperatures.

Figure B.9 shows the fuel macroscopic capture cross-sections versus the fuel density, for the energy group 3. For such analysis the fuel temperature is kept at 1200 K. As shown in Fig. B.9, Eq. (B.3) well predicts the cross-sections dependence on the ratio ρ/ρ_0.

In Section B.1.2, it was mentioned that the functional form expressed by Eq. (B.4) is adopted for the calculation of the macroscopic cross-sections in the lead domain.

Figures B.10 and B.11 show the lead macroscopic capture cross-sections versus the lead temperature and density, respectively, for the energy group 3. As it can be deduced by comparing the two figures, the effect forced by the temperature variation is one order of magnitude lower than the one caused by the density variation. It is worth mentioning that the density range employed in Fig. B.11 is calculated from the temperature range considered in Fig. B.10, according to the lead thermal expansion coefficient:

$$\rho = \rho_0 \left[1 - \beta_{lead} \left(T - T_0\right)\right] \tag{B.23}$$

The use of approximation expressed by Eq. (B.4) is acceptable for the lead domain, according to the purpose of the work.

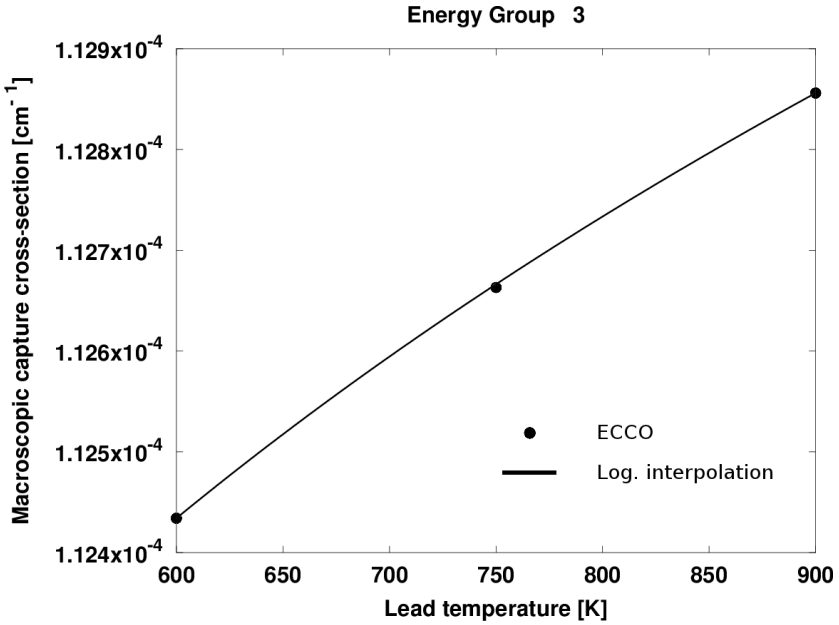

Figure B.10: *Lead macroscopic capture cross-section versus temperature of energy group 3.*

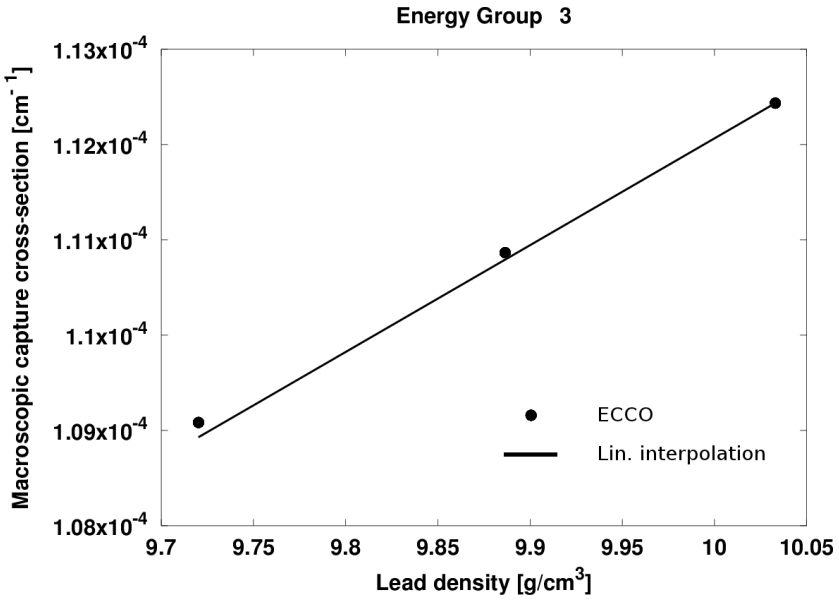

Figure B.11: *Lead macroscopic capture cross-section versus density of energy group 3.*

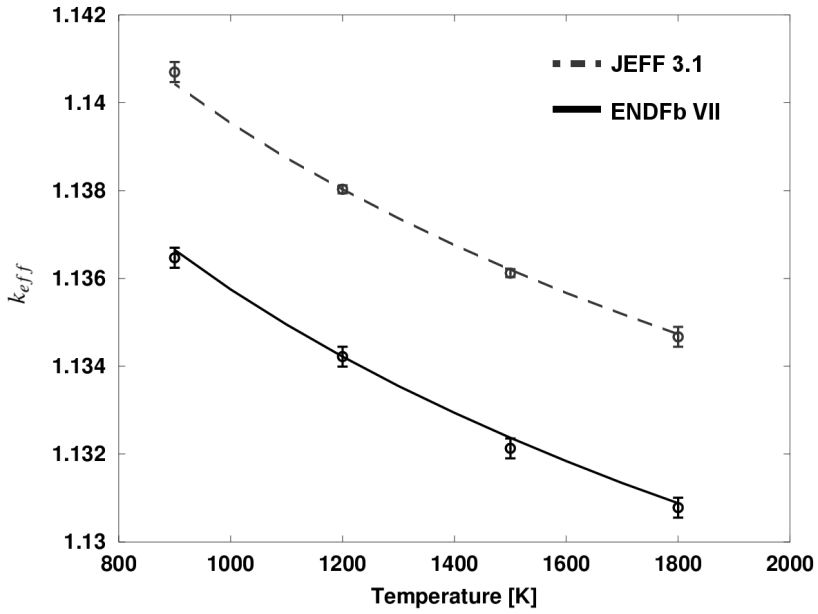

Figure B.12: *k_{eff} estimate versus fuel temperature. SERPENT: bullets, COMSOL: lines.*

B.2.2 Validation of the adopted neutron diffusion model

After assessing the cross-section functional dependence, the overall multi-group diffusion model implemented in COMSOL is assesed against the SERPENT code by comparing, for several cases, the multiplication factor k_{eff}. For this comparison, the albedo γ_r coefficient in COMSOL is set equal to zero, in order to simulate an infinite lattice of pins, as in SERPENT. The γ_z coefficient is kept constant and calculated in order to have the same k_{eff} both in SERPENT and COMSOL codes at nominal conditions. Within the COMSOL environment, the eigenvalue solver is employed to estimate the k_{eff}. The analysed cases can be summarized as follows:

- Fuel temperature ranging from 900 K to 1800 K, the other material properties and the geometry are kept at nominal condition.
- Fuel axial expansion varying from -0.5% to +1% of the nominal active length, the other material properties are kept at nominal condition.[2]
- Lead density variation from -2% to +1% of the nominal density, the other material properties and the geometry are kept at nominal condition.[3]

For this study, two nuclear data libraries are adopted, namely: JEFF 3.1 (Koning et al., 2006) and ENDFb VII (Chadwick et al., 2006). The set of group constants employed as input in the COMSOL model is generated by means of a SERPENT run at nominal conditions with both libraries.

Figure B.12 shows the k_{eff} of the infinite lattice of pins predicted by COMSOL and SERPENT versus the fuel temperature. COMSOL results are presented in solid and dashed lines, while SERPENT results are depicted with bullets with an error bar of

[2]These values correspond approximatively to a fuel temperature ranging from 750 K to 2100 K.
[3]These values correspond approximatively to a lead temperature ranging from 600 K to 900 K.

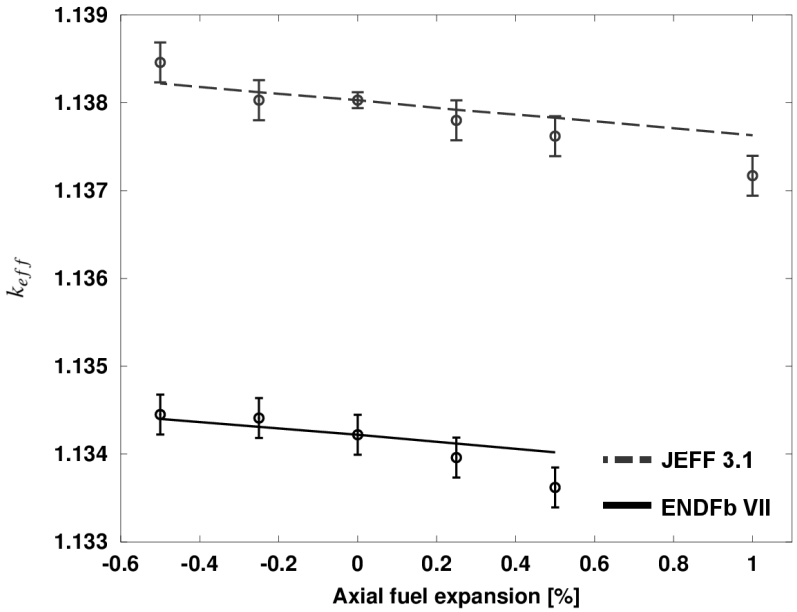

Figure B.13: *k_{eff} estimate versus relative fuel axial expansion. SERPENT: bullets, COMSOL: lines.*

± 2 standard deviations. As it can be seen in Fig. B.12, the COMSOL neutronic model results have a good agreement with the Monte Carlo predictions. Despite the difference between the absolute k_{eff} estimates given by the two libraries, the trend of the curves is similar.

Figures B.13 and B.14 show the predicted k_{eff} versus the fuel axial expansion and the lead density variation, respectively. In these cases, the differences between COMSOL and SERPENT are greater than the previous case, but still acceptable for the preliminary evaluation of the coupled effects involving thermal-mechanical expansion in the fuel pin.

For brevity, only results obtained employing the nuclear data library is JEFF 3.1 are shown in the following.

Figures B.15 and B.16 show the total neutron fluxes calculated by the two codes versus the z-coordinate and their relative difference, respectively. As it can be seen in Fig. B.15, the flux profiles appear in good agreement. Figure B.16 shows that the difference between the flux computed by the COMSOL model and the SERPENT code is higher than the statistical uncertainty of the Monte Carlo run. The error in the COMSOL estimation is higher nearby the upper and lower interfaces. However, the maximum error is lower than 4%.

In conclusion, the adoption of the six-group diffusion approach in the MP model appears to be a reasonable approximation for analysing the ELSY single-channel.

B.3 Results and discussion

B.3.1 Steady state behaviour of the system

In this sub-section, the capability of the proposed MP model to evaluate, in the same computational environment, the most relevant variables of the coupled physics is ex-

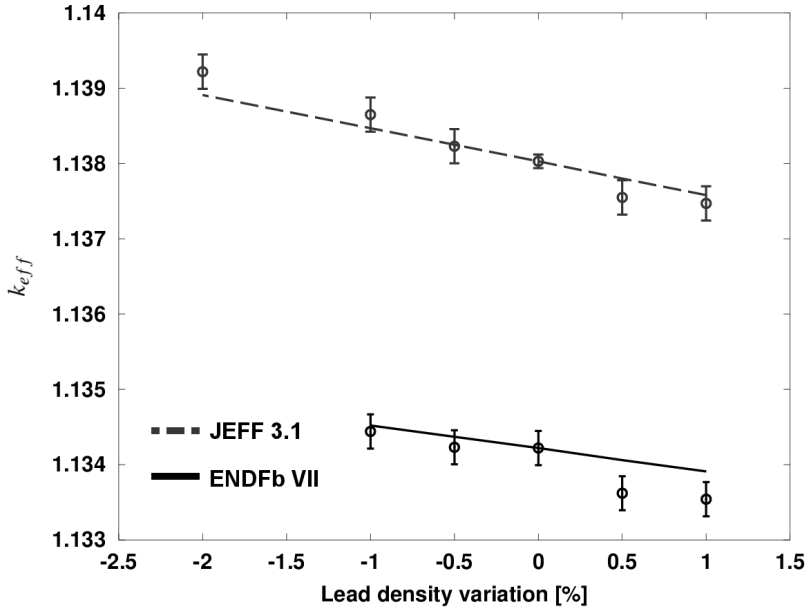

Figure B.14: *k_{eff} estimate versus lead density variation. SERPENT: bullets, COMSOL: lines.*

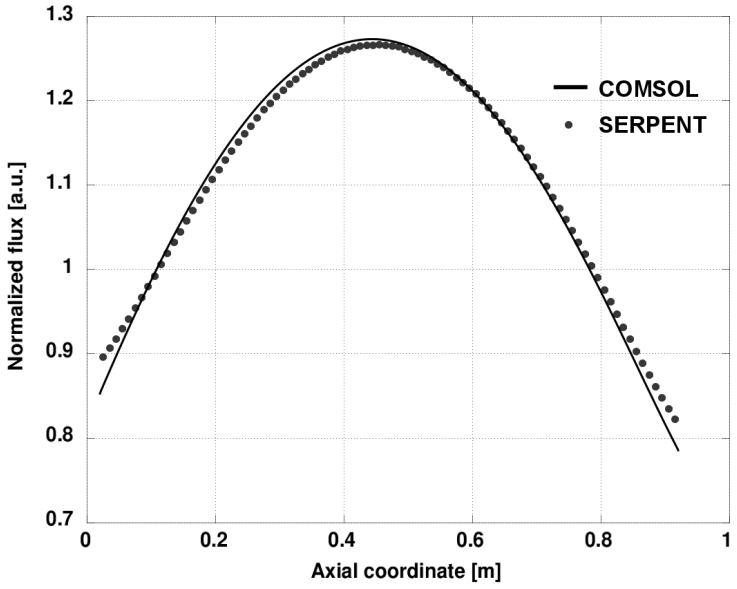

Figure B.15: *Axial neutron flux profiles within the active height. SERPENT: bullets, COMSOL: lines.*

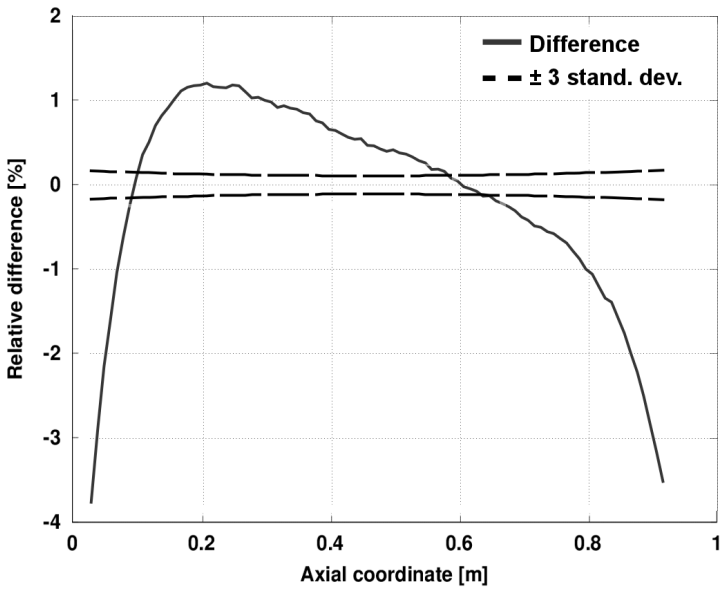

Figure B.16: *Relative difference between axial neutron fluxes computed by COMSOL and SERPENT.*

ploited to analyse the nominal steady-state behaviour of the system.

Figure B.17 shows the spatial descriptions of temperature field. The maximum fuel temperature is reached quite above the mid of the active height. The fuel temperature profile reflects the axial shape of the neutron flux. Nevertheless, a certain asymmetry in the temperature field is due to the heat transfer with the lead, whose temperature grows along the channel length. Figure B.18 shows the cladding outer temperature and lead bulk temperature versus the z-coordinate, at nominal power conditions, useful for a preliminary verification of the respect of the temperature constraint (about 550°C) . The maximum difference between the cladding outer surface temperature and the lead bulk temperature, of about 15°C, is reached at the mid active height ,where the neutron flux features its maximum value.

Figure B.19 shows results from the fluid-dynamic analysis, specifically, the velocity field in the lead domain. It can be noticed that the employed inactive inlet channel allows for the complete hydro-dynamic development of the fluid flow. It is worth recalling that the model is focused on the active height, and the modelling of the whole channel (e.g., lower plenum, diagrid, etc.) is beyond the aim of this work. The modelled inactive channel is only accounted for the proper lead flow development, in order to avoid a inaccurate estimation of the heat transfer between the lead and the cladding, within the first centimetres of the active height. The lead velocity at the wall is not zero in Fig. B.19, due to the wall function treatment available in COMSOL.

In Fig. B.20, the effects of the thermal expansions of fuel and cladding, leading axially to a different gap reduction, are clearly visible. The gap thermal resistance undergoes a sensible variation along the axial coordinate, being lower at the mid-height, where the power generation is higher. This is typically neglected when simulations are performed by means of the conventional coupling of neutronic and thermo-hydraulic codes (Bandini et al., 2011). Such figure presents an example of the potentialities provided by the fully-coupling between neutronics and thermal-elasticity.

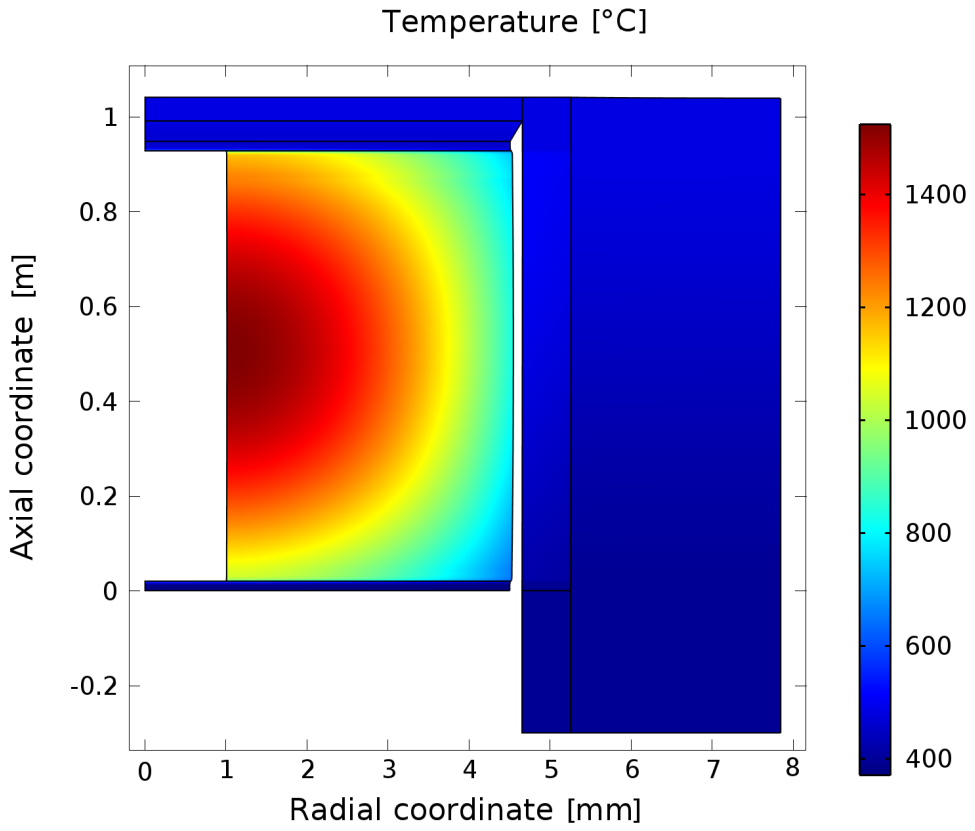

Figure B.17: *Channel temperature field at nominal power conditions.*

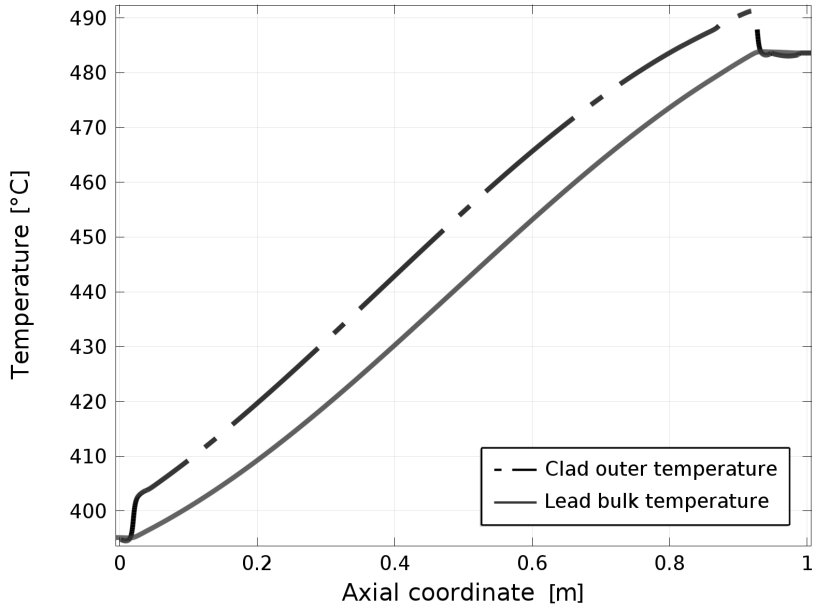

Figure B.18: *Cladding outer temperature and lead bulk temperature versus the z-coordinate, at nominal power conditions.*

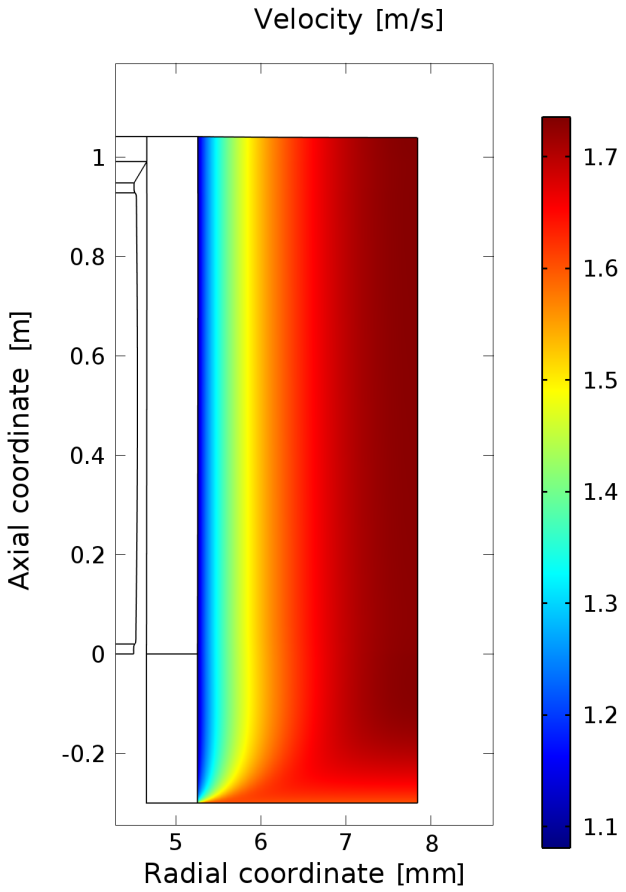

Figure B.19: *Velocity field inside the fluid domain.*

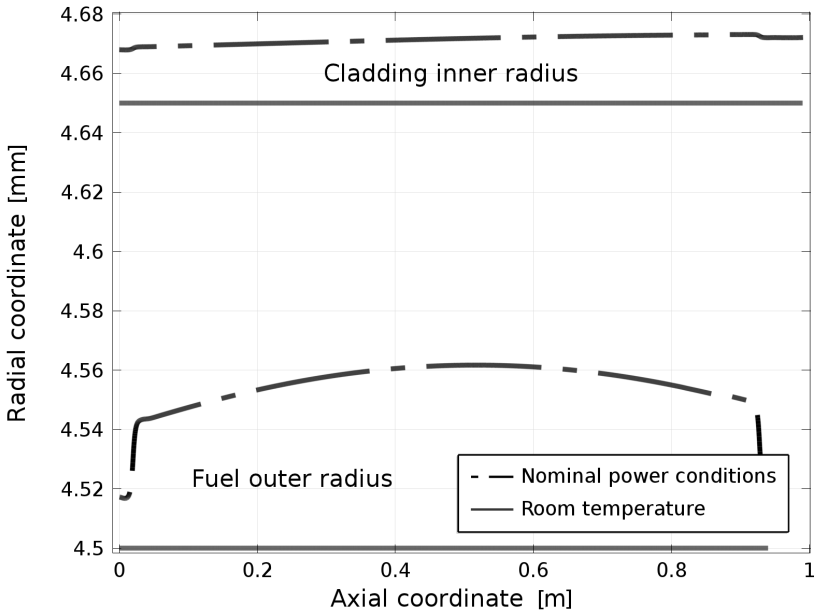

Figure B.20: *Outer fuel radius and inner cladding radius, as a function of the axial coordinate, at nominal power conditions and at room temperature conditions.*

B.3.2 Transient behaviour of the system

In this sub-section, two scenarios are considered as examples of the MPM potential to investigate the reactor transient behaviour, namely: an insertion of reactivity and a perturbed inlet lead temperature transient. For each of the two scenarios, transient analyses are performed both with and without thermal expansion effects. In the latter case, the displacement field is kept at nominal power conditions (i.e., not at room temperature conditions). This comparison allows to appreciate the importance of the thermal expansion modelling in transient analyses.

Reactivity insertion

A step-wise insertion of reactivity (150 pcm) is simulated. Figure B.21 shows the system response to the reactivity insertion in terms of total pin power. The solid line represents the simulation without considering the thermal expansion effects, while the dashed line represents the simulation in the presence of these effects. An insertion of reactivity leads to a k_{eff} greater than one. As a consequence, the power begins to rise, as shown in Fig. B.21, with a prompt effect on the fuel temperature (Fig. B.22), whose increase corresponds to a negative feedback limiting the power to a maximum value, which is almost two times the nominal value. The negative temperature feedback is given by two major contributions: the Doppler effect, and the thermal expansion effect. The first contribution acts on the neutron cross-sections and is taken into account as discussed in Section B.2. The thermal expansion feedback on neutronics is due to the reduction of the fuel-to-coolant mass ratio and is intrinsically modelled by the moving mesh technique. When considered, the axial expansion of the fuel gives further negative feedback, by lowering the maximum peak and the stationary power level, and the fuel temperature. When comparing the two analyses (with and without thermal expansion), notwithstanding that the Doppler effect plays the major role in limiting the power rise, the thermal effects lead to a sensible difference of the end-of-transient power levels.

Figure B.23 shows the fuel column (fuel and thermal insulators) relative axial expansion compared to the nominal power conditions. As expected, thermal expansion promptly follows the temperature rise. Thermal expansion also leads to an average gap size reduction of about 10%, as shown in Fig. B.24, reducing the overall gap thermal resistance by a similar value (in the present work, the helium thermal conductivity is kept constant).

Figure B.25 shows the cladding outer surface temperature at different instants during the reactivity insertion transient. Such insertion of 150 *pcm* (about 0.4 $) gives rise to an increase of about 40°C of the maximum cladding temperature in few seconds. This figure points out the potential of the MPM approach to describe in detail point-wise values of important quantities during transient analysis.

Perturbed inlet lead temperature

In this case study, t he inlet lead temperature is raised by 20°C in one second.

Figure B.26 shows the system response to the transient in terms of total pin power. Initially, a positive reactivity is inserted by the hot lead entering the channel, as effect of the lower lead density, which increases the fuel-to-coolant mass ratio. This causes a rise in the power level. After few seconds, the increase of the fuel temperature (Fig.

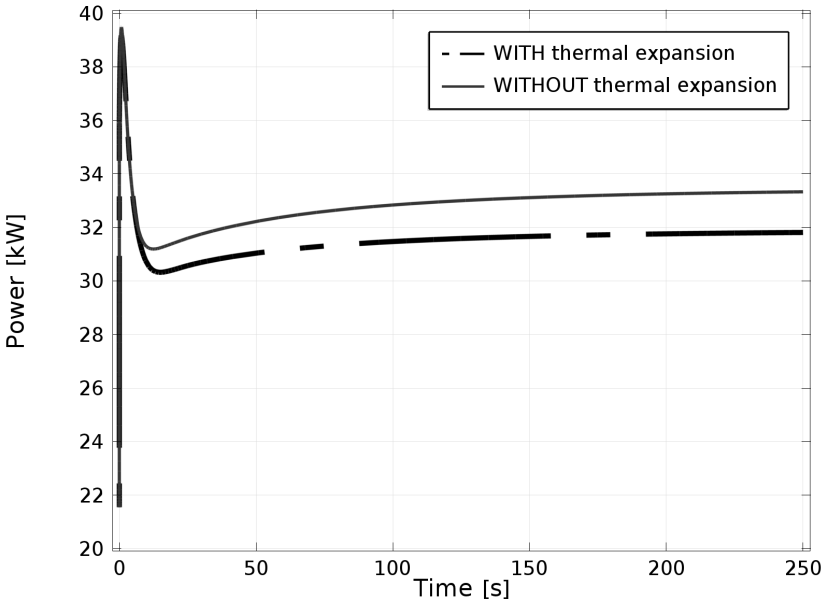

Figure B.21: *Total pin power during the transient case study with a reactivity insertion of 150* pcm.

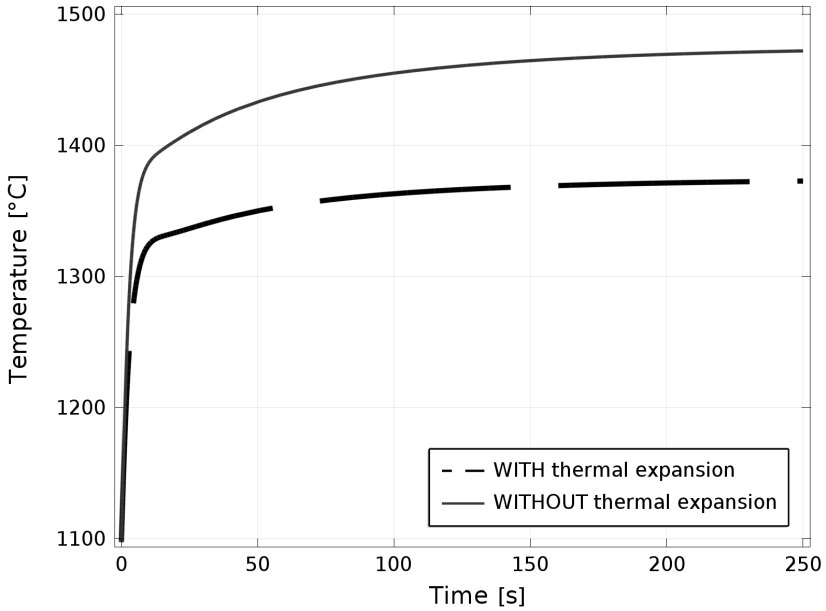

Figure B.22: *Average fuel temperature during the transient case study with a reactivity insertion of 150* pcm.

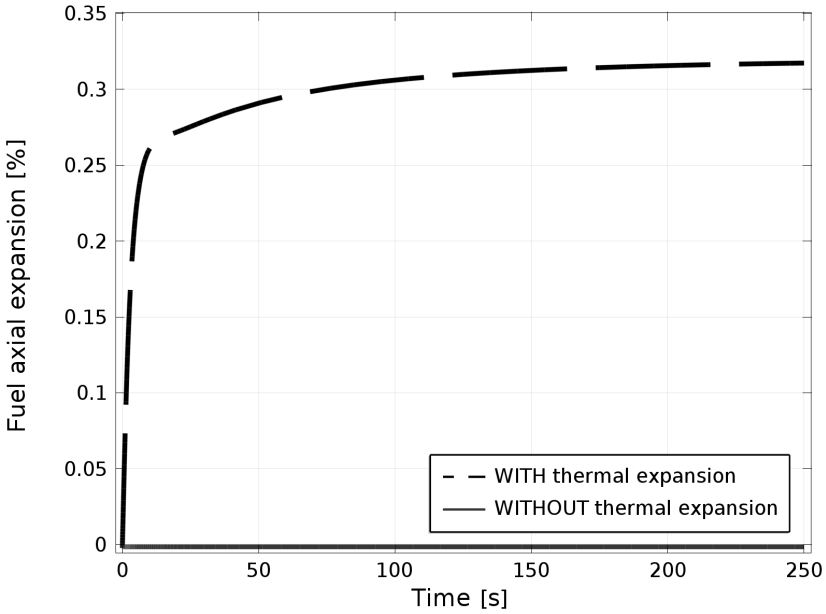

Figure B.23: *Fuel axial expansion during the transient case study with a reactivity insertion of 150* pcm.

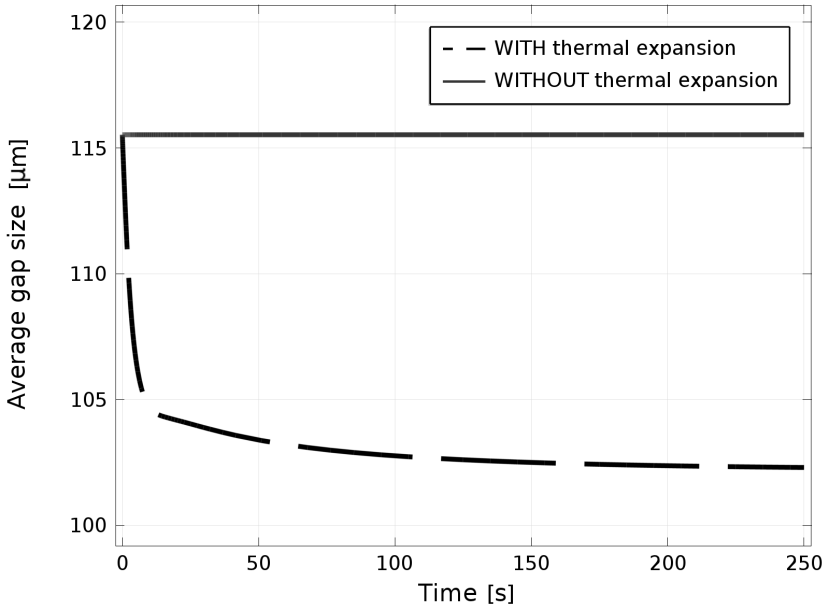

Figure B.24: *Average gap size during the transient case study with a reactivity insertion of 150* pcm.

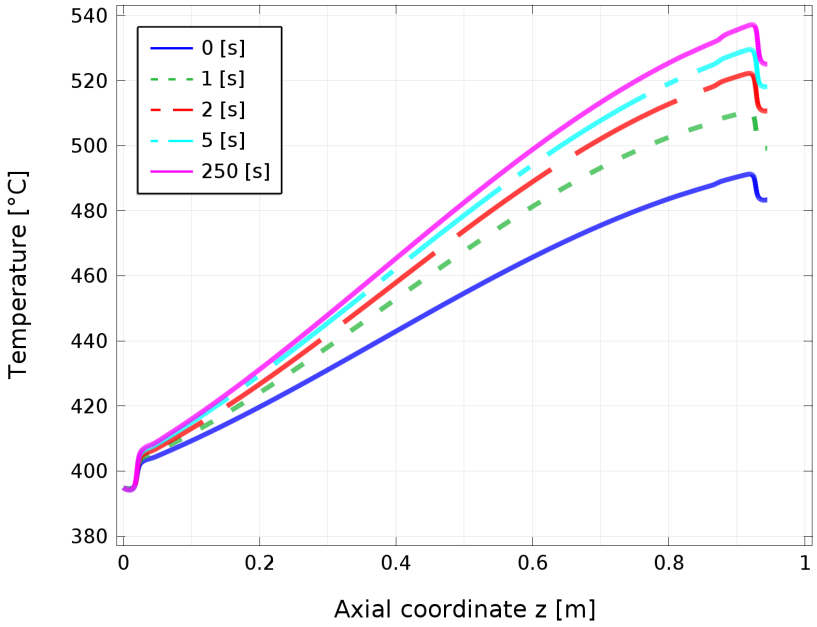

Figure B.25: *Axial profile of the cladding outer surface temperature during the transient case study with a reactivity insertion of 150* pcm.

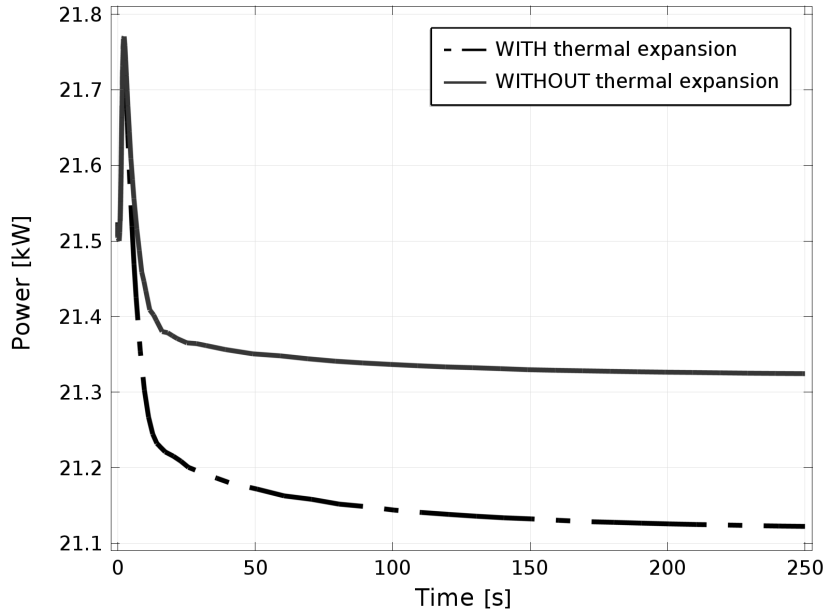

Figure B.26: *Total pin power during the transient case study with inlet lead temperature increase of 20°C.*

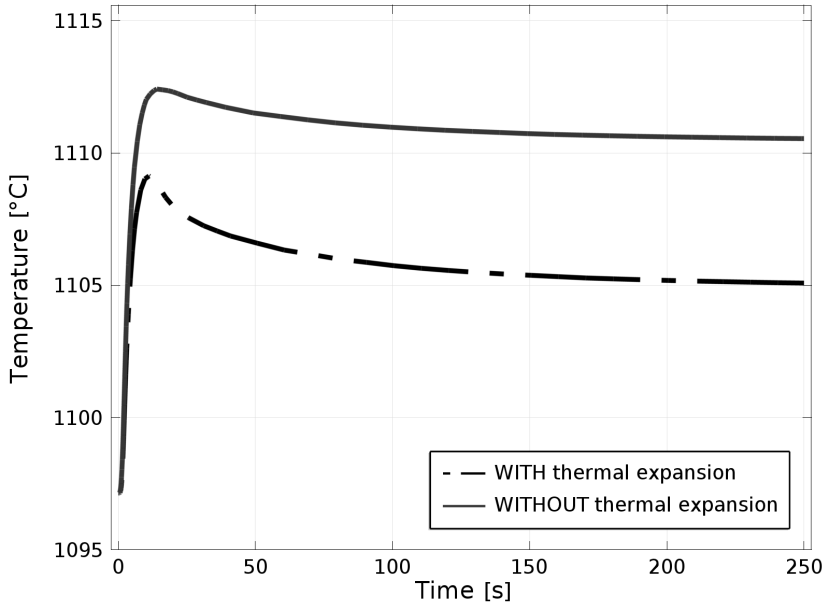

Figure B.27: *Average fuel temperature during the transient case study with inlet lead temperature increase of 20°C.*

B.27) smoothly reduces the reactivity and stabilises the power level to a value lower than the initial one.

Also in this transient, the fuel thermal expansion effects are significant (see Figs. B.26 and B.27): the final pin power level and the final fuel average temperature variations are reduced of about 0.2 kW ($\sim$ 50%) and 5°C ($\sim$ 60%), respectively, when compared to the simulation without considering the thermal expansion effects.

Figure B.28 shows the cladding outer surface temperature at different instants during the perturbed lead inlet temperature transient. The hotter coolant causes an increase of the cladding outer surface temperature at the beginning of the active height. The perturbation propagates along the z-axis with a delay related to the lead velocity (about 1.2 m/s) and the system thermal inertial. It is worth recalling that, in this work, the diagrid expansion is not simulated. This effect may play a significant role reducing the reactivity of the system (Sarotto et al., 2009).

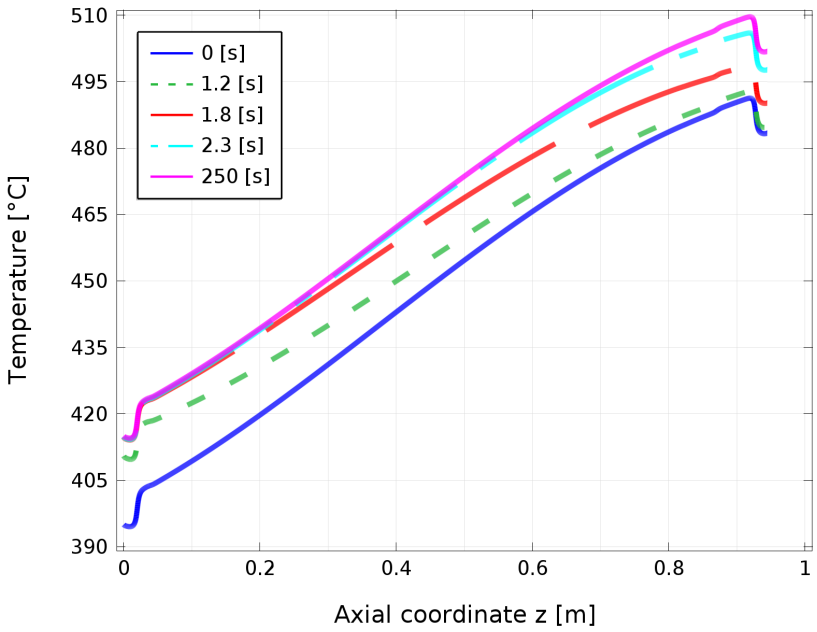

Figure B.28: *Axial profile of the cladding outer surface temperature during the transient case study with inlet lead temperature increase of 20°C.*

Appendix B Nomenclature

Latin symbols

$\mathbf{C}$	stifness tensor $[Pa]$
c_i	concentration of the i^{th} precursor group $[m^{-3}]$
C_p	specific heat $[J\ kg^{-1}\ K^{-1}]$
$C_{\varepsilon 1}$	$k-\varepsilon$ model empirical constant [-]
$C_{\varepsilon 2}$	$k-\varepsilon$ model empirical constant [-]
C_μ	$k-\varepsilon$ model empirical constant [-]
D	neutron diffusion coefficient $[m]$
E_f	average energy released per fission $[J]$
$\mathbf{I}$	identity matrix [-]
k	turbulent kinetic energy $[m^2\ s^{-2}]$
k_{eff}	effective neutron multiplication factor [-]
K	thermal conductivity $[W\ m^{-1}\ K^{-1}]$
K_T	lead turbulent thermal conductivity $[W\ m^{-1}\ K^{-1}]$
$\mathbf{n}$	surface normal unit vector [-]
p	fluid pressure $[Pa]$
p_{out}	outlet pressure $[Pa]$
Pr_T	turbulent Prandtl number [-]
Pr_{T_∞}	maximum turbulent Prandtl number defined in Eq. (B.12) [-]
Q	volumetric heat source $[W\ m^{-3}]$
$q(z)''$	radiative heat flux $[W\ m^{-2}]$
r	radial coordinate $[m]$
Re_∞	free stream Reynolds number used in Eq. (B.12) [-]
t	time $[s]$
T	temperature $[K]$
$T_{cladding}$	cladding inner surface temperature $[K]$
T_{fuel}	fuel outer surface temperature $[K]$
T_{in}	inlet lead temperature $[K]$
T_{ref}	reference temperature used in Eq. (B.19) $[K]$
T_0	reference temperature used in Eqs. (B.3) and (B.23) $[K]$
T_1	generic temperature used in Eq. (B.22) $[K]$
T_2	generic temperature used in Eq. (B.22) $[K]$
$\mathbf{u}$	displacement vector $[m]$
$\mathbf{v}$	velocity vector $[m\ s^{-1}]$
v_g	neutron speed of the g^{th} group $[m\ s^{-1}]$
v_{in}	inlet lead velocity $[m\ s^{-1}]$
x	Cartesian x-coordinate of the SERPENT model $[m]$
y	Cartesian y-coordinate of the SERPENT model $[m]$
z	axial coordinate $[m]$

Greek symbols

α_{th}	linear thermal expansion coefficient $[K^{-1}]$
α	coefficient used in Eq. (B.3) [-]
β	total delayed neutron fraction [-]
β_i	delayed neutron fraction of the i^{th} precursor group [-]
β_{lead}	volumetric lead thermal expansion coefficient $[K^{-1}]$
γ_r	radial albedo coefficient used in Eq. (B.21) [-]
γ_z	axial albedo coefficient used in Eq. (B.20) [-]
ε	turbulent dissipation rate $[m^2\ s^{-3}]$
$\varepsilon_{cladding}$	cladding inner surface emissivity [-]
ε_{fuel}	fuel outer surface emissivity [-]
$\boldsymbol{\epsilon}$	strain tensor [-]
η	lead dynamic viscosity $[Pa\ s]$
η_T	lead eddy viscosity (= $\rho C_\mu K^2/\varepsilon$) $[Pa\ s]$
λ_i	dacay constant of the i^{th} precursor group $[s^{-1}]$
ν	average number of neutrons emitted per fission [-]
ρ	density $[kg\ m^{-3}]$
ρ_0	reference density used in Eqs. (B.3), (B.4), and (B.23) $[kg\ m^{-3}]$
$\boldsymbol{\sigma}$	Cauchy stress tensor $[Pa]$
σ_B	Stefan Boltzmann constant $[W\ m^{-2}K^{-4}]$
σ_ε	$k-\varepsilon$ model empirical constant [-]
σ_k	$k-\varepsilon$ model empirical constant [-]
Σ	macroscopic cross-section $[m^{-1}]$
Σ_a	macroscopic absorption cross-section $[m^{-1}]$
Σ_f	macroscopic fission cross-section $[m^{-1}]$
$\Sigma_{s,gg'}$	macroscopic group transfer cross-section (from group g to g') $[m^{-1}]$
$\Sigma_{s,g'g}$	macroscopic group transfer cross-section (from group g' to g) $[m^{-1}]$
Σ_0	reference macroscopic cross-section used in Eqs. (B.3) and (B.4) $[m^{-1}]$
Σ_1	generic macroscopic cross-section used in Eq. (B.22) $[m^{-1}]$
Σ_2	generic macroscopic cross-section used in Eq. (B.22) $[m^{-1}]$
ϕ	neutron flux $[m^{-2}\ s^{-1}]$
$\chi_{d,g}$	fraction of delayed neutrons generated in the g^{th} group [-]
$\chi_{p,g}$	fraction of prompt neutrons generated in the g^{th} group [-]

Subscripts

g	g^{th} neutron energy group

APPENDIX C

A multi-physics reduced order model for the analysis of Lead Fast Reactor single channel[1]

In the previous Appendix B, the potential of Multi-Physics approach has been highlighted. However, the main drawback of the MP is that the computational burden is quite high, which may mean a long computational time. In a design process, it is often necessary to run again a simulation with just one or few parameters changed. Moreover, a process of optimization, employing the full order model, might be unfeasible. In this context, a *parametrized* MP model with *real-time* simulation could be an even more powerful tool for design-oriented studies.

In this work, the Reduced Basis method (Rozza et al., 2008; Quarteroni et al., 2011), with basis functions computed by a Proper Orthogonal Decomposition (POD) (Sirovich, 1987; Holmes et al., 1996; Chatterjee, 2000), has been employed to develop a reduced order model of a multi-physics parametrized LFR single-channel model, which is based on the work presented in Appendix B. The work focused on the methodological approach and to the coupling between the neutronics and heat transfer in time-invariant settings. In order to address the potential of such approach, two different kinds of parameters have been taken into account, namely one related to a *geometric* quantity (i.e., the inner radius of the fuel pellet) and one related to a *physical* quantity (i.e., the inlet lead velocity).

The capabilities of the presented ROM has been tested and compared with the high-fidelity finite element model (upon which the ROM has been constructed) on different aspects. In particular, the comparison focused on the system reactivity prediction (with and without thermal feedbacks on neutronics), the neutron flux and temperature field

[1] The main results and methodologies presented in this Appendix are contained in: Sartori, A., Cammi, A., Luzzi, L., Rozza, G., "A multi-physics reduced order model for the analysis of Lead Fast Reactor single channel. In preparation.

reconstruction, and on the computational time.

The Appendix is organized as follows. In Section C.1, the parametrized MP model is described and the essential ingredients of the RB methodology, employed in this work, are presented in Section C.2. In Section C.3, the results obtained by the developed reduced order model are compared with respect to the high-fidelity FE model. The adopted Nomenclature is reported at the end of the Appendix.

C.1 Parametrized multi-physics model

A parametrized LFR single channel model has been developed starting from the work detailed in Appendix B on page 93, where reference is made to the European Lead-cooled System (ELSY) (Alemberti et al., 2011). In particular, as shown in Fig. C.1 (for clarity, the aspect ratio of the image is not preserved), a $r - z$ model has been considered, where two varying parameters have been taken into account:

$$\mu_1 \in [0.1, 0.43] \quad (\text{cm}), \tag{C.1}$$

which is the inner radius of the fuel pellet, and the second parameter

$$\mu_2 \in [0.8, 1.6] \quad (\text{m/s}), \tag{C.2}$$

is the inlet lead velocity. This two parameters have been employed in order to address the potential of reduced order techniques including both a geometric and a physical parameter. The development of a detailed and exhaustive simulation tool for fuel pin design, where more parameters and physical phenomena are taken into account, is beyond the aim of the present contribution, which is focused on the methodological approach with some simplifications.

C.1.1 Multi-physics approach

The work focused on the coupling between neutronics and heat transfer, in time-independent settings, where thermal feedbacks on neutronics are explicitly taken into account relying on ad hoc expressions, whose validity has been addressed in (Aufiero et al., 2013). In the following equations, the dependence of neutron flux and temperature on the parameter $\mu = (\mu_1, \mu_2)$ has to be intended, but is not reported in order to not overburden the notation.

Neutronics

As far as the neutronics is concerned, the multi-group neutron diffusion equations (Duderstadt and Hamilton, 1976), in the stationary formulation, which is a generalized eigenvalue problem, have been employed with six energy groups. In equation it reads as follows:

$$\left(-\nabla \cdot \underline{\underline{D}} \nabla + \underline{\underline{\Sigma_a}} + \underline{\underline{\Sigma_s}}\right) \underline{\Phi} = \lambda_{\min} \underline{\chi} \underline{F}^T \underline{\Phi}, \tag{C.3}$$

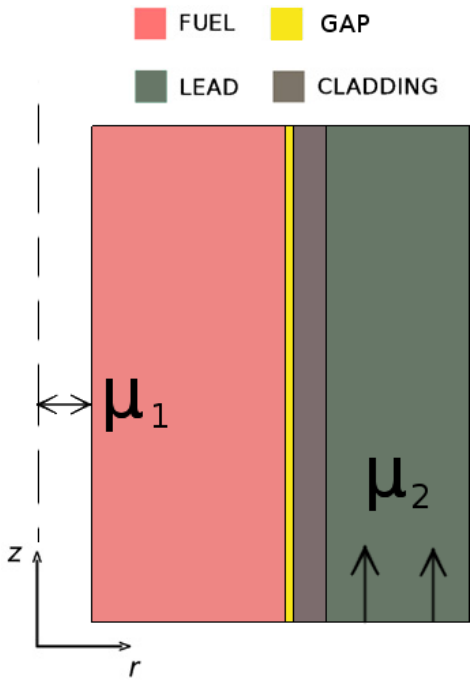

Figure C.1: *Longitudinal* (r, z) *view of the modelled geometry.*

where

$$
\begin{cases}
\underline{\Phi} = \begin{bmatrix} \Phi_1(\mathbf{r}) \\ \vdots \\ \Phi_6(\mathbf{r}) \end{bmatrix}, \\
\underline{\underline{D}} = \begin{bmatrix} D_1(\mathbf{r}) & \cdots & 0 \\ & \ddots & \\ 0 & \cdots & D_6(\mathbf{r}) \end{bmatrix}, \\
\underline{\underline{\Sigma_a}} = \begin{bmatrix} \Sigma_a^1(\mathbf{r}) & \cdots & 0 \\ & \ddots & \\ 0 & \cdots & \Sigma_a^6(\mathbf{r}) \end{bmatrix}, \\
\underline{\underline{\Sigma_s}} = \begin{bmatrix} \sum\limits_{g' \neq 1} \Sigma_s^{1 \to g'}(\mathbf{r}) & \cdots & -\Sigma_s^{6 \to 1}(\mathbf{r}) \\ & \ddots & \\ -\Sigma_s^{1 \to 6}(\mathbf{r}) & \cdots & \sum\limits_{g' \neq 6} \Sigma_s^{6 \to g'}(\mathbf{r}) \end{bmatrix}, \\
\underline{\chi} = \begin{bmatrix} \chi^1 \\ \vdots \\ \chi^6 \end{bmatrix}, \\
\underline{F}^T = \begin{bmatrix} \nu\Sigma_f^1(\mathbf{r}) & \cdots & \nu\Sigma_f^6(\mathbf{r}) \end{bmatrix}.
\end{cases}
\tag{C.4}
$$

The subscript 1 refers to the fastest group and 6 to the thermal one; Φ is the neutron flux, D is the diffusion coefficient, $\nu\Sigma_f$ are the number of neutrons emitted per fission reaction, Σ_a is the absorption cross section, $\Sigma_s^{i\to j}$ is the scattering cross section from group i to group j, χ is the fission yield. The neutronic parameters have been computed by means of the Monte Carlo SERPENT code (SERPENT, 2011) (see Appendix B on page 93). Within the fuel domain, the dependency of the macroscopic neutron cross sections on the local temperature and density is taken into account by means of the following expression (Aufiero et al., 2013):

$$\Sigma(T,\rho) = \frac{\rho}{\rho_0}\left[\Sigma_0 + \alpha \log\left(\frac{T}{T_0}\right)\right]. \tag{C.5}$$

For the lead cross sections, the above functional form is reduced to:

$$\Sigma(T,\rho) = \frac{\rho}{\rho_0}\Sigma_0, \tag{C.6}$$

neglecting the Doppler broadening effects. For the sake of simplicity, the cross sections are kept constant within the cladding and gap domains.

Heat transfer

As to the heat transfer modelling within the cladding and gap domains is considered, the following energy balance equation is adopted:

$$\nabla \cdot (K \nabla T) = 0, \tag{C.7}$$

with the corresponding values for the thermal conductivity. Within the helium gap, the model takes into account only the conductive contribution, neglecting the radiative contribution. In the fuel domain, the following equation is employed:

$$-\nabla \cdot (K \nabla T) = Q, \tag{C.8}$$

where the volumetric heat source Q is given by the calculated neutron fluxes:

$$Q = \sum_{g=1}^{6} \Sigma_f^g \cdot E_f \cdot \Phi_g \,. \tag{C.9}$$

The heat transfer within the lead domain is given by the following equation:

$$-\nabla \cdot [(K + K_T)\nabla T] = \rho C_p \mathbf{v} \cdot \nabla T, \tag{C.10}$$

where, for the sake of simplicity, a uniform velocity field has been assumed, and the lead turbulent thermal conductivity K_T has been retrieved from the work presented in Appendix B, where a standard RANS $k-\varepsilon$ has been implemented. In order to speed-up and simplify the calculations, effective and constant values of the thermo-physical properties C_p and K are adopted for the considered materials (MOX, Helium, T91 steel and lead).

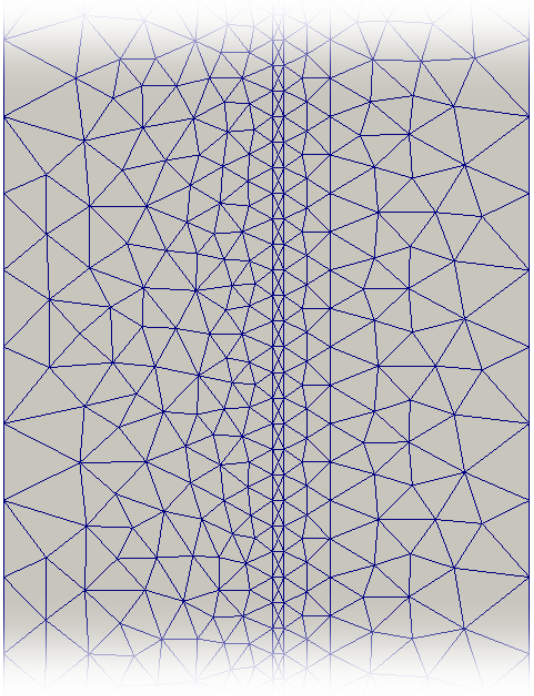

Figure C.2: *Meshed geometry.*

Boundary conditions

As far as the heat transfer modelling is concerned, the symmetry conditions are imposed at the inner radius of the fuel domain and at the outer radius of the fluid domain. Homogeneous Neumann conditions are imposed at the bottom and top of the domain.

The albedo boundary conditions (Duderstadt and Hamilton, 1976) have been employed for the neutron fluxes, leading to a good compromise between accuracy and computational requirements. In particular, the albedo boundary condition are imposed at the upper, lower and radial boundaries of the model domain, namely:

$$\mathbf{n} \cdot (D_g \nabla \Phi_g) = -\gamma_z \Phi_g \tag{C.11}$$

$$\mathbf{n} \cdot (D_g \nabla \Phi_g) = -\gamma_r \Phi_g \tag{C.12}$$

The γ_z and γ_r coefficients have been chosen in order to have the system critical at the nominal conditions.

Numerical simulations

The set of partial differential equations have been discretized according to the finite element method (Quarteroni and Valli, 2008), with linear-order Lagrangian elements. In Fig. C.2, the employed mesh is depicted, which features $60\,490$ elements.

The discrete equations have been solved within the computational environment offered by the open-source library `FEniCS` (Logg et al., 2012). In particular, a segregated approach for the neutronics and heat transfer has been employed, relying on the fixed point iteration for the non-linearities (Ortega and Rheinboldt, 2000). The generalized

eigenvalue problem has been solved relying on the `SLEPc` library (Hernandez et al., 2005), and the neutron flux has been normalized to the nominal power.

The reduced order model has been obtained relying on a procedure developed on purpose within the `FEniCS` library.

C.2 Reduced basis strategies for the coupled problem

In this Section, the fundamental mathematical aspects of the Reduced Basis (RB) method, used in the present work, are presented. More details about the RB methodology can be found in (Patera and Rozza, 2007; Rozza et al., 2008; Quarteroni et al., 2011; Rozza, 2014) and for particular application of the RB method to the generalized eigenvalue problem given by the multi-group neutron diffusion equation, the reader may refer to (Sartori et al., 2014c). Thereafter, the strategy employed in this work for achieve an efficient Offline/Online computational decoupling for handling non-linear terms will be presented.

The basic principle of a reduced order technique is to project a *parametrized* discrete the problem onto an *ad hoc* built space (the reduced space), which is spanned by basis functions that are *characteristic* of the studied problem.

C.2.1 Methodology

The RB method is built upon a fine approximation (i.e., finite element or finite volume), assumed as truth solution. Hence, let the finite element discretization of the considered multi-physics problem be the following: for a given $\mu \in \mathcal{D}$ find $\phi(\mu) \in V^{\mathcal{N}}$ and $T(\mu) \in W^{\mathcal{N}}$ such that

$$a\left(\phi, v; \mu, \Sigma(T)\right) = \lambda_{\min} m\left(\phi, v; \mu, \Sigma(T)\right), \quad \forall v \in V^{\mathcal{N}}, \tag{C.13}$$

$$d(T, w; \mu) = f\left(w; \mu, S(\phi)\right), \quad \forall w \in W^{\mathcal{N}} \tag{C.14}$$

where $V^{\mathcal{N}}$ and $W^{\mathcal{N}}$ are given finite element space of dimensions proportional to $\mathcal{N}$, which is typically very large. Eqs. (C.13) and (C.14) are the abstract formulations of the neutronic problem (C.3) and of the heat transfer problem, respectively. The term $\Sigma(T)$ is meant to underline that the neutronic flux ϕ is coupled with the temperature T by means of the cross sections. Similarly, the term $S(\phi)$ is to express that the volumetric heat source in the heat transfer equations is given by the neutron fluxes.

It is assumed that the operators a, m, d and f depend affinely on the parameter μ:

$$a\left(\phi, v; \mu, \Sigma(T)\right) = \sum_{q=1}^{Q_a} \Theta_a^q(\mu) a^q\left(\phi, v; \Sigma(T)\right), \tag{C.15}$$

$$m\left(\phi, v; \mu, \Sigma(T)\right) = \sum_{q=1}^{Q_m} \Theta_m^q(\mu) m^q\left(\phi, v; \Sigma(T)\right), \tag{C.16}$$

$$d(T, w; \mu) = \sum_{q=1}^{Q_d} \Theta_d^q(\mu) d^q(T, w), \tag{C.17}$$

$$f\left(w; \mu, S(\phi)\right) = \sum_{q=1}^{Q_f} \Theta_f^q(\mu) f^q\left(w; S(\phi)\right), \tag{C.18}$$

for given integers Q_a, Q_m, Q_d and Q_f.

The RB method is aimed at constructing reduced order solutions ϕ^{N_f} and T^{N_T} such that

$$a\left(\phi^{N_f}, v; \mu, \Sigma(T^{N_T})\right) = \lambda^N_{\min} m\left(\phi^{N_f}, v; \mu, \Sigma(T^{N_T})\right), \qquad \forall v \in V^{N_f} \subset V^{\mathcal{N}}, \tag{C.19}$$

$$d(T^{N_T}, w; \mu) = f\left(w; \mu, S(\phi^{N_f})\right), \qquad \forall w \in W^{N_T} \subset W^{\mathcal{N}}. \tag{C.20}$$

The reduced spaces V^{N_f} and W^{N_T} have dimension equal to N_f and N_T, respectively, (in general $N_f \neq N_T$) and are defined as follows:

$$V^{N_f} = \text{span}\left\{\xi^f_1, \cdots, \xi^f_{N_f}\right\}, \tag{C.21}$$

$$W^{N_T} = \text{span}\left\{\xi^T_1, \cdots, \xi^T_{N_T}\right\}, \tag{C.22}$$

where ξ^f and ξ^T are properly computed basis functions for the neutron flux and temperature, respectively. Therefore, the RB approximations ϕ^{N_f} and T^{N_T} can be expressed as a projection of the basis functions

$$\phi^{N_f} = \sum_{i=1}^{N_f} \phi_{N,i}\, \xi^f_i, \tag{C.23}$$

$$T^{N_T} = \sum_{j=1}^{N_T} T_{N,j}\, \xi^T_j. \tag{C.24}$$

Then, by denoting

$$\mathcal{Z}_f = [\xi^f_1 | \cdots | \xi^f_{N_f}], \tag{C.25}$$

$$\mathcal{Z}_T = [\xi^T_1 | \cdots | \xi^T_{N_T}], \tag{C.26}$$

the reduced order problems (C.19) and (C.20) can be rewritten as follows

$$a\left(\mathcal{Z}_f \boldsymbol{\phi}_N, v; \mu, \Sigma(\mathcal{Z}_T \mathbf{T}_N)\right) = \lambda^N_{\min} m\left(\mathcal{Z}_f \boldsymbol{\phi}_N, v; \mu, \Sigma(\mathcal{Z}_T \mathbf{T}_N)\right), \qquad \forall v \in V^{N_f}, \tag{C.27}$$

$$d(\mathcal{Z}_f \mathbf{T}_N, w; \mu) = f\left(w; \mu, S(\mathcal{Z}_f \boldsymbol{\phi}_N)\right), \qquad \forall w \in W^{N_T}, \tag{C.28}$$

where

$$\left(\boldsymbol{\phi}_N\right)_i = \phi_{N,i}, \tag{C.29}$$

$$\left(\mathbf{T}_N\right)_j = T_{N,j}. \tag{C.30}$$

It is now discussed the strategy employed in this work to achieve an efficient Offline/Online computational split for the considered multi-physics problem. For the sake of brevity, the discussion is limited to a representative term of the coupling between the neutronics and temperature in the bilinear forms $a^q\left(\phi, v; \Sigma(T)\right)$ and $m^q\left(\phi, v; \Sigma(T)\right)$, which can be formulated as follows:

$$c(T, \Phi, v) = \int_\Omega \Sigma(T)\, \Phi\, v \mathrm{d}\mathbf{x}, \tag{C.31}$$

where Σ is a generic cross section (e.g., absorption, scattering, fission) and Φ is the neutron flux[2]. The corresponding trilinear form of the RB approximation can be stated as follows:

$$c(T^{N_T}, \Phi^{N_f}, v) = \int_\Omega \Sigma(T^{N_T})\, \Phi^{N_f}\, v \mathrm{d}\mathbf{x}\,. \tag{C.32}$$

In the present work, it has been chosen to project Σ onto the reduced space spanned by the snapshots of the temperature, i.e.,

$$\Sigma(T^{N_T}) = \sum_{q=1}^{N_T} \sigma_q\, \xi_q^T\,. \tag{C.33}$$

Substituting Eq. (C.33) into (C.32), it follows that

$$\begin{aligned} c(T^{N_T}, \Phi^{N_f}, v) &= \int_\Omega \sum_{q=1}^{N_T} \sigma_q\, \xi_q^T\, \Phi^{N_f}\, v \mathrm{d}\mathbf{x} \\ &= \sum_{q=1}^{N_T} \sigma_q \int_\Omega \xi_q^T\, \Phi^{N_f}\, v \mathrm{d}\mathbf{x} \\ &= \sum_{q=1}^{N_T} \sigma_q\, c^q\left(\xi_q^T\right). \end{aligned} \tag{C.34}$$

In this way, the following third order tensors can be computed and stored during the Offline phase

$$C_N^q = \mathcal{Z}_f' C_{\mathcal{N}}^q \mathcal{Z}_f, \tag{C.35}$$

where $\mathcal{Z}_f$ is the vector of the basis functions of the neutron flux (see Eq. (C.25)), and $C_{\mathcal{N}}^q$ are the matrices associated to $c^q\left(\xi_q^T\right)$. It must be pointed out that such tensors may require high storage requirements. Different approaches could be pursued as well. For example, compressive tensor approximations (Carlberg et al., 2011) or hyper-reduction techniques, such as *gappy* POD (Carlberg et al., 2013), might be employed to alleviate this storage issue. It is worth mentioning that the non-linearities can be tackled by means of the Empirical Interpolation Method (Barrault et al., 2004) as well in order to recover an affine formulation (to allow Offline/Online computational decomposition).

C.3 Numerical results

In the following, the main results obtained both during the Offline and Online phases are presented.

C.3.1 Sampling

During the Offline phase, the RB space is built and the matrices associated to the algebraic formulation of the reduced order model are constructed and stored. The effectivity of the RB approximation relies on the RB space, which is spanned by the selected basis

[2]The actual type of cross section and the energetic group are not relevant for the purpose of this reasoning.

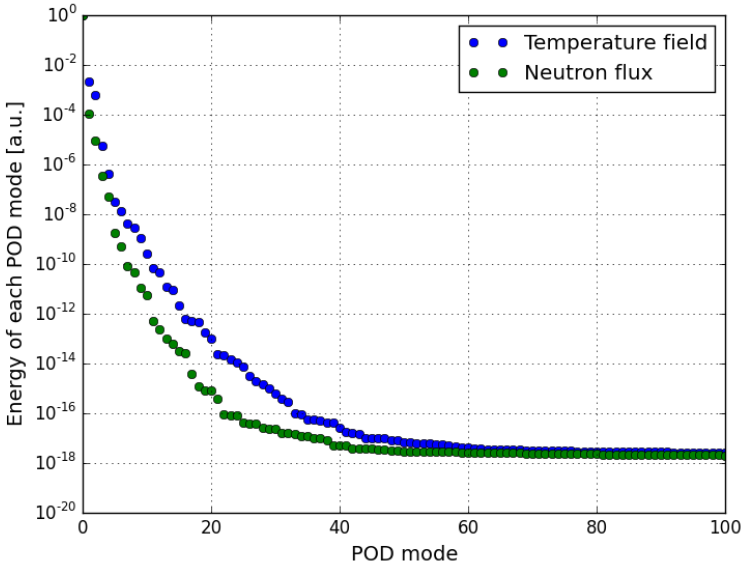

Figure C.3: *Energy of the POD modes.*

functions. For the present work, the full-order problem has been solved for 100 instances of the parameter $\mu = (\mu_1, \mu_2)$, which have been randomly chosen. During the iterative solution of the MP problem, 646 snapshots (i.e., solutions) have been stored. In order to eliminate redundancy from the vector of the snapshots, the Proper Orthogonal Decomposition (POD) (Sirovich, 1987; Holmes et al., 1996; Chatterjee, 2000) has been performed on it. In Fig. C.3, energy (i.e., the information retained) by each POD mode of temperature (blue dots) and neutron flux (green dots) is reported. As it can be seen in Fig. C.3, the energy of the POD modes of the temperature decreases slower than the modes of the neutron flux. Therefore, it is expected that a greater number of POD modes has to be employed for the temperature with respect to the neutron flux in order to have the same accuracy.

C.3.2 Reactivity prediction

The POD technique build a set of modes whose importance is decreasing, meaning that the accuracy of the reduced order model is expected to improve as functions of the number of POD modes employed, and the rate of improvement is decreasing. However, the energy of the POD modes refers to the information present in the vector of the snapshots, not to the whole parameter space. Therefore, a sensitivity on the error as function of the number of POD modes employed has to be performed. Since the energy of the POD modes of neutron flux decreases more rapidly than the modes of temperature, the first sensitivity has been performed by studying the average error on the minimum eigenvalue of Eq.(C.3), *without* the thermal feedbacks. The error between the value of the reactivity provided by the ROM and FE solution $e_\lambda(\mu)$ has been computed as it follows:

$$e_\lambda(\mu) = |\lambda_N(\mu) - \lambda_{\mathcal{N}}(\mu)|, \tag{C.36}$$

Table C.1: *Average absolute error $e_\lambda(\mu)$ as function of the basis functions employed for the neutron flux N_f, without thermal feedbacks. Values have been computed for 100 samples, randomly chosen.*

# basis functions N_f	$e_\lambda(\mu)$
2	1.286×10^{-2}
3	9.936×10^{-3}
4	1.088×10^{-3}
5	9.227×10^{-4}
10	1.097×10^{-4}
14	8.887×10^{-6}

Table C.2: *Average absolute error $e_\lambda(\mu)$ as function of the basis functions employed for the temperature N_T, taking into account the thermal feedbacks. Values have been computed for 100 samples, randomly chosen, and employing 14 basis functions for the neutron flux.*

# basis functions N_T	$e_\lambda(\mu)$
2	2.688
3	8.694×10^{-1}
10	7.499×10^{-4}
14	4.241×10^{-5}
20	2.652×10^{-5}

where $\lambda_N(\mu)$ and $\lambda_\mathcal{N}(\mu)$ is the minimum eigenvalue of the ROM and FE model, respectively. In Table C.1, the average absolute error $e_\lambda(\mu)$ is reported as function of the number of basis functions N_f employed for the neutron flux. Values have been computed for 100 instances of the parameter μ_1. The average error drops below the pcm when 14 basis functions are employed. If the number of POD modes is further increased, the average error does not decrease anymore. In order to improve the accuracy, the number of snapshots retained should be increased. As an alternative, different sampling technique could be taken into account, such as Centroidal Voronoi Tessellation (Burkardt et al., 2006; Sartori et al., 2014c), or by means of a greedy algorithm (Haasdonk and Ohlberger, 2008; Rozza et al., 2008; Nguyen et al., 2009; Quarteroni et al., 2011) provided that an efficient *a posteriori* error bound is available.

The sensitivity study on the number of basis functions for the temperature field is performed employing 14 basis functions for the neutron flux. In particular, the error $e_\lambda(\mu)$ is computed *taking into account* the thermal feedbacks given by Eq. (C.5) and (C.6). For this analysis, 100 randomly chosen instances of the parameter $\mu = (\mu_1, \mu_2)$ have been considered. The average absolute error $e_\lambda(\mu)$ as function of the basis functions employed for the temperature N_T is reported in Table C.2. When 20 basis functions for the temperature are employed, the average error is of the order of pcm. Further increasing the number of basis functions there is no appreciable reduction of the error.

C.3.3 Neutron flux shape reconstruction

The neutron fluxes provided by both the high-fidelity FE model and the developed ROM have been compared for two different instances of the parameter $\mu = (\mu_1, \mu_2)$ taking into account the thermal feedbacks. In particular, 14 and 20 basis functions have been employed for the neutron flux and temperature, respectively. In Figs. C.4 and C.5, the normalized neutron flux provided by the high-fidelity FE model and the ROM is depicted, as well as the spatial error between the two solutions for $\mu = (0.146, 1.445)$

and $\mu = (0.387, 1.466)$, respectively. The outcomes provided by the ROM are in good agreement with the FE ones, and the spatial error is almost uniform throughout the computational domain.

C.3.4 Temperature field reconstruction

In the following, the capabilities of the ROM for the reconstruction of the temperature field are presented for two randomly selected instances of $\mu = (\mu_1, \mu_2)$. For this analysis, 14 and 20 basis functions have been employed for the neutron flux and temperature, respectively. In Figs. C.6 and C.7, the temperature field provided by the high-fidelity FE model and the ROM is depicted, as well as the spatial error between the two solutions for $\mu = (0.366, 1.188)$ and $\mu = (0.144, 1.137)$, respectively. The outcomes provided by the two models (i.e., the FE and ROM) are in satisfactory agreement. The error is greater within the fuel domain because the equations are more involved in such computational domain with respect to the clad and lead domains.

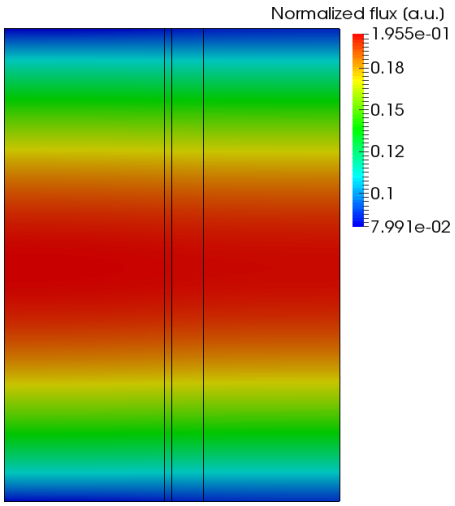

(a) *"Truth"*

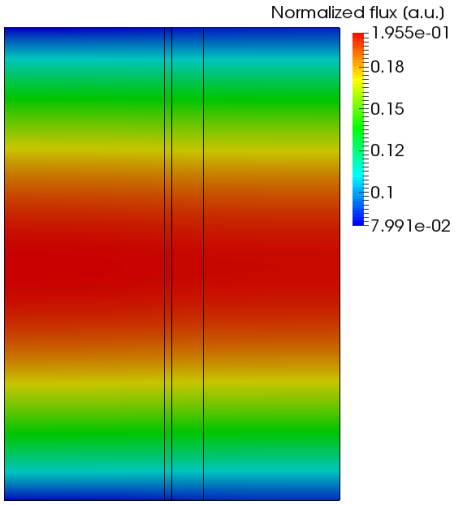

(b) *ROM*

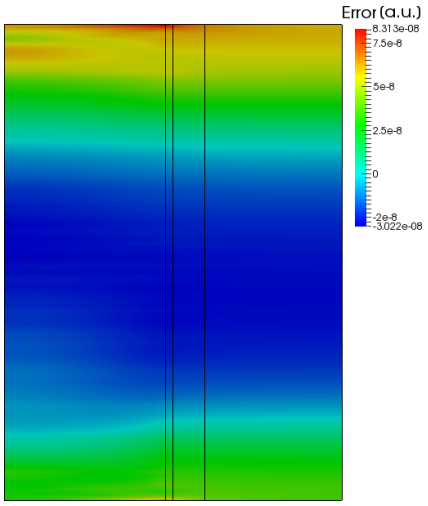

(c) *Error*

Figure C.4: *Normalized neutron flux provided by the FE model (a), by the ROM (b), and the spatial error (c) for a representative configuration* $\mu = (0.146, 1.445)$.

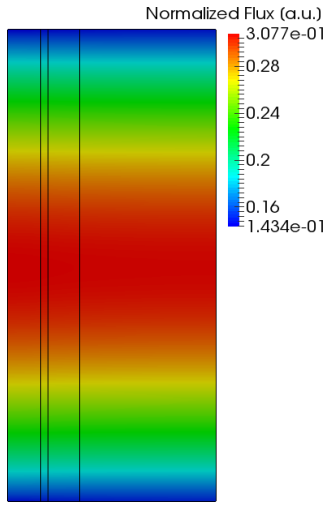

(a) *"Truth"*

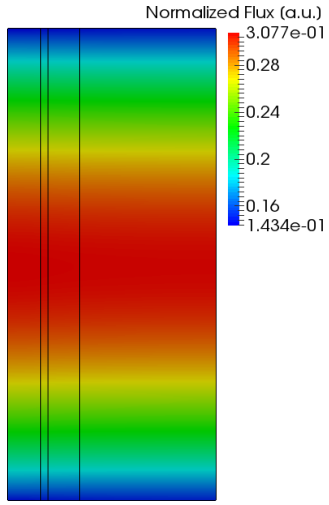

(b) *ROM*

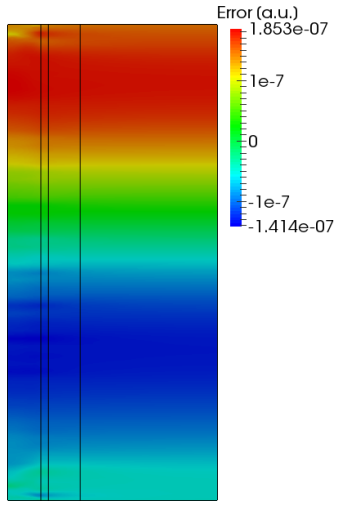

(c) *Error*

Figure C.5: *Normalized neutron flux provided by the FE model (a), by the ROM (b), and the spatial error (c) for a representative configuration* $\mu = (0.387, 1.466)$.

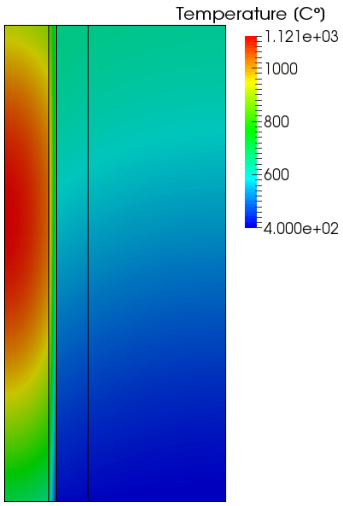

(a) *"Truth"*

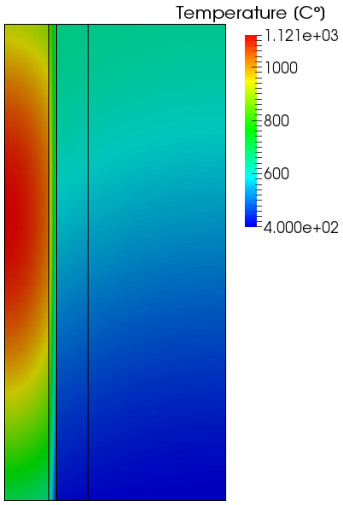

(b) *ROM*

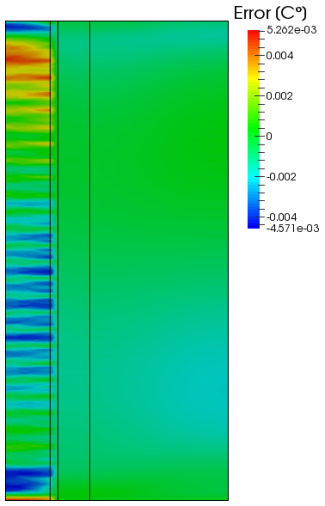

(c) *Error*

Figure C.6: *Temperature field provided by the FE model (a), by the ROM (b), and the spatial error (c) for a representative configuration* $\mu = (0.366, 1.188)$.

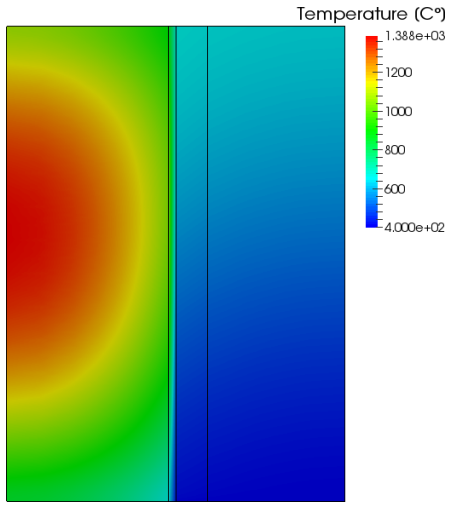

(a) *"Truth"*

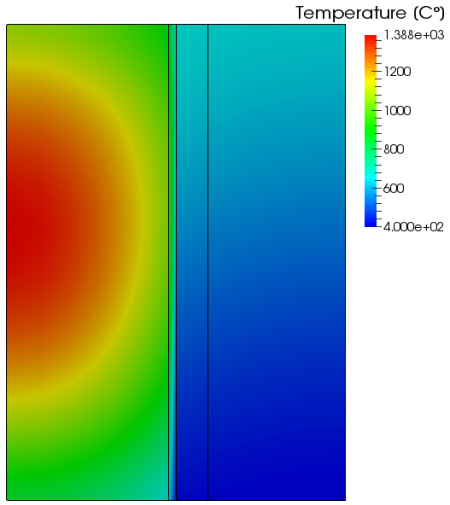

(b) *ROM*

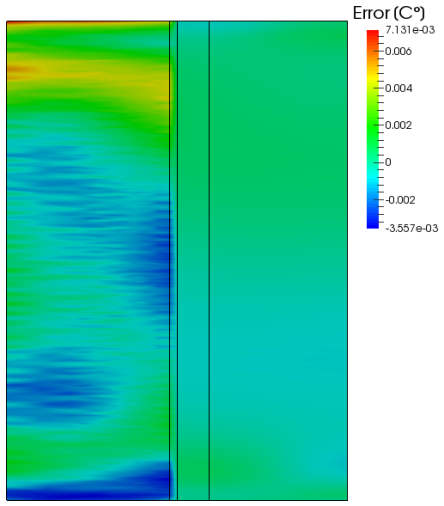

(c) *Error*

Figure C.7: *Temperature field provided by the FE model (a), by the ROM (b), and the spatial error (c) for a representative configuration* $\mu = (0.144, 1.137)$.

Table C.3: *Average computational time and speed-up.*

	Computational time		
Plot	Finite Element	ROM	Speed-up
NO	$\sim$60 min	$\sim$0.3 s	$\sim$ 11 800
YES	$\sim$60 min	$\sim$2.3 s	$\sim$ 1500

C.3.5 Speed test

The average computational time required to solve the multi-physics problem according to the high-fidelity FE model and to the ROM is reported in Table C.3. The proposed model allows a computational time of at least three orders of magnitude. It is worth recalling that the reduced order model is mesh-independent if no plot are required. Whether plots are produced, the mesh size has to be taken into account, therefore the performance is different.

Moreover, for the sake of completeness, it must be introduced the computational break-even, i.e., the number of full order simulations after that the RB method is more efficient and recommended. The break-even can be defined as follows[3]:

$$\text{break-even} = \frac{\text{Whole Offline time}}{\text{Time of one FE simulation}} = \frac{\sim 101\,\text{h}}{\sim 1\,\text{h}} = 101\,.$$

Therefore, if more than 101 full-order simulations have to be computed, the reduced order model should be preferred.

C.4 Concluding remarks and perspectives

In this Appendix, the reduced basis method, with basis functions computed by a proper orthogonal decomposition, has been employed to develop a reduced order model of a multi-physics parametrized LFR single channel. This model is proposed as proof of concept to address the potential of reduced order techniques in a many-query context. The work focused on the methodological approach and to the coupling between neutronics and heat-transfer phenomena in time-invariant settings, where a particular strategy for achieve a competitive Offline/Online computational split is developed. As far as the parametrized model is concerned, two different kinds of parameters have been taken into account, namely one related to a *geometrical* quantity (i.e., the inner radius of the fuel pellet) and one related to a *physical* quantity (i.e., the inlet lead velocity).

The capabilities of the proposed reduced order model has been tested and compared with the high-fidelity finite element model (upon which the reduced order model has been constructed) on several aspects. In particular, the comparison focused on the system reactivity prediction (with and without thermal feedbacks on neutronics), the neutron flux and temperature field reconstruction, as well as on the computational time. According to such analysis, the presented reduced order model is capable to provide outcomes as accurate as the high-fidelity finite element model, employing 14 and 20 basis functions for the neutron flux and temperature, respectively. The reactivity is correctly predicted up to the order of the pcm. In addition, the reduced order model fosters a computational speed-up of at least three orders of magnitude.

[3] The hours are to be intended as *cpu* hours, not "*real world time*" hours.

The present contribution is a first step towards a more detailed and complex simulation tool for design-oriented studies (e.g., sensitivity, optimization, shaping, etc.) of innovative nuclear reactor concepts. To this aim, the coupling with the thermo-elasticity, as well as the adoption of a more dedicated turbulence model (e.g., $k-\omega$) are foreseen. Different techniques for handling the non-linearities, such as the Empirical Interpolation Method, might be considered as well. The extension to the time-dependent settings could give important insights for accidental scenarios.

Appendix C Nomenclature

Latin symbols

C_p	specific heat [$J\ kg^{-1}\ K^{-1}$]
D	neutron diffusion coefficient [m]
E_f	average energy released per fission [J]
K	thermal conductivity [$W\ m^{-1}\ K^{-1}$]
K_T	lead turbulent thermal conductivity [$W\ m^{-1}\ K^{-1}$]
$\mathbf{n}$	surface normal unit vector [-]
Q	volumetric heat source [$W\ m^{-3}$]
r	radial coordinate [m]
T	temperature [K]
T_0	reference temperature used in Eq. (C.5) [K]
u	generic trial function [-]
$\mathbf{v}$	velocity vector [$m\ s^{-1}$]
v	generic test function [-]
w	generic trial function [-]
$\mathbf{x}$	generic vector of spatial coordinates [(m, m)]
V	generic Hilbert space for the neutron fluxes [-]
W	generic Hilbert space for the temperature [-]
z	axial coordinate [m]

Greek symbols

α	coefficient used in Eq. (C.5) [-]
γ_r	radial albedo coefficient used in Eq. (C.12) [-]
γ_z	axial albedo coefficient used in Eq. (C.11) [-]
Θ^q	generic coefficient of the q^{th} term [-]
λ	eigenvalue associated to Eq. C.3 [-]
μ	vector of parameters $[m, m/s]$
μ_1	varying parameter: inner fuel radius $[m]$
μ_2	varying parameter: inlet lead velocity $[m/s]$
ν	average number of neutrons emitted per fission [-]
ξ	generic basis function [-]
ρ	density $[kg\ m^{-3}]$
ρ_0	reference density used in Eqs. (C.5) and (C.6) $[kg\ m^{-3}]$
σ_q	generic coefficient of the q^{th} term [-]
Σ	macroscopic cross section $[m^{-1}]$
Σ_a	macroscopic absorption cross section $[m^{-1}]$
Σ_f	macroscopic fission cross section $[m^{-1}]$
$\Sigma_s^{g\to g'}$	macroscopic group transfer cross section (from group g to g') $[m^{-1}]$
Σ_0	reference macroscopic cross section used in Eqs. (C.5) and (C.6) $[m^{-1}]$
ϕ	weak solution of neutron flux $[m^{-2}\ s^{-1}]$
Φ	neutron flux $[m^{-2}\ s^{-1}]$
χ^g	fraction of prompt neutrons generated in the g^{th} group [-]
ψ	generic test function [-]
Ω	generic spatial domain $[m^2]$

Subscripts / superscripts

$'$	transpose
f	reference to neutron flux
g	g^{th} neutron energy group
N	reference to the reduced order model
N^f	reference to the reduced order model of neutron flux
N^T	reference to the reduced order model of temperature
$\mathcal{N}$	reference to the full order model
T	reference to the temperature field

APPENDIX $\mathcal{D}$

Algorithms and benchmarks

During the PhD work, an implementation of the certified reduced basis method has been developed within the computational environment offered by the open-source finite element library `FEniCS`. Such procedure has been tested on different problems, whose solutions are either known or easily benchmarkable beside being non-trivial.

It is worth mentioning that the developed procedure has begun to be used for teaching purposes within the SISSA doctoral programme Mathematical Analysis, Modelling and Applications (AMMA), as well as within the Master in High Performance Computing held by SISSA and ICTP.

D.1 Heat transfer: thermal block

D.1.1 Parametrized formulation

The strong formulation of this parametrized problem is given by: for some parameter $\mu \in \mathbb{P}$, find $u(\mu)$ such that

$$\begin{cases} \nabla \cdot k_\mu \nabla u(\mu) = 0 & \text{in } \Omega, \quad \text{(D.1)} \\ u(\mu) = 0 & \text{on } \Gamma_{\text{top}}, \quad \text{(D.2)} \\ k_\mu \nabla u(\mu) \cdot n = 0 & \text{on } \Gamma_{\text{side}}, \quad \text{(D.3)} \\ k_\mu \nabla u(\mu) \cdot n = \mu_2 & \text{on } \Gamma_{\text{base}}. \quad \text{(D.4)} \end{cases}$$

The output of interest $s(\mu)$ is computed as

$$s(\mu) = \mu_2 \int_{\Gamma_{\text{base}}} u(\mu). \quad \text{(D.5)}$$

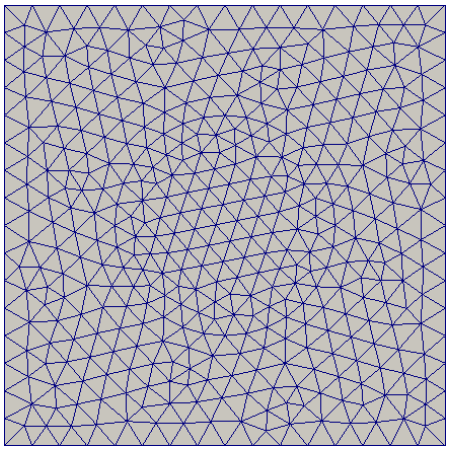

Figure D.1: *Finite element mesh.*

D.1.2 Finite element model

The Finite Element method, employing P1 elements, has been chosen as the "truth" model. In Fig. D.1 is reported the mesh, which features 812 elements. The chosen ranges for the parameters are

$$\mu_1 \in [0.1, 10] \tag{D.6}$$

$$\mu_2 \in [-1, 1] \tag{D.7}$$

D.1.3 Basis functions selection

The basis functions have been obtained by orthogonalization, through a Gram-Schimdt procedure, of snapshots computed for greedly selected parameters spanning a Ξ_{train} with cardinality equal to 6500. In Fig. D.2 the graph showing the maximum absolute error bound with respect to the number of basis functions employed is reported.

In Fig. D.3, the first four snapshots are depicted.

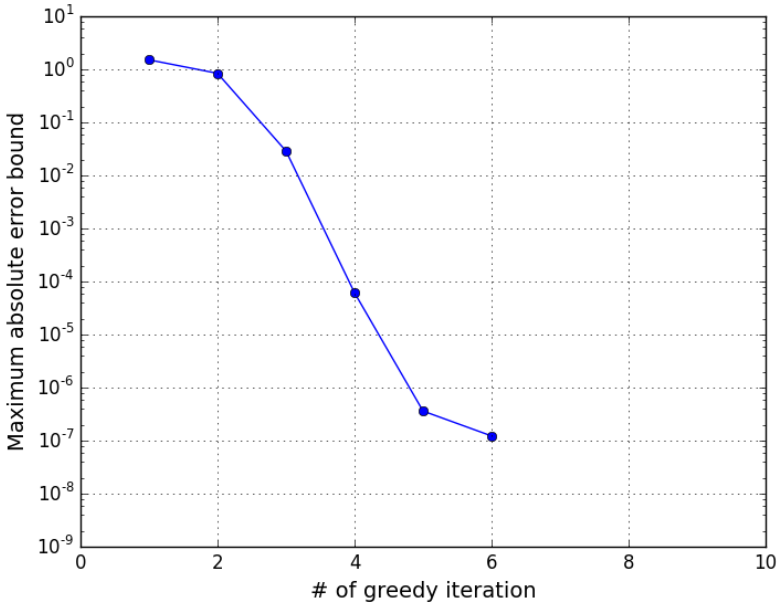

Figure D.2: *Maximum absolute error bound with respect to the number of basis functions employed.*

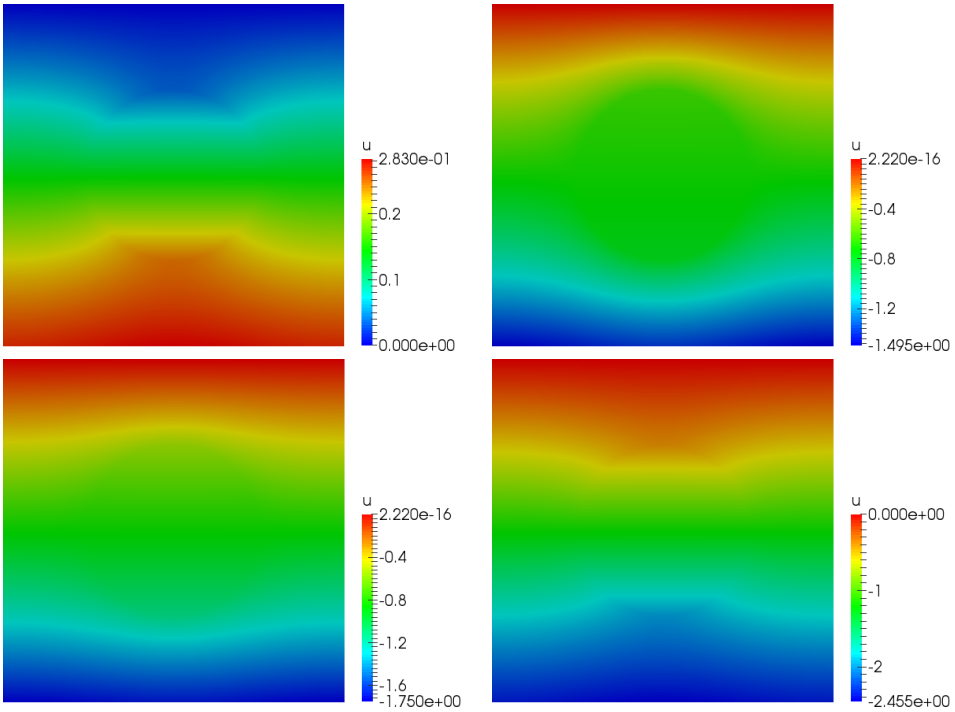

Figure D.3: *First four basis functions.*

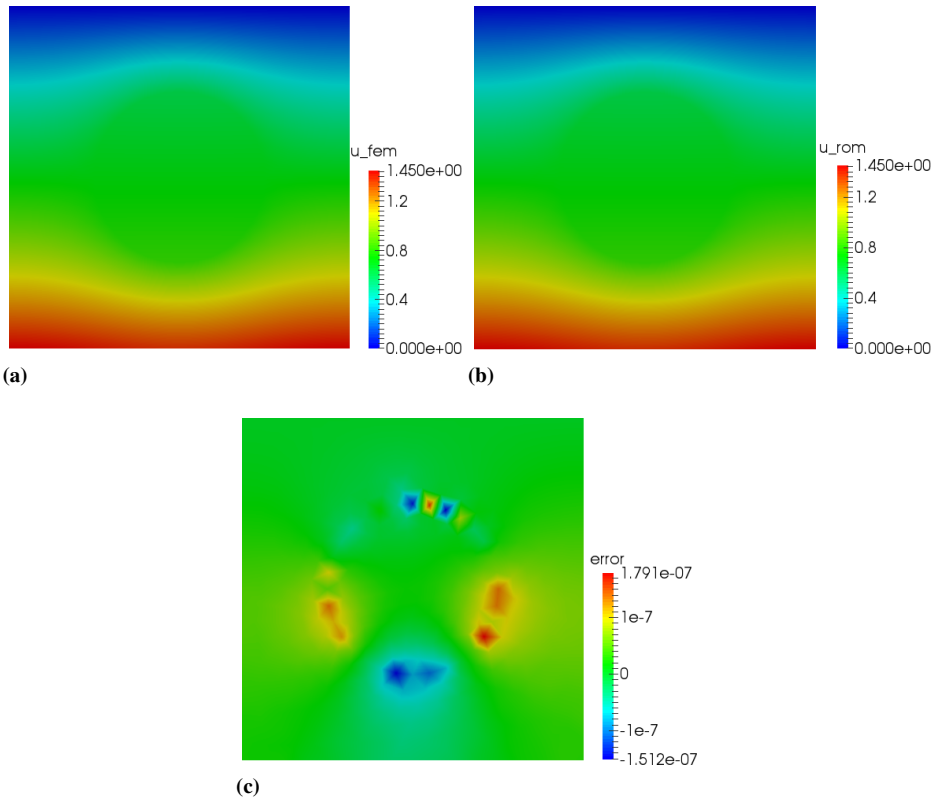

(a) (b) (c)

Figure D.4: *Comparison between FE model (a), ROM (b) for* $\mu = (6.68, 0.94)$. *The difference between the two solutions is reported in (c).*

Table D.1: *Output error bounds and effectivity metrics as function of* N.

N	$\Delta^s_{N,\text{ave}}$	$\eta^s_{N,\max}$	$\eta^s_{N,\text{ave}}$
2	0.68	5.22	1.59
3	4.85×10^{-5}	5.35	2.98
4	1.33×10^{-9}	5.22	2.96
5	1.41×10^{-12}	54.16	3.73

D.1.4 ROM performances

In Fig. D.4, the outcomes provided by the FE model and the ROM, for a randomly chosen $\mu = (6.68, 0.94)$ and $N = 5$, are compared, and the difference between the two is plotted as well.

In Tab. D.1 the output error bounds and effectivity metrics as function of basis functions employed are presented. The values have been averaged over 100 samples.

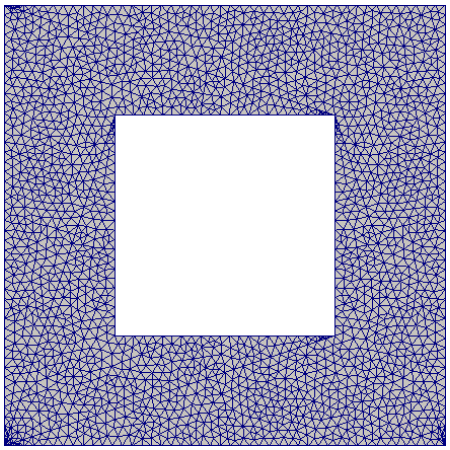

Figure D.5: *Finite element mesh.*

D.2 Heat transfer: thermal block with a parametrized hole

D.2.1 Parametrized formulation

The bilinear form associated to the left-hand-side of the problem is given by:

$$a_o(w, v; \mu) = \int_{\Omega_o(\mu)} \nabla w \cdot \nabla v + \mu_3 \left(\int_{\Gamma_{o,5}} w\, v + \int_{\Gamma_{o,6}} w\, v + \int_{\Gamma_{o,7}} w\, v + \int_{\Gamma_{o,8}} w\, v \right). \tag{D.8}$$

A constant heat flux is imposed on the interior walls and in equation it reads:

$$F_o(v) = \int_{\Gamma_{o,1}} v + \int_{\Gamma_{o,2}} v + \int_{\Gamma_{o,3}} v + \int_{\Gamma_{o,4}} v. \tag{D.9}$$

The output of interest $s_o(\mu)$ is computed as

$$s_o(\mu) = F_o(u(\mu)). \tag{D.10}$$

D.2.2 Finite element model

The Finite Element method, employing P1 elements, has been chosen as the "truth" model. In Fig. D.5 the mesh of the reference domain is reported, and features 4136 elements. The RB triangulation of the reference domain is depicted in Fig. D.6.

D.2.3 Basis functions selection

The basis functions have been obtained by orthogonalization, through a Gram-Schimdt procedure, of snapshots computed for greedly selected parameters spanning a Ξ_{train} with cardinality equal to 3000. In Fig. D.7 the graph showing the maximum absolute error bound with respect to the number of basis functions employed is reported.

In Fig. D.8, the first four snapshots are depicted.

Figure D.6: *RB triangulation.*

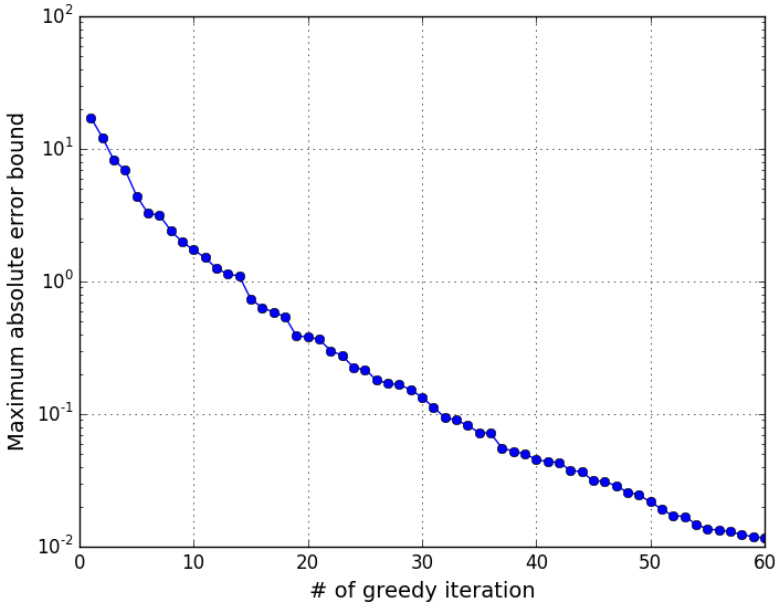

Figure D.7: *Maximum absolute error bound with respect to the number of basis functions employed.*

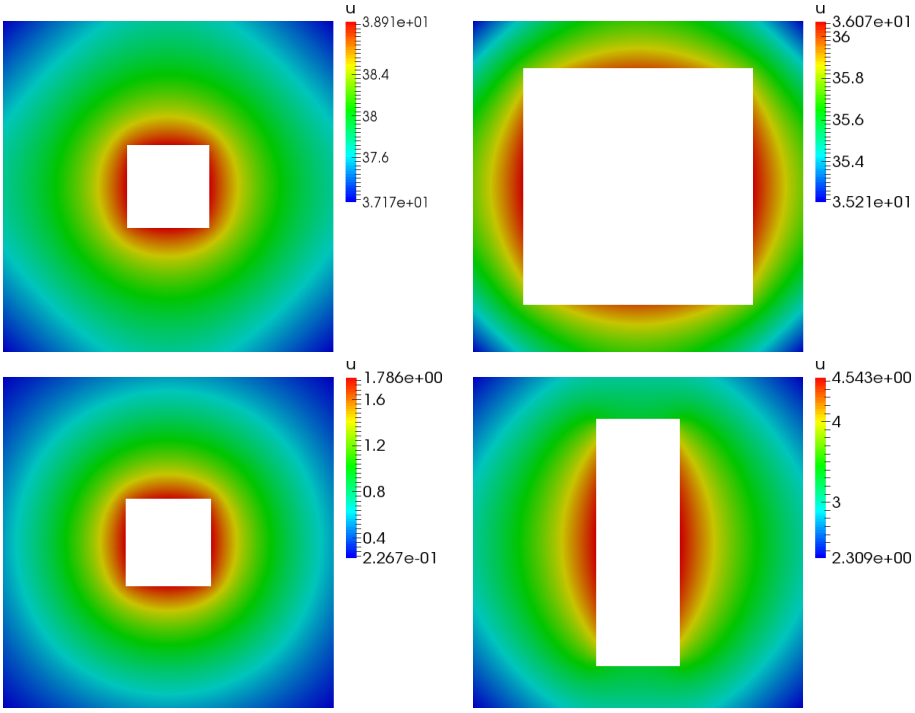

Figure D.8: *First four basis functions.*

Table D.2: *Output error bounds and effectivity metrics as function of N.*

N	$\Delta^s_{N,\text{ave}}$	$\eta^s_{N,\max}$	$\eta^s_{N,\text{ave}}$
10	7.50×10^{-1}	17.65	10.93
20	4.20×10^{-2}	17.94	11.34
30	4.02×10^{-3}	16.17	11.01
40	5.60×10^{-4}	20.81	11.37
50	1.12×10^{-4}	14.96	11.36
60	3.48×10^{-5}	14.33	11.08

D.2.4 ROM performances

In Fig. D.9, the outcomes provided by the FE model and the ROM, for a randomly chosen $\mu = (1.176, 0.761, 0.530)$ and $N = 60$, are compared, and the difference between the two is plotted as well.

In Tab. D.2 the output error bounds and effectivity metrics as function of basis functions employed are presented. The values have been averaged over 100 samples.

D.3 Heat transfer: thermal fin

D.3.1 Problem description

This problem address the performance of a heat sink for cooling electronic components. The heat sink is modelled as a spreader (see Fig. D.10, depicted in blue) which supports a plate fin exposed to flowing air (depicted in red, Fig. D.10). The heat transfer from the fin to the air is taken into account with the Biot number, which is the parameter μ_1. The second parameter is the relative length of the fin with respect to the spreader, and it

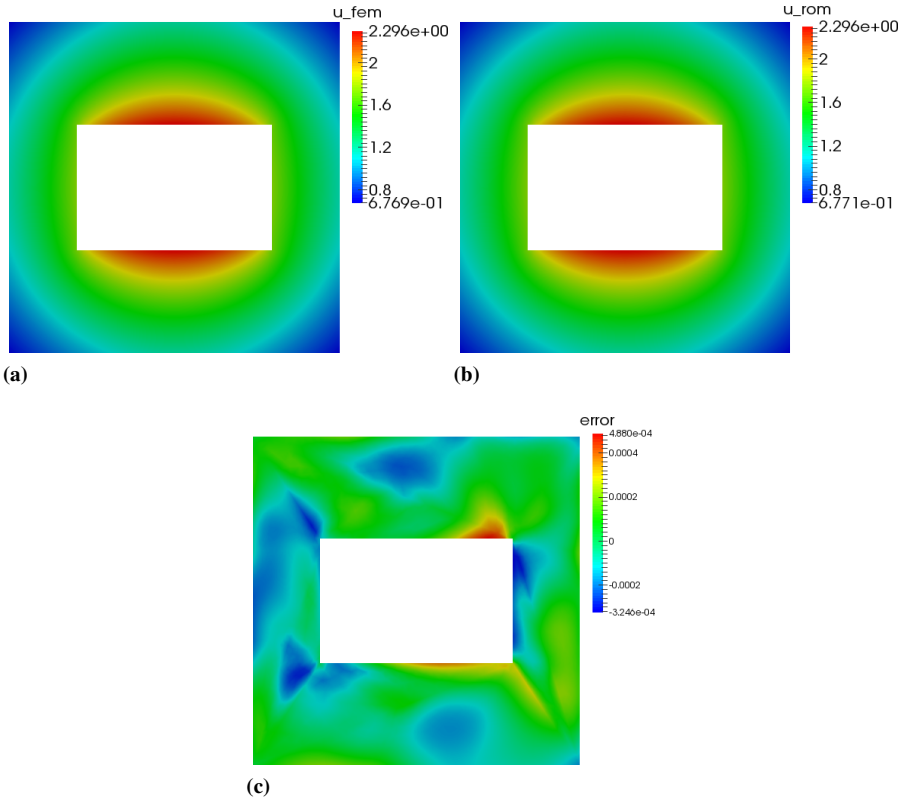

Figure D.9: *Comparison between FE model (a), ROM (b) for* $\mu = (1.176, 0.761, 0.530)$. *The difference between the two solutions is reported in (c).*

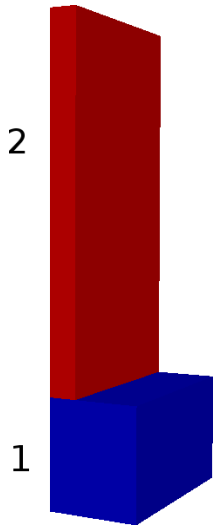

Figure D.10: *Subdomain division.*

is labelled as μ_2. The third parameter μ_3 is the ratio between the thermal conductivity of the spreader and the of the fin. The ranges of the parameters are the following:

$$\mu_1 \in [0.1, 1.0],$$

$$\mu_2 \in [0.5, 10.0],$$

$$\mu_3 \in [1.0, 10.0].$$

D.3.2 Boundary conditions

Uniform heat flux is imposed at the base of the spreader. Robin boundary conditions are imposed on the vertical face of the fin. The homogeneous Neumann conditions are imposed at all other surfaces.

D.3.3 Parametrized formulation

The bilinear form associated to the left-hand-side of the problem is given by:

$$a_o(w, v; \mu) = \mu_3 \int_{\Omega_o^1} \nabla u_o(\mu) \cdot \nabla v + \int_{\Omega_o^2(\mu_2)} \nabla u_o(\mu) \cdot \nabla v + \mu_1 \int_{\Gamma_{\text{side}}} u_o(\mu)\, v. \quad \text{(D.11)}$$

A constant heat flux is imposed on the bottom wall and in equation it reads:

$$F_o(v) = \int_{\Gamma_{\text{bottom}}} v. \quad \text{(D.12)}$$

The output of interest $s_o(\mu)$ is computed as

$$s_o(\mu) = F_o(u(\mu)). \quad \text{(D.13)}$$

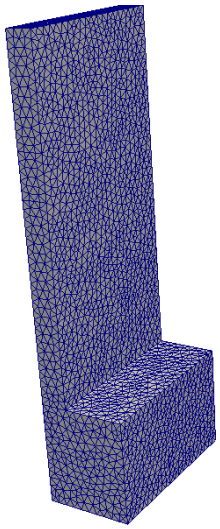

Figure D.11: *Finite element mesh.*

D.3.4 Finite element model

The Finite Element method, employing P1 elements, has been chosen as the "truth" model. In Fig. D.11 the mesh of the reference domain is reported, and features 22 979 elements.

D.3.5 Basis functions selection

The basis functions have been obtained by orthogonalization, through a Gram-Schimdt procedure, of snapshots computed for greedly selected parameters spanning a Ξ_{train} with cardinality equal to 3000. In Fig. D.12 the graph showing the maximum absolute error bound with respect to the number of basis functions employed is reported.

In Fig. D.13, the first four snapshots are depicted.

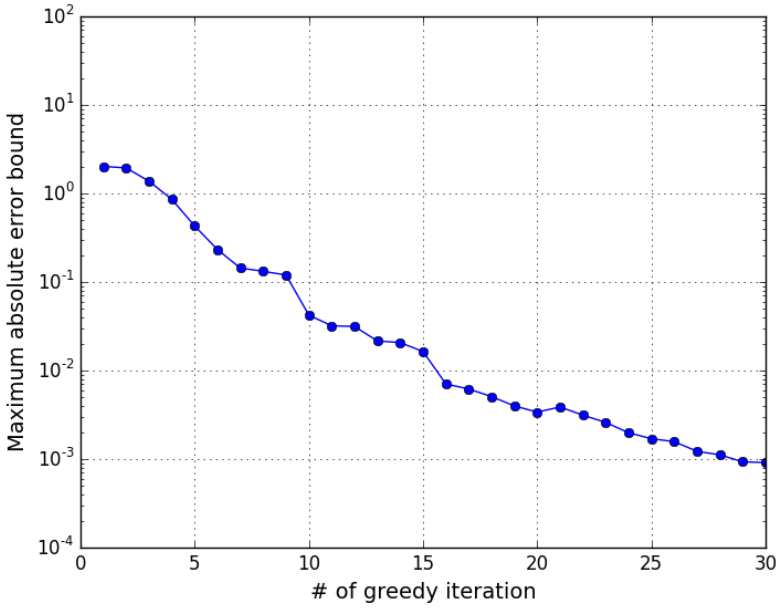

Figure D.12: *Maximum absolute error bound with respect to the number of basis functions employed.*

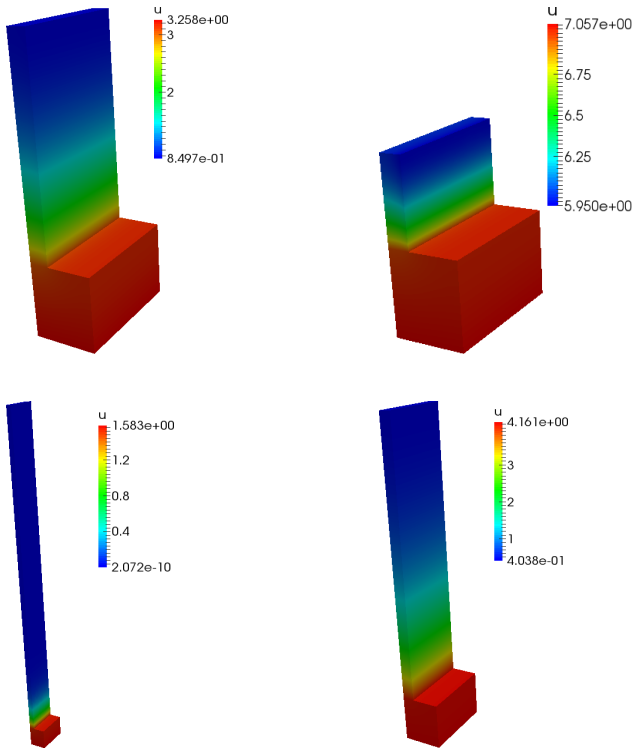

Figure D.13: *First four basis functions.*

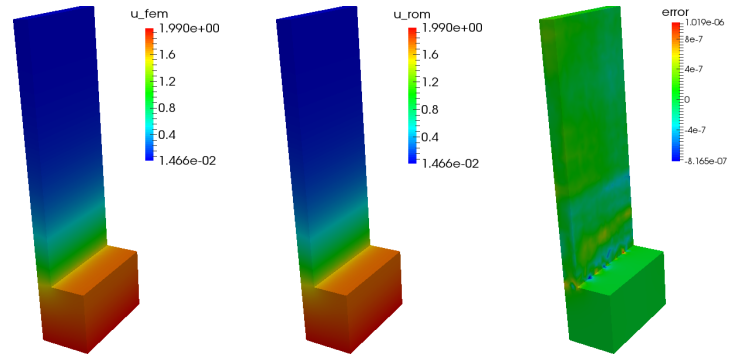

(a) (b) (c)

Figure D.14: *Comparison between FE model (a), ROM (b) for* $\mu = (0.75, 2.39, 1.74)$. *The difference between the two solutions is reported in (c).*

Table D.3: *Output error bounds and effectivity metrics as function of* N.

N	$\Delta^s_{N,\text{ave}}$	$\eta^s_{N,\max}$	$\eta^s_{N,\text{ave}}$
10	3.11×10^{-4}	7.46	4.26
20	2.71×10^{-6}	8.12	4.28
30	1.94×10^{-7}	8.82	4.64

D.3.6 ROM performances

In Fig. D.14, the outcomes provided by the FE model and the ROM, for a randomly chosen $\mu = (0.75, 2.39, 1.74)$ and $N = 30$, are compared, and the difference between the two is plotted as well.

In Tab. D.3 the output error bounds and effectivity metrics as function of basis functions employed are presented. The values have been averaged over 100 samples.

D.4 A linear elasticity block

D.4.1 Parametrized formulation

Figure D.15 reports the subdomain division of the elastic block that has been modelled. The bilinear form associated to the left-hand-side of the problem is given by:

$$a(w, v) = \sum_{p=1}^{8} \mu_p \int_{\Omega^p} \frac{\partial v_i}{\partial x_j} C_{ijkl} \frac{\partial w_k}{\partial x_l} + 10 \int_{\Omega^9} \frac{\partial v_i}{\partial x_j} C_{ijkl} \frac{\partial w_k}{\partial x_l}, \tag{D.14}$$

where μ_p is the ratio between the Young modulus of the Ω^p and Ω^9 subdomains, respectively, and μ_p

$$\mu_p \in [1.0, 100.0] \qquad \text{for } p = 1, \dots, 8. \tag{D.15}$$

The following boundaries conditions have been applied:

$$\begin{cases} \mathbf{n} \cdot w = \mu_9 \quad \text{on } \Gamma_1, & \text{(D.16)} \\ \mathbf{n} \cdot w = \mu_{10} \quad \text{on } \Gamma_2, & \text{(D.17)} \\ \mathbf{n} \cdot w = \mu_{11} \quad \text{on } \Gamma_3, & \text{(D.18)} \\ w = 0 \quad \text{on } \Gamma \setminus (\Gamma_1 \cup \Gamma_2 \cup \Gamma_3), & \text{(D.19)} \end{cases}$$

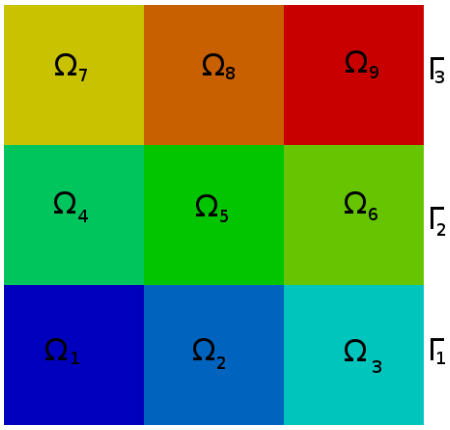

Figure D.15: *Subdomain division.*

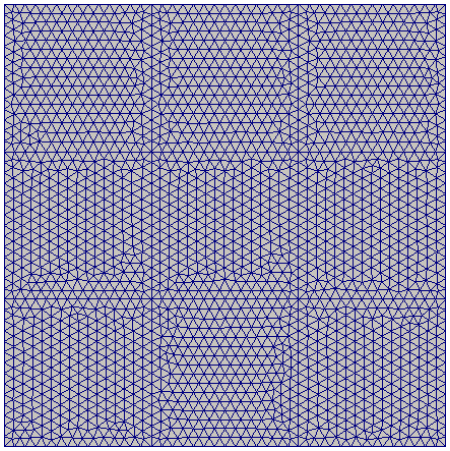

Figure D.16: *Finite element mesh.*

where

$$\mu_p \in [-1.0, 1.0] \qquad \text{for } p = 9, \dots, 11. \tag{D.20}$$

The output of interest $s(\mu)$ is computed as

$$s(\mu) = \int_{\Gamma_1 \cup \Gamma_2 \cup \Gamma_3} w(\mu). \tag{D.21}$$

D.4.2 Finite element model

The Finite Element method, employing P1 elements, has been chosen as the "truth" model. In Fig. D.16 is reported the mesh, which features 4152 elements.

D.4.3 Basis functions selection

The basis functions have been obtained by orthogonalization, through a Gram-Schimdt procedure, of snapshots computed for greedly selected parameters spanning a Ξ_{train} with cardinality equal to 2048. In Fig. D.17 the graph showing the maximum absolute error bound with respect to the number of basis functions employed is reported.

In Fig. D.18, the first four snapshots are depicted.

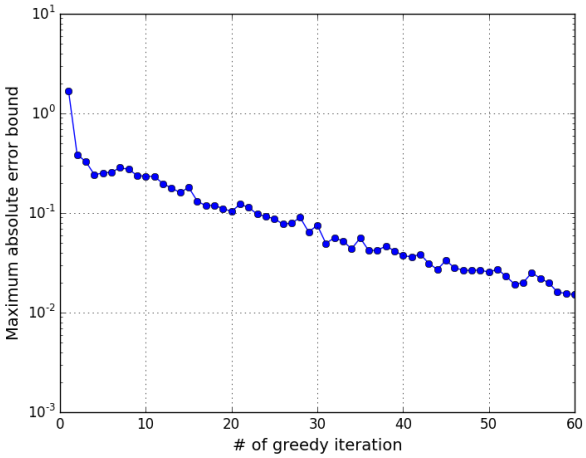

Figure D.17: *Maximum absolute error bound with respect to the number of basis functions employed.*

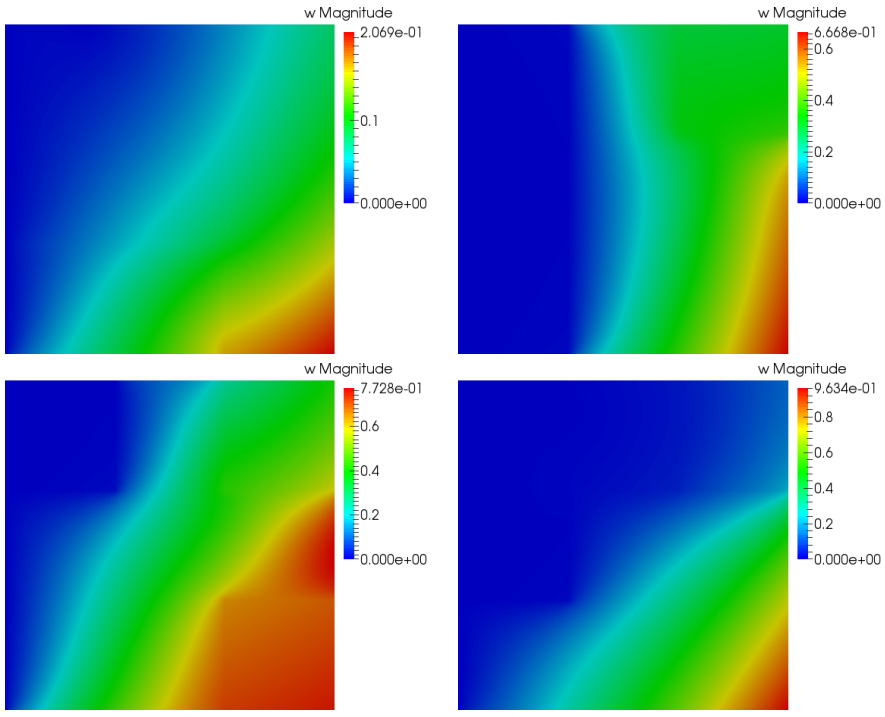

Figure D.18: *First four basis functions.*

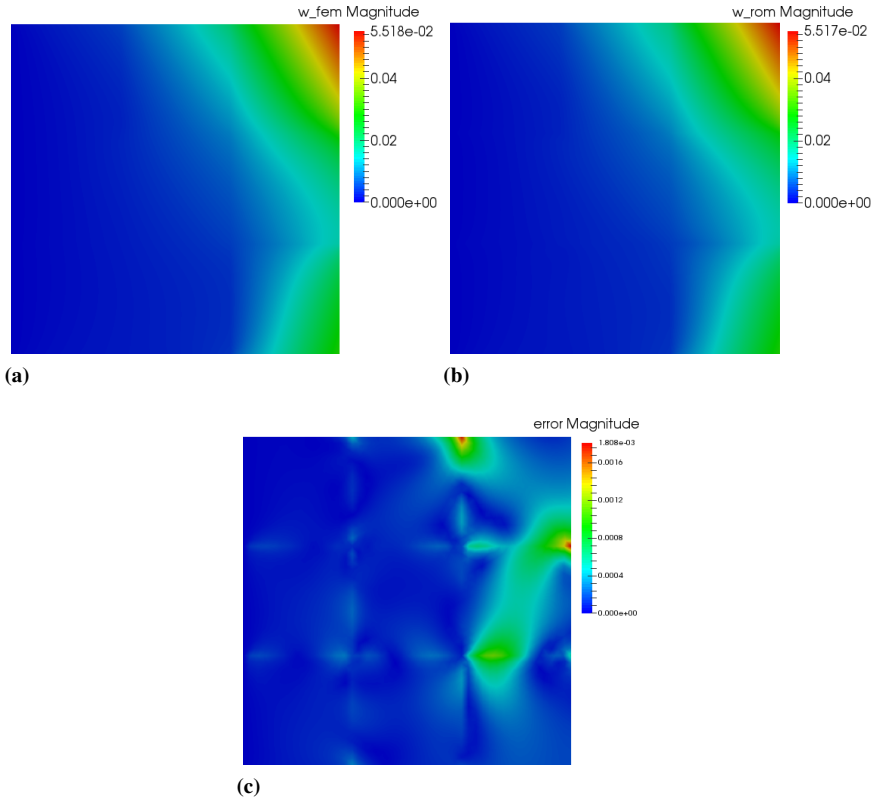

Figure D.19: *Comparison between FE model (a), ROM (b) for* $\mu = (7.737, 7.124, 0.729, 4.620, 3.072, 6.314, 3.590, 7.687, -0.804, 0.129, -0.232)$. *The difference between the two solutions is reported in (c).*

D.4.4 ROM performances

In Fig. D.19, the outcomes provided by the FE model and the ROM, for a randomly chosen

$$\mu = (7.737, 7.124, 0.729, 4.620, 3.072, 6.314, 3.590, 7.687, -0.804, 0.129, -0.232),$$

and $N = 53$, are compared, and the difference between the two is plotted as well.

In Tab. D.4 the output error bounds and effectivity metrics as function of basis functions employed are presented. The values have been averaged over 100 samples.

Table D.4: *Output error bounds and effectivity metrics as function of* N.

N	$\Delta^s_{N,\text{ave}}$	$\eta^s_{N,\max}$	$\eta^s_{N,\text{ave}}$
10	0.21	365.99	25.02
20	1.56×10^{-3}	20.74	1.25
30	6.03×10^{-4}	27.11	1.79
40	1.76×10^{-4}	138.70	2.22
50	1.00×10^{-4}	58.82	1.62
60	4.50×10^{-5}	17.58	1.16

List of Figures

1.1 Geometry employed in SERPENT code for representing the system configuration. . . . 11
1.2 Geometry of the pin employed in SERPENT code. . . . 11
1.3 Mesh employed for the finite element calculations. . . . 14
1.4 The four reactor configurations simulated. The perturbed areas, with respect to nominal configuration (Case i), are highlighted in red. . . . 19
1.5 Reactivity calculations for the configuration corresponding to Case i. . . . 21
1.6 Thermal flux shape for Case i: reference (a), POD (b), and MM (c). Data are reported in arbitrary units. . . . 22
1.7 Reactivity calculations for the configuration corresponding to Case ii. . . . 24
1.8 Thermal flux shape for Case ii: reference (a), POD (b), and MM (c). Data are reported in arbitrary units. . . . 25
1.9 Reactivity calculations for the configuration corresponding to Case iii. . . . 27
1.10 Reactivity calculations for the configuration corresponding to Case iv. . . . 29
1.11 The first four POD basis functions for the thermal group. . . . 30
1.12 The first four MM basis functions for the thermal group. . . . 31
1.13 Energy of POD functions for the thermal group. . . . 32
1.14 Relative information taken into account with respect to the number of functions employed for the POD spatial basis. . . . 32

2.1 Conceptual flow chart for the Offline step. . . . 41
2.2 Conceptual flow chart for the Online step. . . . 41
2.3 Exponential fit of the $\beta_{\text{inf}-\text{sup}}$ stability constant. . . . 50
2.4 Simplified 3D model employed 52
2.5 Three different positions of the control rod, in red, followed by water, in blue. . . . 52
2.6 $y - z$ view of the parametrized domain. . . . 52
2.7 Domain decomposition of: the original domain with $\mu = -10\,\text{cm}$ (a) and (b); reference domain (c). . . . 53
2.8 (a) Reference domain Ω, and (b) Original domain $\Omega(\mu)$. . . . 54
2.9 Spatial mesh adopted for the one rod model. . . . 55

2.10 Non-dimensional maximum relative error bound, with respect to the number of basis functions employed. . . . 56
2.11 Thermal neutron flux shape [1/cm^2 s] provided by the ROM, employing $N = 70$ basis functions, at the last time step. . . . 57
2.12 Thermal neutron flux shape [1/cm^2 s] assumed as "truth" solution, at the last time step. . . . 57
2.13 3D model of the TRIGA reactor with three control rods. . . . 59
2.14 Control rods spatial domain subdivision. . . . 60
2.15 Spatial mesh adopted for the three rods model. . . . 60
2.16 Non-dimensional maximum relative error bound, with respect to the number of basis functions employed. . . . 62
2.17 Employed sections to visualize the thermal flux. . . . 63
2.18 Thermal flux [1/cm^2 s], provided by the ROM, inside the control rod spatial domains for different combination of the parameters. . . . 64
2.19 Thermal flux [1/cm^2 s], assumed as "truth" solution, inside the control rod spatial domains for different combination of the parameters. . . . 64

3.1 Map of the TRIGA Mark II reactor core (a), and $x - z$ model employed for the RB method. . . . 73
3.2 RB triangulation of the reference domain. . . . 74
3.3 RB triangulation of the original domain $\Omega_o(\mu)$. . . . 75
3.4 Delaunay triangulation (blue line) and Voronoi tessellation (dotted line) of the initial set (a), of the next iteration (b), and at last iteration. . . . 77
3.5 Energy of the POD modes. . . . 78
3.6 High fidelity FE spatial flux distribution [cm^{-2} s^{-1}]. . . . 79
3.7 Neutron flux distribution [cm^{-2} s^{-1}] provided by the ROM, as function of N. . . . 80
3.8 Spatial error between the ROM and the FE solution [a.u.], as function of N. . . . 81

A.1 Map of the TRIGA Mark II reactor core. . . . 90
A.2 Fuel rod structures. Values are measured in centimeters [cm]. . . . 90
A.3 Control rod structure. Values are measured in centimeters [cm]. . . . 91

B.1 Analysed fuel pin and surrounding lead. Radial sizes at nominal conditions (room temperature), expressed in mm. . . . 96
B.2 Longitudinal (r, z) view of the modelled geometry. . . . 96
B.3 Main boundary conditions applied for the neutronic model. . . . 100
B.4 Main boundary conditions applied for the thermal-fluid dynamic model. 100
B.5 Meshed geometry 102
B.6 Transversal (x, y) cross section view of the SERPENT geometry. . . . 103
B.7 Longitudinal (x, z) cross section view of the SERPENT geometry. . . . 103
B.8 Fuel macroscopic capture cross-section versus temperature of energy group 3. . . . 104
B.9 Fuel macroscopic capture cross-section versus density of energy group 3. 105
B.10 Lead macroscopic capture cross-section versus temperature of energy group 3. . . . 106

B.11 Lead macroscopic capture cross-section versus density of energy group 3. 106
B.12 k_{eff} estimate versus fuel temperature. SERPENT: bullets, COMSOL: lines. . . . 107
B.13 k_{eff} estimate versus relative fuel axial expansion. SERPENT: bullets, COMSOL: lines. . . . 108
B.14 k_{eff} estimate versus lead density variation. SERPENT: bullets, COMSOL: lines. . . . 109
B.15 Axial neutron flux profiles within the active height. SERPENT: bullets, COMSOL: lines. . . . 109
B.16 Relative difference between axial neutron fluxes computed by COMSOL and SERPENT. . . . 110
B.17 Channel temperature field at nominal power conditions. . . . 111
B.18 Cladding outer temperature and lead bulk temperature versus the z-coordinate, at nominal power conditions. . . . 111
B.19 Velocity field inside the fluid domain. . . . 112
B.20 Outer fuel radius and inner cladding radius, as a function of the axial coordinate, at nominal power conditions and at room temperature conditions. 112
B.21 Total pin power during the transient case study with a reactivity insertion of 150 *pcm*. . . . 114
B.22 Average fuel temperature during the transient case study with a reactivity insertion of 150 *pcm*. . . . 114
B.23 Fuel axial expansion during the transient case study with a reactivity insertion of 150 *pcm*. . . . 115
B.24 Average gap size during the transient case study with a reactivity insertion of 150 *pcm*. . . . 115
B.25 Axial profile of the cladding outer surface temperature during the transient case study with a reactivity insertion of 150 *pcm*. . . . 116
B.26 Total pin power during the transient case study with inlet lead temperature increase of 20°C. . . . 116
B.27 Average fuel temperature during the transient case study with inlet lead temperature increase of 20°C. . . . 117
B.28 Axial profile of the cladding outer surface temperature during the transient case study with inlet lead temperature increase of 20°C. . . . 118

C.1 Longitudinal (r, z) view of the modelled geometry. . . . 123
C.2 Meshed geometry. . . . 125
C.3 Energy of the POD modes. . . . 129
C.4 Normalized neutron flux provided by the FE model (a), by the ROM (b), and the spatial error (c) for a representative configuration $\mu = (0.146, 1.445)$. 132
C.5 Normalized neutron flux provided by the FE model (a), by the ROM (b), and the spatial error (c) for a representative configuration $\mu = (0.387, 1.466)$. 133
C.6 Temperature field provided by the FE model (a), by the ROM (b), and the spatial error (c) for a representative configuration $\mu = (0.366, 1.188)$. 134
C.7 Temperature field provided by the FE model (a), by the ROM (b), and the spatial error (c) for a representative configuration $\mu = (0.144, 1.137)$. 135

D.1 Finite element mesh. . . . 142

D.2 Maximum absolute error bound with respect to the number of basis functions employed. . . . 143
D.3 First four basis functions. . . . 143
D.4 Comparison between FE model (a), ROM (b) for $\mu = (6.68, 0.94)$. The difference between the two solutions is reported in (c). . . . 144
D.5 Finite element mesh. . . . 145
D.6 RB triangulation. . . . 146
D.7 Maximum absolute error bound with respect to the number of basis functions employed. . . . 146
D.8 First four basis functions. . . . 147
D.9 Comparison between FE model (a), ROM (b) for $\mu = (1.176, 0.761, 0.530)$. The difference between the two solutions is reported in (c). . . . 148
D.10 Subdomain division. . . . 149
D.11 Finite element mesh. . . . 150
D.12 Maximum absolute error bound with respect to the number of basis functions employed. . . . 151
D.13 First four basis functions. . . . 151
D.14 Comparison between FE model (a), ROM (b) for $\mu = (0.75, 2.39, 1.74)$. The difference between the two solutions is reported in (c). . . . 152
D.15 Subdomain division. . . . 153
D.16 Finite element mesh. . . . 153
D.17 Maximum absolute error bound with respect to the number of basis functions employed. . . . 154
D.18 First four basis functions. . . . 154
D.19 Comparison between FE model (a), ROM (b) for a given μ. The difference between the two solutions is reported in (c). . . . 155

List of Tables

1.1 Isotopic composition of the SERPENT input materials. 12
1.2 Neutronic parameters generated by the SERPENT code. 12
1.3 Reactivity calculations for the configuration corresponding to Case i. . . 20
1.4 Reactivity calculations for the configuration corresponding to Case ii. . 23
1.5 Reactivity calculations for the configuration corresponding to Case iii. . 26
1.6 Reactivity calculations for the configuration corresponding to Case iv. . 28

2.1 Neutronic parameters generated by means of the SERPENT code. . . . 39
2.2 Computational time per single cpu per single time step. 58
2.3 Relative error bounds in L^2 norm, at the last time step. 58
2.4 Effectivity. 58
2.5 Computational time per single cpu per single time step. 63
2.6 Relative error bounds in L^2 norm, at the last time step. 65
2.7 Effectivity. 65

3.1 Neutronic quantities employed for the simulations (Sartori et al., 2014b). 74
3.2 Absolute error $e_\lambda(\mu)$ [pcm] with respect to number of basis functions employed. Values have been computed for 100 samples, randomly chosen. 79
3.3 Error $e_\Phi(\mu)$ between the neutron flux provided by the ROM and by the high fidelity FE model. 82
3.4 Average computational time [s] and speed-up. 82

B.1 Main parameters of the analysed core single-channel (Sarotto et al., 2009) 95
B.2 Energy structure adopted in multi-group neutron diffusion 95
B.3 Segregated groups 102
B.4 Isotopic composition of the SERPENT input materials. 104

C.1 Average absolute error $e_\lambda(\mu)$ as function of the basis functions employed for the neutron flux N_f, without thermal feedbacks. Values have been computed for 100 samples, randomly chosen. 130

C.2 Average absolute error $e_\lambda(\mu)$ as function of the basis functions employed for the temperature N_T, taking into account the thermal feedbacks. Values have been computed for 100 samples, randomly chosen, and employing 14 basis functions for the neutron flux. 130
C.3 Average computational time and speed-up. 136

D.1 Output error bounds and effectivity metrics as function of N. 144
D.2 Output error bounds and effectivity metrics as function of N. 147
D.3 Output error bounds and effectivity metrics as function of N. 152
D.4 Output error bounds and effectivity metrics as function of N. 155

List of Algorithms

2.1 Greedy algorithm (no time dependency) 50
2.2 Efficient greedy algorithm (no time dependency) 51
2.3 Efficient POD-greedy algorithm (time-dependent) (Quarteroni et al., 2011) 51

Bibliography

Alemberti, A., Carlsson, J., Malambu, E., Orden, A., Struwe, D., Agostini, P., Monti, S., 2011. European lead fast reactor–ELSY. Nuclear Engineering and Design 241, 3470–3480.

Alloni, D., di Tigliole, A.B., Cammi, A., Chiesa, D., Clemenza, M., Magrotti, G., Pattavina, L., Pozzi, S., Prata, M., Previtali, E., et al., 2014. Final characterization of the first critical configuration for the triga mark ii reactor of the university of pavia using the monte carlo code mcnp. Progress in Nuclear Energy 74, 129–135.

Amestoy, P.R., Duff, I.S., L'Excellent, J.Y., 2000. Multifrontal parallel distributed symmetric and unsymmetric solvers. Computer Methods in Applied Mechanics and Engineering 184, 501–520.

Ascher, U.M., Petzold, L.R., 1997. Computer Methods for Ordinary Differential Equations and Differential-Algebraic Equations. SIAM.

Atwell, J., King, B., 2004. Reduced order controllers for spatially distributed systems via proper orthogonal decomposition. SIAM Journal on Scientific Computing 26, 128–151.

Aufiero, M., Cammi, A., Fiorina, C., Luzzi, L., Sartori, A., 2013. A multi-physics time-dependent model for the Lead Fast Reactor single-channel analysis. Nuclear Engineering and Design 256, 14–27.

Avramova, M.N., Ivanov, K.N., 1997. Verification, validation and uncertainty quantification in multi-physics modeling for nuclear reactor design and safety analysis. International Journal of Heat and Mass Transfer 40, 4191–4196.

Balay, S., Abhyankar, S., Adams, M.F., Brown, J., Brune, P., Buschelman, K., Eijkhout, V., Gropp, W.D., Kaushik, D., Knepley, M.G., McInnes, L.C., Rupp, K., Smith, B.F., Zhang, H., 2014. PETSc Web page. URL http://www.mcs.anl.gov/petsc.

Ballarin, F., Faggiano, E., Manzoni, A., Quarteroni, A., Rozza, G., 2013. Patient-specific haemodynamics of coronary artery bypass grafts: clinical imaging and reduced order models .

Bandini, G., Meloni, P., Polidori, M., 2011. Thermal-hydraulics analyses of ELSY lead fast reactor with open square core option. Nuclear Engineering and Design 241, 1165–1171.

Barrault, M., Maday, Y., Nguyen, N.C., Patera, A.T., 2004. An 'empirical interpolation' method: application to efficient reduced-basis discretization of partial differential equations. Comptes Rendus Mathematique 339, 667–672.

Bergmann, M., Colin, T., Iollo, A., Lombardi, D., Saut, O., Telib, H., 2014. Reduced order models at work in aeronautics and medicine, in: Quarteroni, A., Rozza, G. (Eds.), Reduced Order Methods for Modeling and Computational Reduction. Springer International Publishing. volume 9 of *MS&A - Modeling, Simulation and Applications*, pp. 305–332.

Buchan, A., Pain, C., Fang, F., Navon, I., 2013. A POD reduced-order model for eigenvalue problems with application to reactor physics. International Journal for Numerical Methods in Engineering .

Burkardt, J., Gunzburger, M., Lee, H.C., 2006. Centroidal Voronoi tessellation-based reduced-order modeling of complex systems. SIAM Journal on Scientific Computing 28, 459–484.

Cammi, A., Di Marcello, V., Luzzi, L., Memoli, V., 2011. The Multi-Physics Modelling Approach Oriented to Safety Analysis of Innovative Nuclear Reactors, in: Acosta, M. (Ed.), Advances in Energy Research. Nova Science Publishers, Inc., Hauppauge, NY. volume 5, pp. 171–214.

Cammi, A., Ponciroli, R., di Tigliole, A.B., Magrotti, G., Prata, M., Chiesa, D., Previtali, E., 2013. A zero dimensional model for simulation of TRIGA mark II dynamic response. Progress in Nuclear Energy 68, 43 – 54.

Carlberg, K., Bou-Mosleh, C., Farhat, C., 2011. Efficient non-linear model reduction via a least-squares Petrov–Galerkin projection and compressive tensor approximations. International Journal for Numerical Methods in Engineering 86, 155–181.

Carlberg, K., Farhat, C., Cortial, J., Amsallem, D., 2013. The gnat method for nonlinear model reduction: effective implementation and application to computational fluid dynamics and turbulent flows. Journal of Computational Physics 242, 623–647.

CASL, 2012, . Consortium for Advanced Simulation of Light Water Reactors (CASL). http://www.casl.gov/.

Chadwick, Oblozinsky, Herman, Greene, McKnight, Smith, Young, MacFarlane, Hale, Frankle, Kahler, Kawano, Little, Madland, Moller, Mosteller, Page, Talou, Trellue, White, Wilson, Arcilla, Dunford, Mughabghab, Prity-chenko, Rochman, Sonzogni, Lubitz, Trumbull, Weinman, Brown, Cullen, Heinrichs, McNabb, Derrien, Dunn, Larson, Leal, Carlson, Block, Briggs, Cheng, Huria, Zerkle, Kozier, Courcelle, Pronyaev, , van der Marck, 2006. ENDF/B-VII.0: Next Generation Evaluated Nuclear Data Library for Nuclear Science and Technology. Nuclear Data Sheets 102, 2931.

Chatterjee, A., 2000. An introduction to the proper orthogonal decomposition. Current Science 78, 808–817.

Chen, P., Quarteroni, A., Rozza, G., 2013. Simulation-based uncertainty quantification of human arterial network hemodynamics. International journal for numerical methods in biomedical engineering 29, 698–721.

COMSOL, 2011, . COMSOL Multiphysics 4.2a, User's Guide. COMSOL Inc.

Cuong, N.N., Veroy, K., Patera, A.T., 2005. Certified real-time solution of parametrized partial differential equations, in: Handbook of Materials Modeling. Springer, pp. 1529–1564.

Du, Q., Faber, V., Gunzburger, M., 1999. Centroidal Voronoi tessellations: applications and algorithms. SIAM review 41, 637–676.

Duderstadt, J.J., Hamilton, L.J., 1976. Nuclear Reactor Analysis. John Wiley and Sons, New York.

Eaton, J.W., Bateman, D., Hauberg, S., 2008. GNU Octave Manual Version 3.

Fu, L., Zhengpei, L., Yongming, H., 1997. Harmonics synthesis method for core flux distribution reconstruction. Progress in Nuclear Energy 31, 369–372.

Gelsomino, F., Rozza, G., 2011. Comparison and combination of reduced-order modelling techniques in 3D parametrized heat transfer problems. Mathematical and Computer Modelling of Dynamical Systems 17, 371–394.

General Atomic, 1964, . TRIGA Mark II Reactor General Specifications and Description. General Atomic Company, U.S.A.

Geuzaine, C., Remacle, J.F., 2009. Gmsh: A 3-D finite element mesh generator with built-in pre-and post-processing facilities. International Journal for Numerical Methods in Engineering 79, 1309–1331.

GIF, 2010, . Generation IV International Forum, Annual Report. Available at: http://www.gen-4.org/PDFs/GIF-2010-Annual-Report.pdf.

Ginestar, D., Miro, R., Verdu, G., Hennig, D., 2002. A transient modal analysis of a BWR instability event. Journal of Nuclear Science and Technology 39, 554–563.

Girardi, E., Guérin, P., Dulla, S., Nervo, M., Ravetto, P., 2012. Comparison of direct and quasi-static methods for neutron kinetic calculations with the EDF R and D COCAGNE code. Technical Report. American Nuclear Society, Inc., 555 N. Kensington Avenue, La Grange Park, Illinois 60526 (United States).

Grepl, M.A., Patera, A.T., 2005. A posteriori error bounds for reduced-basis approximations of parametrized parabolic partial differential equations. ESAIM: Mathematical Modelling and Numerical Analysis 39, 157–181.

Haasdonk, B., Ohlberger, M., 2008. Reduced basis method for finite volume approximations of parametrized linear evolution equations. ESAIM: Mathematical Modelling and Numerical Analysis 42, 277–302.

Hernandez, V., Roman, J.E., Vidal, V., 2005. SLEPc: A scalable and flexible toolkit for the solution of eigenvalue problems. ACM Trans. Math. Software 31, 351–362.

Holmes, P., Lumley, J., Berkooz, G., 1996. Turbolence, Coherent Structures, Dynamical Systems and Symmetry. Cambridge University Press.

Huynh, D., Knezevic, D., Chen, Y., Hesthaven, J.S., Patera, A., 2010. A natural-norm successive constraint method for inf-sup lower bounds. Computer Methods in Applied Mechanics and Engineering 199, 1963–1975.

Huynh, D.B.P., Rozza, G., Sen, S., Patera, A.T., 2007. A successive constraint linear optimization method for lower bounds of parametric coercivity and inf–sup stability constants. Comptes Rendus Mathematique 345, 473–478.

Ito, K., Ravindran, S., 1998. A reduced basis method for control problems governed by pdes, in: Control and estimation of distributed parameter systems. Springer, pp. 153–168.

Ito, K., Ravindran, S.S., 2001. Reduced basis method for optimal control of unsteady viscous flows. International Journal of Computational Fluid Dynamics 15, 97–113.

Jones, E., Oliphant, T., Peterson, P., et al., 2001–. SciPy: Open source scientific tools for Python. URL http://www.scipy.org/.

Kirk, B.S., Peterson, J.W., Stogner, R.H., Carey, G.F., 2006. `libMesh`: A C++ Library for Parallel Adaptive Mesh Refinement/Coarsening Simulations. Engineering with Computers 22, 237–254.

Knezevic, D.J., Peterson, J.W., 2011. A high-performance parallel implementation of the certified reduced basis method. Computer Methods in Applied Mechanics and Engineering 200, 1455 – 1466.

Koning, A., Forrest, R., Kellett, M., Mills, R., Henriksson, H., Rugama, Y., 2006. The JEFF-3.1 Nuclear Data Library. Technical Report. NEA – OECD. JEFF Report 21.

Lamarsh, J.R., 1977. Introduction to nuclear reactor theory, 3rd Edition. Addison-Wesley Publishing Company.

Lassila, T., Manzoni, A., Rozza, G., 2012. On the approximation of stability factors for general parametrized partial differential equations with a two-level affine decomposition. ESAIM: Mathematical Modelling and Numerical Analysis 46, 1555–1576.

Lehoucq, R.R.B., Sorensen, D.D.C., Yang, C.C., 1998. Arpack User's Guide: Solution of Large-Scale Eigenvalue Problems with Implicityly Restorted Arnoldi Methods. Volume 6. SIAM.

Liang, Y., Lee, H., Lim, S., Lin, W., Lee, K., Wu, C., 2002. Proper orthogonal decomposition and its applications–part I: theory. Journal of Sound and Vibration 252, 527–544.

Logg, A., Mardal, K.A., Wells, G.N., et al., 2012. Automated Solution of Differential Equations by the Finite Element Method. Springer. doi:10.1007/978-3-642-23099-8.

Machiels, L., Maday, Y., Oliveira, I.B., Patera, A.T., Rovas, D.V., 2000. Output bounds for reduced-basis approximations of symmetric positive definite eigenvalue problems. Comptes Rendus de l'Académie des Sciences-Series I-Mathematics 331, 153–158.

Maday, Y., 2006. Reduced basis method for the rapid and reliable solution of partial differential equations, in: Proceedings of International Conference of Mathematicians, Madrid. European Mathematical Society Eds.

Mahadevan, V.S., Ragusa, J.C., Mousseau, V.A., 2012. A verification exercise in multiphysics simulations for coupled reactor physics calculations. Progress in Nuclear Energy 55, 12–32.

Manzoni, A., Quarteroni, A., Rozza, G., 2012. Computational Reduction for Parametrized PDEs: Strategies and Applications. Milan Journal of Mathematics 80, 283–309.

MATLAB® and SIMULINK® software, 2005, . The MathWorks, Inc.

Merzari, E., Ninokata, H., 2011. Proper orthogonal decomposition of the flow in a tight lattice rod-bundle. Nuclear Engineering and Design 241, 559–572.

Miró, R., Ginestar, D., Verdú, G., Hennig, D., 2002. A nodal modal method for the neutron diffusion equation. Application to BWR instabilities analysis. Annals of Nuclear Energy 29, 1171–1194.

Mylonakis, A., Varvayanni, M., Catsaros, N., Savva, P., Grigoriadis, D., 2014. Multi-physics and multi-scale methods used in nuclear reactor analysis. Annals of Nuclear Energy 72, 104–119.

Nguyen, N.C., Rozza, G., Huynh, D.B.P., Patera, A.T., 2010. Reduced Basis Approximation and a Posteriori Error Estimation for Parametrized Parabolic PDEs: Application to Real-Time Bayesan Parameter Estimation, John Wiley & Sons, Ltd, 2010, Ch. 8, 157–185.

Nguyen, N.C., Rozza, G., Patera, A.T., 2009. Reduced basis approximation and a posteriori error estimation for the time-dependent viscous Burgers' equation. Calcolo 46, 157–185.

Noor, A.K., Peters, J.M., 1980. Reduced basis technique for nonlinear analysis of structures. Aiaa journal 18, 455–462.

Obaidurrahman, K., Singh, O.P., 2010. Spatial neutronic coupling aspects in nuclear reactors. Nuclear Engineering and Design 240, 2755–2760.

Ortega, J., Rheinboldt, W., 2000. Iterative Solution of Nonlinear Equations in Several Variables. Society for Industrial and Applied Mathematics.

Patera, A.T., Rozza, G., 2007. Reduced Basis Approximation and A Posteriori Error Estimation for Parametrized Partial Differential Equations, MIT Pappalardo Graduate Monographs in Mechanical Engineering, online at http://augustine.mit.edu.

Pearson, K., 1901. On lines and planes of closest fit to system of points in space. Philosophical Magazine 2, 559–572.

Peterson, J.S., 1989. The reduced basis method for incompressible viscous flow calculations. SIAM Journal on Scientific and Statistical Computing 10, 777–786.

Pironneau, O., Hecht, F., Morice, J., 2012. freeFEM++, v3.19. URL http://www.freefem.org/ff++.

Pitton, G., Rozza, G., 2015. Recent advances on nonlinear Reduced Order Modelling for stability and bifurcations problems in incompressible fluid dynamics. Submitted.

Prill, D., Class, A., 2014. Semi-automated proper orthogonal decomposition reduced order model non-linear analysis for future BWR stability. Annals of Nuclear Energy 67, 70 – 90.

Prud'homme, C., Rovas, D.V., Veroy, K., Machiels, L., Maday, Y., Patera, A.T., Turinici, G., 2002. Reliable real-time solution of parametrized partial differential equations: Reduced-basis output bound methods. Journal of Fluids Engineering 124, 70–80.

Quarteroni, A., Rozza, G., Manzoni, A., 2011. Certified reduced basis approximation for parametrized partial differential equations and applications. Journal of Mathematics in Industry 1, 1–49.

Quarteroni, A., Valli, A., 2008. Numerical approximation of partial differential equations. Volume 23. Springer.

Rimpault, G., 2005. Algorithmic features of the ECCO cell code for treating heterogeneous fast reactor subassemblies, in: International Topical Meeting on Reactor Physics and Computations, Portland, Oregon.

Rozza, G., 2014. Fundamentals of Reduced Basis Method for problems governed by parametrized PDEs and applications, in: CISM Lectures notes "Separated Representation and PGD based model reduction: fundamentals and applications". Chinesta, F. and Ladeveze, P. (eds.), Springer Vienna.

Rozza, G., Huynh, D., Patera, A., 2008. Reduced basis approximation and a posteriori error estimation for affinely parametrized elliptic coercive partial differential equations. Archives of Computational Methods in Engineering 15, 1–47.

Salah, A.B., Hamidouche, T., D'Auria, F., 2008. Application of Best Estimate Computational Tools for Safety Accident Analysis in Nuclear Plants, in: LÃn, W. (Ed.), Energy Conversion: New Research. Nova Science Publishers, Inc., Hauppauge, NY. volume 5, pp. 143–159.

Sarotto, M., Artioli, C., Grasso, G., Gugiu, D., 2009. ELSY core design static, dynamic and safety parameters with the open square FA. Technical Report. ENEA FPN-P91X-006.

Sartori, A., Baroli, D., Cammi, A., Chiesa, D., Luzzi, L., Ponciroli, R., Previtali, E., Ricotti, M.E., Rozza, G., Sisti, M., 2014a. Comparison of a Modal Method and a Proper Orthogonal Decomposition approach for multi-group time-dependent reactor spatial kinetics. Annals of Nuclear Energy 71, 217 – 229.

Sartori, A., Baroli, D., Cammi, A., Luzzi, L., Rozza, G., 2014b. A Reduced Order Model for Multi-Group Time-Dependent Parametrized Reactor Spatial Kinetics, in: Proceedings of the 2014 22nd International Conference on Nuclear Engineering (ICONE22), Prague, Czech Republic, July 7-11, 2014, Paper 30707. © ASME 2014.

Sartori, A., Cammi, A., Luzzi, L., Rozza, G., 2014c. A reduced basis approach for modelling the movement of nuclear reactor control rods. Submitted to Journal of Nuclear Engineering and Radiation Science .

Sartori, A., Cammi, A., Luzzi, L., Rozza, G., 2014d. Reduced basis approaches in time-dependent non-coercive settings for modelling the movement of nuclear reactor control rods. Submitted to Communication in Computational Physics. Revision 2015 .

Sartori, A., Cammi, A., Luzzi, L., Rozza, G., 2015. Multi-physics reduced order models for analysis of Lead Fast Reactor single channel. In preparation for Annals of Nuclear Energy .

Schultz, M.A., 1961. Nuclear reactor kinetics and control. McGraw-Hill.

SERPENT, 2011, . PSG2 / Serpent Monte Carlo Reactor Physics Burnup Calculation Code. URL http://montecarlo.vtt.fi.

Sirovich, L., 1987. Turbulence and the dynamics of coherent structures. I–III. Quarterly of Applied Mathematics 45, 561–590.

Stacey, W.M., 1969. Space-Time Nuclear Reactor Kinetics. Academic Press.

Tuček, K., Carlsson, J., Wider, H., 2006. Comparison of sodium and lead-cooled fast reactors regarding reactor physics aspects, severe safety and economical issues. Nuclear Engineering and Design 236, 1589–1598.

Veroy, K., Prud'homme, C., Rovas, D.V., Patera, A.T., 2003. A posteriori error bounds for reduced-basis approximation of parametrized noncoercive and nonlinear elliptic partial differential equations, in: Proceedings of the 16th AIAA computational fluid dynamics conference, pp. 23–26.

Watson, D.F., 1981. Computing the n-dimensional Delaunay tessellation with application to Voronoi polytopes. The computer journal 24, 167–172.

Weigand, B., Ferguson, J.R., Crawford, M.E., 1997. An extended Kays and Crawford turbulent Prandtl number model. International Journal of Heat and Mass Transfer 40, 4191–4196.

Wenfeng, L., Zhengpei, L., Fu, L., Yaqi, W., 2001. The three-dimensional power distribution control in load following of the heating reactor. Annals of Nuclear Energy 28, 741–754.

Wols, F., 2010. Transient analyses of accelerator driven systems using modal expansion techniques, M.S. Thesis, Delft University of Technology.

Xia, L., Jiang, J., Javidnia, H., Luxat, J.C., 2012. Performance evaluation of a 3-D kinetic model for CANDU reactors in a closed-loop environment. Nuclear Engineering and Design 243, 76–86.

Xia, L., Jiang, J., Luxat, J.C., 2014. Power distribution control of candu reactors based on modal representation of reactor kinetics. Nuclear Engineering and Design 278, 323–332.

Zanon, L., Veroy-Grepl, K., 2013. The reduced basis method for an elastic buckling problem. PAMM 13, 439–440.

Ringraziamenti

RINGRAZIO in primo luogo la mia sposa Lidia che in questi tre anni ha saputo sopportarmi, supportarmi, incoraggiarmi e donarmi due splendidi angioletti. Un grazie speciale va ai miei genitori che mi hanno permesso di arrivare fino a qui. Ringrazio di cuore anche i miei suoceri che ci hanno aiutato in quest'ultimo non facile periodo.

Ringrazio i Professori Antonio Cammi e Lelio Luzzi perché mi hanno guidato con pazienza in questo percorso, insegnandomi con parole ed esempi a crescere. Ringrazio il Professore Gianluigi Rozza che mi ha svezzato al mondo del Reduced Order Modelling e ha permesso di lavorare alla SISSA. Ringrazio il Professor Marco Ricotti per le sue parole.

Un grazie particolare va a Davide Baroli che un bel giorno mi disse: "Lo sai che esistono i POD?". Senza di lui questa tesi sarebbe stata molto diversa.

Ringrazio i miei colleghi d'ufficio Manu e Ponci: sono stati due anni spumeggianti e arricchenti. Grazie a Giuseppe per le belle discussioni matematiche e i suoi "ringraziamenti".

Ringrazio anche gli altri compagni d'avventura: Stefano (fin dal primo anno di università), Matteo, Carlo, Claudia, Marco.

Grazie dal profondo del cuore a Don Raffaele e Don Pierino, sotestegni e punti di riferimento.